



HAL
open science

Self-organized wave-like beating of actin bundles in a minimal actomyosin system

Marie Pochitaloff-Huvalé

► **To cite this version:**

Marie Pochitaloff-Huvalé. Self-organized wave-like beating of actin bundles in a minimal actomyosin system. Chemical Physics [physics.chem-ph]. Sorbonne Université, 2018. English. NNT : 2018SORUS318 . tel-02409881

HAL Id: tel-02409881

<https://theses.hal.science/tel-02409881>

Submitted on 13 Dec 2019

HAL is a multi-disciplinary open access archive for the deposit and dissemination of scientific research documents, whether they are published or not. The documents may come from teaching and research institutions in France or abroad, or from public or private research centers.

L'archive ouverte pluridisciplinaire **HAL**, est destinée au dépôt et à la diffusion de documents scientifiques de niveau recherche, publiés ou non, émanant des établissements d'enseignement et de recherche français ou étrangers, des laboratoires publics ou privés.

Sorbonne Université

Ecole doctorale Physique en Ile-de-France

Laboratoire Physico Chimie Curie — Institut Curie

**Auto-organisation de faisceaux d'actine oscillants
dans un système minimal d'actomyosine**

Par Marie Pochitaloff-Huvalé

Thèse de doctorat de Physique

Dirigée par Pascal Martin

Présentée et soutenue publiquement le 16 Octobre 2018

Devant un jury composé de :

Mathilde	Badoual	Professeur	Examinatrice
Laurent	Blanchoin	Directeur de recherche	Examineur
Kinneret	Keren	Professeur	Rapportrice
Pascal	Martin	Directeur de recherche	Directeur de thèse
Guillaume	Romet-Lemonne	Directeur de recherche	Rapporteur
Raphaël	Voituriez	Directeur de recherche	Président du jury



Manuscripts do not burn
The Master and Margarita — Mikhail Bulgakov



Acknowledgements

Doing a PhD is often described as a marathon ending by a final sprint, this image well illustrates the perseverance and the tenacity that we have to reinforce through these very intense years. During this marathon, we encountered many difficulties that we had to overcome patiently, in that sense the PhD was also an obstacle course, during which I found a precious help among many people that I would like to deeply thank for their moral and scientific support.

I want to thank Pascal, my supervisor, to let me work on that project I found exciting, I am convinced that his will of perfection had really forced me to make my minimal system robust and improved my skills for presentation and writing.

I would like to thank the members of the jury for reviewing my work, it was a pleasure to discuss with you and receive your feedback on my work, it encourages me to continue in research ! First my examiners Kinneret Keren and Guillaume Romet-Lemonne, I am very grateful for your positive reports and your enthusiasm, thank you to the president of the jury Raphaël Voituriez, sorry for not having more theory in my work. I would like to thank in particular Mathilde Badoual and Laurent Blanchoin, who were also members of my jury but also followed my advances in my thesis committee and supported me during all my thesis.

It is the Thesis Advisory Committee (Cécile Sykes, Julie Plastino, Mathilde Badoual, Laurent Blanchoin and Nicolas Minc) that pushed me to go to the project I was the most excited about among the two initial projects I had at the beginning of my PhD. I chose the most ambitious and the most risky but it was worth it ! Thank you !

I would like to thank Laurent Blanchoin and his team in Grenoble who welcomed me, trained me and make me aware of the difficulties of working with an in vitro system, thanks Laurent for your support ad your advices during all my PhD; Christophe for never making fun of me despite my dummy questions and the ugly pictures I sent you when my experiments did not work; Hajer for sharing with me your energy, your motivation,

you were doing experiments with me two weeks before your defense, you provided me a very precious help.

This work was made possible through the support I found in the lab, in fact the Sykes / Plastino team almost adopted me : I participated at their journal club, where I learned a lot on actin biochemistry. I was running every Tuesday to arrive on time at 12 pm not to have to make cakes. Julie and Cecile were always helpful when my experiments did not work and encouraged me a lot for not giving up. Thanks a lot ! Thank you Bassam for our nice discussions and the single molecule experiments we have done together, it was great to work with you ! I would like to thank Axel or his precious help at the end of my thesis for his sharp advices to improve my manuscript and my thesis presentation, thanks a lot Axel to have taken the time despite your tight schedule. I would like to thank the members of the Martin team, who created a good atmosphere; Mathieu, my predecessor, who trained me as a Jedi Master in Matlab and experiments, thanks for your patience and the fun we had in Nikon Center ! Even though we worked on different projects, I'm thankful to Atitheb, who developed Matlab codes for some of my PhD projects, good luck for your PhD ! and Mélanie, for her positive attitude and the absurd jokes we made together and continuing to encourage me through hard times even after the end of your PhD, thanks Mélanie, I hope our ways will cross again in the future. Thank you Jonathan and Martial as alumni of the team for all your support. I would like to thank Laurence for guiding me through administrative procedures. Thank you Brigitte for your kindness and your warm welcome every morning, it was a good start for working days !

My time at Curie was made enjoyable in large part due to the many friends and colleagues I made along the way, and to the stimulating discussions we had, on a professional as well as personal, I want to express my gratitude. I would thus like to thank all my fellow labmates from UMR 168, including but not limited to: Tatiana, Mohamed, Chiara, Quentin, Bastien, Patricia, Alicia, Laura, Valentina, Fanny, Aude, Fabrice Thibault, Carles, Remy, Jean-Patrick, Louis, Nadir, Kocella, Kotryna, Amanda, Simon, Perrine and many more. Special mention to my office-mates Patricia and Isabelle, my ballet-mate Sarah, who gave me precious advices for my manuscript, not be desperate when my experiments were not working, wedding organization, LaTeX ... Julien who was always there to explain me actin biochemistry, myosin, TIRF, that ?black actin does not exist?. I am very thankful to Majdouline Antoine and Camille, who helped and supported me so much during my PhD (actin, pyrene assay, TIRF, Matlab) and have so kindly prepared me surprise with Julien for my PhD defense ! I wish you all the best for the future !

There are all the friends from ESPCI with whom life was happy and carefree : Dou-
nia, Simon, Simon Aymeric, Baptiste, Sacha, Romain, Alice, Alice, Eva, Marine, Elodie,
Corentin, Hubert, Emeric, Romain friends with whom I spent quality time.

I would like to thank my family for their encouragements and support ! Last but not
least, I would like to thank my husband Antoine ♡. My words lack when I want to express
it all.

The Curie Institute is a truly exceptional environment to do research in, not least
because of the access we have to great equipment and expertise. I gratefully acknowledge
John and Fahima for the biochemistry platform, Vincent, Francois Ludovic and Lucie
from the Nikon Center, for their training and their invaluable help with the microscopes.
I would like to thank all the people who somehow contributed to my ending up here,
teachers and mentors, and I would like to mention specifically: Timo Betz, Jacques Prost,
Rob Philips, Jane Kondev, Hernan Garcia.

My thoughts also go to Maxime Dahan and his family. I want to address my profound
gratitude to Maxime for helping me in difficult time in my PhD, he was a truly great
mentor.

Abbreviations

- **Arp2/3 complex:** Actin-related proteins 2 and 3 complex
- **ATP/ADP:** Adenosine TriPhosphate / Adenosine DiPhosphate
- **BSA:** Bovine Serum Albumin
- **DIC:** Differential Interference Contrast microscopy
- **DRC:** Dynein Regulatory Complex
- **DTT:** Dithiothreitol
- **EDTA:** Ethylene Diamine Tetraacetic Acid (chelating agent which sequesters Ca^{2+})
- **EGTA:** Ethylene Glycol-bis(β -aminoethyl ether)-N,N,N',N'-Tetraacetic Acid.
- **F-actin:** Filamentous-actin
- **G-actin:** Globular actin
- **GFP:** Green Fluorescence Protein
- **GTP/GDP:** Guanosine TriPhosphate / Guanosine DiPhosphate
- **HMM:** Heavy Mero Myosin
- **LMM:** Light Mero Myosin
- **NPF:** "Nucleation Promoting Factor" (promoting factor of actin nucleation)
- **WASP:** "Wiskott-Aldrich Syndrome Protein", (protein containing VCA domain, which can activate Arp 2/3 complex and initiate nucleation with branching, notably in lamellipodia of motile cells)
- **Pi:** Inorganic phosphate
- **PLL-g-PEG:** Poly-L-Lysine-grafted-Poly(Ethylene Glycol)

-
- **pWA**: VCA domain with a polyproline region, used *in vitro* to activate Arp 2/3 complex and to initiate branching nucleation in presence of actin
 - **TIRF microscopy**: Total Internal Reflection Fluorescence microscopy
 - **Tris**: Tris(hydroxymethyl)aminomethane
 - **SEM**: Scanning Electron Microscopy
 - **VCA, WA**: C-terminal domain of proteins of WASP/scar family. The region "verprolin homology", named V or W, is recruiting two actin monomers; the region cofilin homology, named C, and the acid sequence, named A respectively, is recruiting and activating Arp2/3 complex

Contents

Acknowledgements	v
Abbreviations	ix
General Introduction	3
1 Self-organization and Spontaneous oscillations	5
1.1 Self-Organization	5
1.1.1 What is self-organization ?	5
1.1.2 Self-organization in biological systems	6
1.1.3 Spontaneous oscillations	10
1.2 Spontaneous beating of eukaryotic flagella	14
1.2.1 Cilia and flagella : motile organelles	14
1.2.2 The axoneme : the core structure of cilia and flagella	15
1.2.3 Beating properties	16
1.2.4 Existing theoretical approaches of flagellar beating	25
2 The actomyosin system	31
2.1 The actin cytoskeleton	31
2.1.1 Actin : From monomers to filaments	31
2.1.2 Actin binding proteins	36
2.2 The myosins	40
2.2.1 Myosin topology	41
2.2.2 The chemomechanical cycle of myosin	43
2.2.3 Duty ratio and processivity	45
2.2.4 Experiments to characterize motor action	46
2.2.5 Recap of myosin II and myosin V properties (Table 2.3)	51
3 Materials and Methods	53
3.1 Micropatterning of an actin nucleation promoting factor	55

3.1.1	Surface passivation	55
3.1.2	Patterning of a nucleation promoting factor	56
3.1.3	Experimental chambers	57
3.2	The actomyosin polymerization mix	58
3.3	Image acquisition	60
3.4	Image analysis	62
3.4.1	Tracking of the actin bundles	62
3.4.2	Beating pattern analysis	64
4	Self-organized wave-like beating of actin bundles	67
4.1	Architecture of the actin network with or without myosins	67
4.1.1	In the absence of myosins	67
4.1.2	In the presence of active myosins : assembly of tight actin bundles .	71
4.2	Dynamic analysis: Spontaneous oscillations	74
4.2.1	General description of beating properties in the case of myosin II .	74
4.2.2	Comparing beating properties with myosin II to those with myosin V	78
4.2.3	Effect of bundle length on beating properties	81
4.2.4	Varying the concentration of the molecular motors	89
4.3	Distribution of myosin motors along a beating actin bundle	91
5	Conclusion and Discussion	99
5.1	Comparison to other oscillating systems	100
5.2	3D beating of actin bundles	103
5.3	How does myosin sense the shape of actin bundles?	105
6	Perspectives	109
	Appendices	115
A	Experimental protocol	117
A.1	Proteins preparation	117
A.1.1	G actin solution	117
A.1.2	Minimal set of proteins which ensures actin polymerization	117
B	References of purified proteins	119
B.1	Actin and actin-related proteins	119
B.1.1	Preparation of the proteins	119
B.1.2	Characteristics and storage conditions of the proteins	119
B.2	HMM Myosins	120

General Introduction

Living systems consume energy to move, change shape, divide and control their own morphology. To fulfill all these key processes, living systems are highly dynamic and require active mechanics over a broad range of length scales: from transport within cells at the molecular scale, mitosis and motility at the cellular scale, to morphogenesis of organs and whole animals at the multicellular scale. The diversity of the dynamics is ensured by the cytoskeleton. The cytoskeleton is composed of different biopolymers that are able to assemble and disassemble, resulting in networks of different architectures. The microtubule cytoskeleton is made of pipe-like filaments that are very rigid, whereas the actin cytoskeleton consists of cable-like filaments that are semi-flexible. Within the actin and microtubule cytoskeletons, motor proteins are present to exert forces that can deform, contract the network, or mediate transport of cargoes along the filaments, which provide tracks for these directed movements.

Understanding the incredible complexity of cellular processes constitutes a significant challenge for both biologists and physicists. To tackle this problem, two mainstream approaches have been developed. The top-down approach considers the cell in all its complexity and consists in perturbing the system to study the role of its molecular components. Development of genetic tools and super resolution microscopy has allowed to increase our knowledge with high precision. The second approach starts in the opposite way, by reducing the complexity of the system to identify general biophysical principles underlying cellular processes. To reach this goal, many *in vitro* model systems of purified motors and filaments that lack biochemical regulation have been recently developed. This bottom-up approach of reconstructing biological functionality with minimal components is useful because it allows to delineate between generic (*i.e.* that do not depend on molecular details) and specific properties in the more complicated biological systems.

Cytoskeletal filaments and molecular motors have been extensively studied at the single molecule level : we have a pretty good idea about how cytoskeletal filaments assemble/disassemble, their mechanical properties, their structure, as well as the mechanism of force

production and movement by single molecular motors (Howard, 2001). However their collective behavior remains poorly understood and cannot be explained only from their single molecule properties.

The main goal of my thesis was to study an *in vitro* minimal system comprising a network of actin filaments and myosin motors. Micropatterning of a nucleation promoting factor of actin polymerization allowed for the geometrical control of the network architecture by governing the spatial assembly of the actin filaments, which emerged out of the pattern parallel to each others and with the same polarity. We worked with two types of myosin motor, myosin II and myosin V, that we added in bulk to study how molecular motors reorganized such a network.

This experimental configuration led to the self-assembly of tight actin bundles that displayed periodic wave-like beating resembling that observed in eukaryotic flagella, *e.g.* in sperm cells. My work provides a detailed description of this dynamic phenomenon, aiming at clarifying the underlying biophysical mechanism and discuss its relevance for more complex biological systems.

Chapter 1

Self-organization and Spontaneous oscillations

1.1 Self-Organization

1.1.1 What is self-organization ?

Self-organization refers to the emergence of an overall order in time and space of a given system from the collective interaction of its many individual components (Camazine et al., 2001; Karsenti, 2008; Wedlich-Söldner and Betz, 2018). A large variety of examples are found in physical, chemical and biological systems, such as sand grains assembling into rippled dunes, chemical reactants forming swirling spirals, cells making up highly structured tissues, or birds joining together in a flocking formation (Fig. 1.1). When wind blows over a uniform field of sand, a pattern of regularly spaced ridges (Fig. 1.1.A) is formed through a set of forces attributable to gravity and wind acting on the sand particles (Anderson, 1990; Forrest and Haff, 1992). In the Belousov-Zhabotinsky chemical reaction, the mixture alternates between red and blue (Fig. 1.1.B) owing to changes in the charge state of the iron ions that catalyze the reaction. The mechanism for this reaction is very complex and is thought to involve around 18 components (Field and Foersterling, 1986). A group of animals can also show global order by synchronizing to some extent their behavioral state (Fig. 1.1.D) : In the case of starlings, they align their individual direction of motion, which results in flocks forming a tight sphere-like formation, frequently expanding and contracting and changing shape, seemingly without any sort of leader (Okubo, 1986). The pattern is an emergent property of the system rather than a property imposed on the system by an external ordering influence. Emergence refers to a process by which a system of interacting subunits acquire collectively qualitative

new properties that cannot be understood and predicted as the simple addition of their subunit individual contributions.

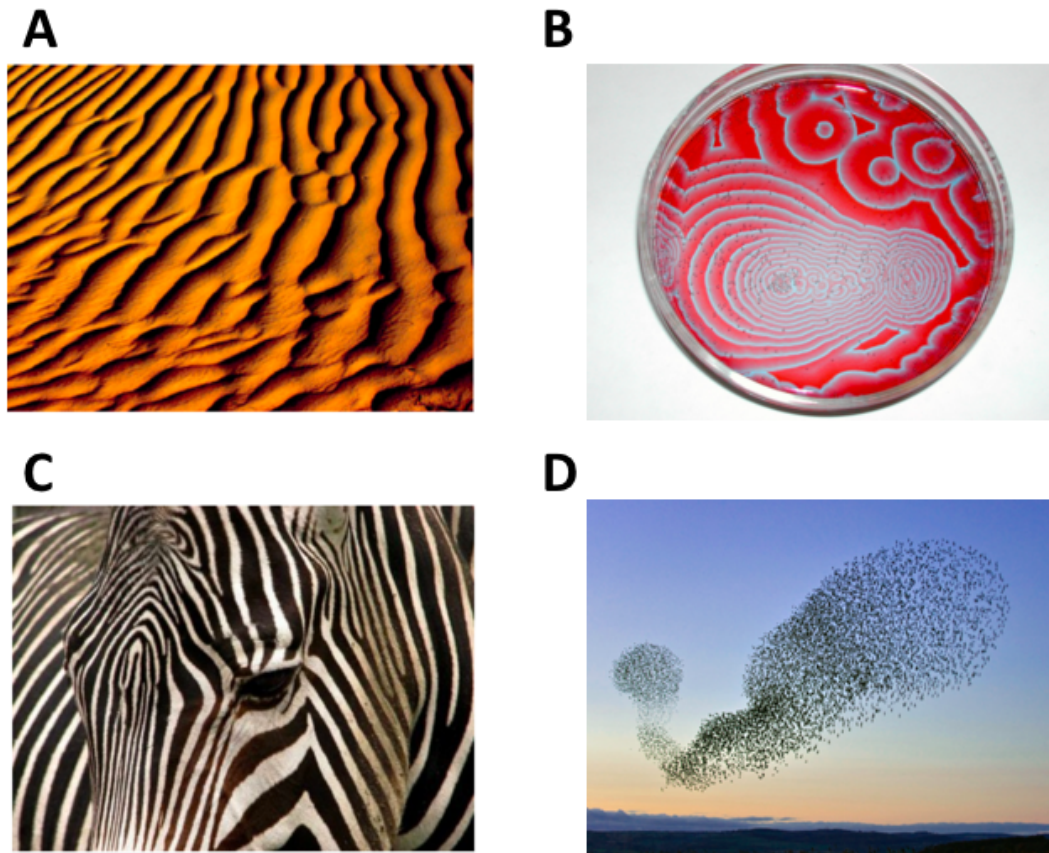


Figure 1.1: Examples of self-organization at the macroscopic scale. **A:** Rippled sand dunes, the wavelength is approximately 8 cm (Ball, 2012). **B:** Spiral waves produced by the Belousov-Zhabotinsky chemical reaction in a 14-cm-diameter Petri dish, in which the mixture alternates between red and blue owing to changes in the charge state of the iron ions that catalyze the reaction (Ball, 2012). **C:** Pattern of black and white stripes on zebra coat (complexitylabs.io/ecological-self-organization.) **D:** Flock of starling birds (www.telegraph.co.uk/news/earth/wildlife/8315106/Starling-flocks-how-they-form-into-incredible-wildlife-spectacles.html)

1.1.2 Self-organization in biological systems

Cellular systems Using the hydrolysis of Adenosine TriPhosphate (ATP) or Guanosine TriPhosphate (GTP) as a chemical energy source, cellular materials are known to produce a broad range of self-organized phenomena, most of which have evolved to perform a variety of cellular functions, including cell division, motility, shape changes, contraction (Karsenti, 2008; Wedlich-Söldner and Betz, 2018). All of them are supported by networks of cytoskeletal filaments and molecular motors, which form structures fundamentally out of equilibrium. This self-organization spans over several orders of magnitude in space and

time and involves a complex interplay between biochemical and biophysical processes. For example, molecular motors and cytoskeletal networks interact to drive the cell cycle (Fig. 1.2.A) : they are responsible for cell-shape changes, chromosome segregation, and cleavage to form two daughter cells from a mother cell. The movement of keratocytes is ensured by an interplay between the well-orchestrated dynamics of the actin cytoskeleton assembly at the leading edge of the cell and myosin motors contracting the cytoskeleton at the trailing edge of the cell (Allard and Mogilner, 2013) (Fig. 1.2.B). At a multicellular level, the compaction of a 8-cell-stage embryo, which is characterized by the transformation of the embryo from a loose cluster of spherical cells into a tightly packed spheroid (Fig. 1.2.C), is an important step of embryogenesis that will trigger the establishment of the first tissue-like structure of the embryo (White et al., 2016).

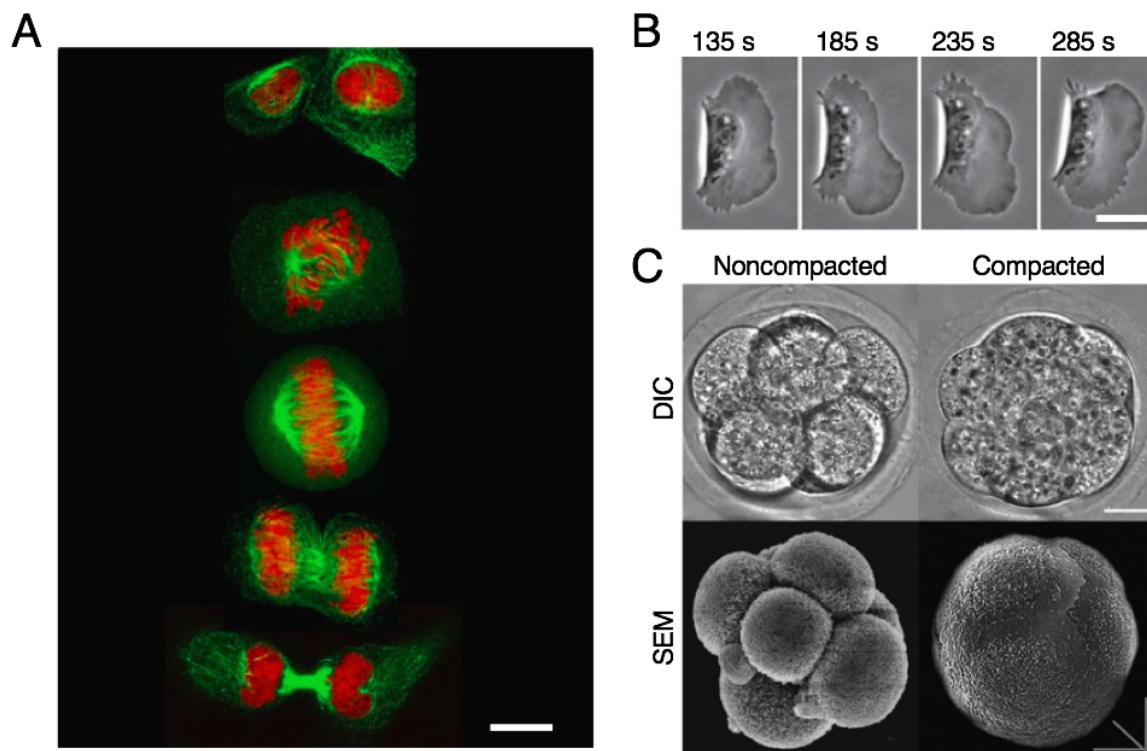


Figure 1.2: Examples of self-organization in cellular systems **A:** During the cell cycle, the cell undergoes a large panel of shape changes (<https://bigpictureeducation.com/cell-division-images>). Chromatin is labeled in red, the microtubules of the cytoskeleton in green. **B:** A keratocyte is a crawling cell, which protrudes its leading edge and contracts its trailing edge to move (Allard and Mogilner, 2013). Scale bar : 10 μm . Time (in s) is indicated at the top of each picture. **C:** Embryo compaction at 8 cell state (White et al., 2016). The embryo is shown before and after compaction, using Differential Interferential Contrast microscopy (DIC, top) and Scanning Electron Microscopy (SEM, bottom). Scale bars : 10 μm for DIC and 15 μm for SEM.

***In vitro* systems** Designing molecular or cellular systems that mimic cellular processes *in vitro*, detached from the complexity of the cell and/or of the *in vivo* environment of the cell, is a powerful approach for dissecting complex cellular phenomena. In particular, *in vitro* experiments have shed light on the key role of geometrical constraints for the selection of the emergent structures of the cytoskeleton.

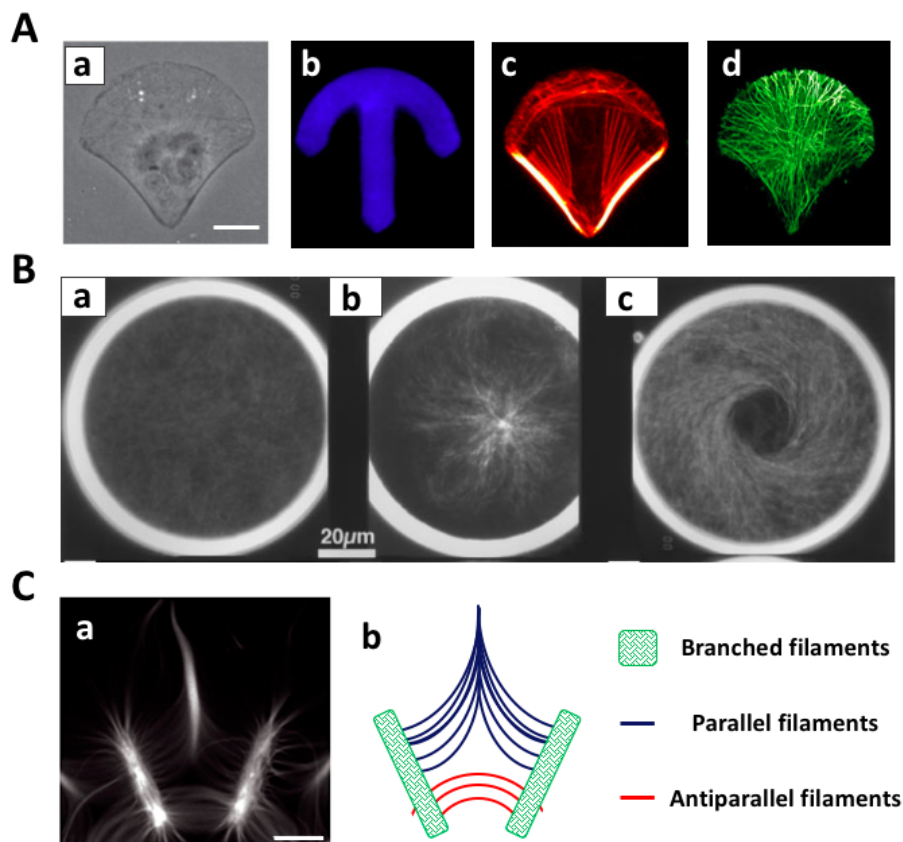


Figure 1.3: Examples of *in vitro* self-organization of cytoskeletal filaments due to geometrical constraints. **A:** RPE1 cell visualized in phase contrast (a) and plated on a fibronectin crossbow micropattern (b). Using a fluorescent label on actin, one sees that actin polymerizes in membrane ruffles on the curved adhesive edge, but assembles in contractile stress fibers anchored to fibronectin on the cell lateral edges. (c) Microtubule plus-end trajectories. Scale bar: 10 μm . Figure adapted from (They et al., 2006). **B:** Self-organization in the constrained geometry of micro-fabricated chambers etched in glass. Formation of a vortex as observed by dark-field microscopy in a chamber of diameter 90 μm and depth 5 μm . Microtubule polymerization has been initiated by heating the sample to 37 $^{\circ}\text{C}$. After 0.5 min, microtubules nucleate uniformly in the sample (a). After 1.5 min, an aster forms in the centre of the chamber (b). After 3 min, a steady-state vortex structure is observed (c). Figure from (Nédélec et al., 1997). **C:** Actin network formed from a star-branch array of a nucleation promoting factor of actin polymerization. Panel (a) shows a fluorescence image of the actin network in a micropatterned network. Panel (b) depicts the diversity of actin network structures formed: actin meshwork (green) on the patterned region, and parallel (blue) and antiparallel (red) filaments out of the pattern. Scale bar: 10 μm . Figure adapted from (Reymann et al., 2010)

At the single cell level, imposing adhesive constraints sets specific polarities and organization of the cytoskeleton (Thery et al., 2006) (Fig. 1.3.A). When microtubules with molecular motors are confined *in vitro* in a cylindrical geometry (Fig. 1.3.B.(a)), the system will first form an aster-like structure that is positioned almost at the center (Fig. 1.3.B.(b)), but when the microtubules continue to grow in this confined geometry, a vortex-like structure then emerges (Fig. 1.3.B.(c)) (Nédélec et al., 1997). In the case of the actin network, filaments can become aligned in parallel or antiparallel configurations by controlling the orientation of their growth thanks to surface micropatterning of a nucleation-promoting factor; the pattern can precisely set the geometrical boundary conditions of filament growth and orientation (Fig. 1.3.C.(a)) (Reymann et al., 2010). On micropatterned regions, a branched meshwork is formed. Only non-branched filaments grow out of the micropattern, with their barbed ends oriented outward. Filaments out of the patterns align parallel to each other, orthogonal to the nucleation region due to steric interactions. Away from the nucleation region, filaments can form either parallel or antiparallel network (Fig. 1.3.C.(b)), in a reproducible manner. Moreover, reconstituted systems with purified proteins allow to control their biochemical composition, and thus to modify this composition to shed light on the role of molecular components on self-organization. One can this way observe transitions between different "states" by varying components. Such approach naturally allows to develop a phase diagram such as in thermodynamics. For instance, one can study the effect of connectivity within the network and of motor concentrations on contractility of actin gels, by measuring the size of actomyosin condensates at steady state and the speed of their formation (Fig. 1.4), (Alvarado et al., 2013; Soares e Silva et al., 2011). These actomyosin systems raised the concept of active gels, which rely on contractility through active force generation and dissipation in a viscoelastic environment (Prost et al., 2015).

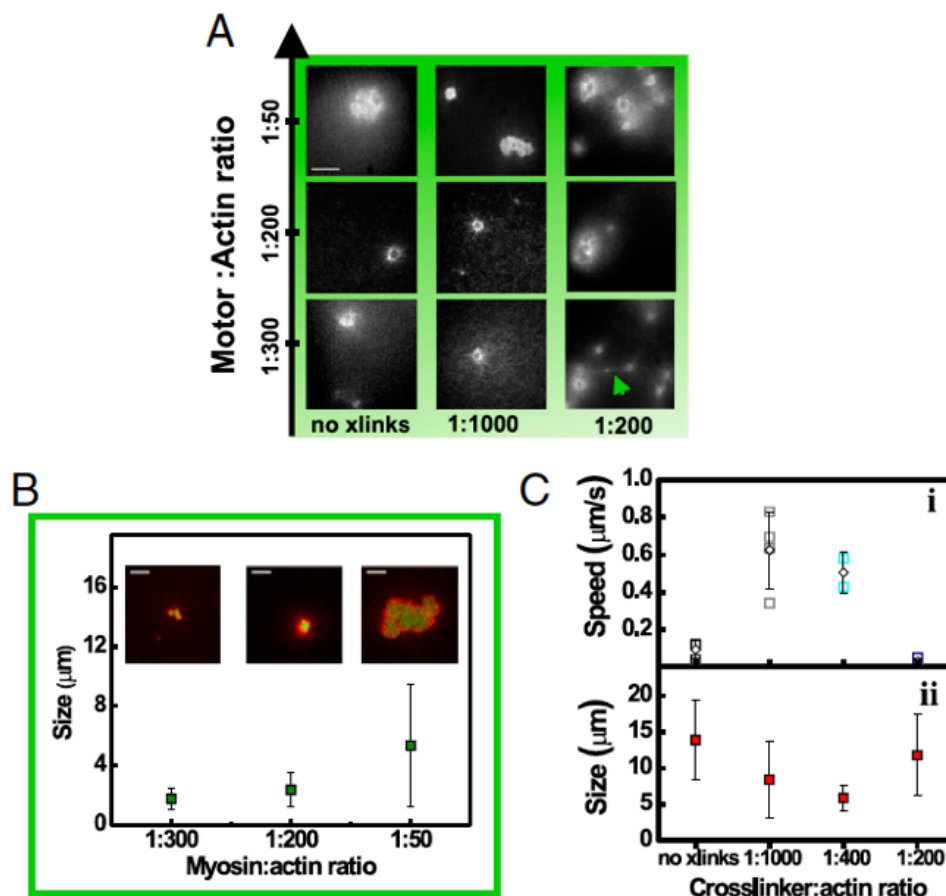


Figure 1.4: Phase diagram in a reconstituted system. The effect of motor and cross-link density on active coarsening of an actin network is characterized. **A:** Steady-state actin patterns observed in active networks containing varying concentrations of myosin motors and cross-links. Scale bar, 10 μm . **B:** The average size of actomyosin condensates increases with increasing motor density at fixed ratio of crosslinkers. Confocal images show that this size increase results from an increased degree of coalescence. Scale bars 5 μm . **C:** (*top*) The average speed of foci movement depends non monotonically on cross-link density at a fixed ratio of actin:myosin. Open squares represent individual data points; open diamonds represent the average speed for each cross-linker density. (*bottom*) The cross-linker density-dependence on the size of actomyosin condensates mirrors that of the contraction speed. All error bars represent Standard Deviations. Figure from (Soares e Silva et al., 2011)

1.1.3 Spontaneous oscillations

An important aspect of self-organization in living systems deals with the emergence of spontaneous oscillations. In cells, many of these oscillations arise from interactions between cytoskeletal filaments and assemblies of molecular motors that consume energy from ATP or GTP hydrolysis to power the oscillatory movements. Oscillations involving molecular motors can be found *in vivo* in many instances.

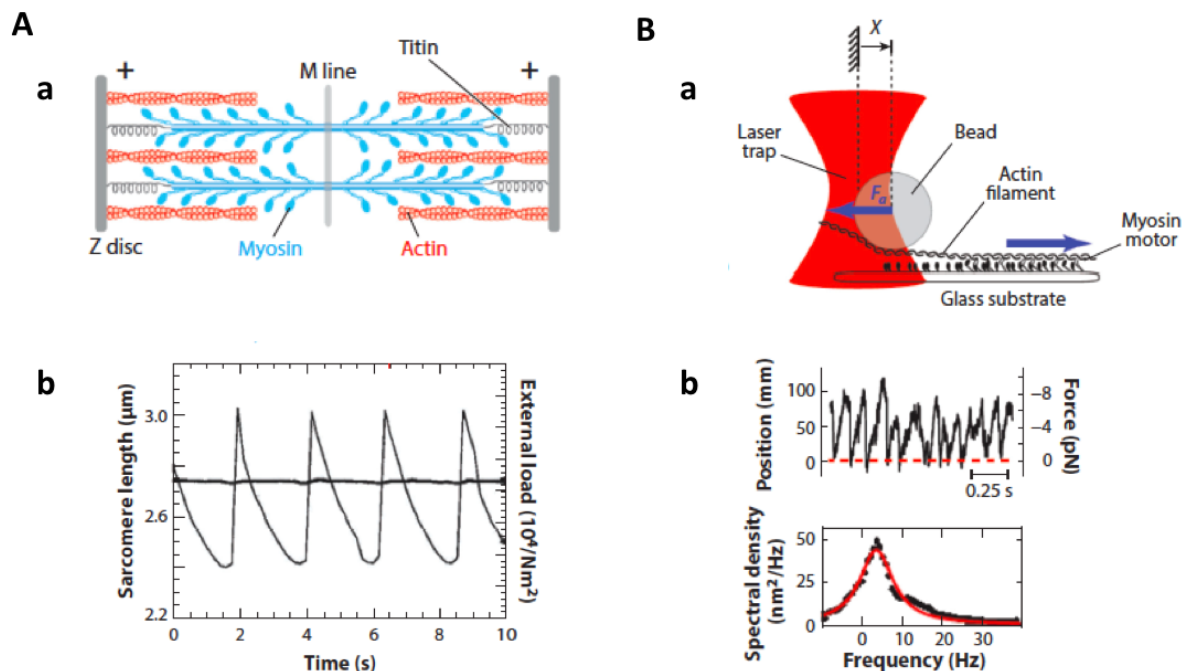


Figure 1.5: Oscillations with actin filaments and myosin motors. **A:** Sarcomere oscillations : (a) Schematic representation of the structure of a sarcomere. (b) Time course of a sarcomere length (*gray line*) in presence of an external load (*black line*) from (Beta and Kruse, 2017), adapted from (Guenther and Kruse, 2007). **B:** *In vitro* motor oscillations (a) Schematic of a gliding assay under elastic loading. Motors develop a force F_a on the actin filament held in an optical trap that exerts an elastic restoring force F . (b) Bead position as a function of time and corresponding spectral density from (Beta and Kruse, 2017), adapted from (Plaças et al., 2009)

A classic example is given by sarcomeres (Okamura and Ishiwata, 1988), (Fig. 1.5.A), which are the basic functional units of skeletal muscles. Myosin ("thick") filaments interdigitate with antiparallel ("thin") actin filaments such that the structure shortens when the motors are active. In presence of an external load on the sarcomere, this system can undergo periodic cycles of contractions and extensions can emerge. The asymmetric time course of the length of the oscillating sarcomere defines the system as a "relaxation oscillator", with a faster extension phase than the contraction phase. It has been suggested that the oscillations come from a collective effect in elastically-coupled motors (Jülicher and Prost, 1997) and not from chemical (Ca^{2+}) waves that drive the movement (Fabiato and Fabiato, 1978). This hypothesis has been confirmed with an *in vitro* reconstituted system, where an actin filament held by optical tweezers was brought into contact with a substrate covered with Heavy-MeroMyosin myosin II motors and started to oscillate spontaneously (Plaças et al., 2009) (Fig. 1.5.B).

Actin and myosins are also involved in the oscillations that have been observed beneath

the cell membrane, in a region called the cell cortex (Bornens et al., 1989; Paluch et al., 2005; Salbreux et al., 2007). The cell cortex consists in a thin layer of actin beneath the cell membrane that myosin motors can contract by generating forces. The contractile stresses generated by myosin motors can destabilize the cortex and fracture it. For example, the cortex oscillates after depolymerization of all microtubules in suspended lymphocytes (Bornens et al., 1989), or in fibroblasts after loss of adhesion (Salbreux et al., 2007).

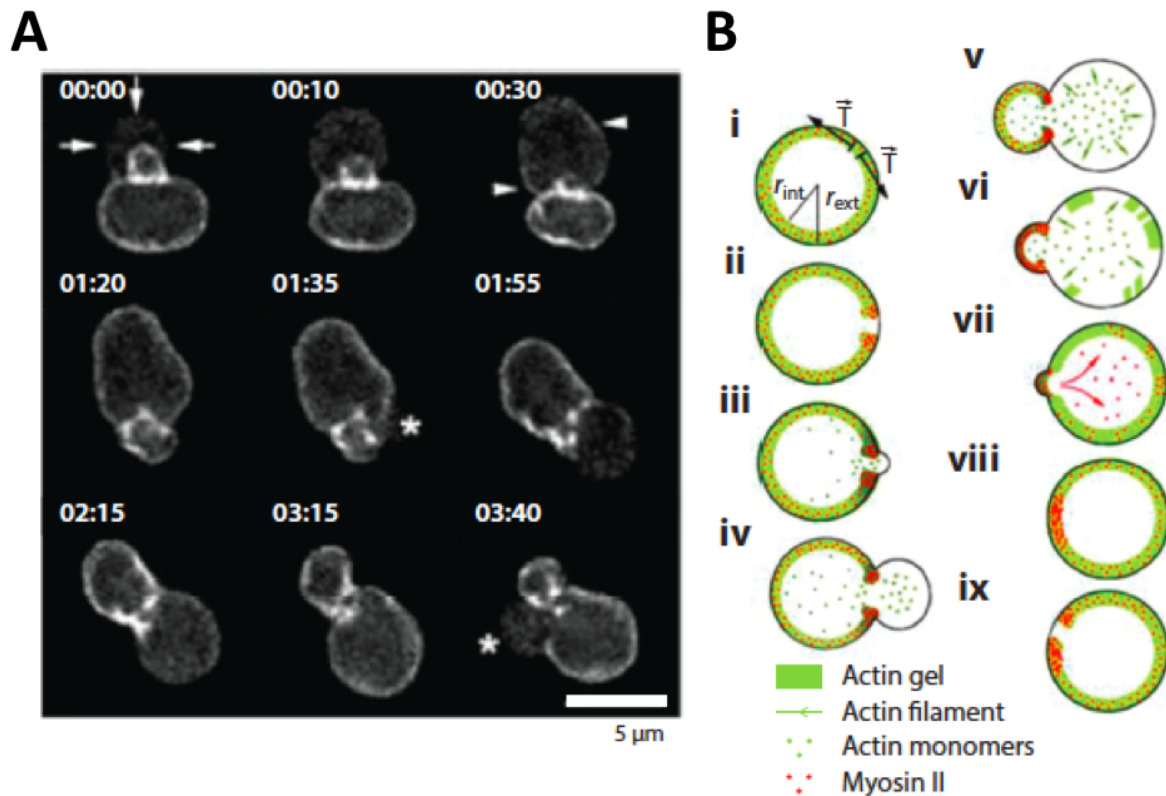


Figure 1.6: Cortex oscillations of lymphoblast fragments. **A:** Distribution of fluorescently labeled actin. **B:** Schematic description of the oscillation mechanism adapted from (Paluch et al., 2005)

In their studies on cell fragments, Paluch *et al.* showed that the oscillations in suspended cells resulted from localized breakage of the cortex (Paluch et al., 2005), which then retracted through the action of myosin, and subsequently reassembled (Fig. 1.6).

Other examples include oscillations of the mitotic spindle to determine the division plane in eukaryotic cells (Grill et al., 2005) and the regular beating of eukaryotic cilia and flagella (Howard, 2009; Satir and Christensen, 2007). Related to this last example, Sanchez *et al.* developed a minimal model system composed of microtubules and molecular motors which self-assemble into active bundles exhibiting beating patterns resembling those found in eukaryotic cilia and flagella.

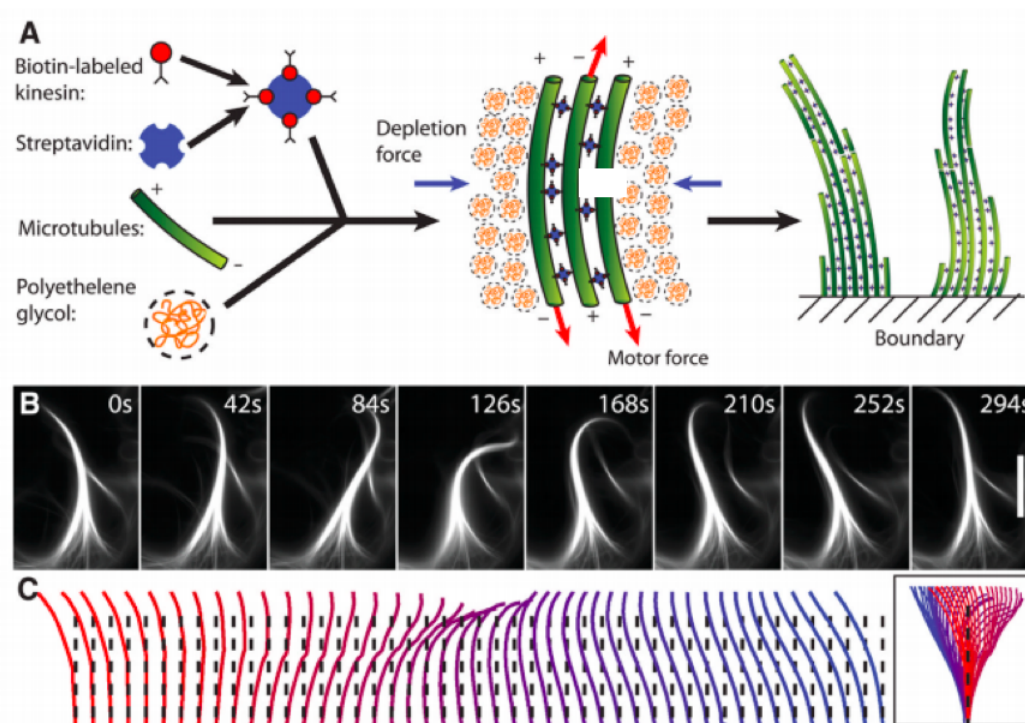


Figure 1.7: A minimal system of microtubules, molecular motors and depleting agent (polyethylene glycol) assembles into actively beating bundles. **A:** Schematic illustration of all components required for the assembly of active bundles. **B:** A sequence of images illustrating the beating pattern of an active bundle over one beat cycle. Scale bar is 30 μm . **C:** The conformations of the bending microtubule bundle indicates a fairly symmetric beating pattern that is reminiscent of those found in cilia and flagella. Figure from (Sanchez et al., 2011)

This observation allowed the authors to identify few essential components for the assembly of beating microtubule bundles: microtubules, kinesin assemblies and a depleting agent to promote filament bundling (Fig. 1.7). The examples shown in Figure 1.5B and in Figure 1.7 suggest that oscillations in *in vitro* systems may emerge as a generic property of the motor assemblies under elastic loading, as proposed on the basis of general theoretical models developed by Frank Jülicher and Jacques Prost. The oscillatory instability is associated to a region of negative slope in the force-velocity relationship of motor assembly (Jülicher and Prost, 1997). Another proposed mechanism for motor-induced oscillations relies on a force-dependence of the rate at which a motor detaches from a filament (Grill et al., 2005). If this rate increases with the applied force, the spontaneous detachment of a single motor leads to an increase of the load on all other motors, which in turn increase their detachment rates. This mechanism can result in the coordinated detachment of all the motors. This scenario is well-illustrated in everyday life by the tug of war, when one person in the team releases the rope, it becomes suddenly one step harder for the remaining people of the team to still hold the rope.

1.2 Spontaneous beating of eukaryotic flagella

This section is a brief overview of biological flagellar beating in eukaryotes to later compare its phenomenology to that of beating bundles of actin filaments that I produced *in vitro* during my PhD using a minimal actomyosin system.

1.2.1 Cilia and flagella : motile organelles

Cilia and flagella are hair-like appendages that produce motility through repetitive episodes of bending-wave propagation. This rhythmic and undulating motion is called flagellar beating and can propel a cell through liquid media or displace a fluid over the surface of a group of cells in a tissue (Bruot and Cicuta, 2016; Ginger et al., 2008).

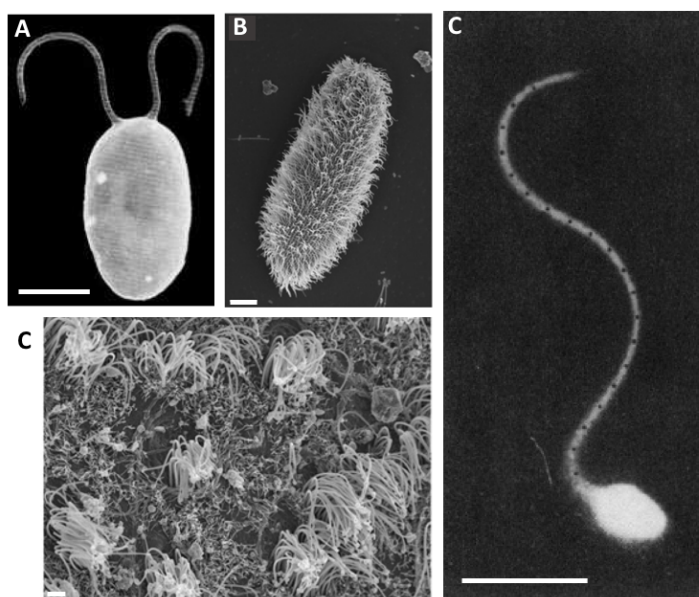


Figure 1.8: Diversity of cilia and flagella. **A:** Flagella of *Chlamydomonas reinhardtii*. Scale bar: 10 μm . **B:** Cilia of *Paramecium tetraurelia*. Scale bar: 10 μm . **C:** Flagellum of spermatozoan. Scale bar: 10 μm . Figure from (Rikmenspoel and Isles, 1985) **D:** Scanning electron micrographs of the epithelium lining the ventricles of a mouse brain (4 days old), showing many cilia. Scale bar: 1 μm . Figures (A,B,D) adapted from (Vincensini et al., 2011),

Although they are both called flagella, note that bacterial flagella and eukaryotic flagella differ in structure and mode of action: eukaryotic flagella contain linear motors that are uniformly distributed along the length of the flagellum whereas rotatory motors are located at the base of bacterial flagella. As a result, bacterial flagella are passive rigid helical structures that rotate whereas eukaryotic flagella actively bend to beat (Bray, 2001). Despite their different names, cilia and flagella are instead endowed with the same structure, which is called the axoneme. The typical length of eukaryotic cilia and flagella is 10 μm with a diameter of 0.2 μm diameter (Marshall, 2004; Neidhardt et al., 1996).

Cilia tend to be shorter (around 7 μm) than flagella (from 12 μm (*Chlamydomonas reinhardtii*) to 70 μm (sperm)) (Bruot and Cicuta, 2016). Typically, cells possess one or two long flagella at their extremity, whereas ciliated cells are covered with many short cilia, partially or all-over their surface (Alberts et al., 2008). Cilia and flagella cover a wide range of functions for animals and plants as diverse as clams and algae (Fig. 1.8) : They can for instance be used for feeding, reproduction or protection from infection in the bronchi of the lung.

1.2.2 The axoneme : the core structure of cilia and flagella

Cilia and flagella are highly ordered structures containing more than 650 different proteins (Pazour et al., 2005). The core of this structure is called the axoneme (Fig. 1.9). An axoneme is mostly composed of microtubules with a pipe-like structure, and dyneins. In an axoneme, dyneins are assembled uniformly onto a scaffold of nine cylindrically arranged doublets of microtubules. These nine microtubule doublets are surrounding a pair of single microtubules, called the central pair (Nicastro et al., 2006). Neighboring outer doublets are linked together through strands of proteins called nexin links. Those doublets are also connected to the central pair by radial spokes, acting as spacers to maintain the cylindrical geometry of the axoneme, and anchored to the basal body.

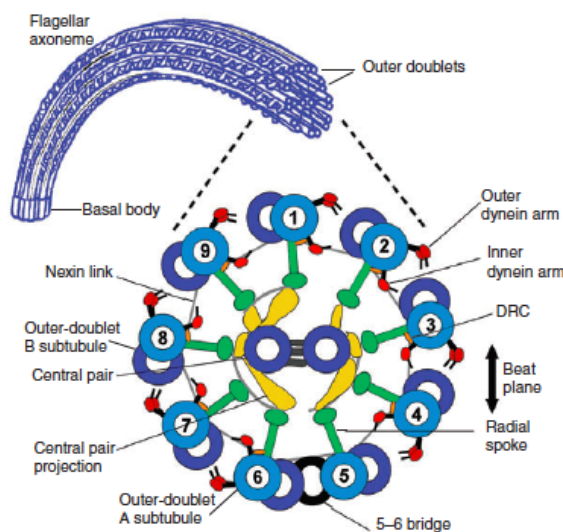


Figure 1.9: Cross section of the flagellar axoneme. Dyneins are assembled onto a scaffold of nine cylindrically arranged doublets of microtubules. These nine microtubules doublets are surrounding a pair of single microtubules, called the central pair. The neighboring outer doublets are linked together through strands of proteins called nexin links. Those doublets are connected to the central pair by radial spokes, and anchored to the basal body. Here, doublets 5 and 6 are connected by a rigid bridge that prevents their relative sliding; its position defines the beating plane (perpendicular to the bridge). Figure from (Lindemann and Lesich, 2010) DRC : dynein regulatory complex.

In the axoneme, dyneins are bound to two outer neighboring doublets : the active longitudinal motion of the dyneins along the microtubule tracks causes the microtubule doublets to slide with respect to one another (Fig. 1.10.A) (Summers and Gibbons, 1971). This sliding movement is then converted into bending by the nexins linkers and the basal attachment of the microtubules, which both limit inter microtubule sliding and maintain the structural integrity of the axoneme (Fig. 1.10.B).

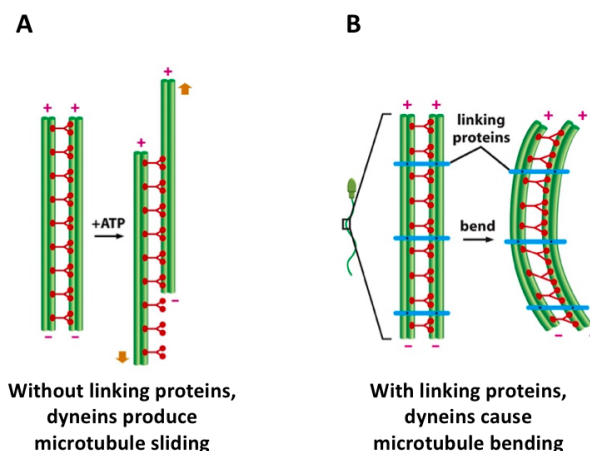


Figure 1.10: Bending of an axoneme. **A:** Isolated doublet can be obtained by exposing axonemes to trypsin, which breaks the linkages holding neighboring microtubules. The addition of ATP—the source of energy for the motors—allows dyneins to slide one pair of doublet microtubules with respect to the other pair. **B:** In intact axonemes (such as in sperm), the linking proteins (nexin) prevent the relative sliding of the doublets and motor action causes a bending motion. Figure adapted from (Alberts et al., 2008) and experiments from (Summers and Gibbons, 1971)

1.2.3 Beating properties

Taylor highlighted in 1951 that self-propelled cells work at very low Reynolds numbers ($Re \ll 1$), so that viscous drag dominates and inertia can be neglected (Taylor, 1951). Cilia and flagella undergo periodic oscillatory motion, thanks to motors that coordinate an oscillatory bending motion of the axoneme. The beating pattern typically consists of rather symmetrical and propagating waves, often planar or helical. Their frequency typically varies from 5 to 100 Hz (Satir and Christensen, 2007). These waves normally travel from the base to the tip of the flagellum, although there are exceptions such as the flagella of the kinetoplastid *Critidia oncopelti*, which exhibit waves in the opposite direction (Douglas and Holwill, 1972). The simplest waveform seen in eukaryotic flagella is a planar sinusoidal wave that travels steadily from the anchored base to the free tip of the flagellum. The amplitude of the wave at any given point along the longitudinal axis of the flagellum is defined by the maximal tangent angle that the flagellum can reach (in

deg) or by the maximal distance with respect to the reference, from which the flagellum is straight. This pattern of beating is seen in many animal sperm that are streamlined for efficient swimming. The most studied flagella of this type are from the sea urchin spermatozoan, the *Chlamydomonas reinhardtii* and the bull sperm (Fig. 1.11). I will briefly describe their properties and focus more into details on the bull sperm studies.

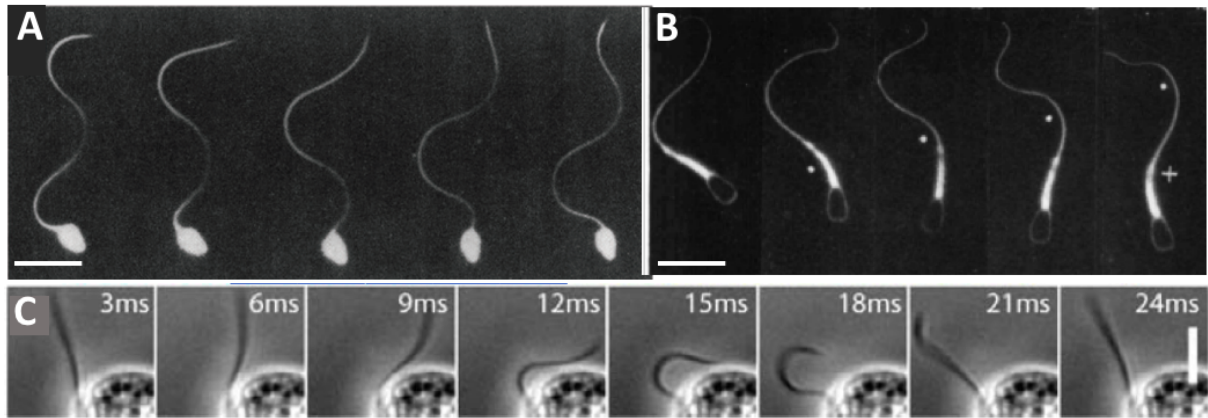


Figure 1.11: Beating pattern of three eukaryotic flagella. **A:** Sea urchin sperm. Scale bar: 10 μm . The snapshots are taken at 10-ms time intervals. Figure from (Rikmenspoel and Isles, 1985). **B:** Bull sperm. Scale bar 20 μm . The snapshots are taken at 10-ms time intervals. Figure from (Gray, 1957). **C:** *Chlamydomonas reinhardtii*. Scale bar: 5 μm . Figure from (Sanchez et al., 2011)

Table 1.1: Flagellar beating properties in different species

Species	Length (μm)	Frequency (Hz)	Speed of swimming ($\mu\text{m/s}$)	Maximum amplitude (μm)	Wavelength (μm)	References
<i>Chlamydomonas</i>	14	70	60	5	14	(1-2)
Sea urchin sperm	41	33	180	4	24	(3)
Bull sperm	55	6	100	5	54	(4-5)

Data from: (1) (Brokaw and Luck, 1983); (2)(Bayly et al., 2010); (3) (Gray, 1955); (4) (Rikmenspoel, 1984); (5) (Gray, 1957).

Sea urchin sperm Historically, the beating waveforms of sea urchin sperm were the first studied (Gray, 1955) (Fig. 1.11.A). Sea urchin spermatozoa show planar beating when close to a surface, and the wave of the sperm tail travels with an almost constant amplitude along the tail. Bending waves are composed of nearly circular arcs separated by short straight regions. The wave speed along flagella is around 800 $\mu\text{m/s}$ for a speed of propulsion around 200 $\mu\text{m/s}$. The amplitude of the wave is $4 \pm 0.5 \mu\text{m}$, the wavelength is $24 \pm 2 \mu\text{m}$ for a flagellum length of $41 \pm 2 \mu\text{m}$.

Chlamydomonas reinhardtii For *Chlamydomonas reinhardtii*, waveforms exhibit an asymmetric pattern : the beat cycle starts with the "power stroke", where the flagellum straightens and changes its orientation, thus pushing the fluid. It returns to its initial position curled up, in the "recovery stroke", thus minimizing the interaction with the fluid (Bruot and Cicuta, 2016). The maximal amplitude of the wave is 5 μm , the wavelength is 14 μm for a flagellum length of 14 μm , suggesting that the length of the flagellum sets the wavelength. (Bayly et al., 2010; Brokaw and Luck, 1983). Sartori and colleagues measured the flagellar beating waveforms in axonemes with high temporal and spatial precision (Sartori et al., 2016). To characterize the shape of the filament through the beating, they introduced the tangent angle ψ with respect to the horizontal axis of the laboratory frame (Fig. 1.12.A.(ii)). As shown in Figure 1.12.A.(iii), the beating of *Chlamydomonas reinhardtii* is periodic and *Chlamydomonas* axonemes swim counterclockwise in circles at a slow angular rotation speed (Fig. 1.12.A.(i-iii)). As the power spectrum of the tangent angle (averaged over the flagellar length) shows (Fig. 1.12.B.(i)), the beating can be decomposed in harmonics, but the peak at the fundamental frequency ($n = 1$) accounts for 90% of the total power, so the higher harmonics ($n = 2; 3; 4; \dots$) can be neglected for reconstructing the flagellar shape. The static and fundamental modes provide a good description of the beats (Fig. 1.12.C). The amplitude ψ_0 of the static mode ($n = 0$) is presented in Figure 1.12.B.(ii), it decreases linearly over the length of the flagellum. This corresponds to an approximately constant static curvature and a time-averaged shape close to a semi-circular arc (radius $\approx 4 \mu\text{m}$). This static curvature confers to the flagellum an asymmetric waveform. The amplitude and the phase of the fundamental mode ($n = 1$) are shown in Figure 1.12.B.(iii-iv). The amplitude is almost uniform along the length of the flagellum, the argument, which determines the phase of the wave, decreases at a roughly constant rate, indicating that the beat is a traveling wave. Because the total phase shift is about 2π along the flagellum, the wavelength of the beat is approximately equal to the length of the axoneme.

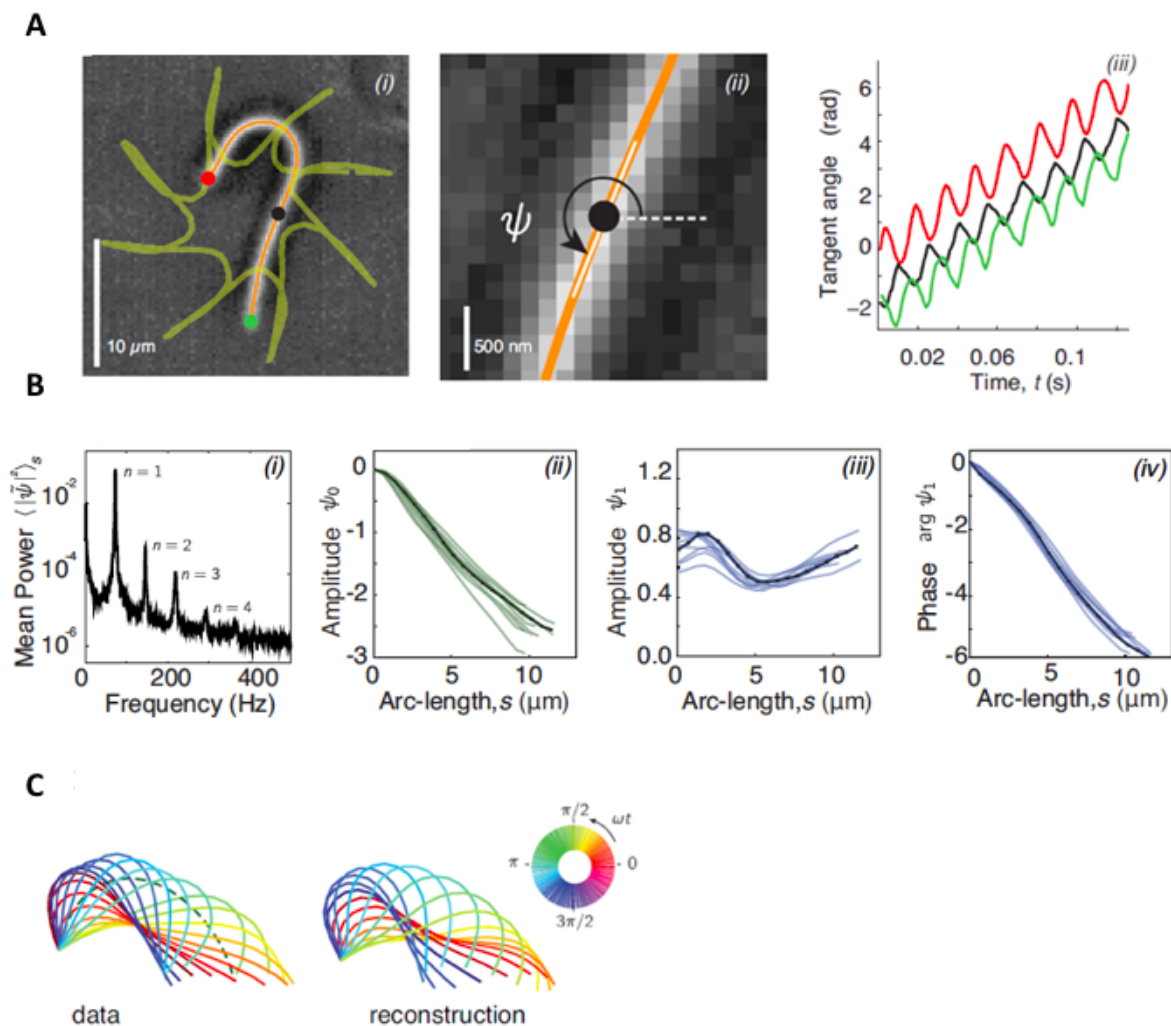


Figure 1.12: Beating properties of the *Chlamydomonas reinhardtii*. **A:** High-precision tracking of isolated, reactivated axonemes. (i) Inverted phase-contrast image of a wild type axoneme. The orange curve represents the tracked centerline. The points depict the basal end (red), the distal end (green) and the center position (black) of the axoneme. The green line depicts the trajectory of the basal end, which is the leading end during swimming. (ii) Same image as in A), magnified around the center region. The tangent angle $\psi(s,t)$ is defined with respect to horizontal axis in the lab frame. (iii) Tangent angle at three different arc-length positions (depicted in A) as a function of time. The linearly increasing tangent angle corresponds to a counter-clockwise rotation of the axoneme during swimming. **B:** Fourier decomposition of the beat. (i) Power spectrum of the tangent angle averaged over the arc-length. The fundamental mode ($n = 1$) and three higher harmonics ($n = 2; 3; 4$) are labeled. (ii) Angular representation of the static ($n = 0$) mode as a function of arc-length. The approximately constant slope indicates that the static curvature is close to constant $\psi_0 = C_0$. (iii) The amplitude and phase (argument) of the fundamental mode are shown in iii and iv, respectively. The approximately linear decrease in phase indicates that the magnitude of the wave vector does not vary during wave propagation. The data of a representative axoneme is highlighted in the panels ii-iv. **C:** Beat shapes of one representative beat cycle of the wild type axoneme highlighted in panel A (left panel, data) and shapes reconstructed from the superposition of the static and fundamental modes, neglecting all higher harmonics. The progression of shapes through the beat cycle is represented by the rainbow color code (see inset). Figure adapted from (Sartori et al., 2016)

Bull sperm To study mammalian sperms, the bull spermatozoan served as a model system, first by analyzing pictures of bull sperm waveforms (Gray, 1958) (Fig. 1.11.B). In more recent studies using automated image analysis of the flagellum (Riedel-Kruse et al., 2007), the tangent angle along the flagellum $\psi(s, t)$ was analyzed (Fig. 1.13.A). Tracking of the flagellum indicates a slight asymmetry in the beating pattern, resulting in curved trajectories of the swimming plane (Fig. 1.13.B). A space-time plot of $\psi(s, t)$ reveals the periodicity of the flagellar beat (Fig. 1.13.C). In contrast to sea urchin spermatozoa, the wave amplitude for bull spermatozoa was found to increase as the wave propagated towards the end of the tail. The maximum amplitude of the wave is $5 \mu\text{m}$, the wavelength is $54 \mu\text{m}$ for a flagellum length of $55 \mu\text{m}$ (Gray, 1957; Rikmenspoel, 1984).

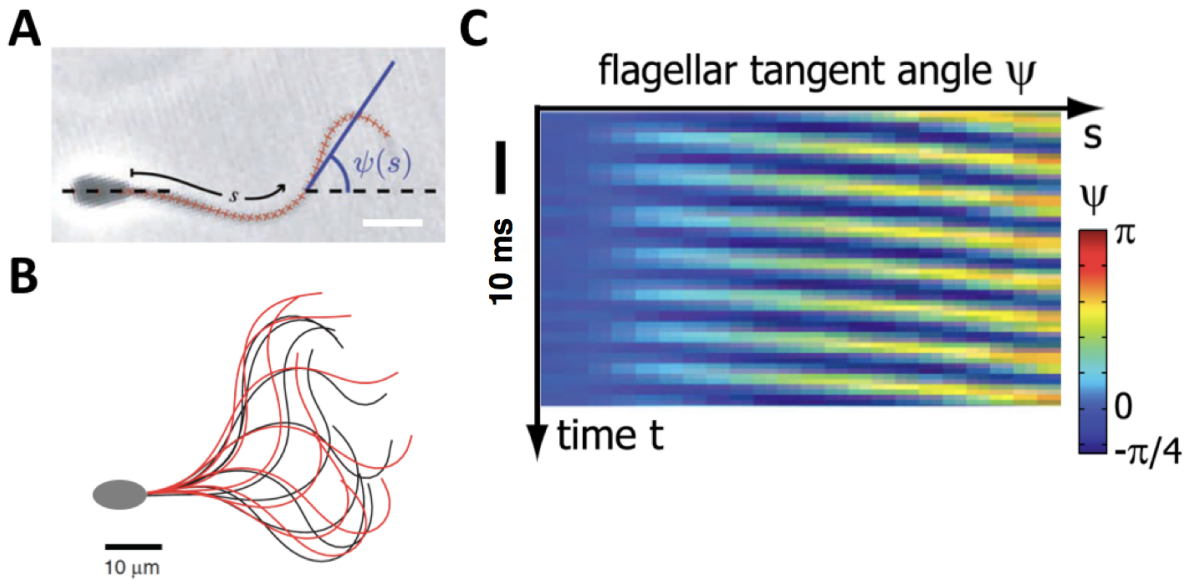


Figure 1.13: Beating properties of the bull sperm. **A:** Snapshot of a beating bull sperm, superimposed on the image are red crosses tracing the contour of the flagellum as determined by the automated image analysis. The tangent angle $\psi(s)$ is measured at each curvilinear abscissa s along the flagellum. The center of the red crosses are separated by $1.4 \mu\text{m}$. Scale bar: $10 \mu\text{m}$. Figure from (Riedel-Kruse et al., 2007). **B:** Beating patterns of a bull sperm, with clamped head. Figure from (Friedrich et al., 2010). **C:** Kymograph of the tangent angle $\psi(s, t)$ reveals the periodicity of the flagellar beat, as well as the growth of the amplitude of angle oscillations as the wave propagates towards the tip of the flagellum. Figure from (Ma et al., 2014).

The time series of the tangent angle over time at a fixed curvilinear abscissa ($s = 28 \mu\text{m}$) exhibits stable oscillations over time (Fig. 1.14.A). By computing the power spectrum at each position, all time series were well-approximated by their zeroth and first Fourier temporal modes.

$$\psi(s, t) \approx \tilde{\psi}^{(0)}(s) + \tilde{\psi}(s) e^{i\omega t} + \tilde{\psi}^*(s) e^{-i\omega t} \quad (1.1)$$

where the star indicates the complex conjugate. Thus, the motion of each point can be described by a sinusoidal oscillation of amplitude $2 |\tilde{\psi}|$ and angular frequency ω

with an average angle $\psi^{(0)}$. The time-averaged tangent angle $\psi^{(0)}(s)$ as a function of the curvilinear abscissa corresponds to the mean shape of the flagellum (Fig. 1.14.B). This relation characterizes the asymmetry of the mean shape of the flagellum (if the mean shape were symmetric the averaged angle would be 0). The amplitude $|\tilde{\psi}|$ increases linearly along the flagellum below $s \approx 45 \mu\text{m}$ and then saturates (Fig. 1.14.C). The phase of the first mode decreases linearly along the curvilinear abscissa, the slope of the plot is inversely related to the wavelength of beating (the slope corresponds to $-2\pi/\lambda$), which is thus uniform over most of the length of the flagellum (Fig. 1.14.D).

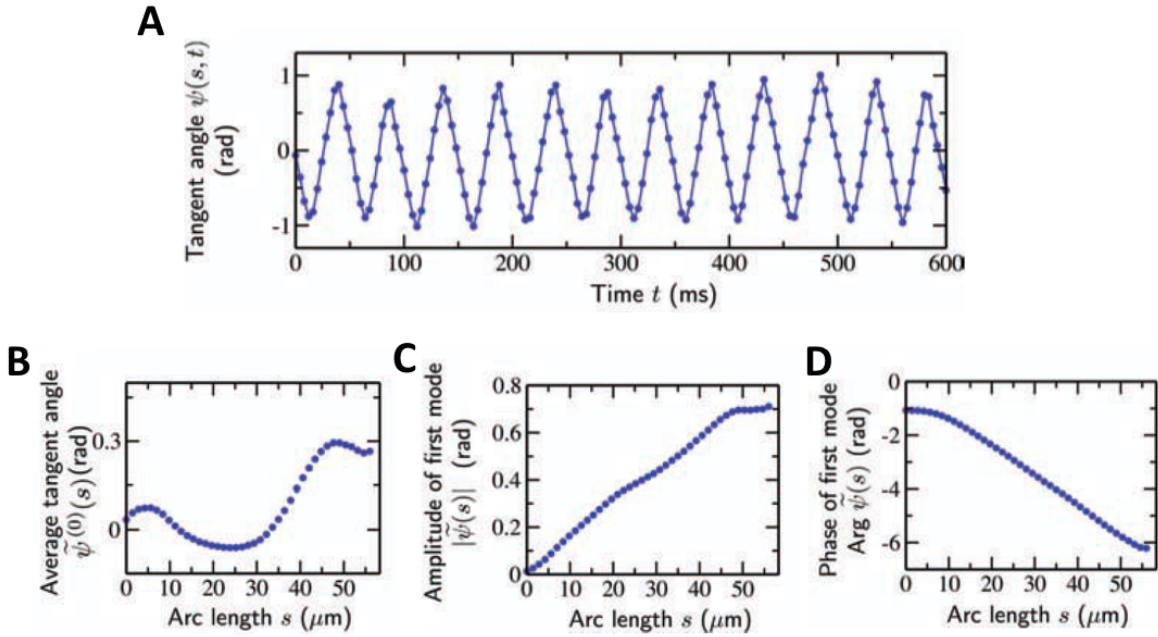


Figure 1.14: Time series analysis and Fourier modes of beat patterns. **A:** Time series of the tangent angle $\psi(s, t)$ at a given position ($s = 28 \mu\text{m}$) along the flagellum. The head of the flagellum was clamped. **B:** The time average of the tangent angle $\psi^{(0)}$ at each point along the flagellum. **C, D:** Amplitude and phase of the first mode $\tilde{\psi}$, respectively. Figures from (Riedel-Kruse et al., 2007).

Effect of viscosity

It has long been demonstrated that the flagellar beat frequency declines when the viscosity of the surrounding medium is increased (Brokaw, 1966; Rikmenspoel, 1984; Woolley et al., 2009). The effect is associated with an increase in bending angle and a decrease in wavelength, in swimming velocity and bending-wave speed (Brokaw, 1966; Rikmenspoel, 1984; Woolley et al., 2009)

In sea urchin sperm When the sea urchin spermatozoan swims at unphysiologically high viscosities of the surrounding medium (1.5 to 4 Pa.s), it has been shown that the

usual planar beat of sea urchin spermatozoa can change into a fully 3D helical beat pattern (Woolley and Vernon, 2001).

In bull sperm The frequency of the flagellar beating in bull sperm decreases almost exactly as the square root of viscosity (Rikmenspoel, 1984), as shown in Figure 1.15.

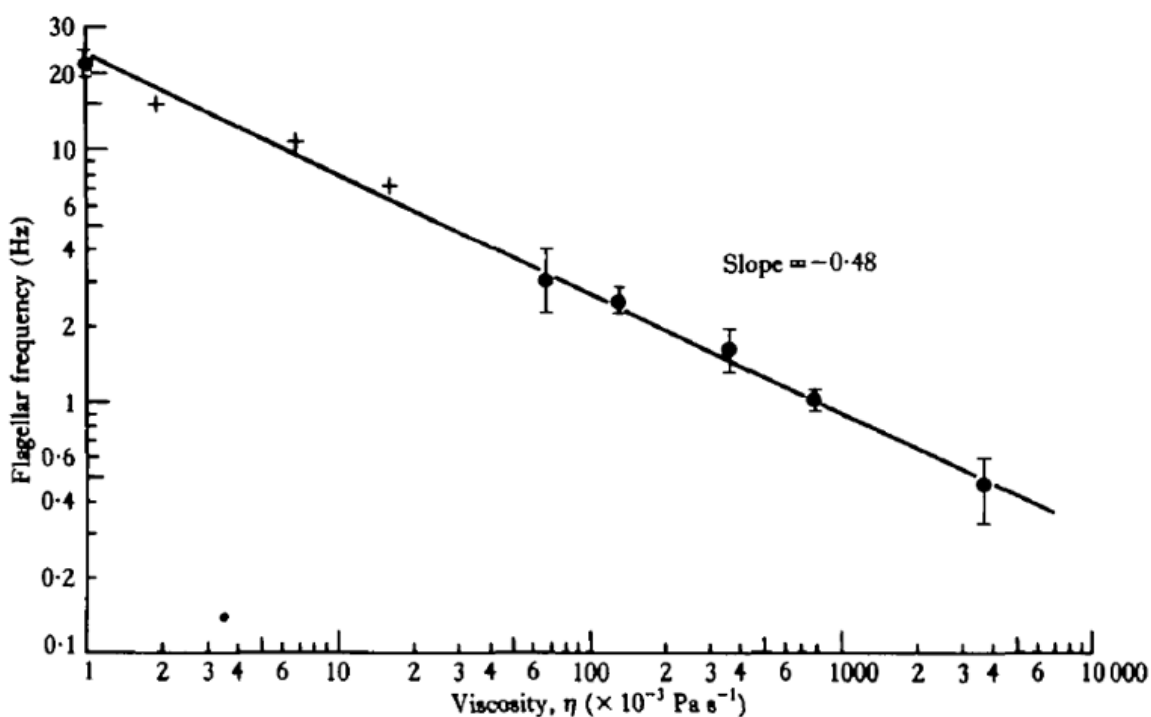


Figure 1.15: Beating frequency of bull sperm at 37 °C as a function of the viscosity of the medium. The black circles represent the measurements of (Rikmenspoel, 1984); The + symbol refers to data from (Rikmenspoel et al., 1973) reported previously. Each point represents the average over 8 to 12 sperm cells. The vertical bars are standard deviations. The line with a slope of - 0.48 was drawn by eye. (Rikmenspoel, 1984). These data suggest a power law relating flagellar frequency f to viscosity η : $f \propto 1/\sqrt{\eta}$

Moreover, the flagellar waveform changes qualitatively at raised viscosity. The amplitude near the base becomes progressively smaller, whereas the amplitude near the tip remains roughly constant over the entire viscosity range. This results in an increasingly trumpet-shaped appearance of the envelope of the flagellar wave (Fig. 1.16).

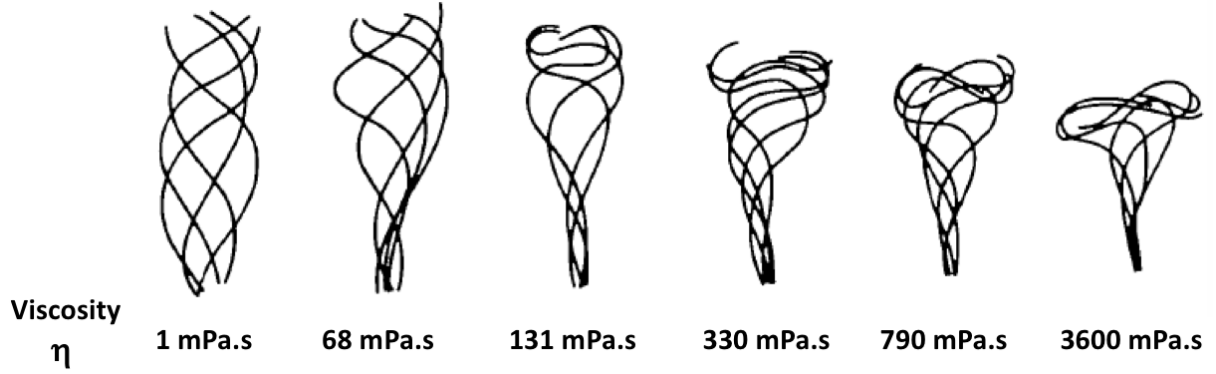


Figure 1.16: Viscosity and beating pattern. Typical waveforms of bull sperm flagellum in media of raised viscosity from 1 to 3600 mPa.s. The forward progression of the sperm was removed. The flagellar waveform changes qualitatively at raised viscosity. The amplitude near the base becomes progressively smaller at higher viscosities, whereas the amplitude near the tip remains roughly constant over the entire range. This results in an increasingly trumpet-shaped appearance of the envelope of the flagellar wave. Figure adapted from (Rikmenspoel, 1984).

More recently, a Fourier analysis of the flagellar beat of a swimming bull sperm cell was computed for the case of normal viscosity $\eta = 0.7$ mPa.s and increased viscosity $\eta = 10$ mPa.s (Friedrich et al., 2010). It shows that the static shape of the flagellum, as determined from $\psi_0(s)$, is less curved at higher viscosities (Fig. 1.17.A). The linear fit of the two curves gives the mean flagellar curvature K_0 , which drops from 19.1 rad.mm^{-1} to 6.5 rad.mm^{-1} . The amplitude of the first mode decreases at higher viscosity and does not exhibit saturation in contrast to what observed at normal viscosity.

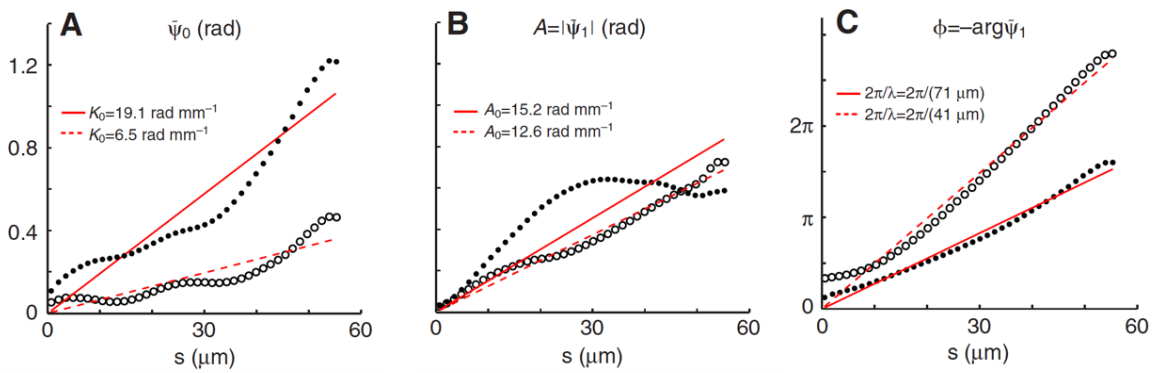


Figure 1.17: Variation of beating properties at high viscosity. **A:** The time-averaged of tangent angle, $\psi^{(0)}$, at each point along the flagellum for the case of normal viscosity $\eta = 0.7$ mPa.s (black disks) and increased viscosity $\eta = 10$ mPa.s (white disks). The linear fit gives the mean flagellar curvature K_0 . **B**, **C:** Amplitude and phase, respectively, of the first Fourier mode $\tilde{\psi}$ for the case of normal viscosity $\eta = 0.7$ mPa.s (black disks) and increased viscosity $\eta = 10$ mPa.s (white disks). The linear fits give respectively the amplitude rise A_0 and the wavelength λ of the wave. Figures from (Friedrich et al., 2010)

A linear fit of the relation between the amplitude of the first mode and the curvilinear abscissa gives the amplitude rise of the flagellar bending waves A_0 (Fig. 1.17.B). The phase of the first mode, as a function of the curvilinear abscissa, indicates higher delays for wave propagation at higher viscosity (Fig. 1.17.C). The linear fit of the plots gives the wavelength λ of the principal flagellar bending wave, (the slope of the linear fit corresponds to $2\pi/\lambda$). At higher viscosity the wavelength is almost divided by 2 compared to normal viscosity. The Table 1.2 summarizes the changes in the beating properties of the flagella.

Table 1.2: Changes of flagellar beat properties with viscosity

Viscosity η (mPa.s)	Frequency f (Hz)	Mean curvature K_0 (rad/mm)	Amplitude A_0 (rad/mm)	Wavelength λ (μm)	Speed v ($\mu\text{m/s}$)
0.7	31	13.1	14.6	66	117
10	18.5	6.6	12.0	39	43

Data from (Friedrich et al., 2010).

Effect of length on frequency

The effect of flagellar length on beating properties has been studied on demembraneted axonemes. When flagella are severed transversely, the proximal segments continue to beat but with an increased beat frequency, even if the flagellum length is reduced below the half of its original length (Gibbons, 1975; Woolley et al., 2009). The waveforms are generally similar, but the amplitude of the bends and the bending angle decrease with the length. Bending angle measurements indicate that for fragments shorter than 20 μm , the maximum angle varies linearly with the length of the fragment, as shown in Figure 1.18.

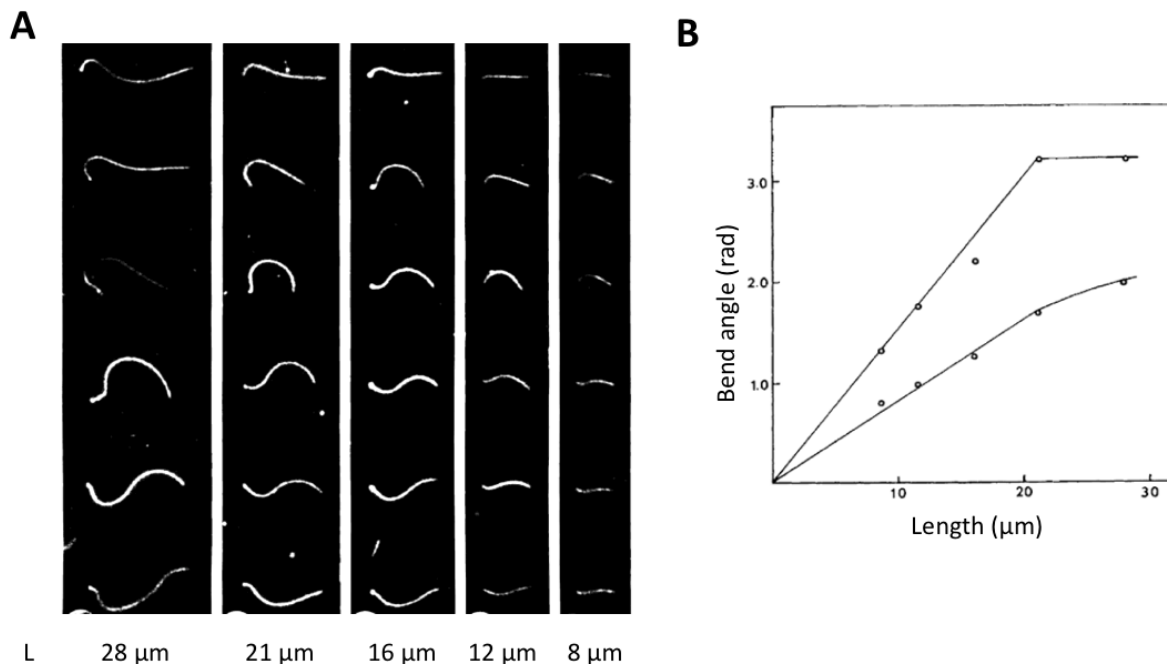


Figure 1.18: Effect of flagellum length on beating properties. **A:** Movement of axonemal fragments of 28, 21, 16, 12, 8 μm . **B:** Relation between the maximal bend angles developed and the length of the fragments in (A). The upper (lower) curve shows angles of the principal (reverse) bends convex upwards (downwards) in the picture panels of (A). Figure adapted from (Gibbons, 1975)

1.2.4 Existing theoretical approaches of flagellar beating

The oscillatory pattern of the axoneme implies that the action of dyneins is coordinated. There must be two switching sets of dynein domains within the axoneme that are either active (mediating bending/sliding) or inactive (prevented to do the same by opposing shear forces) (Brokaw, 1975; Jülicher and Prost, 1997) to obtain bending alternatively in the two opposite directions (Fig. 1.19). How the motor activity is controlled to generate the observed wave-like beating of the axoneme remains unclear.

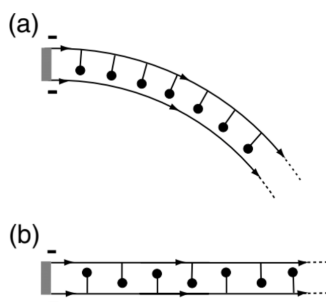


Figure 1.19: Asymmetric (a) and symmetric (b) motor filament pairs. The arrows indicate the polarity of the filaments. In case (a), spontaneous bending occurs in a steady state. In case (b) both filaments play identical roles, no spontaneous bending occurs. Figure from (Camalet and Jülicher, 2000)

I briefly introduce the theory of Camalet and coworkers (Camalet and Jülicher, 2000; Camalet et al., 1999) to present the general concepts that are used in the field to describe the axonemal beat. The theory presented by Camalet describes the two-dimensional beat of an axoneme, where two filaments slide relative to each others. The centerline of the axoneme in space is given by $\mathbf{r}(s)$, where s is the arc length of the axoneme with $s = 0$ at the base, *i.e.* at the head of the cell, and $s = L$ at the tip, the filament-separation is a (Fig. 1.20).

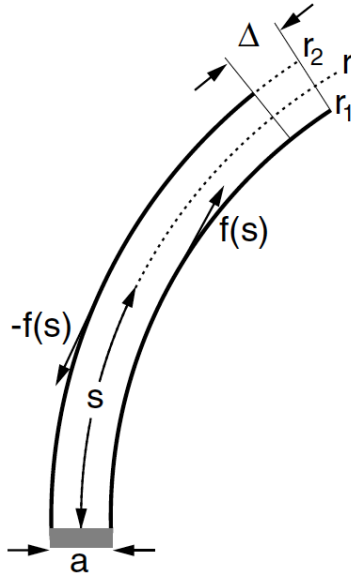


Figure 1.20: The complex structure of the axoneme is reduced to a pair of sliding filaments: Two filaments are spaced apart by the distance a . The filaments are connected at the base and free to slide at Δ . The arc-length of the filament pair is described by s . The motors (not shown) generate local forces $f(s)$. Figure from (Camalet and Jülicher, 2000)

The relative sliding distance of the filaments $\Delta(s)$ at position s is determined by assuming that the filaments are incompressible (*i.e.* the filament-separation a remains constant) and by subtracting the arc length of the filaments. Using the definition of curvature $C(s)$ related to the tangent angle on the filament pair $\psi(s) : \partial_s \psi(s) = C(s)$, we get :

$$\Delta(s) = a \int_0^s C(s') ds' = a \int_0^s \frac{\partial \psi(s')}{\partial s'} ds' = a(\psi(s) - \psi(0)) \quad (1.2)$$

Hence the tangent angle of the filament is linearly related to the internal sliding of the filament. The enthalpy functional G takes into account the bending of the filaments and the internal stresses due to active and passive elements inside the axoneme,

$$G = \int_0^L \left[\frac{\kappa}{2} C^2 + f \Delta + \frac{\Lambda}{2} \partial_s \mathbf{r}^2 \right] ds \quad (1.3)$$

where L is the length of the flagellum, κ the bending elasticity of the flagellum (which is assumed to be the same at all positions), f is the effective active force per unit lengths exerted by the motors (drives bending) and Λ is the Lagrange multiplier ensuring that s is the arc length. After a partial integration and using equation (1.2), we find

$$G = \int_0^L [\frac{\kappa}{2}C^2 - aFC + \frac{\Lambda}{2}\partial_s \mathbf{r}^2] ds \quad (1.4)$$

where

$$F(s) = - \int_0^L f(s') ds' \quad (1.5)$$

Determining the variation δG with respect to variation δr , which gives by definition the external forces applied to the axoneme:

$$\frac{\delta G}{\delta r} = \partial_s [(\kappa \partial_s C - af)\mathbf{n} - \tau \mathbf{t}] \quad (1.6)$$

where $\tau = \Lambda + \kappa C^2 - aFC$ plays the role of a physical tension and \mathbf{n} and \mathbf{t} are the normal and tangent on the outline \mathbf{r} .

For simplicity, it is assumed that the hydrodynamics of the surrounding fluid can be described by two local friction coefficients ξ_{\parallel} and ξ_{\perp} for tangential and normal motion respectively. The condition of force balance reads :

$$\partial_t r = -(\frac{1}{\xi_{\perp}} \mathbf{nn} + \frac{1}{\xi_{\parallel}} \mathbf{tt}) \cdot \frac{\delta G}{\delta r} \quad (1.7)$$

Here \mathbf{nn} and \mathbf{tt} are the normal and tangential projection operators.

Injecting the expression (1.6) of $\delta G/\delta r$ into the dynamic equation (1.7), we can get a differential equation of the tangent angle $\psi(s, t)$. To study the linear stability of the system, we work in the limit of small tangent angles. Moreover under the simplifying assumption of a symmetric beating. We have to exclude antisymmetric terms such as $f \leftrightarrow -f$ and $\psi \leftrightarrow -\psi$. Then using equation (1.6) with $\partial_s F(s, t) = f(s, t)$

$$\xi_{\perp} \partial_t \psi = -\kappa \partial_s^4 \psi + a \partial_s^2 f \quad (1.8)$$

The second term on the right-hand side describes the active contribution of the motors to force balance. In a passive system, this term is zero and we are left with force balance between friction (on left-hand side of the equality) and elasticity (first term on the right-hand side); this equation, which is known as the elasto-hydrodynamic equation, describes the bending modes of slender rods (Howard, 2001).

Four different boundary conditions have been discussed by Camalet :

- clamped head, free tail
- fixed head, free tail
- swimming flagellum with viscous load ζ
- clamped head, external force applied to the tail.

To apply the boundary conditions to our system, it is more instinctive to work with transverse deformation h than with the tangent angle ψ , $\partial_s h = \psi$, which can be injected in equation 1.8 above:

$$\xi_{\perp} \partial_t h = -\kappa \partial_s^4 h + a \partial_s^2 f \quad (1.9)$$

I will focus on the first case where the head is clamped, which gives the following boundary conditions:

$$\begin{aligned} h(0) &= 0 \\ \partial_s h \big|_{s=0} &= 0 \\ \partial_s^2 h \big|_{s=L} &= 0 \\ [\kappa \partial_s^3 h - a f] \big|_{s=L} &= 0 \end{aligned} \quad (1.10)$$

In the case of oscillatory patterns, one can express $h(s, t) = \sum_{-\infty}^{+\infty} h_n(s) e^{in\omega t}$, and $f(s, t) = \sum_{-\infty}^{+\infty} f_n(s) e^{in\omega t}$, as Fourier series in time (with $h_{-n} = h_n^*$, ensure that h is real) where ω is the angular beating frequency which leads to:

$$\kappa \partial_s^4 h_n - a \partial_s^2 f_n(s) = -i\omega \xi_{\perp} h_n \quad (1.11)$$

and the boundary conditions

$$\begin{aligned} h_n(0) &= 0 \\ \partial_s h_n \big|_{s=0} &= 0 \\ \partial_s^2 h_n \big|_{s=L} &= 0 \\ [\kappa \partial_s^3 h_n - a f_n(s)] \big|_{s=L} &= 0 \end{aligned} \quad (1.12)$$

The forcing term f_n describes the activity of motors and the passive internal visco-elastic elements. Three different mechanisms have been proposed to describe how the mechanical activity of the motors (through the term f_n) is regulated by the shape of the axoneme; the description assumes the existence of a linear response function between f_n and a parameter related to shape:

- Sliding control

$$f_n(s) = \chi(n\omega)\Delta_n(s) \quad (1.13)$$

where Δ_n represents a Fourier mode of the sliding distance and $\chi(n\omega)$ is the corresponding linear response.

In this model the activity of dyneins is regulated by the sliding between the two filaments within the axoneme. Assuming a load-dependent detachment rate of motors $k_{off} = k_0 \exp(f_L/f_c)$, where f_L is the load and f_c is a characteristic force giving the scale of the load that can affect k_{off} , one can derive the following expression for χ (Riedel-Kruse et al., 2007):

$$\chi(n\omega) = k + in\omega\lambda - \rho K_{CB}\Omega \frac{i\omega\alpha + (\omega/\alpha)^2}{1 + (\omega/\alpha)^2} \quad (1.14)$$

A similar expression was obtained from a generic two-state model of collective motor dynamics that does not explicitly assume load-dependent detachment of the motors (Camalet and Jülicher, 2000; Jülicher and Prost, 1997). Here k is the stiffness, λ is the friction per unit length of the passive internal elements, the last term is the linear response of the active motors themselves, with ρ the motor density, K_{CB} is the cross-bridge elasticity of the motors, α is the characteristic ATP-cycling rate and Ω plays the role of activity parameter.

As seen in Equation 1.14, the active term leads to both negative elasticity and friction, which can precisely cancel the passive terms k and λ , respectively, resulting in an oscillatory instability called a Hopf bifurcation (where χ vanishes at a specific value of ω). This property is generic of large groups of molecular motors coupled elastically to the environment : such system can show a dynamic instability leading to oscillations (Brokaw, 1975; Jülicher and Prost, 1997). *In vitro* experiments have demonstrated that oscillatory instabilities can indeed emerge as an intrinsic property of motor groups under elastic loading (Okamura and Ishiwata, 1988; Plaças et al., 2009)

- Curvature control

$$f_n(s) = \beta(n\omega)\partial_s\psi_n(s) \quad (1.15)$$

where $\partial_s\psi_n$ represents a Fourier mode of the curvature and $\beta(n\omega)$ is the corresponding linear response.

In this model of feedback, the activity of the dyneins is regulated by the local curvature of the axoneme *i.e.* its degree of bending. This was one of the earliest ideas (Brokaw, 1971, 1972a,b) after the proposal of the sliding bending mechanism.

Many simulation studies were undertaken by Brokaw showing the feasibility of the approach.

- geometrical clutch

$$f_n(s) = \gamma(n\omega)f_{\perp,n}(s) \quad (1.16)$$

where $f_{\perp,n}$ represents Fourier mode of the normal force felt by the motors and $\gamma(n\omega)$ is the corresponding linear response.

In this model of feedback, the dynein detachment is regulated by transverse forces separating curved adjacent doublets. This model proposed that in bending axoneme, transverse forces develop that pull neighboring microtubule doublets apart and that this increase in interdoublet spacing leads to a decrease in the probability of dynein engagement (Lindemann, 1994a,b). Such models are based on observations in electron micrographs showing that the spacing between two neighboring microtubule doublets is larger when the dyneins are unbound than when they are bound (Gibbons and Gibbons, 1974). Although neither curvature nor geometrical clutch mechanism is supported by a direct experimental evidence with microscopy, they have been shown to produce traveling waves in computer models (Lindemann, 2002). Dynamic curvature regulation has also recently been proposed to account for the symmetric and asymmetric beats of *Chlamydomonas reinhardtii* flagella (Sartori et al., 2016). Note that in the geometrical clutch model, the filament-separation a is not constant, unlike in the model used for the calculation, thus the general equation of the tangent angle and transverse deformation would be modified.

Note that χ , β and γ have real and imaginary parts that can become negative (Eq. 1.14), as the result of motor activity (Sartori et al., 2016).

Chapter 2

The actomyosin system

2.1 The actin cytoskeleton

The actin cytoskeleton is a network of semi-flexible filaments, which are active polymers that can elongate or shrink depending on the surrounding environment. As a result, the network can continuously reorganize in order to adapt to changing conditions. The actin cytoskeleton is involved in various key cellular processes such as motility, morphogenesis, polarity, transport and cell division.

2.1.1 Actin : From monomers to filaments

Actin structure

The actin protein exists in two forms : the monomeric Globular actin (G-actin) form and the polymerized Filamentous actin (F-actin) form. G-actin is a 43-kDa-protein composed of 4 subdomains (Kabsch et al., 1990), which binds to a divalent cation — Magnesium under physiological conditions (Blanchoin and Pollard, 2002) — and a nucleotide (ATP or ADP). G-actin is asymmetrical, hence the monomers are arranged head-to-tail in a filament. That confers polarity to the actin filament, *i.e.* both ends are structurally different: Subdomains 1 and 3 constitute the "barbed end" of the actin filament and subdomains 2 and 4 compose the "pointed end" (Fig. 2.1). The actin filament forms a double-stranded helix, with a twist repeating every 37 nm and diameter of a 5-9 nm (Howard, 2001).

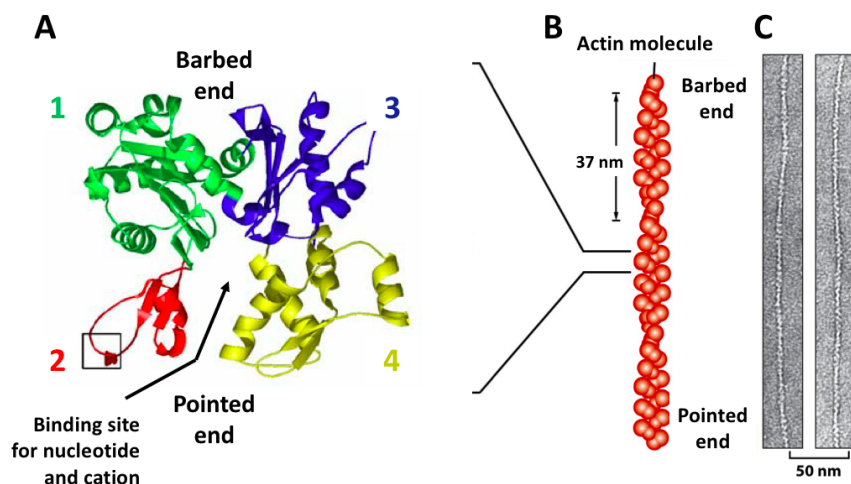


Figure 2.1: Structure of G-actin. **A:** The asymmetric topology of G-actin, with its 4 subdomains represented in different colors, its binding site, its barbed end (formed by the subdomains 1 and 3) and its pointed end (formed by the subdomains 2 and 4). Adapted from (Kim et al., 2006). **B:** The arrangement of monomers within the filament forms a double stranded helix, with a twist repeating every 37 nm and diameter of a 5-9 nm. **C:** Electron micrograph of negatively stained actin filament. (B,C) adapted from (Alberts et al., 2008).

The assembly of actin filament induces a conformational transition in the actin subunit: G-actin has a twisted conformation and F-actin has a flat conformation (Oda et al., 2009), obtained by a rotation of 20 degree of subdomains 1-2 with respect to subdomains 3-4 (Fig. 2.2).

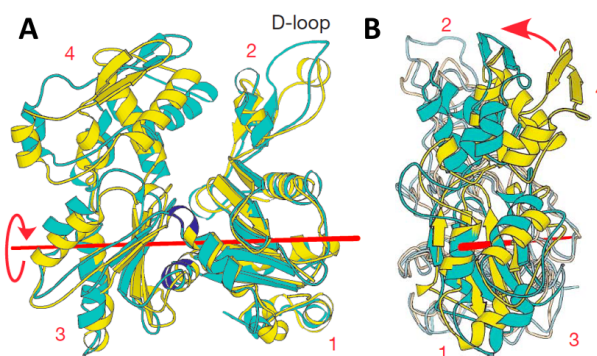


Figure 2.2: Transition from the G-actin conformation to the flat conformation in F-actin. **A:** Front view. The structures of the subunits in the F-actin (cyan) and in the G-actin (yellow) are superimposed on subdomains 1 and 2. Subdomains 3 and 4 are rotated with respect to subdomains 1 and 2 about the rotational axis indicated by the red line in the direction indicated by the red arrow. **B:** Side view from the left-hand side of subdomains 3 and 4 in (A). Figure adapted from (Oda et al., 2009)

Actin mechanics

Just as thermal forces cause a spring to undergo fluctuations in length, thermal forces cause a flexible filament to undergo fluctuations in shape (Fig. 2.3.A). The persistence length L_p is a measure of the length scale below which a polymer keeps the memory of the monomer orientation under thermal fluctuations. By comparing the value of the persistence length L_p to the filament length L , three classes of polymer can be defined :

- if $L_p \ll L$: the filament is classified as a flexible polymer
- if $L_p \sim L$: the filament is classified as semi-flexible
- if $L_p \gg L$: the filament is classified as rigid

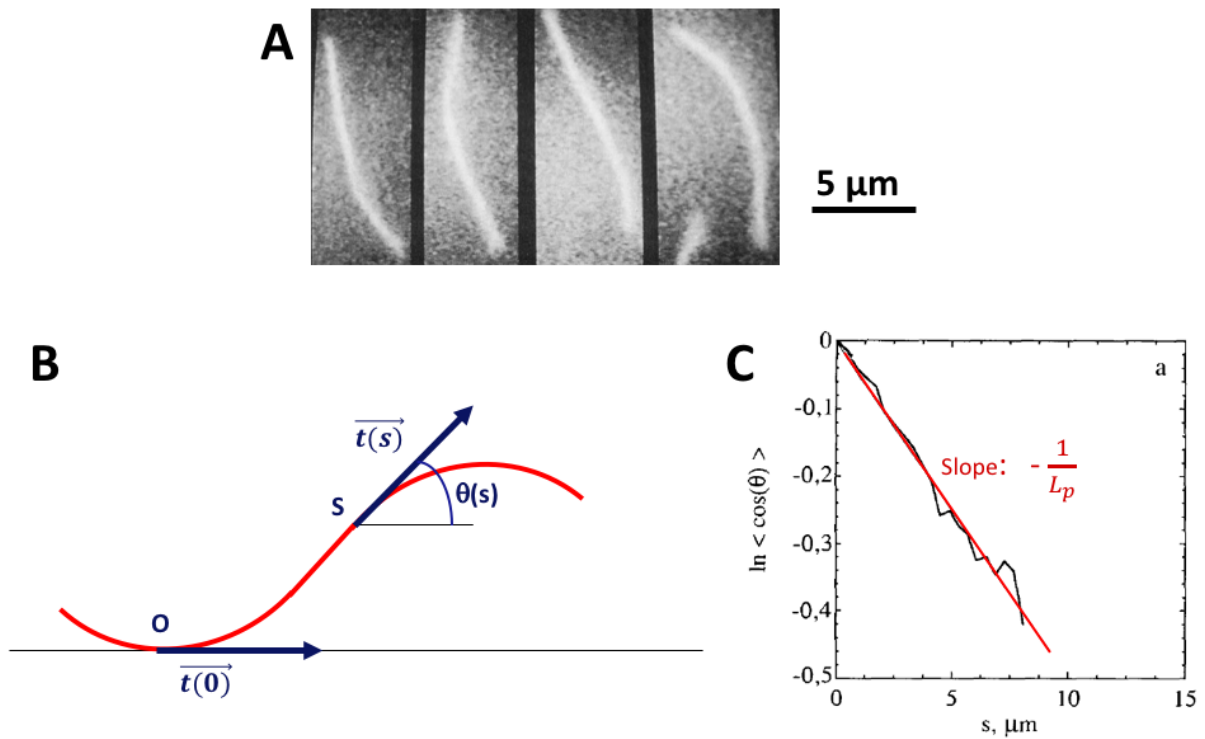


Figure 2.3: Persistence length of an actin filament. **A:** Recorded shape of an unstabilized F-ADP-actin filament undergoing thermal fluctuation at 6-s intervals. **B:** Schematic representation of a filament. For each point of curvilinear abscissa s , the tangent angle $\theta(s)$ with respect to the tangent at the origin O is measured. As the distance between O and S increases, the tangent angle $\theta(s)$ and the tangent angle at the origin become uncorrelated, as the result of thermal fluctuations. **C:** The persistence length can be measured from the exponential decay of tangent-tangent correlation along a chain, *i.e.* the persistence length is the characteristic scale over which memory of the tangent angle is lost. The slope of the graph corresponds to $-\frac{1}{L_p}$. Figure adapted from (Isambert et al., 1995)

The persistence length can be measured from the decay of tangent-tangent correlation along a chain, *i.e.* the persistence length is the scale over which memory of the initial

tangent angle is lost (Howard, 2001), as seen in Figure 2.3.B and C.

$$\langle \vec{t}(s) \cdot \vec{t}(0) \rangle = \langle \cos(\theta(s) - \theta(0)) \rangle = \exp\left(-\frac{s}{L_p}\right) \quad (2.1)$$

where θ and s represent the tangent angle and the curvilinear abscissa along the chain, respectively.

The persistence length is related to the flexural (or bending) rigidity K of the filament:

$$L_p = \frac{K}{k_B T} \quad (2.2)$$

where k_B is the Boltzmann constant and T is the temperature in Kelvin. The more flexible the filament, the smaller the persistence length, the greater the curvature that the filament can achieve under thermal fluctuations. The persistence length of the actin filament, when it is not bound to other proteins, is $9 \pm 0.5 \mu\text{m}$ (Isambert et al., 1995), which is in the range of the actin filament length in cells. Hence in a cell, actin is considered as a semi-flexible filament (Fig. 2.3). It has a flexural rigidity of $K = 3.6 \cdot 10^{-26} \text{ N.m}^2$ (Howard, 2001; Isambert et al., 1995).

Actin polymerization kinetics

The actin filaments polarity is associated with the different dynamics of polymerization/depolymerization at the two filaments ends : at large concentrations of G-actin, actin filaments elongate and the barbed end is the fast growing end, whereas the pointed end is the slow growing end (Pollard, 1986). The barbed end of the actin filament has an association rate of G-actin (k_+), ten times higher than that of the pointed end (Pollard, 1986). Nucleotides regulate the actin polymerization/ depolymerization process by tuning the values of association/dissociation rates at both ends of the filament (Fig. 2.4).

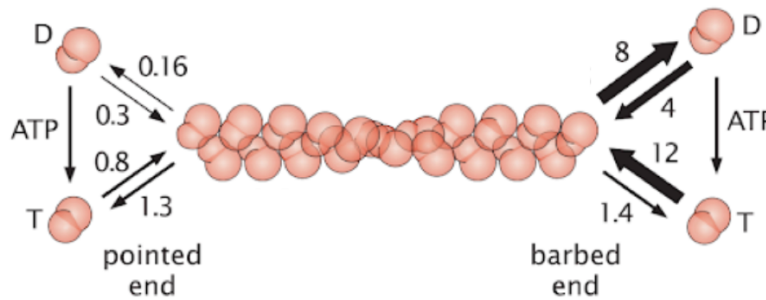


Figure 2.4: Association/dissociation rates of actin. G-actin is bound to ATP (respectively ADP) represented by the letter T (D). The association rates have units of $\mu\text{M}^{-1} \cdot \text{s}^{-1}$. Dissociation rates have units of s^{-1} . The ratio of the dissociation to the association rate gives C_c , the critical concentration. Figure from (Philips et al., 2009), adapted from (Pollard and Borisy, 2003)

G actin has a strong affinity for ATP, which is abundant in cells, and thus filaments mostly assemble from ATP-G-actin. Upon incorporation into a filament, an actin subunit hydrolyzes its nucleotide at a relatively fast rate of 0.3 s^{-1} (Blanchoin and Pollard, 2002). ATP-F-actin is transformed into ADP-Pi (Pi : Phosphate inorganic) F-actin and then ADP-F-actin, after a release of Pi, which is 100 times slower than ATP hydrolysis (Carrier and Pantaloni, 1986). Thus, the nucleotide state of F-actin is an indicator of the filament age.

Table 2.1: Rate constants for actin polymerization and depolymerization at both ends of the actin filament. These values were obtained by *in vitro* measurements in a buffer with a fairly low ionic strength (50 mM KCl, 1 mM MgCl_2 , 0.2 mM of ATP or ADP, 1mM EGTA; (Pollard, 1986))

	Nucleotide	Rate Constant	Barbed end	Pointed end
Association ($\mu\text{M}^{-1} \cdot \text{s}^{-1}$)	ATP	k_+^{ATP}	12	0.8
	ADP	k_+^{ADP}	4	0.3
Dissociation (s^{-1})	ATP	k_-^{ATP}	1.4	1.3
	ADP	k_-^{ADP}	8	0.16
Critical concentration (μM)	ATP	C_c^{ATP}	0.12	1.6
	ADP	C_c^{ADP}	2	0.5

Table 2.1 recapitulates the measured values of association and dissociation rates at both filament ends (see also Fig. 2.4). For each end of the filament, the critical concentration is defined by the ratio of their respective dissociation and association rate constants:

$$C_c = \frac{k_-}{k_+} \quad (2.3)$$

When the concentration of actin monomers in solution exceeds the critical concentration, actin monomers start to assemble at the corresponding end of the filaments. To assemble subunits into filaments, energy is required to overcome a nucleation process, which is the thermodynamically limiting step. This process implies the formation of a trimer from three monomers (Sept and McCammon, 2001). As soon as the trimer is formed, the actin filament can rapidly elongate.

2.1.2 Actin binding proteins

More than 60 families of proteins can bind to actin in order to control the dynamics and the organization of the actin cytoskeleton (Remedios et al., 2003). The actin binding proteins have a variety of roles such as regulating actin assembly, facilitating nucleation, or disassembling filaments (Table 2.2). In the next part, I will only briefly describe the proteins used during my PhD : profilin and the Arp2/3 complex.

Table 2.2: Examples of actin-binding proteins and their function

Category	Proteins	Function	References
Nucleation	Arp 2/3 Complex	to form	(1)
	Formin	new filaments	(2)
Assembly	Profilin	to regulate the kinetics of	(3)
	Capping protein	polymerization, stop elongation	(4)
Disassembly	ADF/Cofilin	to recycle	(5)
	Gelsolin	actin filaments	(6)
Stabilization	tropomyosin	to maintain an actin network even in unfavourable conditions	(7)
Crosslinking	α -actinin	to crosslink	(8)
	Fascin	actin filaments	

References: (1) : (Mullins et al., 1998); (2) : (Kovar and Pollard, 2004); (3) : (Schutt et al., 1993); (4) : (Akin and Mullins, 2008); (5) : (Bamburg et al., 1980); (6): (McCloughlin et al., 1993) ; (7) (Cooper, 2002); (8) (Courson and Rock, 2010).

Profilin: prevents *de novo* formation of actin filaments

Profilin is a 14-kDa-protein that binds actin monomers at their barbed end (Fig. 2.5) to regulate the actin-filaments assembly (Schutt et al., 1993).

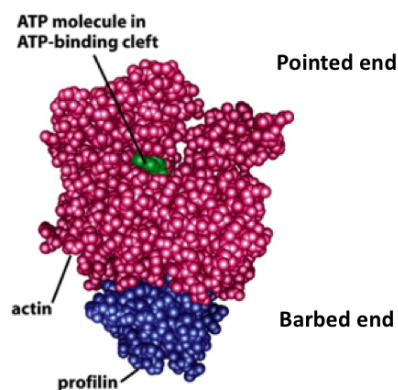


Figure 2.5: Schematic of proflin bound to G-actin. Proflin binds to the barbed end of the actin monomer. Figure from (Alberts et al., 2008)

In the cytoplasm of cells, the monomeric actin concentration varies from a few micromolar to $\sim 150 \mu\text{M}$ in cytoplasm (Blanchoin et al., 2014; Carrier and Pantaloni, 1997), whereas proflin can be at concentrations as high as $100 \mu\text{M}$. Thus, proflin binds to the majority of G-actin present within the cell. In the absence of proflin, actin filament would spontaneously polymerize in all the cytoplasm because the G-actin concentration is above the critical concentrations (Table 2.1). Proflin interacts more strongly with ATP-actin than with ADP-actin, with dissociation rate at thermal equilibrium $K_D^{ATP} = 0.1 - 0.5 \mu\text{M}$ and $K_D^{ADP} = 0.5 - 2 \mu\text{M}$ (Vinson et al., 1998).

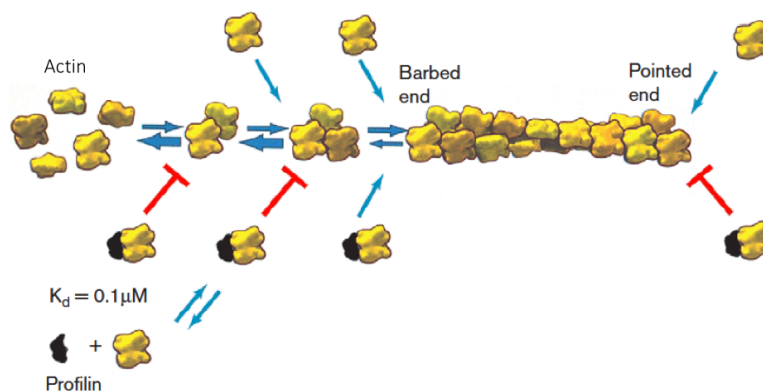


Figure 2.6: Proflin tunes the kinetics of assembly and disassembly of actin filaments and prevents the spontaneous nucleation of new filaments. Figure adapted from (Amann and Pollard, 2000).

When actin monomers are bound to proflin, they can still add onto free barbed ends of actin filaments but at a slower rate compared to that of free G-actin. Fortunately, proflin does not remain bound to the actin subunit : once incorporated into the filament,

once profilin has been released, the barbed end is again capable of incorporating new monomers. Hence, profilin affects the association and dissociation rates of G-actin to a filament (Fig. 2.6): For example, in presence of $8 \mu\text{M}$ of profilin and with an excess of ATP, the association rate at the barbed end decreases from 11.6 to $8 \mu\text{M}^{-1} \cdot \text{s}^{-1}$ and the dissociation rate increases from 1.4 to 2 s^{-1} (Gutsche-Perelroizen et al., 1999). When actin monomers are bound to profilin, it is very hard to overcome the nucleation process. In summary, profilin sequesters a pool of monomeric actin and inhibits actin polymerization in the bulk (Pollard, 1984) by preventing the spontaneous nucleation of actin filaments in cells.

In the presence of profilin, nucleation factors are needed to promote *de novo* actin assembly.

The Arp 2/3 complex and its activation by pWA: nucleation of an actin branch from a pre-existing filament

The Actin-Related-Protein 2 and 3 complex (Arp2/3 complex) mediates the formation of branched actin networks by allowing the nucleation of new actin filaments from the side of a preexisting filament, at a 70° angle from the mother filament (Mullins et al., 1998), forming a Y shape branch (Fig. 2.7). Newly formed filaments then elongate spontaneously by monomer addition at their barbed end (Blanchoin et al., 2000; Machesky et al., 1999).

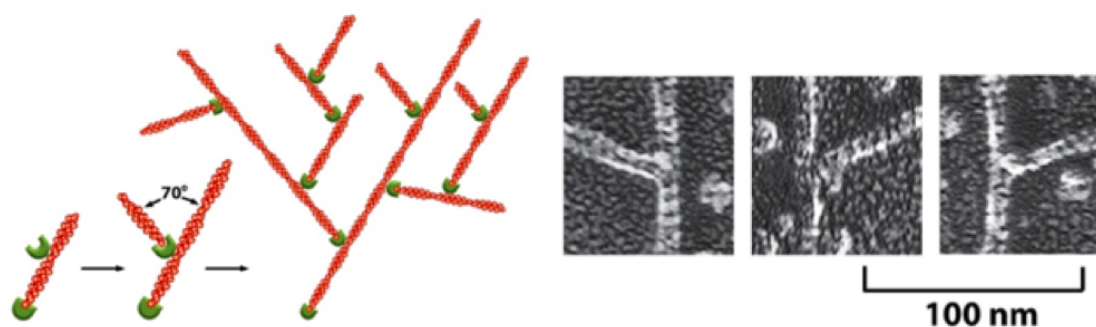


Figure 2.7: The Arp 2/3 complex mediates branched actin networks. Schematic representation of a branched actin network (*left*) and electron micrographs (*right*). Figure adapted from (Alberts et al., 2008; Mullins et al., 1998)

The Arp2/3 complex results from the assembly of 7 polypeptides. The two main subunits Arp2 and Arp3 have a 3D structure very close to that of actin monomers (Fig. 2.8). Their role is to mimic an actin dimer. From this dimer, a new actin monomer can be added, creating the nucleation trimer that triggers actin filament elongation.

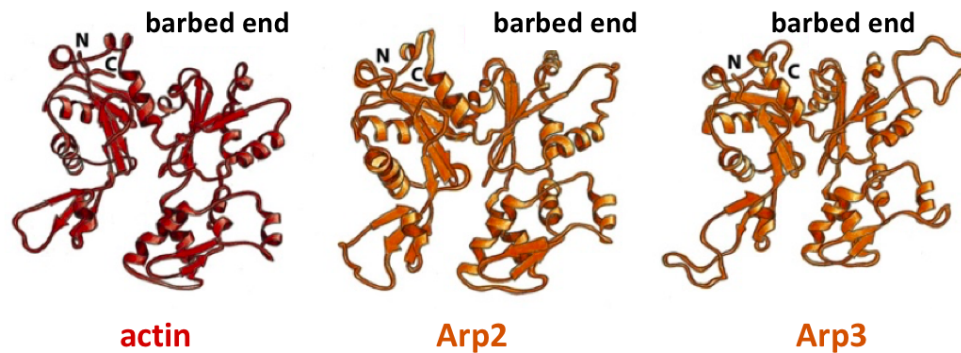


Figure 2.8: Arp2 and Arp 3 have a structure close to that of actin monomers. Figure adapted from (Alberts et al., 2008).

The Arp2/3 complex is constitutively inactive but can be activated by a nucleation promoting factor (NPF) from the Wiskott-Aldrich Syndrom Protein (WASP/WAVE) family (Machesky et al., 1999; Marchand et al., 2001). During my thesis, I used short constructs of the WASP protein, called pWA, which contains the activating domains of the Arp 2/3 complex. It consists in the C-terminal of the WASP/Scar protein, which is composed of 4 domains:

- a proline rich region (p) that can bind profilin-actin (Chereau et al., 2005).
- a verprolin homology domain (V) that recruits monomers of actin,
- a cofilin-like region (C)
- an acidic domain (A),

C and A domains recruit and activate the Arp2/3 complex (Rotty et al., 2013). The nucleation of branched actin networks by the Arp2/3 complex requires the presence of nucleation-promoting factor (pWA), actin monomers and an actin microfilament called a primer (Fig. 2.9).

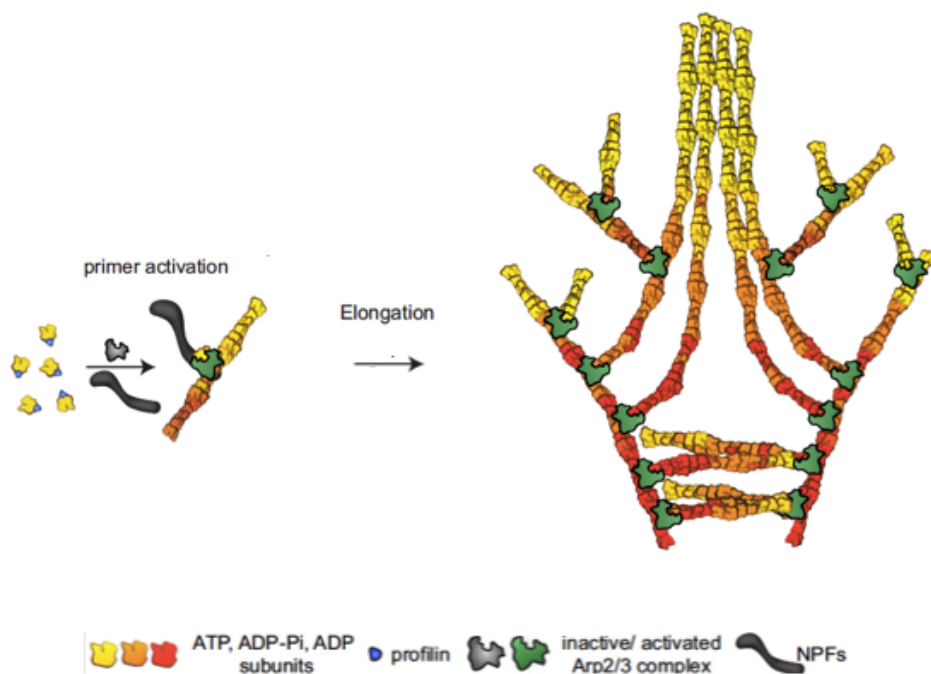


Figure 2.9: A branched actin network results from the autocatalytic branching activity of the Arp2/3 complex. Activated by nucleation promoting factors, the Arp2/3 complex generates a branched network from the side of a preexisting actin filament, called a primer. This yields dense and rigid actin networks. Figure adapted from (Blanchoin et al., 2014)

The Arp2/3 complex activated by pWA allows to bypass the inhibition of nucleation by profilin (Machesky et al., 1999). The reaction is autocatalytic, because the progressive generation of new filaments is fueling the reaction. Thus, nucleation in the presence of actin bound to profilin can occur, but only where the nucleation-promoting factor is located to activate the Arp 2/3 complex and trigger actin polymerization. Therefore, this process allows for a spatial control of actin polymerization.

2.2 The myosins

Myosins are remarkable mechanoenzymes that bind to actin filaments. They operate as molecular motors by converting chemical energy from repeated cycles of ATP hydrolysis onto mechanical energy to generate force and motion. Myosins can act as :

- engine of contraction, such as myosin II for skeletal-muscle contraction (Okamura and Ishiwata, 1988) and force generation within the cell cortex (Salbreux et al., 2007).

- molecular transporters for vesicles along actin filaments within the cell, such as myosin V (Hammer, 2012) and myosin VI (Aschenbrenner et al., 2004; Hasson, 2003)
- link between the cytoskeleton and structures such as membranes or focal adhesion points. Myosin I, for example, is likely to contribute to membrane tension (De La Cruz and Ostap, 2004). Myosin VI is essential for structural integrity of hair-cell bundles of the inner ear (Avraham et al., 1995)

In the last 10 years, there has been great progress in mapping the members of the myosin superfamily, now categorized in more than 35 classes (Bloemink and Geeves, 2011; Foth et al., 2006; Odronitz and Kollmar, 2007). The classification of myosins into families is based on comparison of the genetic sequence similarity in the motor domain (Heissler and Sellers, 2016).

2.2.1 Myosin topology

Myosins can be divided into three main domains as shown on Figure 2.10 :

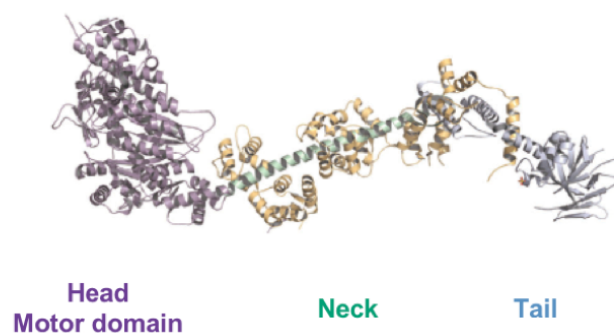


Figure 2.10: The three parts of a myosin, illustrated with a sketch of myosin 1c. The head or motor domain (in lilac), which binds to actin nucleotides (ATP, ADP). The neck (pistachio), which is associated with regulatory chains (yellow). By operating like a lever arm, the neck magnifies conformational changes generated by the head. The tail (blue) ensures myosin interaction with cargoes or other myosins. Figure adapted from (Heissler and Sellers, 2016)

- The head (or motor domain), which binds to actin and uses chemical energy derived from ATP hydrolysis to change conformation.
- The neck associated with light chains. It magnifies the conformational change generated by the head (lever arm).
- The tail insures myosin interaction with cargoes or other myosins. Myosin II can further self-assemble into thick bipolar filaments that contain hundreds of heads

(Fig. 2.12) Some myosins, as myosin II and myosin V that I worked with during my PhD, have a coiled coil domain in this region, which allows them to dimerize, forming a helical structure. Some myosins have a cargo binding domain in this region.

As shown in Figure 2.11 dimerized double-headed myosins II can be split into 2 sub-fragments : heavy meromyosin (HMM) and light meromyosin (LMM).

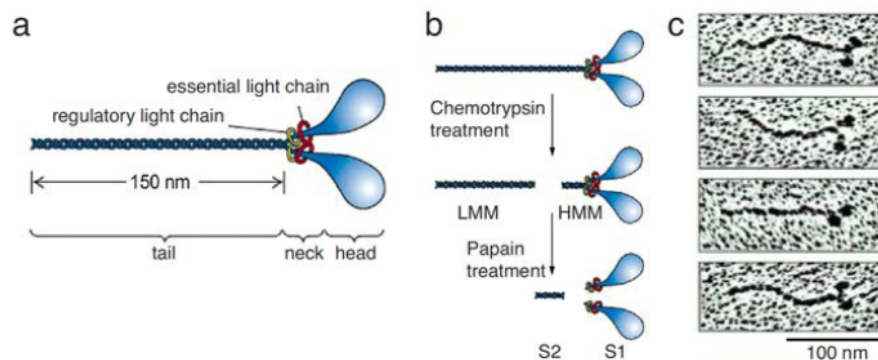


Figure 2.11: Dimerized/double-headed myosin II. a: Schematic presentation of myosin. b: Myosin molecules can be split into Heavy Meromyosin (HMM) that is still an active ATPase and Light Meromyosin (LMM). HMM can be also divided into subfragments S1 and S2 (only S1 is an ATPase). c: Electron micrographs of myosin II. Figure from (Ennomani, 2015), adapted from (Alberts et al., 2002).

A HMM fragment comprises a motor domain, a neck and part of the tail, it can be divided into subfragments S1 and S2. A LMM subfragment does not bind to actin, but allows the motors to assemble by associating their LMM.

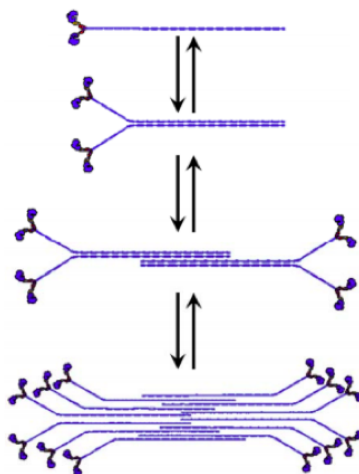


Figure 2.12: Myosins II can form assemblies (called "thick filaments" in muscle) by associating their LMM. Figure from (Luo and Robinson, 2015)

HMM subfragments were used during my thesis, in order to ensure the presence of double headed myosin II but avoid larger assemblies of myosin heads, that can be formed by association of myosin tails (Fig. 2.12).

2.2.2 The chemomechanical cycle of myosin

Remarkably, all myosin motors follow the same basic chemomechanical cycle, but they display a large variety of transition rates between different states in the cycle, allowing each myosin to be finely tuned to a specific task. Switching from attached to detached states on actin filaments, the myosin motors go through a cycle driven by ATP hydrolysis (Fig. 2.13).

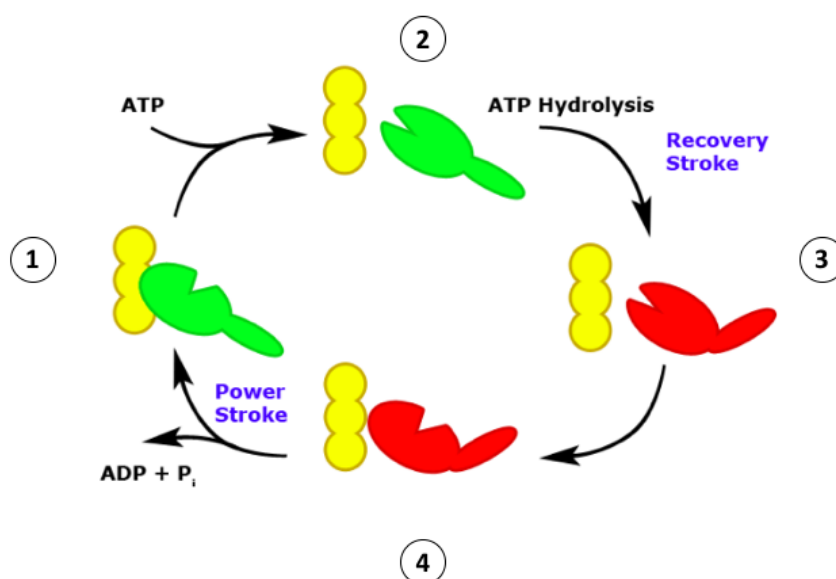


Figure 2.13: Conventional model for the catalytic cycle of myosin. Force is generated by myosin strongly bound on an actin filament (yellow) by the transition ("power-stroke") between two conformational states (red *vs* green) of myosin. (1) Strongly-bound actomyosin complex with no nucleotide (also called the "rigor complex"). (2) ATP binding to myosin dissociates myosin from actin. (3) Myosin hydrolyzes ATP in the actin detached state and changes conformation to reprime its force-generating capacity. (4) Myosin-ADP-P_i weakly rebinds to actin. Release of P_i and ADP is associated to strong binding and force generation ("power-stroke"). Figure from (<https://cbs.umn.edu/ddt/people/ben-binder>)

This catalytic cycle happens in parallel with a mechanical cycle that uses the free energy derived from the hydrolysis of ATP to drive conformational changes in the myosin motor domain. To understand how a conformational change can generate a force, the motor protein can be considered as an elastic element – a spring – which can store mechanical energy. The idea is that the conformational change driven by ATP hydrolysis actively strains the spring: The tension in the spring produces a force dipole, pulling on

a cargo (or any other structure attached to the tail) as well as on the actin filament to which the head is attached. The release of the strain is associated with motion (relative sliding of filaments). This concept forms the basis of the power stroke model (Fig. 2.14).

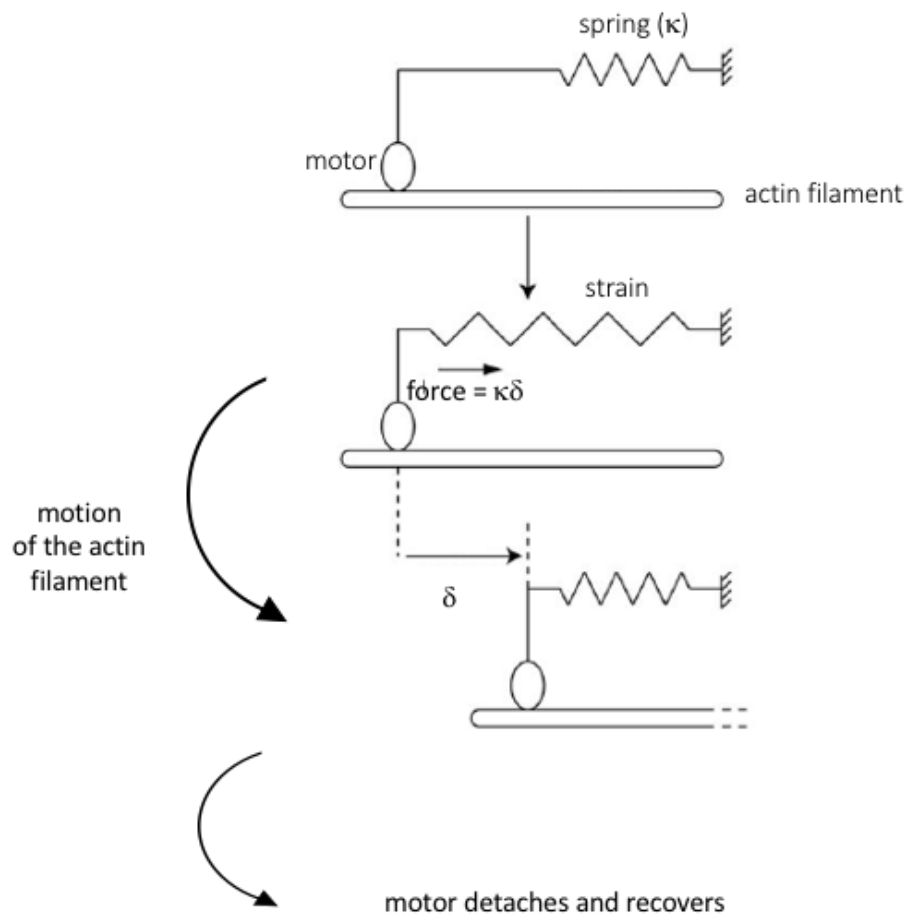


Figure 2.14: Schematic to explain how a conformational change can generate force: the "power-stroke" model. The motor protein is described as an elastic element, a spring, which is set under tension and stores mechanical energy upon hydrolysis of ATP. This strain can drive sliding of the actin filament with respect to the tail, releasing the stored energy. Figure adapted from (Howard, 2001; Richard, 2016)

The power stroke model explains how energy transduction might occur. A directed conformational change within the cross bridge that the motor domain forms between the filament and the tail-attached-cargo. The conformational change in fact happens in the head domain and is allosterically communicated to the neck, which acts as a swinging lever arm (Fig. 2.15), which magnifies the size of the conformational change (Howard, 2001)

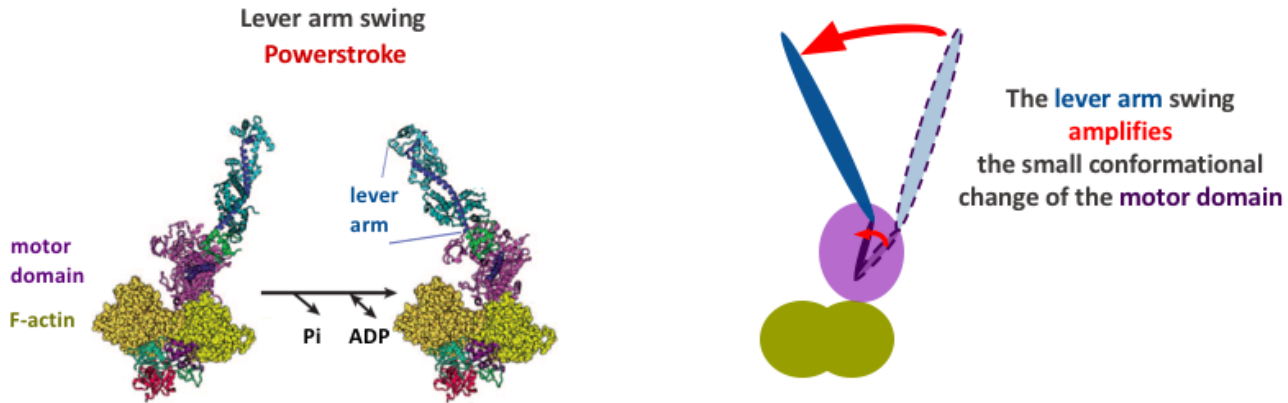


Figure 2.15: The swinging lever arm allows to magnify the conformational change of the motor domain. Figure adapted from (Sweeney and Houdusse, 2010).

2.2.3 Duty ratio and processivity

Myosins vary in their ATPase rate and in the fraction of time of the ATPase cycle that they are strongly bound to actin, a characteristic called the *duty ratio*.

The duty ratio r can be written as :

$$r = \frac{\tau_{on}}{\tau_{on} + \tau_{off}}, \quad (2.4)$$

where τ_{on} is the time spent attached and τ_{off} is the time spent detached during one ATPase cycle. The duty ratio is around 1 if the motor spends most of its time attached during the cycle, or close to 0 if it spends most of its time detached. The duty ratio controls the minimum number N_{min} of heads required for a continuous movement :

$$N_{min} \approx \frac{1}{r} \quad (2.5)$$

If N_{min} myosins are assembled, it guarantees that there will be at least one head bound to the filament at every moment (Harada et al., 1990). Double-headed motors with a high duty ratio ($r > 0.5$), such as myosin V ($r^{MV} = 0.7$ (De La Cruz et al., 1999)), can undergo multiple productive catalytic cycles and mechanical steps before detaching from the actin track. For instance, double-headed myosin V can take at least 40-50 steps on average before detaching from actin (Mehta et al., 1999). Thus, the duty ratio controls another property of myosins, the *processivity*. The processivity characterizes the ability of one molecule to perform mechanochemical cycles while remaining attached to an actin filament. A processive motor can act autonomously as a walker. On the other hand motors

with a low duty ratio (r close to 0), such as myosin II ($r^{MII} = 0.025$ (Veigel et al., 2003)) are said to be non-processive motors. They must oligomerize into large assemblies to produce continuous motility, such as myosin II, which work collectively by assembling in large arrays containing up to 10,000 heads (Howard, 2001). The motility of a myosin can also be characterized by its *run length*. For processive motors, the run length corresponds to the distance covered by the double headed myosin on one filament, whereas for non-processive motors it corresponds to the distance covered by an assembly of those motors.

2.2.4 Experiments to characterize motor action

The development of *in vitro* and imaging techniques has allowed for a direct analysis of mechanical movement of myosins and highlighted the roles of key parameters such as the myosin density, the ATP concentration and the external load (Howard, 2001; Philips et al., 2009).

Motility assay

One of the most important *in vitro* assay is the gliding assay. Motors are absorbed by their tail on a glass surface and fluorescently labeled actin filaments are then added to the system in the presence of ATP. The filaments glide on the myosin-coated surface with a continuous and directed movement (Kron and Spudich, 1986) (Fig 2.16).

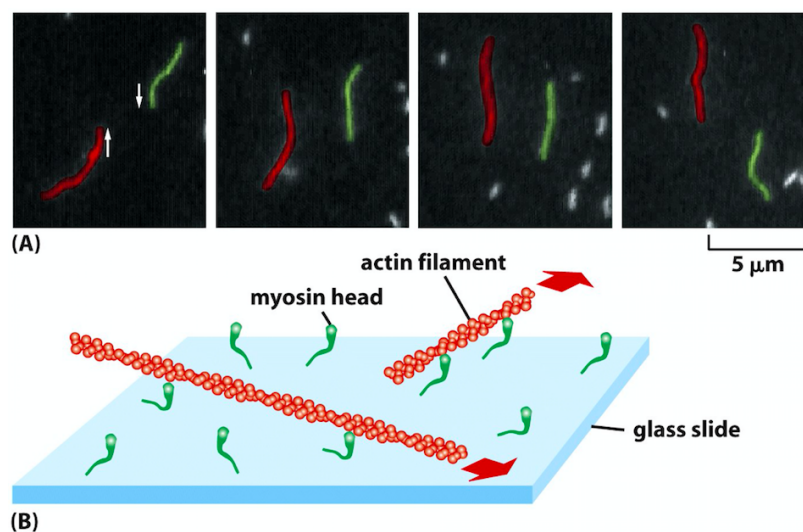


Figure 2.16: *In vitro* motility assay. Actin filaments glide on a myosin coated surface. In this experiment, purified S1 of myosin II were attached to a glass slide and then actin filaments (fluorescently labeled) were added and allowed to bind to myosin heads. **A:** When ATP was added, the actin filaments began to glide along the surface, owing to the many individual steps taken by each of the dozens of myosin heads bound to each filament. The video frames shown in this sequence were recorded 0.6 s apart. The two filaments shown (one red and one green) were moving in opposite directions at a speed of $4 \mu\text{m/s}$. **B:** Schematic of the experiment. The large red arrow indicates the direction of actin filament movement. Figure from (Alberts et al., 2008)

This assay provides a direct measure of motor velocity with purified proteins. It was shown that the speed of myosin II increases with the ATP concentration, until a saturation at 3 - 4 $\mu\text{m/s}$ is observed above 200 μM of ATP (Kron and Spudich, 1986). The speed of the filaments also depends on the ionic strength and on the pH of the solution. Motility disappears when the salt concentration is above 100 mM and when the pH is not within the range of 6.5 - 9.5. Temperature significantly influences filament speed (Bourdieu et al., 1995), which goes from 2 to 10.4 $\mu\text{m/s}$ when the temperature increases from 20 to 30 $^{\circ}\text{C}$ (Fig. 2.17.A).

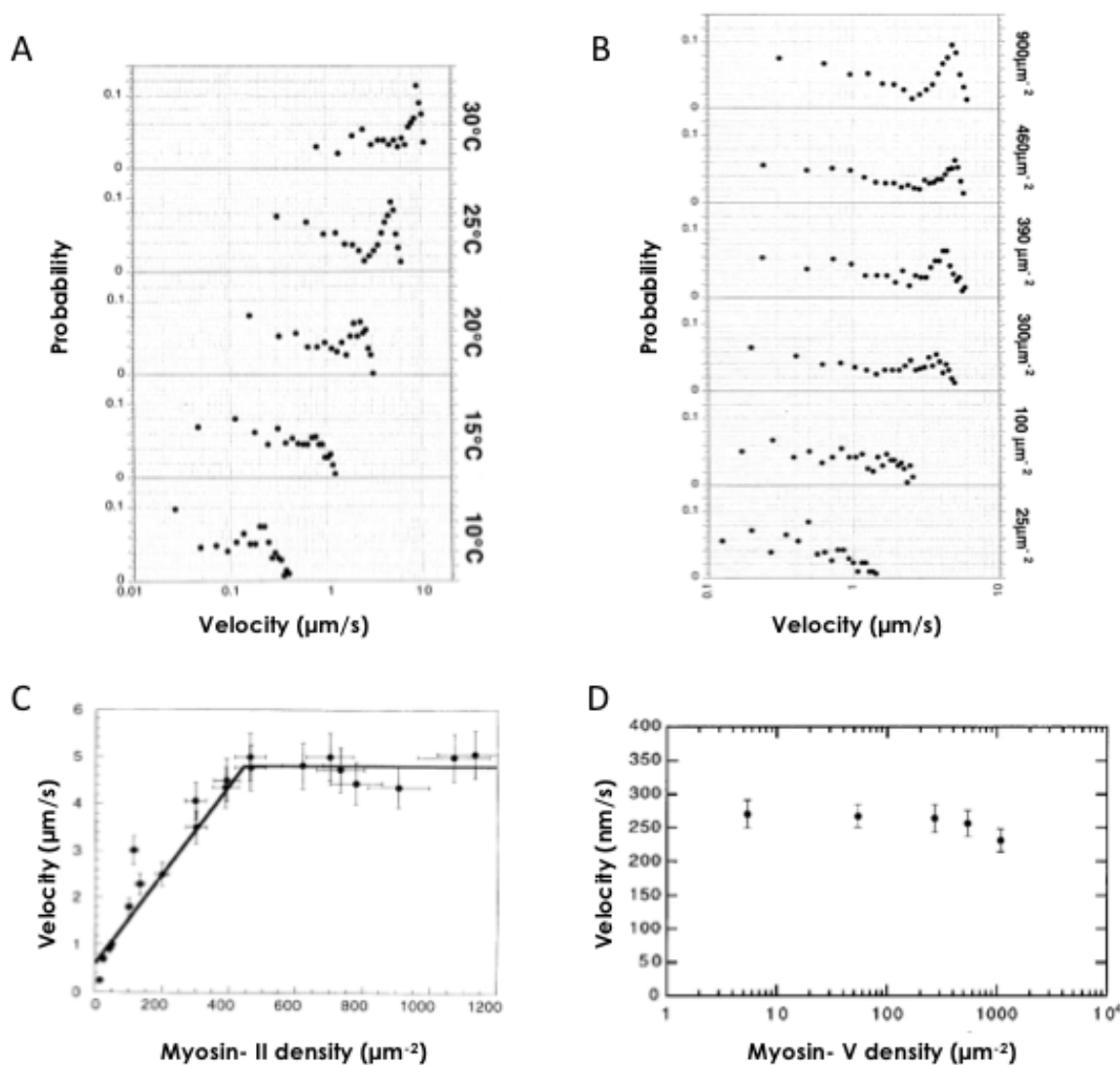


Figure 2.17: Filament speed in *in vitro* motility assays depending on temperature and motor density. **A:** Speed distributions of actin filaments interacting with a myosin II-coated- surface at different temperatures. **B:** Speed distributions of actin filaments interacting with a myosin II-coated-surface at different motor densities. **C:** Velocity of actin filaments as a function of myosin II density. **D:** Velocity of actin filaments as a function of myosin V density. Figures (A, B, C) from (Bourdieu et al., 1995), Figure (D) from (Rock et al., 2000)

For myosin II, the density on the surface influences the speed distribution (Bourdieu et al., 1995) : A peak clearly appears for densities beyond $300 \mu m^{-2}$ and above $450 \mu m^{-2}$, the speed saturates at $5 \mu m/s$. In contrast, the speed of myosin V does not depend on myosin density (Rock et al., 2000) (Fig. 2.17.D). These different behaviors are consistent with the non processivity of myosin II and the processivity of myosin V. One myosin V is able to make a filament glide, whereas myosin II must work within a group to produce a directed movement.

Alternatively, instead of performing a gliding assay, the molecular motors can be attached to a micrometer-sized bead which will move on actin filaments. Bead movements can then be observed with a conventional optical microscope (Spudich et al., 1985).

Optical tweezers

Optical tweezers have been used to investigate the characteristics and mechanisms of the motion of myosin at the single-molecule level (Finer et al., 1994; Molloy et al., 1995; Veigel et al., 2002). Two sorts of bead assays have been developed : In a simple bead assay, the tail of the molecule is bound to the trapped bead and the head interacts with an actin filament stuck to a glass surface (Fig. 2.18.A). This set-up can be used to study processive motors such as myosin V. In the dumbbell assay (Fig. 2.18.B), a single actin filament is held taut in between two beads that are manipulated with a dual optical trap; the filament is brought in proximity of a pedetal on which lie a few myosin molecules.

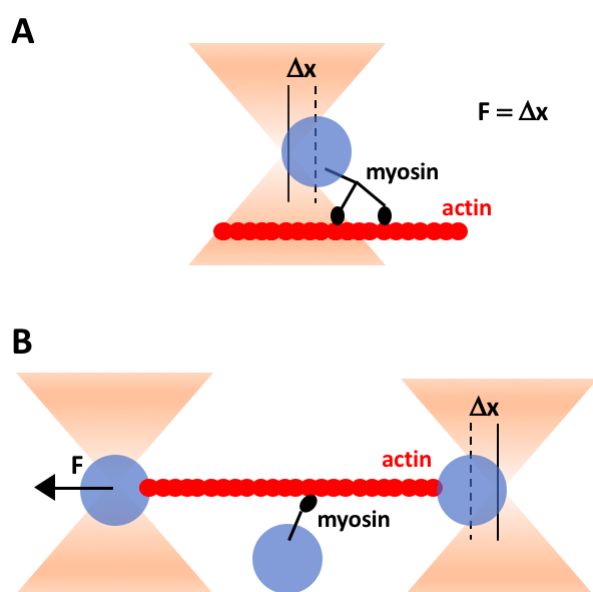


Figure 2.18: Assays with optical tweezers. A: Bead assay with one optical trap. **B:** The "dumbbell assay", using 3 beads and a dual optical trap.

Using a second optical trap greatly reduces the mechanical noise, providing the most stable configuration to study non-processive motors (Figure 2.18.B). This configuration was used to study both myosin II and myosin V (Finer et al., 1994; Svoboda et al., 1993; Visscher et al., 1999).

Bead assay (one bead) Rief and colleagues highlighted the mechanism of processivity of myosin V with one optical tweezer and one trapped bead (Rief et al., 2000). These experiments could use a force-clamp technique (Visscher et al., 1999) to maintain a relatively constant force on the trapped bead by keeping a constant distance between the centers of the bead and the trap (Fig. 2.19.A).

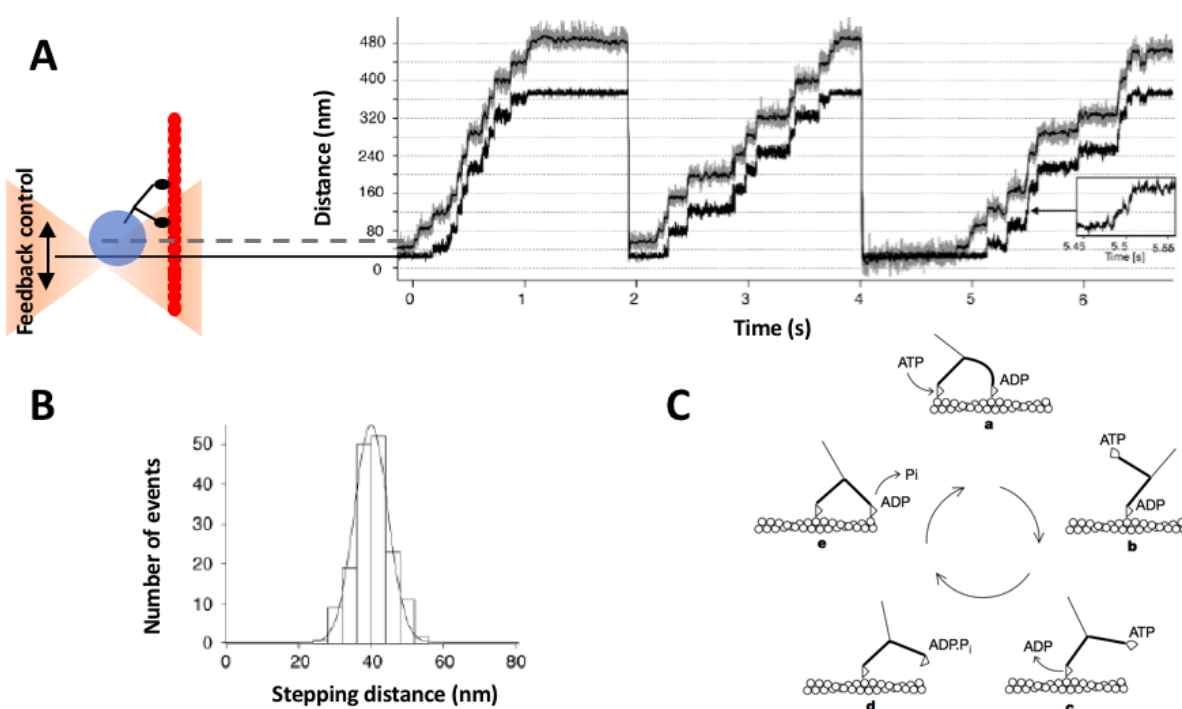


Figure 2.19: Single molecule experiment with a processive motor. **A:** Principle of the force clamp technique to maintain a relatively constant force on the trapped bead by keeping a constant distance between the centers of the bead and the trap. Double-headed myosin V can undergo several steps before detaching. **B:** Histogram of step sizes measured at 2 mM ATP and at an external force of 1 pN. The black line is a Gaussian fit to the data (mean : 40.2 nm, standard deviation : 6.4 nm). Figures (A,B) adapted from (Rief et al., 2000). **C:** Model showing the role of two-headed attachment in the walking cycle of myosin V. The trailing, nucleotide-free head of a teardrop-shaped molecule binds ATP (**a**) and detaches, relieving the axial strain in the molecule (**b**) and bringing the detached head towards the next actin site (**c**). Dissociation of ADP completes the working stroke (**d**). Attachment of the free head is quickly followed by loss of phosphate by actin activation, and a tight binding develops (**e**). Figure from (Walker et al., 2000).

It was shown that double headed myosin V can undergo several steps before detaching, giving a measure of its run length, here 1 μm . A speed can be defined by computing the

ratio of the distance run by the myosin and the duration of the run, here 360 nm s^{-1} (Fig. 2.19.A). Such assay revealed the 36-nm step size of myosin V (Fig. 2.19.B). It also contributed to define the hand-over-hand (walker) model of processive myosins (Fig. 2.19.C).

Dumbbell assay (three beads) In a configuration with three beads (Finer et al., 1994), an actin filament is held taut by two beads and then maintained with optical tweezers close to a third bead coated with myosin. The bead position of one of the beads holding actin shows a brownian motion, which is stochastically interrupted by sequences with lower fluctuations. These lower fluctuations are signatures of motor attachment (indicated with arrows in Figure 2.20.A). An attachment event triggers an offset of the mean position of the bead compared to the position with no attachment. Because of fluctuations, the measured displacements for an ensemble of events have various amplitude and direction (Molloy et al., 1995) (Fig. 2.20.B). A HMM myosin II produces on average a displacement of 5 nm (Veigel et al., 1998). By measuring the applied force to prevent myosin from moving, one estimate a stall force produced of 3-4 pN for myosin II in its attached state (Finer et al., 1994).

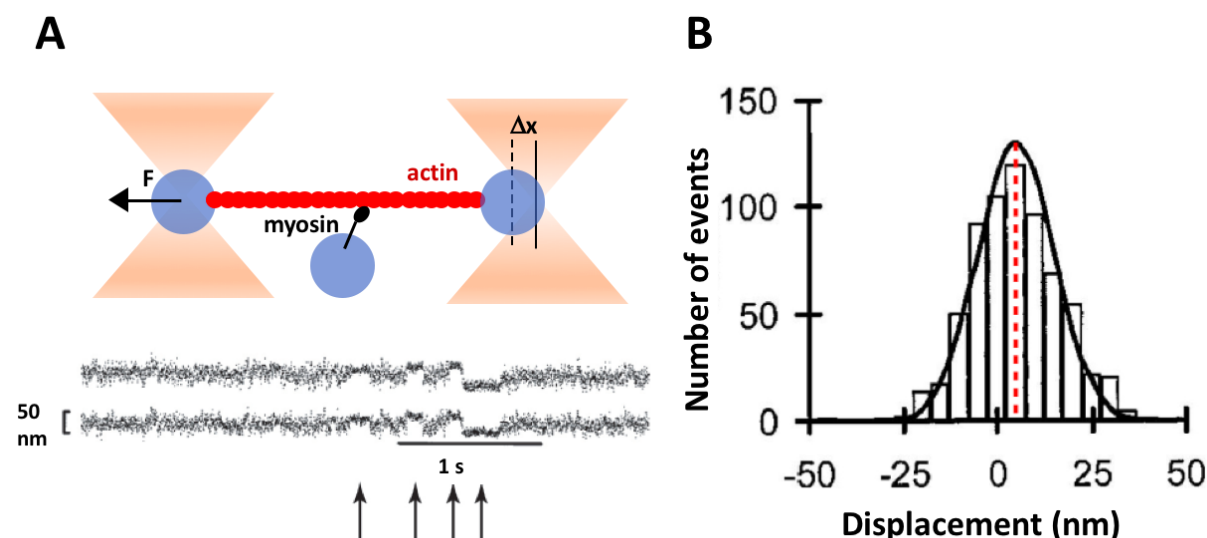


Figure 2.20: Single molecule experiment with a non-processive motor. **A:** In a configuration with three beads (Finer et al., 1994), an actin filament is stretched under two beads maintained with optical tweezers close to a third bead coated with myosin, in a solution containing ATP. The temporal tracks of bead position show brownian motion, which is stochastically interrupted by sequences with lower fluctuations. These lower fluctuations are signatures of motor attachment (indicated with arrows). **B:** An attachment event evokes an offset of the mean position of the bead compared to the position with no attachment, which corresponds to the size of the "power-stroke" (Molloy et al., 1995). A HMM myosin II produces a mean displacement of 5 nm (Veigel et al., 1998). Figure adapted from (Plaçaïs, 2008)

An alternative approach is to observe the movement of the individual molecules by labeling them with a small protein tag (Yildiz et al., 2003). Myosin V was labeled with a single fluorophore at different positions in the light-chain domain : it was observed that the center of mass moves by steps of 37 nm with 1.5 nm precision and 0.5-second-temporal resolution.

2.2.5 Recap of myosin II and myosin V properties (Table 2.3)

Table 2.3: Properties of myosin II and myosin V. * indicates that the value is effective *i.e.* it does not corresponds to the property of an individual myosin but of a group of motors/

Property	myosin II	myosin V
Role in cell	Contraction	Transport
ATPase rate k_{ATP}	25 s^{-1} (1)	10 s^{-1} (2)
Duty ratio r	0.025 (3)	0.7 (4)
Speed v	$5 \text{ }\mu\text{m}\cdot\text{s}^{-1}$ * (5)	$360 \text{ nm}\cdot\text{s}^{-1}$ (2,4)
Powerstroke δ	5 nm (6)	25 nm (7)
Run length l	—	1 μm (2)
Step Δ	200 nm * (3)	36 nm (2)

Data from : (1)(Howard, 2001); (2)(Rief et al., 2000); (3)(Veigel et al., 2003); (4)(De La Cruz et al., 1999); (5) (Bourdieu et al., 1995); (6)(Molloy et al., 1995) ; (7)(Veigel et al., 2002).

The speed v , the rate of ATP hydrolysis k_{ATP} , the duty ratio r , the step Δ and the power stroke δ are related according to (Howard, 2001): $v = \Delta \cdot k_{ATP} = \frac{\delta}{r} \cdot k_{ATP}$

Chapter 3

Materials and Methods

In this chapter, we describe a minimal *in vitro* system to direct the assembly and to control the architecture of actomyosin networks. The experimental strategy has been developed in collaboration with the group of Laurent Blanchoin (iRTSV, Grenoble) and has been previously described (Ennomani, 2015; Reymann, 2011; Reymann et al., 2010, 2014; Richard, 2016). It relies on micropatterning to precisely position nucleation sites of actin polymerization at the surface of a substrate. To trigger the assembly of the actomyosin network, a small volume of solution containing a minimal set of purified proteins ensuring actin polymerization is put between a coverslip micropatterned with an actin nucleation promoting factor (pWA) and a glass slide support. The experimental procedure can be separated in four steps (Fig. 3.1 and Fig. 3.2): First, the micropatterning technique, second, the protein mix preparation, third the imaging, and finally image analysis. The originality of these experiments was to add myosin motors (HMM myosin II or myosin V) and study how they dynamically reorganize the actin network.

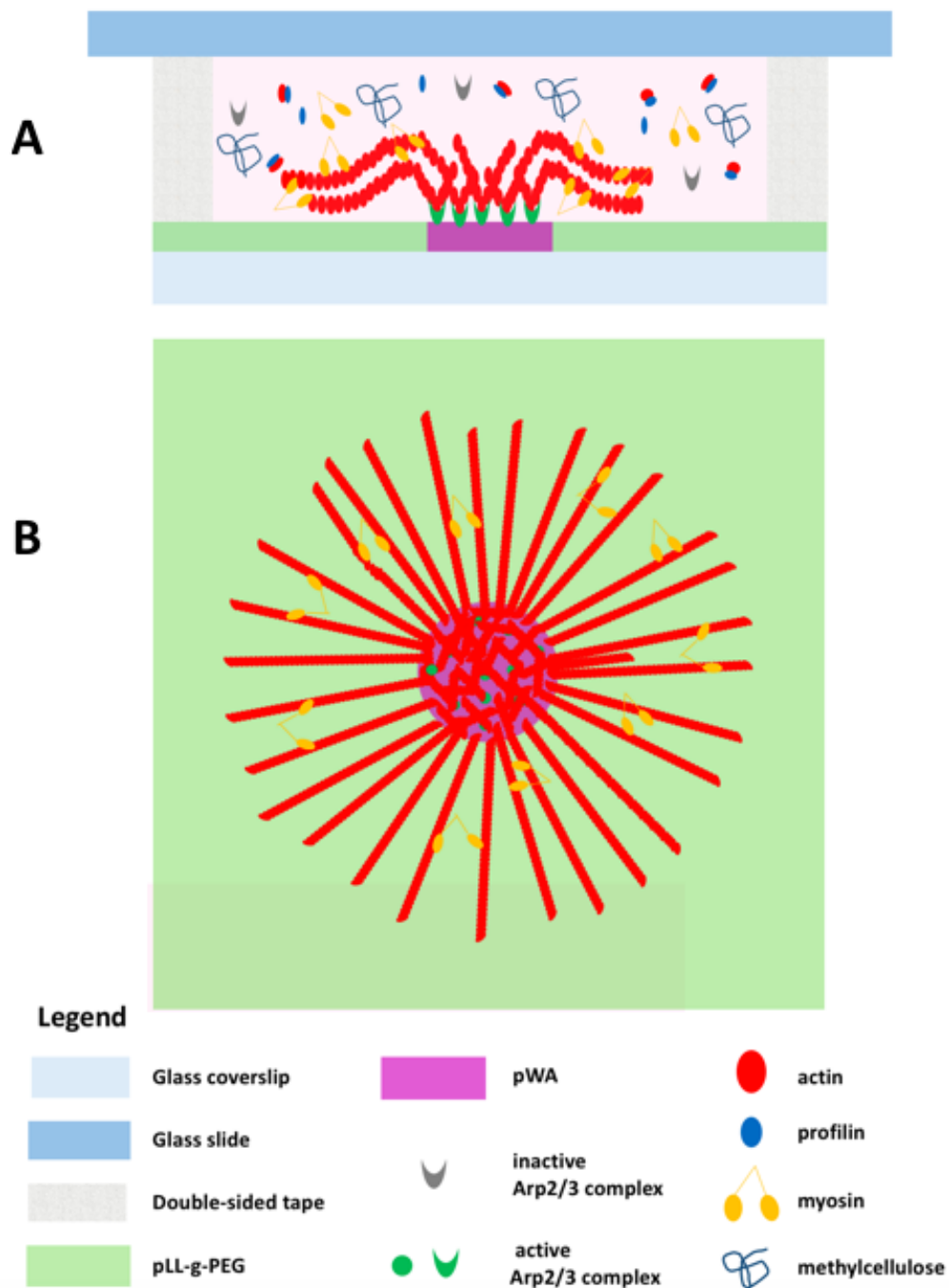


Figure 3.1: Schematic representation of the experiment : an experimental chamber is built between a coverslip and a glass slide with double-sided tape. The coverslip is passivated with PLL-g-PEG, while a patterned region of controlled geometry is coated with the nucleation promoting factor (pWA). pWA activates the Arp 2/3 complex, which triggers actin polymerization at the surface of the pattern. Profilin binds to actin monomers to prevent nucleation of new filaments in bulk. Once nucleated, a filament grows by monomer addition to the barbed end of the filament and can escape from the nucleation zone, giving rise to a parallel network of filaments *i.e.* all the filaments have the same polarity. Methylcellulose is a depleting agent and keeps actin filaments close to the coverslip surface. Myosins are present in solution and interact with the actin filaments. **A**: cross section of the experimental chamber. **B**: top view of the experimental chamber.

3.1 Micropatterning of an actin nucleation promoting factor

The procedure to micropattern a nucleation promoting factor of actin polymerization on glass coverslips is composed of 5 steps (Fig. 3.2). First, a plasma treatment ensures that the surface of glass coverslip is clean. Second, the surface of the coverslip is passivated. Third, the coverslips are insolated through a photomask with deep UV-light to allow coating with the nucleation promoting factor (pWA protein) on the UV-patterned regions. These steps will be described in more details in the following section.

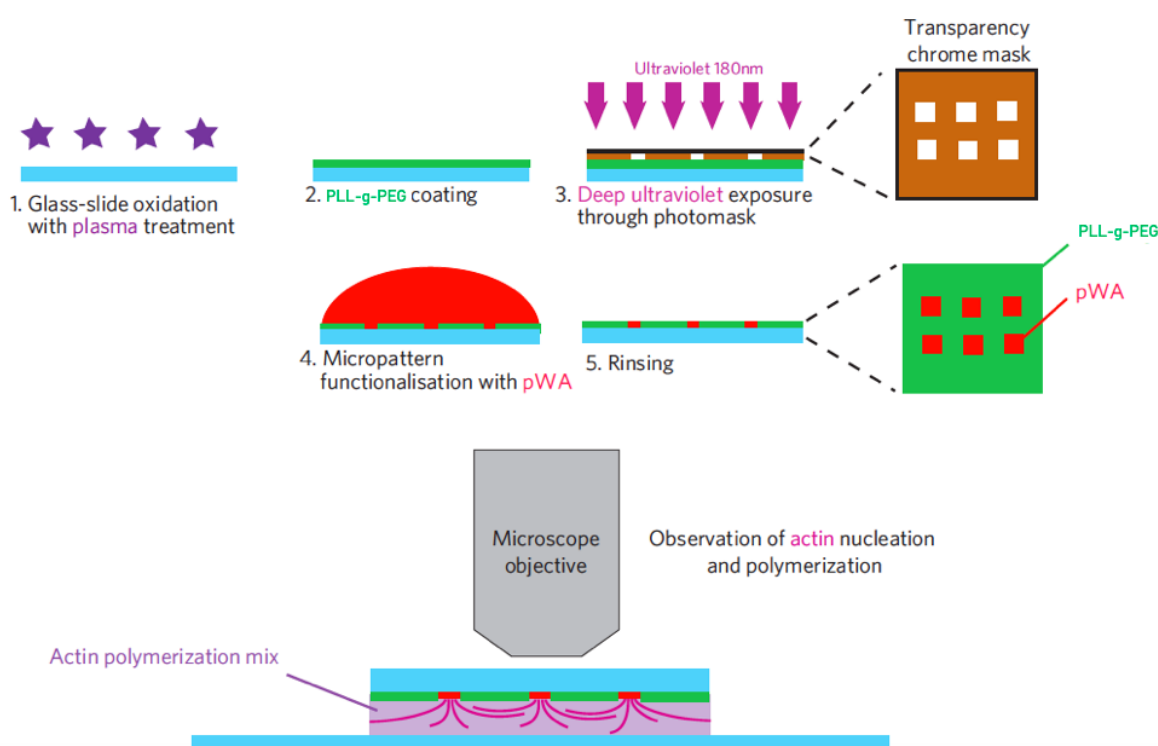


Figure 3.2: Surface micropatterning technique : (1) The coverslip undergoes a plasma treatment . (2) The coverslip is coated with PLL-g-PEG to passivate the surface. (3) The coverslip is covered by a chrome photo mask and exposed to deep UV to define patterns on the coverslips, where the passivating agent (PLL-g-PEG) has been degraded.. (4) pWA is adsorbed on regions of the surface that have been exposed to UV light. Figure from (Reymann et al., 2010)

3.1.1 Surface passivation

Coverslips are washed in three steps : first in ultra-pure water, then in ethanol and wiped, and finally in ultra-pure water again and dried with a nitrogen-gas-flow. Then, the coverslips are vertically disposed in a holder and exposed to an air plasma (80 mW for 2 min) (18 W, Harrick Plasma, Ithaca, NY, (Fig. 3.2.(1))). As a result of this plasma

treatment, the surface of the coverslip is negatively charged when immersed in an aqueous solution. To passivate the coverslips, *i.e.* avoid nonspecific adsorption of proteins, the coverslips are coated with poly(L-lysine)-graft-polyethyleneglycol (PLL-g-PEG). A 100 μL drop of PLL-g-PEG at 0.1 mg/ml in 10 mM HEPES (pH 7.4) per coverslip is put on parafilm and each coverslip is positioned on a droplet with tweezers and incubated for 1 h (Fig. 3.2.(2)). PLL-g-PEG is a comb-copolymer: the PLL part is the backbone that adheres to the glass surface and the PEG part leads to a brush structure preventing protein adsorption by steric repulsion (Fig. 3.3). Afterwards, the coverslips are gently lifted up from the side using tweezers and dried with a nitrogen-gas flow. The coverslips are stored at 4 $^{\circ}\text{C}$ for a maximum period of 2 days.

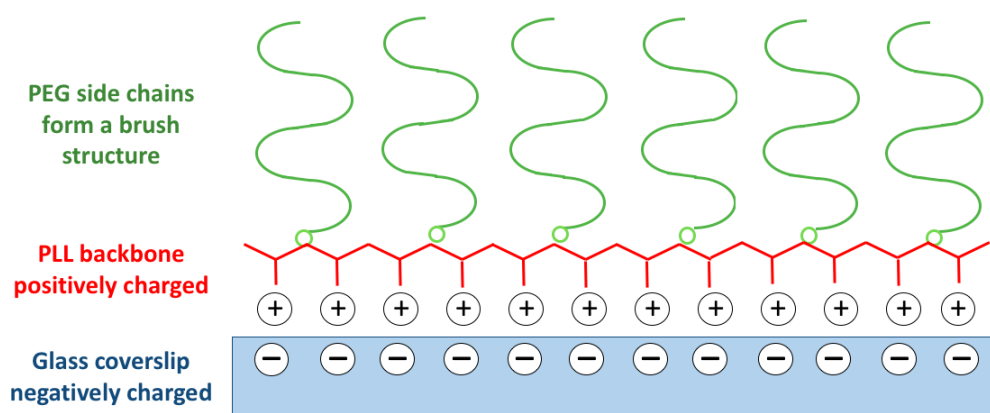


Figure 3.3: Mechanism of glass coverslip passivation with PLL-g-PEG: the PLL part is the backbone that electrostatically adheres to the glass surface and the PEG part leads to a brush structure preventing protein adsorption by steric repulsion

3.1.2 Patterning of a nucleation promoting factor

A chromium synthetic-quartz photomask (Fig. 3.4 ; Toppan Photomasks, Corbeil, France) is cleaned with isopropanol, then with ethanol, and dried using a nitrogen-gas flow. Pegylated coverslips are clamped using a custom-made vacuum-holder (Richard, 2016). The UV lamp is preheated for 5 min. Then, the mask-covered coverslips are exposed for 5 min to deep ultraviolet light (wavelength $\lambda < 200$ nm, UVO Cleaner, Jellight Company, Irvine, CA) (Fig. 3.2.(3)). This treatment destroys the PEG brush, responsible for repelling proteins, leaving place to carboxyl groups that contribute to the strong attachment of proteins on the patterns (Azioune et al., 2009). Then the coverslips are bathed for 10 min in a solution at 1 μM of pWA in 1X KMEI Buffer (Appendix D. 2) (Fig. 3.2.(4)). pWA adsorbs non specifically on the insolated regions of the coverslips. The coverslips are then washed by bathing them in 15 mL of cold 1X KMEI. The passivated surface

is hydrophobic; coverslips are gently lifted up with tweezers from the bath, eliminating droplets on the treated surface.

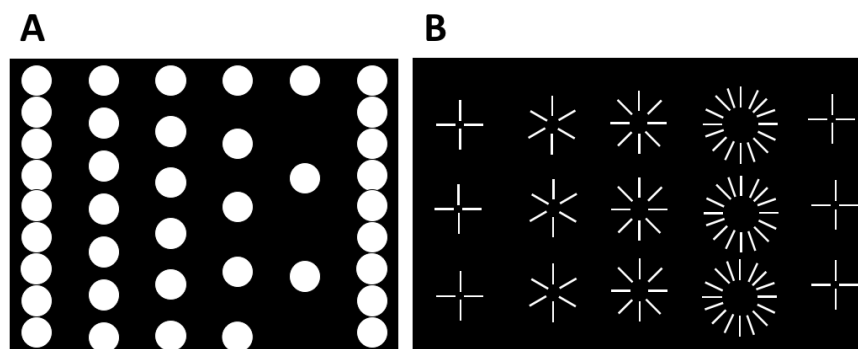


Figure 3.4: Two examples of patterns drawn on the chrome photomask. **A:** The most common pattern used for my experiments is composed of vertical lines of 9- μm -diameter disks with different vertical spacing 0-3-6-10-20 μm repeated periodically every 400 μm along the horizontal axis ; here only one period is shown. The whole pattern has a dimension of 1 cm x 5 cm. **B:** Pattern of stars, with branches at different angles 90, 60, 45, 30 deg. The bars are 30 μm x 3 μm or 38 μm x 3 μm for the 30 deg angle. The pattern shown here is repeated periodically every 250 μm along the horizontal axis

3.1.3 Experimental chambers

Chambers are built on a glass slide with double-sided adhesive tape; stripes of 4-mm width are disposed in parallel with a 4-mm-spacing. The thickness of the double-sided tape is around 100 μm . The functionalized side of the coverslip is then attached on this surface. Typically, 3 channels per slide are made, having each a volume of 15 μL . This allows to test three different conditions with one slide (Fig. 3.5). The chambers are filled by capillarity.

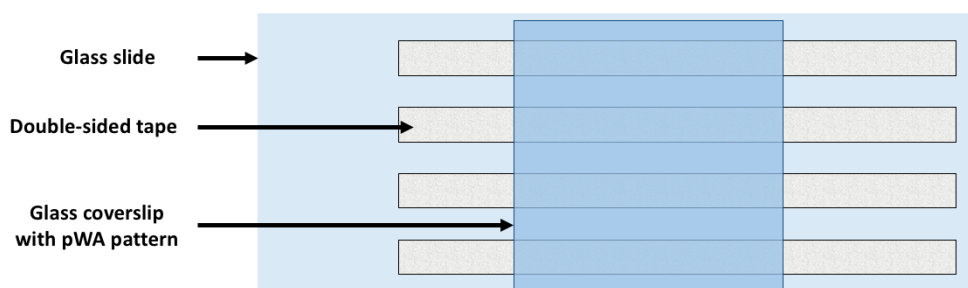


Figure 3.5: Chambers are built on a glass slide using double-sided adhesive tape; 4 mm-wide stripes with a 4-mm gap are disposed in parallel. The functionalized side of the coverslip (with pWA patterns) is then attached on this surface. The 3 channels obtained have each a volume of 15 μL .

3.2 The actomyosin polymerization mix

We prepare a solution containing actin, profilin, the Arp 2/3 complex, myosin, methylcellulose and bovine serum albumin (BSA) (Table 3.1). Profilin is put in large excess compared to monomeric actin to prevent actin nucleation in the bulk and out of the patterns (see Section 2.1.2). When the Arp 2/3 complex reaches the pWA surface, it is activated and then nucleates actin polymerization at the surface and only there (see Section 2.1.2). Methylcellulose is a depleting agent that confines actin filaments near the surface. Myosins are present in solution from the start of the polymerization process and interact with the actin filaments as they emerge from the patterns.

Actin used in my experiments is commercial and was initially purified from rabbit skeletal muscle (see Appendix B). To observe the actin network, we used fluorescently labeled actin with either AlexaFluor™488 or AlexaFluor™568 fluorophores ; fluorescent actin monomers represent 10 % of our G-actin solution. To ensure that we work with G-actin at the beginning of experiments, the actin solution is prepared in a low-salt buffer (G buffer, see Appendix D.1), which favors disassembly of preformed filaments. In the polymerization mix, actin is instead in a high-salt buffer to promote monomers interaction. Ca^{2+} ions that are present in G buffer are sequestered by a chelator and replaced by Mg^{2+} ions to mimic physiological conditions (Blanchoin and Pollard, 2002; Pollard, 1986) (1X KMEI see Appendix D.2). We work at an initial ATP concentration of 4.5 mM. As the result of depleting forces exerted by methylcellulose, the actin network grows close to the coverslip surface; according to Letort *et al* the network forms a sheet with a thickness ≈ 200 nm (Letort et al., 2015). Methylcellulose also increases the macroscopic viscosity of the mix to 800 mPa.s and promotes bundling of actin filaments (Kohler et al., 2008). Finally, we also add reagents to the mix in order to prevent photobleaching of actin (Appendix A.3).

I implemented three types of polymerization mix:

- **actin with no myosins** : this experiment provides the control structure of the actin network in the absence of myosins.
- **actin and myosins**: this is the central experiment of my thesis work. We study how HMM myosin II or myosin V motors reorganize the actin network. We fixed the G-actin concentration, but varied the myosin concentrations.
- **actin, myosins and blebbistatin** : This experiment was implemented to dissociate actin polymerization from myosin reorganization of the actin network. Blebbistatin is a specific inhibitor of myosin II activity. Its effects are reversible as it can

be photo-inactivated with pulses of blue light. (Kovacs et al., 2004; Linsmeier et al., 2016; Sakamoto et al., 2005)

A 15- μ L volume of the actin polymerization mix is injected in the experimental chamber. The chamber is then sealed with polish nail to reduce evaporation before observation under the microscope. Actin polymerization starts as soon as the polymerization mix is injected in the chamber. The observation of the samples can start as soon as 5 minutes after the injection of the polymerization mix and can last up to about one hour.

Table 3.1: Polymerization mix. Myosin concentrations correspond to the number of double-headed myosin molecules per unit volume. For buffer compositions see Appendix D.

Role	Compound	Final Concentration
Ionic strength	KCl	50 mM
Magnesium	Mg^{2+}	10 mM
Energy source	ATP	4.5 mM
Actin Polymerization	Actin Profilin Arp2/3 Complex BSA	2 μ M 8 μ M 80 nM 0.2 w/v %
Anti-photobleaching reagents	Glucose Glucose oxidase Catalase Dithiothreitol	0.6 mM 32 nM 42 nM 56 mM
Depleting agent	Methylcellulose	0.3 w/v %
Molecular motors	HMM myosin II or myosin V	200 - 750 nM 30 - 250 nM

3.3 Image acquisition

We observed the actin networks through fluorescence imaging. Figure 3.6 shows a radial actin network emerging from a micropattern of 9- μm diameter disks with 20- μm spacing.

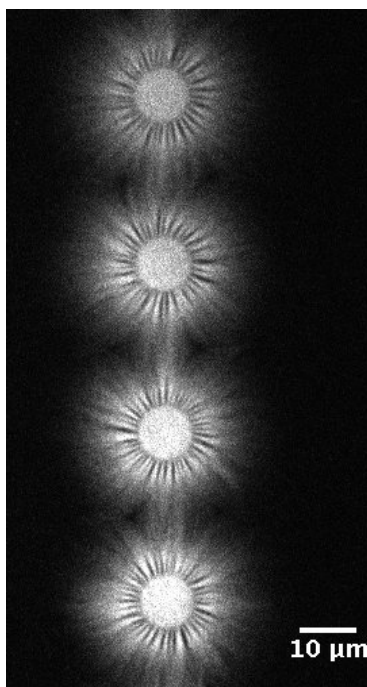


Figure 3.6: Radial actin network obtained with a micropattern of 9- μm diameter disks with 20- μm spacing, 15 minutes after the polymerization mix was injected in the experimental chamber

The fluorophore used to label actin was AlexaFluor™ 488 (Excitation wavelength $\lambda = 499$ nm, Emission wavelength $\lambda = 520$ nm), or AlexaFluor™ 568 (Excitation wavelength $\lambda = 579$ nm, Emission wavelength $\lambda = 603$ nm) and that to label myosin V was GFP (Excitation wavelength $\lambda = 489$ nm, Emission wavelength $\lambda = 510$ nm) (Fig. 3.7). We can notice that there is an overlap between the spectra of GFP Emission and Alexa 568 Excitation. This overlap is relevant for experiments using actin labeled with AlexaFluor™ 568 and myosin V labeled with GFP : The signal observed in the GFP channel is expected to "bleed" in the actin channel. My experiments were performed at the Nikon Imaging Center of the Curie Institute. Samples were imaged at 27 °C in a thermostat-controlled chamber with an Eclipse 80i microscope (Nikon) equipped with a spinning disk confocal head (Perkin) and a Ultra897 iXon camera (EMCCD 512 x 512, pixel size of 16 μm ; Andor), using a x60 oil objective with a numerical aperture of 1.4. The microscope and devices were driven by Metamorph (Molecular Devices, Downington, PA). The observation of actin networks was performed with a 200-ms exposure time and low power of

lasers ($\lambda = 491$ nm for GFP (15 mW) and AlexaFluor™488 (7mW) and $\lambda = 561$ nm for AlexaFluor™ 568 (10 mW)). Images were acquired from every 0.2 s to every 2 s.

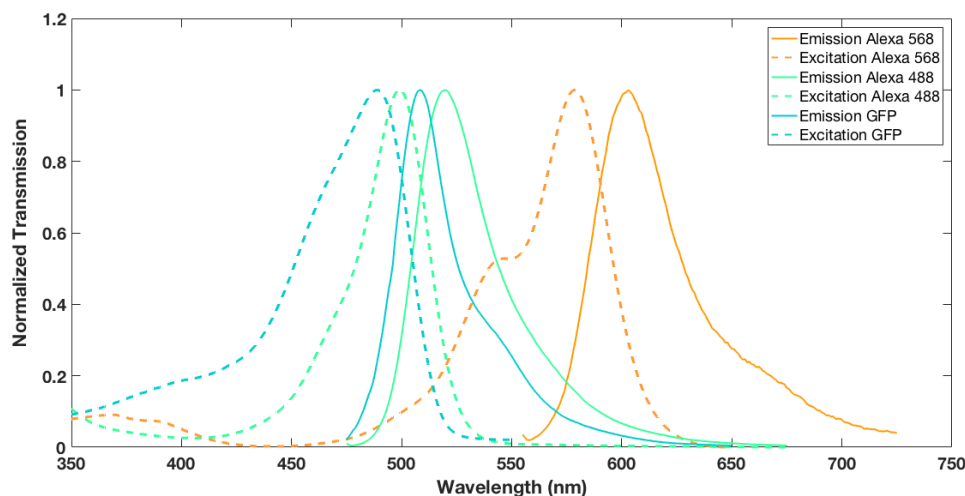


Figure 3.7: Spectra of excitation and emission of fluorophores used in our experiments : AlexaFluor™ 488 (Excitation $\lambda = 499$ nm, Emission $\lambda = 520$ nm), AlexaFluor™ 568 (Excitation $\lambda = 579$ nm, Emission $\lambda = 603$ nm) and GFP for myosin V (Excitation $\lambda = 489$ nm, Emission $\lambda = 510$ nm)

For assays with HMM myosin II in the presence of blebbistatin, the view field was exposed to 405-nm light, after the actomyosin network had been formed, to spatially inactivate blebbistatin thus allowing myosin to exert forces on the actin network (Kovacs et al., 2004; Linsmeier et al., 2016; Sakamoto et al., 2005). We used 100-ms pulses with a repetition rate of 500 ms.

During the duration of an experiment, emitting fluorophores undergo millions of cycles between ground and excited states. After a certain duration, there is the photochemical destruction of the fluorophores, leading to the production of very reactive radicals that can oxidize and destroy surrounding proteins (Song et al., 1995). This photochemical damage, observed through fading of the fluorescence signal, is known as "photobleaching" and can lead to damage or total destruction of the actin network. To improve fluorophore stability, and decrease the effects of photobleaching, our approach consisted in adding to our mix an anti photobleaching buffer (Table 3.1 and Appendix A). We also performed optical sectioning using a spinning disk confocal microscope, which allows to reduce the light intensity for imaging and thus to reduce the photobleaching effect in comparison with epifluorescence microscopy. The anti-photobleaching buffer involves the addition of a reducing agent (Dithiothreitol (DTT)), which removes free radicals. In addition, we implement an enzymatic oxygen scavenging system composed of glucose oxidase, glucose and catalase (Table 3.1). Glucose oxidase catalyzes oxidation of glucose by dioxygen into

gluconic acid. This reaction consumes dioxygen present in the mix, but it also forms hydrogen peroxyde, which can oxydize the neighboring proteins. Catalase eliminates hydrogen peroxyde, by dismutating it. The composition of the anti-photobleaching buffer was derived from protocols of (Ishijima et al., 1996; Plaçais, 2008; Richard, 2016; Veigel et al., 1998).

3.4 Image analysis

3.4.1 Tracking of the actin bundles

For image analysis, we used the freeware ImageJ (NIH, Bethesda). Regions of interest with well-separated actin bundles were selected. If necessary, a rotation was applied on the selected region in order to orient the base of the target bundle vertically (Fig. 3.8.A). In the selected area, neighboring bundles were removed from the grayscale images (*i.e.* the selected parasite pixels were turned to black) to ensure that the tracking freeware did not yield parasite set of coordinates, corresponding to unwanted bundles. This step was illustrated in Figure 3.8.A-B, where the rejected bundles corresponded to areas delimited by yellow contours. Then, the available plugin "Ridge Detection" (http://fiji.sc/Ridge_Detection) was applied to track the shape of the actin bundle on every image of the movie. This plugin is based on the detection algorithm fully described by Steger (Steger, 1998). Basics principles of operation are described in the following paragraph. The algorithm takes into account the surrounding of the line, so it can track a line with a varying width and find the middle. It works on 256-grayscale-levels images. The parameters that we fixed were the line width (between 2-4 pixels), the lowest grayscale values of the line that can be accepted (for us 0) and the highest grayscale values of the line (for us around 100). The output was a stack of images with a black line on a white background fitting the shape of the bundle for each time point (Fig. 3.8.C). This section of analysis was the most time-consuming part of my work: I had to remove almost manually the parasite bundles on each image of my time-lapse acquisition to ensure that the output of ridge detection plugin was a single continuous line corresponding to the bundle I wanted to track.

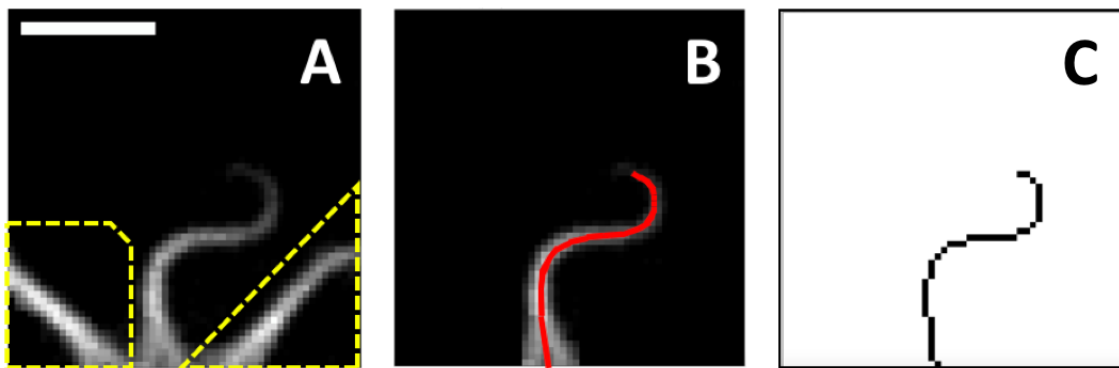


Figure 3.8: The successive steps in ImageJ for image analysis. **A:** Area Selection and orientation of an isolated bundle, such that its base was almost parallel to the vertical axis. The areas with dotted yellow contours turned to black in the next step to eliminate parasite bundles. **B:** Deletion of the parasite bundles around the selected bundle, by putting the pixel value at 0 in the area delimited by dotted yellow contour on the previous step. The Ridge Detection plugin was applied on the image and returns the red line superimposed on the image. **C:** The output of the tracking procedure resulted in a black line (obtained with Ridge Detection) on a white background. Scale bar : 5 μm

How does Ridge Detection plugin work?

Originally, the algorithm for Ridge Detection was developed to extract linear features from aerial or satellite photographs, such as roads or rivers. It is now available in ImageJ as a plugin and is extensively used for image analysis in biology (*e.g.* to detect actin or microtubule filaments (Brangwynne et al., 2007), DNA nanotubes (Glaser et al., 2016)). All along my PhD work, I used this algorithm to extract the curvilinear shape $\psi(s)$ of actin bundles, where ψ represents the angle between the tangent to the bundle and the vertical (y) axis and s is the curvilinear abscissa of the point where ψ is measured. In this section, I will briefly describe the basic principles governing this algorithm without entering into details. In particular, I will not discuss how to convert discrete pixel levels $I(i,j)$ into continuous functions, how to remove contrast differences that might occur between both sides of a line and how to analyze bifurcations in the trajectories (in our case, a mask is applied before image analysis to avoid this problem). The first step consists in smoothing the original image by applying a Gaussian filter with a typical width w , corresponding to 2 - 4 pixels. For our application, this step is not mandatory since fluorescence-intensity profiles along the α axis (normal to the curvilinear axis *i.e.* along vector \mathbf{n}) are already smooth (Fig. 3.9). These intensity profiles $I(\alpha)$ can be fitted by a Gaussian function:

$$I(\alpha) \sim \exp\left[-\frac{(\alpha-\alpha_0)^2}{2\sigma^2}\right]$$
 leading to the mean position of the maximum (respectively minimum) α_0 and the typical width σ of the line along \mathbf{n} . The Cartesian coordinates (X,Y) of this point M yield one value of the position vector $\mathbf{OM}_k(\psi = \widehat{(u_y, \mathbf{t})})$. The operation can be applied to all pixels above a given threshold. To determine the tangent

and normal vectors, respectively \mathbf{t} and \mathbf{n} , the second derivatives of the 2D intensity profiles $I(x,y)$ are computed around this pixel. This is performed by estimating the 2 eigenvalues and the 2 eigenvectors of the Hessian matrix:

$$\begin{bmatrix} \frac{\partial^2 I}{\partial x^2} & \frac{\partial^2 I}{\partial x \partial y} \\ \frac{\partial^2 I}{\partial x \partial y} & \frac{\partial^2 I}{\partial y^2} \end{bmatrix}$$

The eigenvalue of maximum (respectively minimum) absolute value corresponds to the eigenvector giving the direction of \mathbf{n} (respectively \mathbf{t}). If the contrast between the 2 eigenvalues is high enough, the selected pixel belongs to a crest (*i.e.* one large negative eigenvalue) or to a valley (*i.e.* one large positive eigenvalue) on the intensity map $I(x,y)$ (Fig. 3.9). This procedure gives a matrix with white and black pixels, where the ridge of the actin bundle corresponds to the black pixels (Fig. 3.8.C) the detected line corresponding to the shape of actin bundle for each time point :

3.4.2 Beating pattern analysis

The data were analyzed using MATLAB (MathWorks, Massachussets), with a code mostly developed by Mathieu Richard (Richard, 2016), my predecessor on this topic. In this section, we introduce a brief summary of the analysis performed by the program.

Extract and order the (x,y) coordinates of the detected line

First, the code determined the coordinates $(X_j(t), Y_k(t))$ of the black pixels by thresholding the image (with grayscale value inferior to 60) in each image (*i.e.* for a given time t), where (j,k) corresponded to the coordinates of a point in the matrix. For $i = 1$ to $N(t)$, where $N(t)$ corresponded to the number of black pixels in the frame at time t , we thus got a vector of points :

$$[x_i(t), y_i(t)] = [X_j(t), Y_k(t)]$$

In order to calculate in the next step the curvilinear abscissa along the detected line, the coordinates $(x_i(t), y_i(t))$ were then sorted. The origin was set at the base of the actin bundle such as $(x_1, y_1) = (0,0)$. Then the second point (x_2, y_2) was found by searching the point located at the minimal distance from the origin. Next, the first point was excluded and the point with a minimal distance to the second point gave the third point. This process was iterated all along the detected line, excluding the points already sorted and sorting the remaining points by finding the minimal distance between successive points of the detected line. Finally, all the successive points sorted of the detected line were placed into a vector. Once the vector was well-ordered, a smoothing procedure was applied on the

$(x_i(t), y_i(t))$ by performing a moving average over a 5-point window, in order to decrease noise in the shape of the resulting curve.

Curvilinear abscissa and tangent angle

For the following steps, we interpolated the set of coordinates $(x_i(t), y_i(t))$ obtained, by adding 10 points in between successive points, using a cubic interpolation. This interpolation was an artifice for calculations of first and second spatial derivatives to reduce noise. We then computed the curvilinear abscissa s and the tangent angle ψ relative to the y axis at all points (Fig. 3.9).

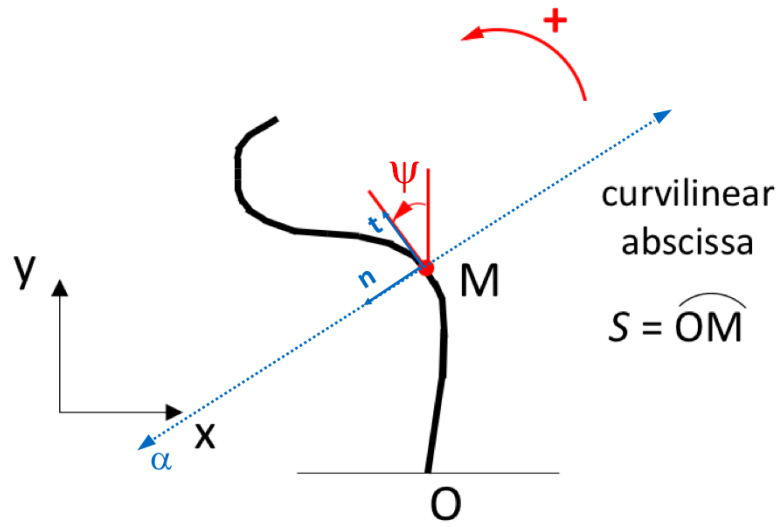


Figure 3.9: Parametrization of the detected line with the curvilinear abscissa s and tangent angle ψ . Also shown the tangent and normal vectors at this point, respectively \mathbf{t} and \mathbf{n} .

First, we evaluate the distance $ds_i(t)$, for $i = 1 \dots N(t)-1$, between the consecutive points $(x_i(t), y_i(t))$, for $i = 1 \dots N(t)$ and $(x_{i+1}(t), y_{i+1}(t))$, for $i = 1 \dots N(t)-1$:

$$ds_i(t) = \sqrt{dx_i(t)^2 + dy_i(t)^2}, \quad (3.1)$$

with $dx_i(t) = x_{i+1}(t) - x_i(t)$ and $dy_i(t) = y_{i+1}(t) - y_i(t)$.

At each point M ($i = m$) of the detected line at a given time t , we calculate the curvilinear abscissa $s(t)$:

$$s(t) = \widehat{OM}(t) = \sum_{i=1}^m ds_i(t) \quad (3.2)$$

The length $L(t)$ of the actin bundle is estimated as the curvilinear abscissa of the last point $N(t)$ at each time t :

$$L(t) = \max(s(t)) = \sum_{i=1}^{N(t)} ds_i(t) \quad (3.3)$$

The tangent angle $\psi(t,s)$ along the detected line, which contains the largest part of the information about the beating obeys :

$$dx(t) = -ds \sin(\psi(t, s)) \quad (3.4)$$

$$dy(t) = ds \cos(\psi(t, s)) \quad (3.5)$$

$$\tan(\psi(t, s)) = -\frac{dx}{dy} \quad (3.6)$$

Once, s and ψ are defined for all points along the detected line, the curvature $C(t)$ can be computed :

$$C = \frac{d\psi}{ds} \quad (3.7)$$

Fourier analysis

Visual observation of actin bundles as a function of time reveals oscillations of the tangent angle $\psi(t, s)$. To analyze the spectral context of these movements, we used Fourier analysis.

$$\psi(t, s) \xrightarrow{\mathcal{F}} \tilde{\psi}(\omega, s)$$

with $\tilde{\psi}(\omega, s) = \int_{-\infty}^{+\infty} \psi(t, s).e^{-i\omega.t} dt$, we can write :

$$\tilde{\psi}(\omega, s) = A(\omega, s).e^{-i\phi(\omega, s)} \quad (3.8)$$

where $A(\omega, s)$ and $\phi(\omega, s)$ represent the amplitude and the phase of the Fourier component at ω .

Chapter 4

Self-organized wave-like beating of actin bundles

In this chapter, I will describe how myosins reorganize parallel actin networks by assembling filaments into bundles and drive spontaneous oscillations that resemble wave-like beating of eukaryotic flagella. I will discuss how the beating properties change depending on the type of myosin involved (either HMM myosin II, which will be abbreviated as myosin II in the following and myosin V) and on the actin bundle length. Finally, I will describe the dynamic localization of the myosins within the actin bundles during beating movements demonstrating a novel feedback mechanism between myosin activity and bundle shape. I restricted the scope of my work to the study of single actin bundles, setting collective effects aside, *i.e.* how the actin bundles interact with their neighbors.

In the following, for all the measured properties I will present their values as their means with an uncertainty corresponding to their standard deviation (mean \pm SD).

4.1 Architecture of the actin network with or without myosins

4.1.1 In the absence of myosins

The polymerization of actin networks was implemented using surface micropatterns of a nucleation promoting factor, as described in Chapter 3. The filaments emerge perpendicularly to the nucleation zone regardless of the geometry. We used 3 geometries : disks (9- μ m, 40- μ m and 60- μ m-diameter), star branches and parallel lines. For both disks and rings we obtain a radial organization of actin filaments growing from the patterns . In the case of star branches and parallel lines, we obtained parallel actin filaments out of

the patterns. In all cases, the elongation speed at the time of our recordings was typically 0.1 - 0.5 $\mu\text{m}/\text{min}$.

Architecture of the actin network

Results from Mathieu Richard's PhD thesis

The architecture of actin networks emerging from surface micropatterns was analyzed extensively by my predecessor Mathieu Richard during his PhD (Richard, 2016). Mathieu worked with actin networks emerging from 3 μm -wide nucleation lines that were spaced by 40 or 80 μm (Fig. 4.1.A,B).

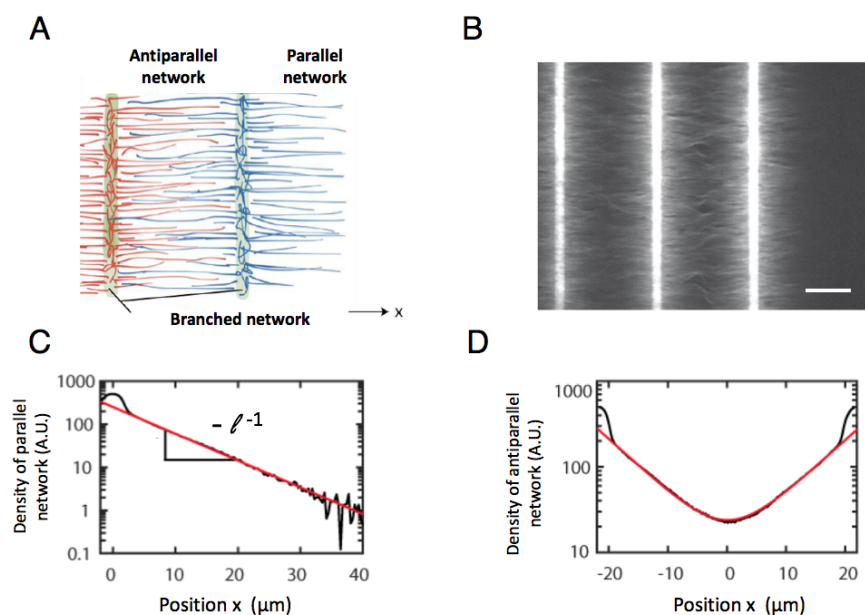


Figure 4.1: From parallel nucleation lines to parallel and antiparallel actin networks.

A: Schematic description of the experiment: actin filaments (red and blue) emerge from two parallel nucleation lines (in green). On a nucleation line, the actin network is branched. The actin network emerging from an isolated line is parallel, as all filaments have the same polarity. When two nucleation lines are facing each other, an antiparallel actin network results from the overlap of two parallel networks of opposite polarities. **B:** Fluorescence image of an actin network that has grown from three nucleation lines with a 40- μm -spacing after 30 min of polymerization. Scale bar: 20 μm . **C:** Fluorescence intensity profile as a function of the distance x along an axis perpendicular to a nucleation line of a parallel actin network after 30 min polymerization (black line) and an exponential fit ($\rho_{\parallel} = \rho_0 \exp(-x/\ell)$, with $\rho_0 = 200$ A.U. and $\ell = 7$ μm) (red line). The nucleation line was 3 μm -wide and $x = 0$ corresponds to its center. **D:** Fluorescence intensity profile of an antiparallel network after 30 min of polymerization (black line) and a fit (red line), corresponding to the superposition of two mirror-symmetric exponentials (with respect to $x = 0$) that have the same characteristic length $\ell = 7$ μm . The two nucleation lines were 3 μm -wide with a 40 μm -spacing ; $x = 0$ corresponds to the middle between the two lines. Figures adapted from (Richard, 2016)

Analyzing the fluorescence intensity profiles of actin (labeled with fluorophore AlexaFluor™ 568), along an axis perpendicular to a single nucleation line, revealed exponential intensity profiles $\rho_{\parallel} = \rho_0 \exp(-x/\ell)$. In other words, surface patterning of a nucleation promoting factor generates networks of parallel actin filaments that do not all have the same length ; the actin-length distribution is exponential. Correspondingly, the antiparallel actin network produced in between two parallel nucleation lines gave a superposition of two mirror-symmetric exponential intensity profiles (Fig. 4.1.C,D). The exponential profiles provide a characteristic length $\ell = 8.2 \pm 1.1 \mu\text{m}$ ($n = 29$), corresponding to the mean length of the actin filaments. By imaging the growing actin network every 5 minutes from $t = 10 \text{ min}$ to $t = 30 \text{ min}$ after injection of the polymerization mix, it was shown that the characteristic length remained constant during the observation time window (Fig. 4.2.A,B), while the actin density doubled (Fig. 4.2.C).

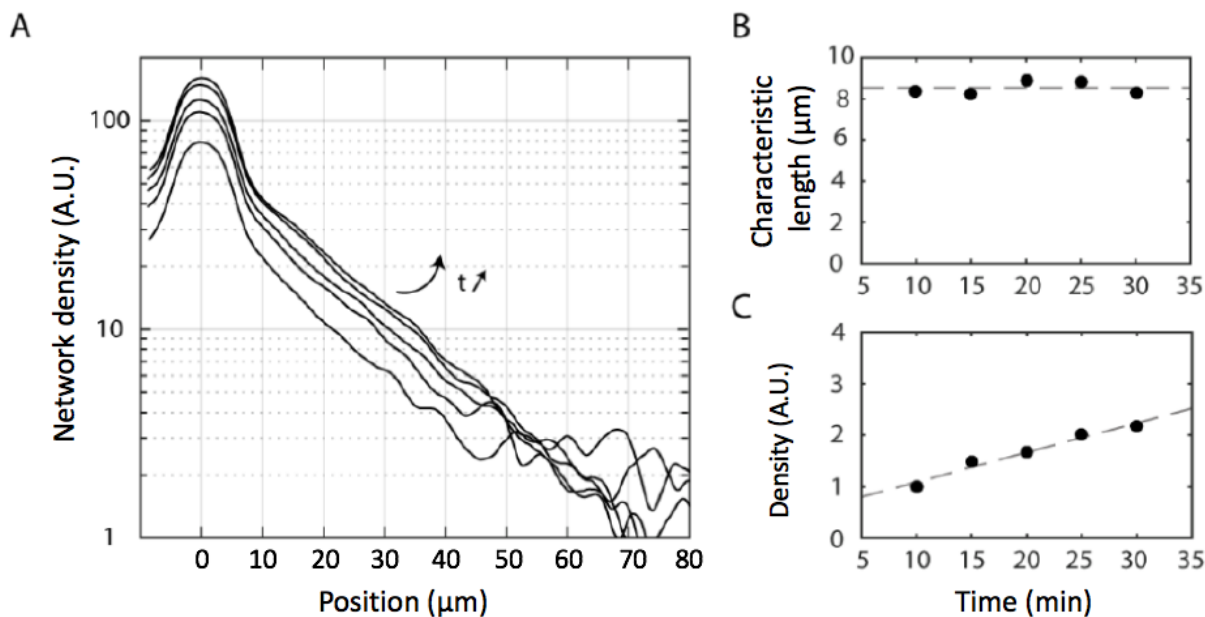


Figure 4.2: Polymerization dynamics of a parallel network. Parallel actin network emerging from a 3 μm -wide nucleation line. A: Fluorescence intensity profile measured every 5 min. **B:** Characteristic length as a function of time (black dots); its mean is shown as a grey dashed line. **C:** Network density (black dots) measured at the position $x = 10 \mu\text{m}$ as a function of time. The dashed line represents a linear fit. Figure from (Richard, 2016)

Moreover, Mathieu showed that the mean actin length ℓ does not depend on the initial concentration of G-actin in the polymerization mix (Fig. 4.3.A), nor on the width of nucleation lines (Fig. 4.3.B), nor on the spacing between nucleation lines (Fig. 4.3.C), nor, or only weakly on the concentration of the Arp2/3 complex (Fig. 4.3.D) (Richard, 2016).

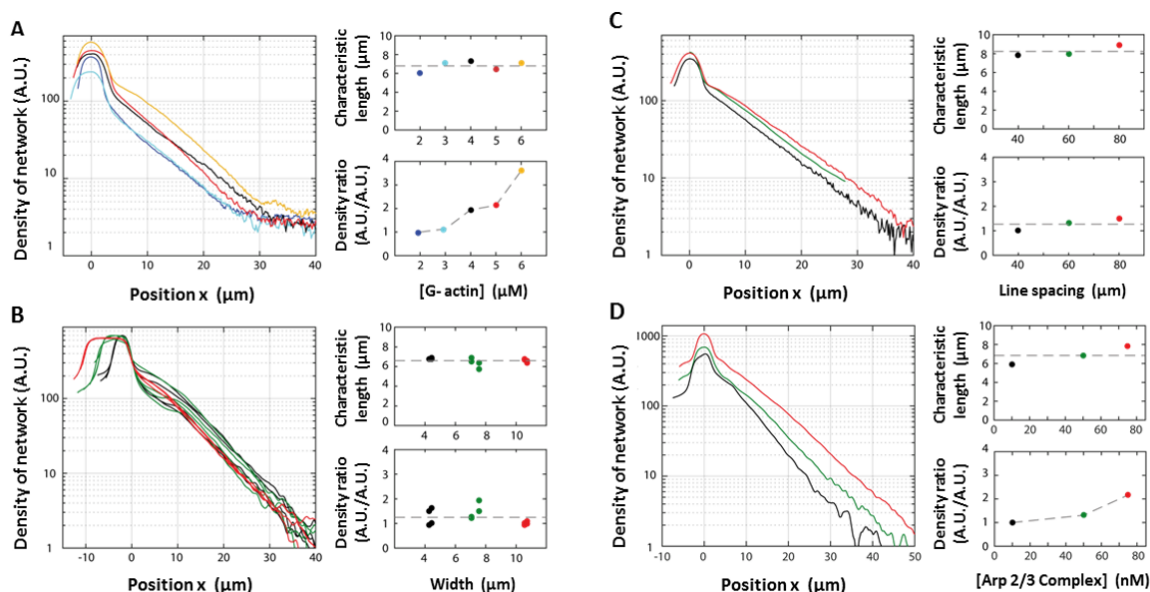


Figure 4.3: Fluorescence intensity profile of parallel actin networks as a function of the initial concentration of G-actin (**A**), the width of nucleation lines (**B**), the spacing between nucleation lines (**C**), and the concentration of the Arp 2/3 complex (**D**). Except when mentioned, the experiments were performed at 4 μM of G-actin, 10 nM of the Arp 2/3 complex and the nucleation pattern was composed of 3- μm -wide lines with a 40- μm -spacing. For all conditions, the actin density was measured at position $x = 10 \mu\text{m}$ and normalized by the intensity measured for the first value of the varying parameters. Figure from (Richard, 2016)

- Fluorescence intensity profiles of actin networks are exponential.
- The mean-actin length ℓ remains constant as the actin network grows, only the actin density increases.
- The mean-actin length ℓ does not depend on the initial concentration of G-actin [range : 2 - 6 μM] in the polymerization mix, or the width [range : 4 - 10 μm] or the spacing [range : 40 - 80 μm] of the nucleation lines, and on the concentration of the Arp2/3 complex [range : 10 - 70nM].

4.1.2 In the presence of active myosins : assembly of tight actin bundles

We observed that the addition of myosin II or myosin V in the polymerization mix results in the self-organization of the actin network into well-separated and dense bundles of filaments of the same polarity (Fig. 4.4). These bundles are curved, showing that myosins apply forces on them.

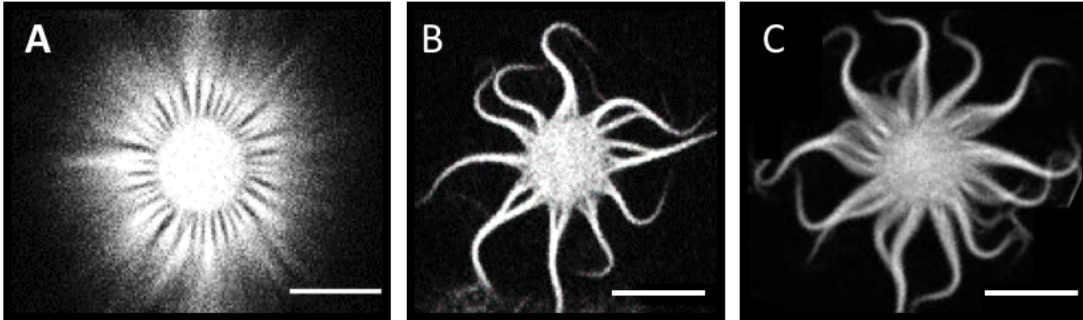


Figure 4.4: Myosin-driven bundling of actin filaments. Actin was labeled with AlexaFluor™ 488 (10 % labelling, see Chapter 3). In the absence of myosin (**A**), a radial actin network emerges from a 9- μm -diameter disk. The radial network is relatively homogeneous, although diffuse bundling can be observed. In the presence of myosin II (**B**), or myosin V (**C**) the actin network self-organizes into dense and well-separated actin bundles. These bundles are curved, showing that myosins apply forces on them. Here, the concentration of myosin II was 500 nM, the concentration of myosin V was 50 nM. Scale bar 10 μm .

Length distribution of the actin bundles

In our experiments, actin is continuously polymerizing and the bundle's length is increasing over time at a speed of $\sim 0.1 - 0.5 \mu\text{m}/\text{min}$. I recorded beating properties of ~ 60 actin bundles in the presence of myosin II and of ~ 80 actin bundles in the presence of myosin V, respectively at time $t = 24 \pm 8 \text{ min}$ and $t = 27 \pm 14 \text{ min}$, after injection of the polymerization mix in the experimental chamber. The bundle length was measured at the position where the actin fluorescence intensity vanished in the background. The histograms of actin bundle length show that myosin V actin bundles have a distribution shifted to the right compared to myosin II actin bundles (Fig. 4.5). In both cases, the length distribution can be fitted by a Gaussian distribution, which yields a mean value and a standard deviation. With myosin II bundles, the bundle length was $L^{MII} = 16 \pm 6 \mu\text{m}$ ($n = 59$). With myosin V, the bundle length was $L^{MV} = 19 \pm 5 \mu\text{m}$ ($n = 79$). The standard deviations of the two distributions are similar (variance test p-value : 0.22), the mean values are statistically different (t-test, p-value = 0.0021). However, we do not think that the actin bundles are longer with myosin V than with myosin II because actin polymerization was faster with myosin V.

At least two potential causes can be invoked to explain the difference in bundle length. First, the shift could be due to the fact that the actin bundles observed with myosin II showed higher fluorescence intensity compared to the bundles with myosin V (compare in Fig. 4.4.B,C) : the bundle extremity was harder to detect with myosin II than with myosin V, because the gain of the camera was lower to ensure that the bright base of myosin II- bundles did not saturate, obscuring their extremity. Second, the experiments with myosin V were launched on average 3 minutes later than with myosin II after injection of the polymerization mix. It was indeed harder to find a good region with myosin II, *i.e.* containing several oscillating actin bundles, than with myosin V. As a result, I began earlier after injection of the polymerization mix to look for oscillating bundles and select the acquisition area than with myosin V, resulting in longer filaments at the time of acquisition in the experiments with myosin V.

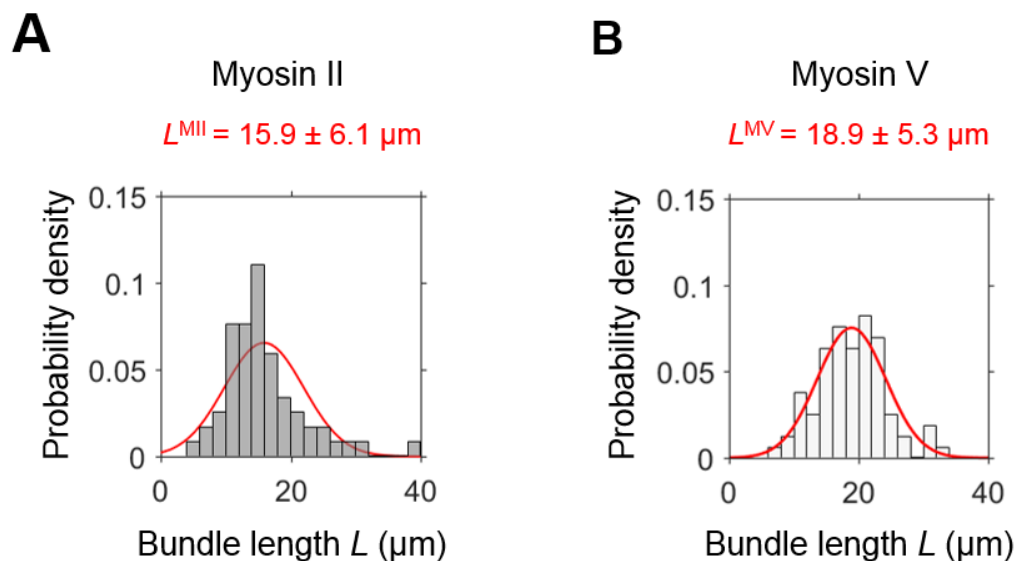


Figure 4.5: Distribution of actin-bundle length in the presence of myosin II (A) or myosin V (B) in the polymerization mix. The bundle length was measured at the position where the actin fluorescence intensity vanished in the background. Distributions can be fitted by a Gaussian curve (in red) : the length of the active bundles is $L^{MII} = 15.9 \pm 6.1 \mu\text{m}$ ($n = 59$). In case of myosin V, the length is $L^{MV} = 18.9 \pm 5.3 \mu\text{m}$ ($n = 79$). The standard deviations of the two distributions are similar (Variance Test p-value : 0.22), the mean values are statistically different (t-test, p-value = 0.0021)

Choice of a pattern geometry to better isolate an single actin bundle from its neighbors

When an actin bundle oscillates (see Section 4.2 below), it can overlap with neighbors and even merge with them, which complicates the study of single bundles. We thus tested

patterns of different geometry: lines and disks of diameters 60, 40 and 9 μm , to select which geometry sets the larger distance between neighboring bundles.

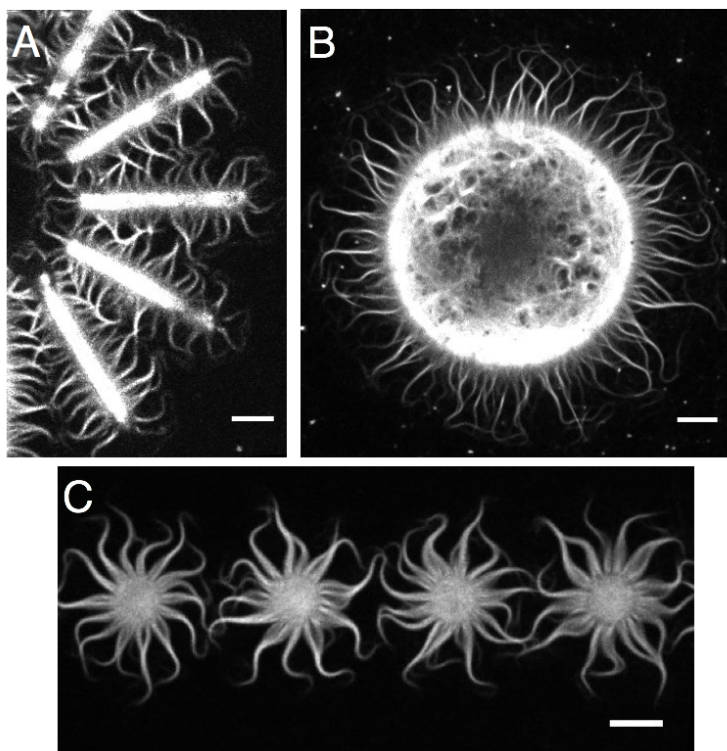


Figure 4.6: Varying the geometry of the patterns. **A:** Actin bundles obtained with nucleation bars of 38 μm x 3 μm . **B:** Actin bundles obtained with a 60- μm -diameter nucleation disk. **C:** Actin bundles obtained with 9- μm -diameter nucleation disks. Scale bars: 10 μm

Nucleation bars in star branches, provide around 10 actin bundles over 38 μm -long bar for different experiments. This configuration corresponds to a spacing of 3.4 ± 0.4 μm between two neighboring actin bundles ($n = 13$, Fig. 4.6.A). With a 60- μm -diameter disk, we obtained 59 ± 7 actin bundles ($n = 3$, Fig. 4.6.B) per disk, resulting in a spacing of 3.2 ± 0.2 μm between two neighboring actin bundles. This spacing is similar to that obtained with nucleation bars, but the radial geometry adds an angle that results in a better separation of the bundles : because the bundles grow perpendicular to the circular edge of the nucleation zone, the farther from the nucleation zone, the larger the distance between the bundles. Increasing the curvature of the nucleation zones must result in larger angular section per actin bundle, as confirmed by our experiments. A 60- μm -diameter disk confers an angular section per actin bundle of 6 ± 1 deg. In one experiment with 40- μm -diameter disk, we observed a spacing of 2.9 μm between two neighboring actin bundles and an angular section per actin bundle of 9 deg. In addition, a 9- μm -diameter disk yields 17 ± 2 actin bundles per disk ($n = 35$, Fig. 4.6.C), a spacing of 1.7 ± 0.2 μm between two neighboring actin bundles and an angular section per actin bundle of 21 ± 3 deg. These results highlight the two effects of the curvature of the nucleation pattern

on actin bundle separation : as the diameter decreases, the spacing of two neighboring actin bundles decreases (here by 53 % between 60 and 9- μm -diameter disks), whereas the angular section available per actin bundle on the pattern increases more (here by 350 % between 60 and 9- μm -diameter disks). Thus, an actin bundle is more likely to be isolated on a 9- μm than on a 60- μm -diameter disk as the tips of its neighboring actin bundles are more distant. We thus selected the 9 μm diameter disks for most of our experiments.

4.2 Dynamic analysis: Spontaneous oscillations

The striking phenomenon that motivated my PhD is that in the presence of myosin motors in the bulk, actin bundles display spontaneous wave-like beating. Oscillations are observed both with myosin II (Fig. 4.7) or myosin V, and could last up to 1 hour (longest duration: 2 hours). In practice, to characterize the bundle movements, we recorded sequences of 5 to 20 periods. The bundle elongation speed can be low enough (0.1 to 0.5 $\mu\text{m}/\text{min}$), that the bundle length is often quasi-static over the time course of our recordings. We also used longer recordings (up to 30 min) to study the effects of bundle elongation on the beating properties, while keeping other parameters constant.

4.2.1 General description of beating properties in the case of myosin II

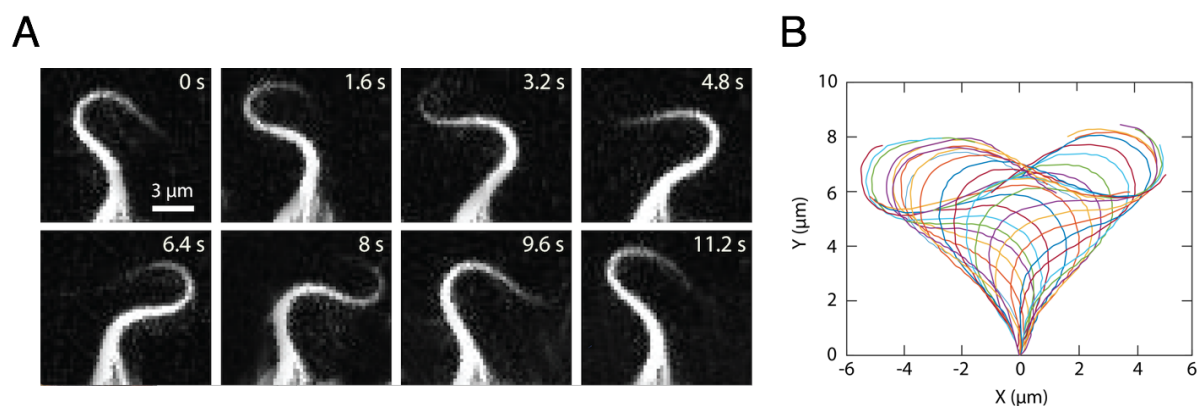


Figure 4.7: Fluorescence image and typical beating pattern of an oscillating actin bundle. **A:** Fluorescence image of a beating actin bundle as a function of time. Actin was labeled with AlexaFluor™ 488 (10 % labelling, see Chapter 3). The actin bundle exhibits here an oscillatory movement with a period of 11 s. The motion is driven by HMM myosin II, which was in the polymerization mix at a concentration of 500 nM. **B:** Superimposition of the detected lines obtained every 0.5 s during one period of oscillation. The beating pattern is nearly symmetric with respect to the vertical line $X = 0$.

We performed tracking of the actin bundle's shape (Chapter 3, Fig. 3.8). From the extracted line, we compute the tangent angle $\psi(s, t)$, at each position of curvilinear abscissa s and as a function of time t . In the example shown in Figure 4.7.A, the superimposition of the detected lines (ridge) over one cycle of beating shows a nearly symmetric pattern with respect to the vertical axis $X = 0$ (Fig. 4.7.B). At a given curvilinear abscissa s , the time series of the tangent angle $\psi(s, t)$ exhibits periodic oscillations, shown at two positions $s = 5 \mu\text{m}$ and $s = 10 \mu\text{m}$ (Fig. 4.8.A (left)). The oscillations look quasi sinusoidal. By performing a temporal Fourier transform on tangent angle data $\psi(s, t)$, we compute a power spectrum (Fig. 4.8.A (right)). The spectrum contains only one peak (Fourier mode) and thus one characteristic frequency $f_0 = 0.09 \text{ Hz}$. This frequency corresponds to a 11 s-period ($T = 1/f_0$), independent on position along the actin bundle, confirming that the oscillations are nearly sinusoidal. Thus, the function $\psi(s, t)$ can be approximated by :

$$\psi(s, t) \approx \psi_0(s) + \psi_1(s)e^{i\omega_0 t} + \psi_1^*(s)e^{-i\omega_0 t} \quad (4.1)$$

The amplitude of the noisy sinusoid was defined as $A = \sqrt{2 \langle (\psi - \langle \psi \rangle)^2 \rangle}$, where $\langle \rangle$ represents a temporal average. The amplitude increases as the position gets closer to the tip: the mean amplitude is here of 81 degrees at $s = 5 \mu\text{m}$ and 134 degrees at $s = 10 \mu\text{m}$. By plotting the amplitude of the noisy sinusoid as a function of the curvilinear abscissa (Fig. 4.8.B), we extract the angular envelope of the beating pattern. The amplitude is linearly growing from base to tip until saturation, here at 134 degrees, close to the tip. The shape of that curve can be characterized by three parameters : ψ_{max} , which corresponds to the maximal bending angle reached along the actin bundle and marks the saturation (here $\psi_{max} = 134 \text{ deg}$), ψ'_1 , which represents the slope in the linear regime (here $\psi'_1 = 16.2 \text{ deg}/\mu\text{m}$) and $s^* = \psi_{max}/\psi'_1$, which delimits the transition between the linear regime and saturation (here $s^* = 8.2 \mu\text{m}$). In addition, the oscillation at $s = 10 \mu\text{m}$ lags the oscillation at $s = 5 \mu\text{m}$ by 3.3 s, which is the signature of a beating wave traveling from the base ($s = 0$) to the tip of the actin bundle (Fig. 4.8.A). To characterize wave propagation, we plot the phase ϕ of the Fourier mode $\psi_1(s)$ as a function of the curvilinear abscissa s (Fig. 4.8.C). We observe a phase delay that linearly accumulates from base to tip. This linear relation between phase and curvilinear abscissa corresponds to a uniform wave-vector $k = -\partial\phi/\partial s$. Because the period and the wave vector are uniform, the wave speed of deformation v is also uniform along the actin bundle ($v = \omega_0/k$, here $v = 1.6 \mu\text{m/s}$). This property is surprising: the speed of propagation is uniform although the architecture of the actin bundle is not uniform, since the bundle gets thinner towards the tip (Fig. 4.7).

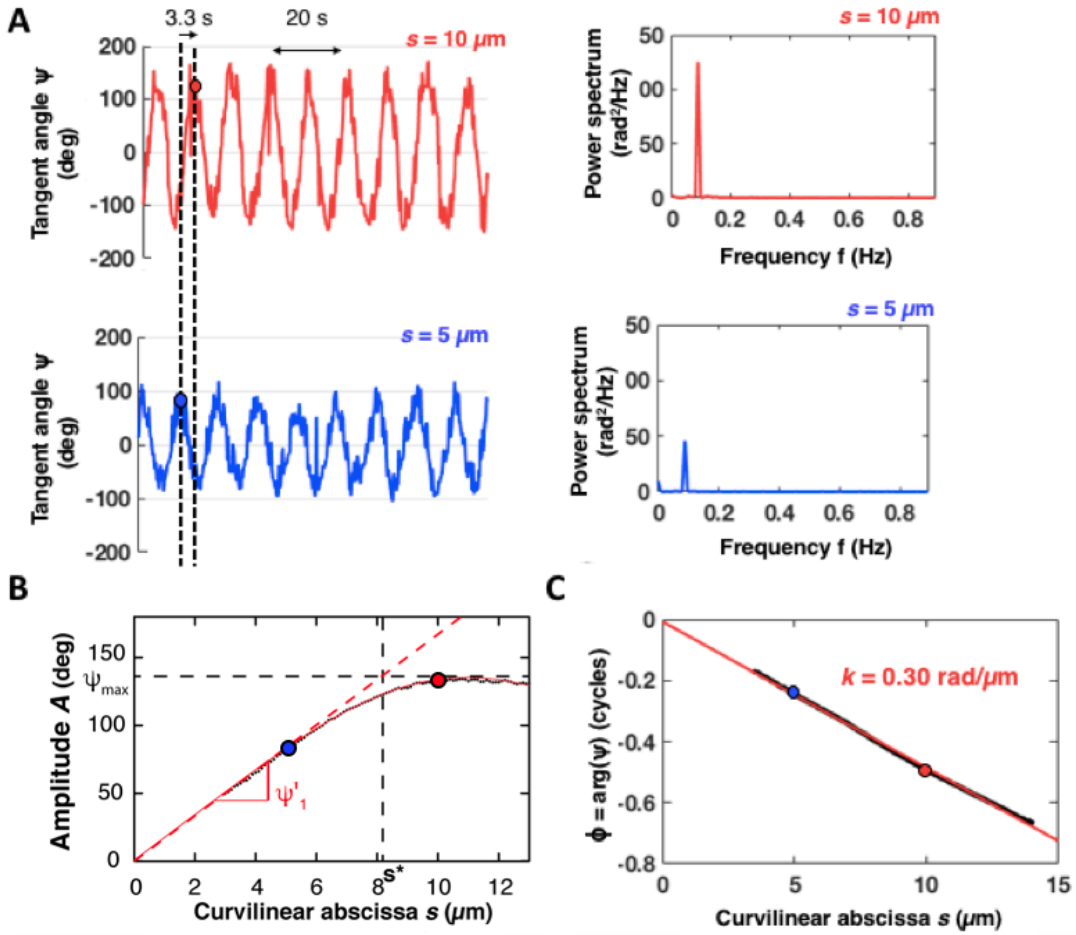


Figure 4.8: Tangent-angle oscillations as a function of position along the actin bundle. **A:** Time series of the tangent angle $\psi(s, t)$ for $s = 5 \mu\text{m}$ (blue) and $s = 10 \mu\text{m}$ (red). The tangent angle exhibits periodic oscillations as a function of time. The oscillations have the same period $T = 11 \text{ s}$ at the two positions. The amplitude increases as the position gets closer to the tip: the amplitude is 81 deg for $s = 5 \mu\text{m}$ and 133 deg for $s = 10 \mu\text{m}$. The power spectra of the tangent angle $\psi(s, t)$ at the two given position are shown on the right of the time series. In both cases, the spectrum shows only one mode at the frequency $f_0 = 0.09 \text{ Hz}$. Black dashed lines indicate the time at which the angle reaches a maximum over the same period for $s = 5 \mu\text{m}$ (blue dot) and $s = 10 \mu\text{m}$ (red dot); there is a 3.3 s delay for the oscillation at $s = 10 \mu\text{m}$ with respect to that at $s = 5 \mu\text{m}$ (vertical dashed lines). **B:** Amplitude A of the noisy angular oscillation. The amplitude is linearly growing from base to tip until saturation, at 135 deg . The shape of that curve can be characterized by three parameters: $\psi_{\max} = 134 \text{ deg}$, which corresponds to the maximal angle reached along the actin bundle (horizontal dashed line) at saturation, $\psi'_1 = 16.2 \text{ deg}/\mu\text{m}$, which represents the slope in the linear regime (red dashed line) and $s^* = \psi_{\max} / \psi'_1 = 8.3 \mu\text{m}$, which delimits the transition between the linear regime and saturation (vertical dashed line). The blue disk indicates the amplitude at the position $s = 5 \mu\text{m}$ ($A = 80 \text{ deg}$) and the red disk indicates the amplitude at the position $s = 10 \mu\text{m}$ ($A = 135 \text{ deg}$). The red line represents a phenomenological fit of form $A = as / (1 + (s/b)^c)$, with $a = 16 \text{ deg}/\mu\text{m} = \psi'_1$; $b = 14 \mu\text{m}$; $c = 4$. **C:** Phase of the Fourier mode shown in (A) as a function of the curvilinear abscissa s . A phase delay accumulates along the actin bundle. The blue disk indicates the phase delay at the position $s = 5 \mu\text{m}$ ($\phi = -0.25 \text{ cycle}$) and the red disk indicates the phase delay at the position $s = 10 \mu\text{m}$ ($\phi = -0.5 \text{ cycle}$). The delay accumulates linearly along the actin bundle, a linear fit is shown in red. The absolute slope provides the wave vector $k = 0.3 \text{ rad}/\mu\text{m}$.

The bending waves can be visualized by plotting snapshots of the tangent angle ψ as a function of the curvilinear abscissa s of the actin bundle (Fig. 4.9).

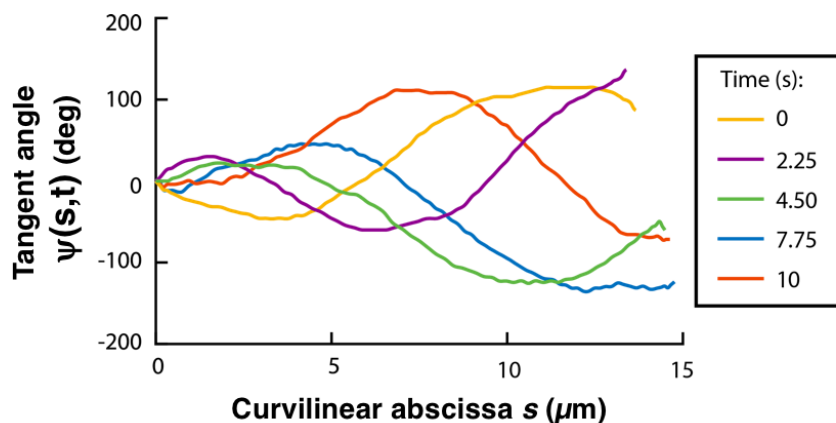


Figure 4.9: Snapshots of the relation between the tangent angle ψ and the curvilinear abscissa s along the bundle. They show wave propagation with growing magnitude from base to tip of the bundle. In this case the bundle length is $L = 15 \mu\text{m}$.

A color plot of the tangent angle $\psi(s, t)$ as a function of space (s) and time (t) sums up all the beating properties described above (Fig. 4.10).

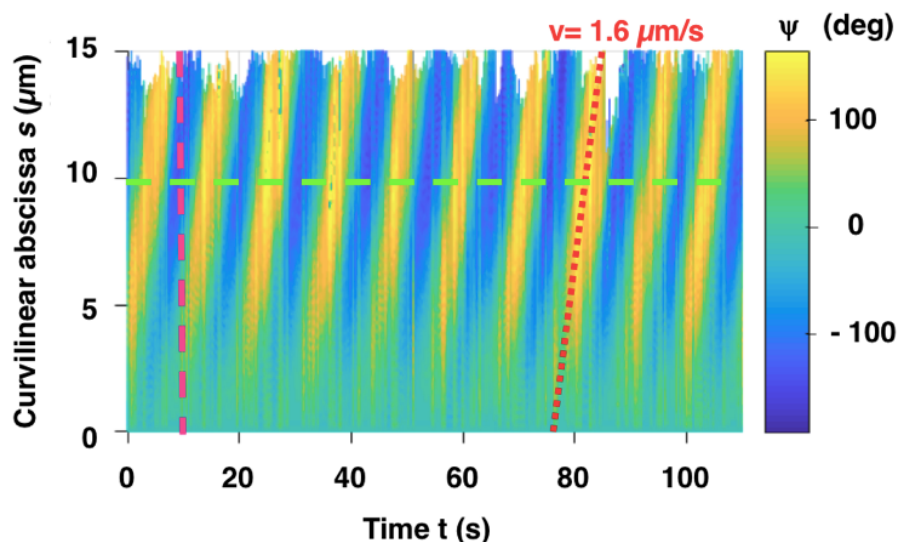


Figure 4.10: Color plot of the tangent angle $\psi(s, t)$ as a function of the curvilinear abscissa s and time t . This color plot summarizes all the informations described above on the beating properties. The tangent angles are color coded as shown on the right. An horizontal cross-section shows the oscillation of the tangent angle as a function of time at a fixed curvilinear abscissa $s = 10 \mu\text{m}$ (Fig 4.8.A). Varying the curvilinear abscissa s , the increase of oscillation amplitude is described by the increased contrast in color oscillations. Vertical readings of the plot (at different given time) show the wave propagation of the tangent angle (Fig. 4.9). By following a given color of the tangent angle, the uniform wave speed of deformation can be extracted, from the slope of the color graph (here $v = 1.6 \mu\text{m/s}$).

By reading the plot horizontally, we collect the oscillation of the tangent angle as a function of time at a fixed curvilinear abscissa (Fig. 4.8A) for $s = 5 \mu\text{m}$ and $s = 10 \mu\text{m}$). Along the curvilinear abscissa, the increase of oscillation amplitude is described by the color code. A vertical reading of the plot (at a given time t) shows the spatial variation of the tangent angle ψ as a function of s (Fig. 4.9). By following a given color of the tangent angle, the uniform wave speed of the deformation can be extracted, from the slope of the color graph (here $v = 1.6 \mu\text{m/s}$).

- Actin bundles exhibit sinusoidal oscillations of their tangent angles.
- A bending wave propagates from base to tip of the actin bundle with a growing amplitude and at a uniform speed.

4.2.2 Comparing beating properties with myosin II to those with myosin V

Myosin V reorganizes radial actin networks into active actin bundles strikingly resembling those obtained with myosin II. In particular, the beating pattern of a single bundle can be described by a 'heart shape' in both cases, with periodic and sinusoidal oscillations of the tangent angle at every position and with a bending-wave propagating at uniform speed from base to tip (Fig. 4.11). Interestingly, despite these qualitative similarities, we found that the kinetics of the beating is much faster with myosin II than with myosin V. In the examples shown in the Figure 4.11, the period is $T = 11 \text{ s}$ for myosin II and $T = 70 \text{ s}$ for myosin V ; the wave speed is $1.6 \mu\text{m/s}$ for myosin II and $0.3 \mu\text{m/s}$ for myosin V.

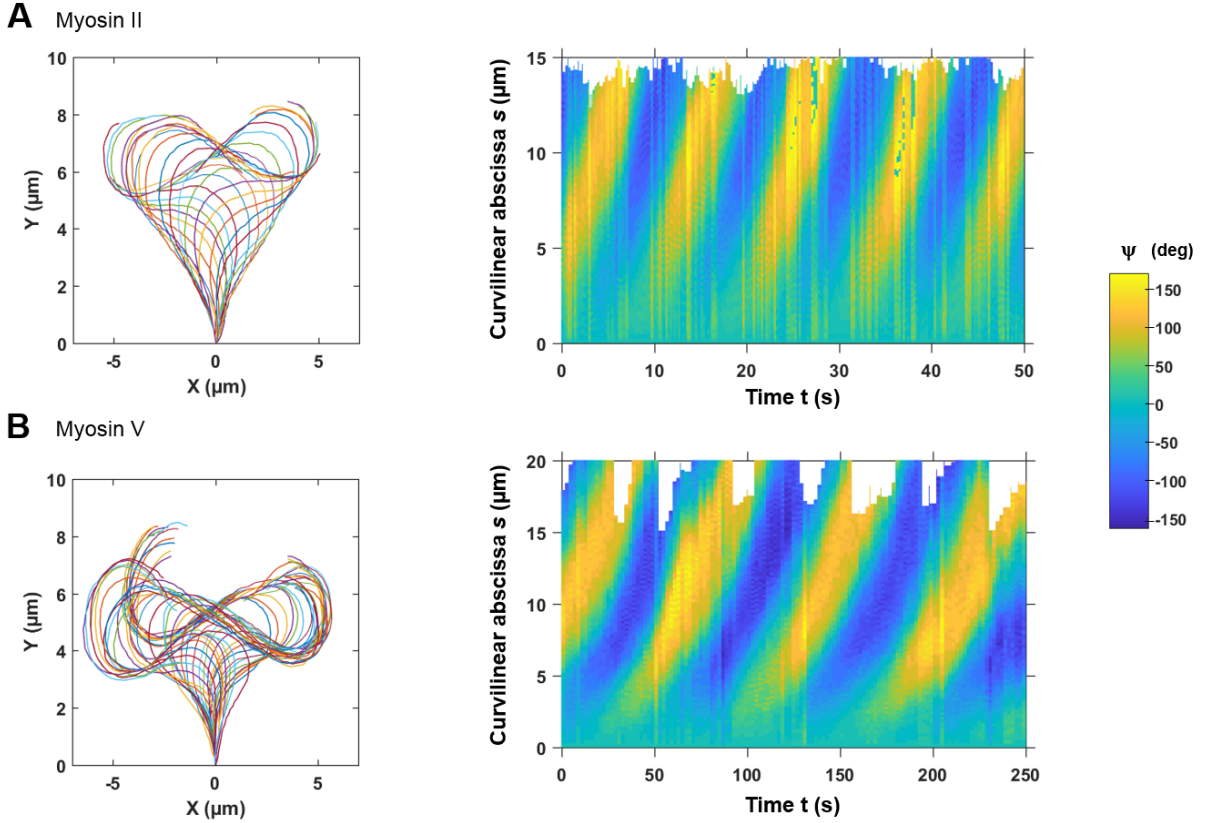


Figure 4.11: Comparing beating properties driven by myosin II with respect to those driven by myosin V. **A:** Beating pattern of an actin bundle ($L = 14 \mu\text{m}$) driven by myosin II (*left*) and associated color plot of tangent angle $\psi(s, t)$ (*right*). The detected lines obtained every 0.5 s during one period of oscillation are superimposed. The shape parameters are here : $\psi_{max} = 135$ degrees, $\psi'_1 = 16 \text{ deg}/\mu\text{m}$ and $s^* = 8.3 \mu\text{m}$. The oscillations exhibit a period of 11 s and a wave speed of $1.6 \mu\text{m}/\text{s}$. Same data as in section 1.2.1. **B:** Beating pattern of an actin bundle ($L = 18 \mu\text{m}$) driven by myosin V (*left*) and associated color plot of tangent angle $\psi(s, t)$ (*right*). The shape parameters are here : $\psi_{max} = 136$ degrees, $\psi'_1 = 18 \text{ deg}/\mu\text{m}$ and $s^* = 7.6 \mu\text{m}$. The detected lines obtained every 2 s during one period of oscillation are superimposed. We can note the difference of time scale compared to myosin II, which conveys the slower kinetics of beating with myosin V : the oscillations exhibit a period of 70 s and a wave speed of only $0.3 \mu\text{m}/\text{s}$.

Looking in more detail at the beating shape for actin bundles of length $L > 11 \mu\text{m}$ (to ensure $L > s^*$ and that the tangent angle $\psi(s)$ saturates), we observed that the maximal angle has the same mean value with myosin II and myosin V. We get $\psi_{max} = 127 \pm 12$ deg for myosin II ($n = 45$) and $\psi_{max} = 127 \pm 12$ deg for myosin V ($n = 65$) (Fig. 4.12.A). However, the mean value of parameter ψ'_1 is significantly higher with myosin V than with myosin II : $\psi'_1 = 15 \pm 4 \text{ deg}/\mu\text{m}$ with myosin V ($n = 65$) and $\psi'_1 = 12 \pm 3 \text{ deg}/\mu\text{m}$ with myosin II ($n = 45$) (Fig. 4.12.B). This difference results in a tighter V-shape of the beating pattern at the base with myosin V than with myosin II (Fig. 4.11). Correspondingly, $s^* = \psi_{max} / \psi'_1$ is 2- μm longer with myosin II than with myosin V: $s^* = 9 \pm 3 \mu\text{m}$ with myosin V ($n = 65$) and $s^* = 11 \pm 4 \mu\text{m}$ with myosin II ($n = 45$) (Fig. 4.12.C).

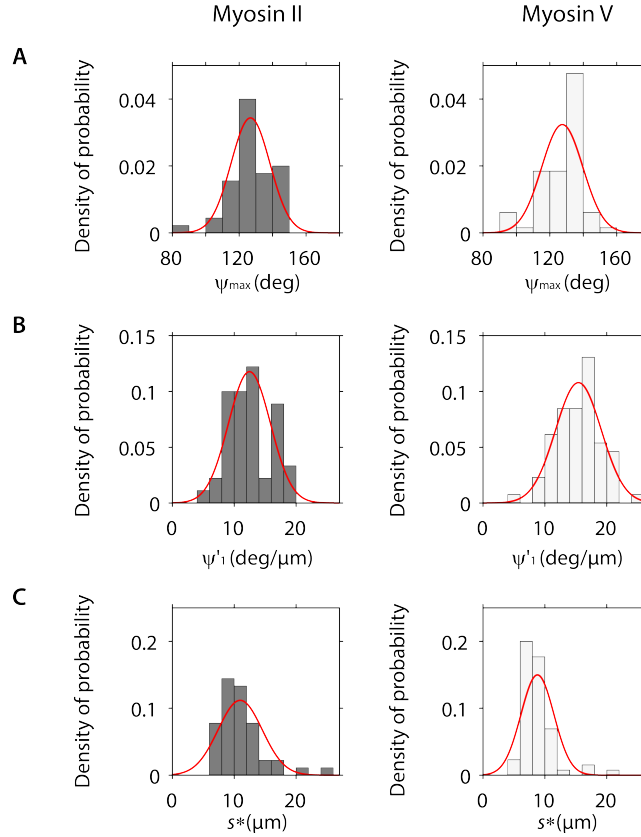


Figure 4.12: Shape parameters of the beating pattern. **A:** Distribution of the maximal angle $\psi_{max} = 127 \pm 12$ deg ($n = 45$) with myosin II (*left*) and $\psi_{max} = 127 \pm 12$ deg ($n = 65$) with myosin V (*right*). The means and the variances of the two distributions are not statistically different (t-test, p-value = 0.77: variance test, p-value = 0.6815). **B:** Distribution of $\psi'_1 = 12 \pm 3$ deg/ μm ($n = 45$) with myosin II (*left*) and $\psi'_1 = 15 \pm 3$ deg/ μm ($n = 65$) and with myosin V (*right*). The mean value of ψ'_1 is higher with myosin V (t-test, p-value = $4.4 \cdot 10^{-5}$), but the two distributions have the same variance (variance test , p-value = 0.54). **C:** Distribution of $s^* = 11 \pm 4$ μm ($n = 45$) with myosin II (*left*) and $s^* = 9 \pm 3$ μm ($n = 65$) with myosin V (*right*). The mean of s^* is higher with myosin II (t-test, p-value = $4.1 \cdot 10^{-4}$), the variance is slightly higher in the distribution with myosin II (variance test, p-value = 0.032). Red lines represent Gaussian fits to the distributions.

Concerning the kinetics, the actin bundles oscillate on average 7.5 time faster with myosin II than with myosin V (Fig. 4.13 (*left*)). In the case of myosin II, the period is $T^{MII} = 16 \pm 8$ s, for a median value of 17 s ($n = 46$), whereas with myosin V the period is $T^{MV} = 120 \pm 84$ s, for a median value of 104 s ($n = 71$). Correspondingly, bending waves propagate 7 times faster along actin bundle in the case of myosin II than myosin V. With myosin II, the wave speed is $v^{MII} = 1.4$ $\mu\text{m/s} \pm 0.8$, for a median value of 1.1 $\mu\text{m/s} \pm 0.8$ ($n = 46$), whereas in the case of myosin V the wave-speed is $v^{MV} = 0.2 \pm 0.1$ $\mu\text{m/s}$ ($n = 71$), for a median value of 0.2 $\mu\text{m/s}$ (Fig. 4.13 (*right*)).

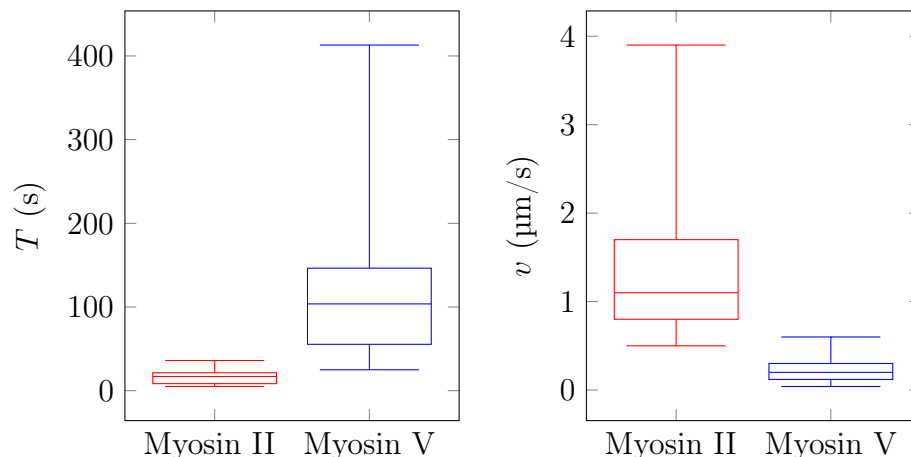


Figure 4.13: Faster beating with myosin II than with myosin V. *Left:* Boxplot of periods measured with myosin II and myosin V (Median values : $T = 17$ s for myosin II; $T = 104$ s for myosin V). The period for myosin II is $T^{MII} = 16 \pm 8$ s, ($n = 46$) in the case of myosin V the period is $T^{MV} = 120 \pm 84$ s ($n = 63$). *Right:* Boxplot of wave-speeds measured with myosin II and myosin V (Median values : $v = 1.1$ $\mu\text{m/s}$ for myosin II; $v = 0.2$ $\mu\text{m/s}$ for myosin V). The wave-speed for myosin II is $v^{MII} = 1.4$ $\mu\text{m/s} \pm 0.8$ ($n = 46$), in the case of myosin V, the wave-speed is $v^{MV} = 0.2 \pm 0.1$ $\mu\text{m/s}$ ($n = 63$). The boxes contain the values from the 1st to the 3rd quartile.

- The beating patterns are strikingly similar for both myosins.
- The kinetics of beating is ~ 7 faster with myosin II than with myosin V.

4.2.3 Effect of bundle length on beating properties

Birth and maturation of a beating bundle

Interestingly, if we look at short actin bundles ($L \leq 10$ μm , *i.e.* $L \leq s^*$) and look at their evolution when they grow over time (from $t = 5$ min to 16 min ; Fig. 4.14), we see that the actin bundles are straight and have low values for the tangent angle ($\psi < 70$ deg). Then, as the bundle gets long enough, the "heart shape" appears and is then maintained. Correspondingly, the color plot of tangent angle indicates the presence of a fixed region in the bundle (no apparent oscillation). This "rootlet" is observed and grows over time until its length saturates. Bending waves appear here only above $s = 7$ μm .

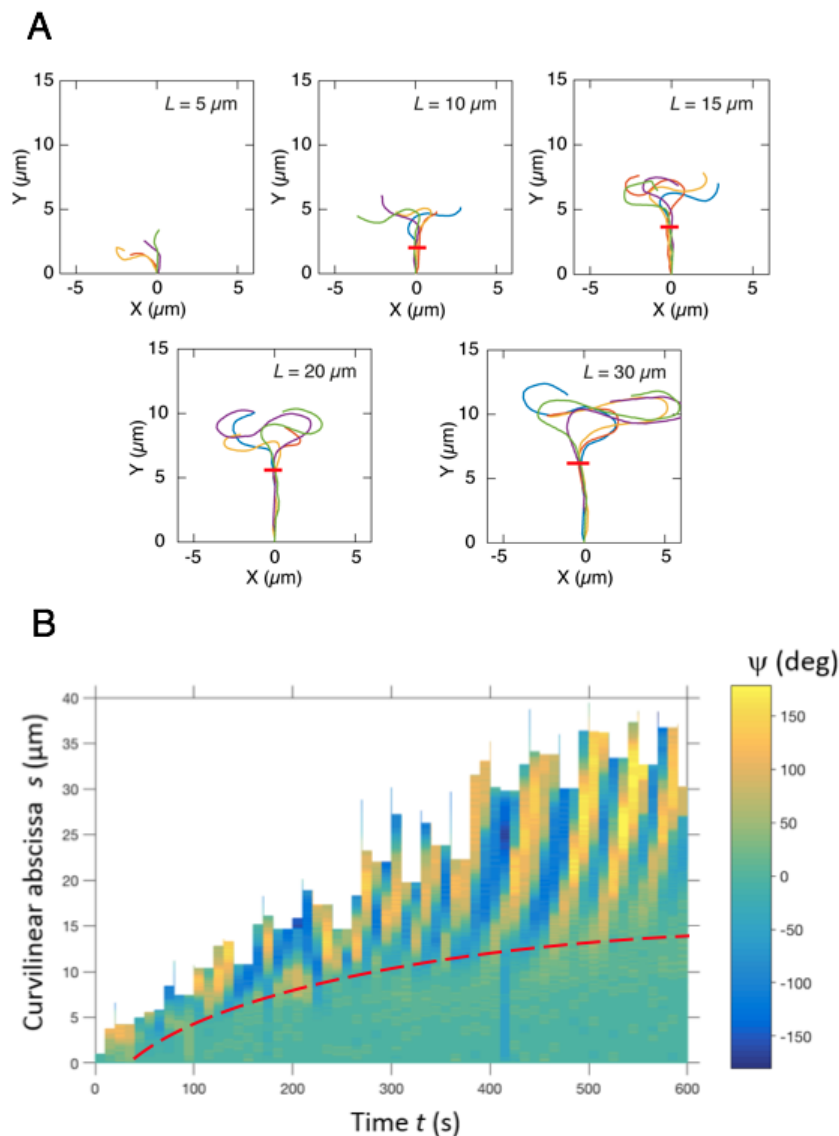


Figure 4.14: Birth of a beating myosin V-bundle. **A:** Beating pattern of a growing bundle at different time points, for which detected line are superimposed from a record every 10 s. We see a transition of beating pattern at $L = 10 \mu\text{m}$ with the formation of the "heart shape". The red bar indicates the tip of the "rootlet" of the actin bundle, *i.e.* the end of the basal region of the bundle that remains fixed. **B:** Color plot of the tangent angle $\psi(s, t)$ as a function of time t and of the curvilinear abscissa s , for the data shown in panel A. The color plot indicates the absence of bending propagation at the base of the bundle when the actin bundle is detected and tracked at the beginning of the experiment (*i.e.* beginning of the record at $t = 5$ min after injection of polymerization mix and for $s < 7 \mu\text{m}$). Red dashed line indicates the tip of the fixed "rootlet" of the actin bundle.

To analyze my experiments (for instance to get the distribution shown in Fig. 4.5), we defined the origin of the curvilinear abscissa s at the point of the bundle where a traveling wave is initiated ; the fixed "rootlet" was excluded from the analysis and thus did not count in the measurement of the bundle length. Thus, the "bundle length" is not measured from the border of the actin nucleation zone but represents the length of

the motile region (*i.e.* $A = 0$ at $s = 0$; see Fig. 4.8). In the case of the example shown in Figure 4.14, I would consider that the bundle is mature at $t = 400$ s and remove 10 μm from the base of the bundle, where no movement occurs, to study the dynamics of oscillations.

Effect of bundle length on beating properties of a mature bundle

During my experiments, the actin bundles are growing and beating at the same time. To study the effect of bundle length on beating properties, while keeping all other parameters constant, I tracked the same myosin II-based actin bundle over 20 minutes.

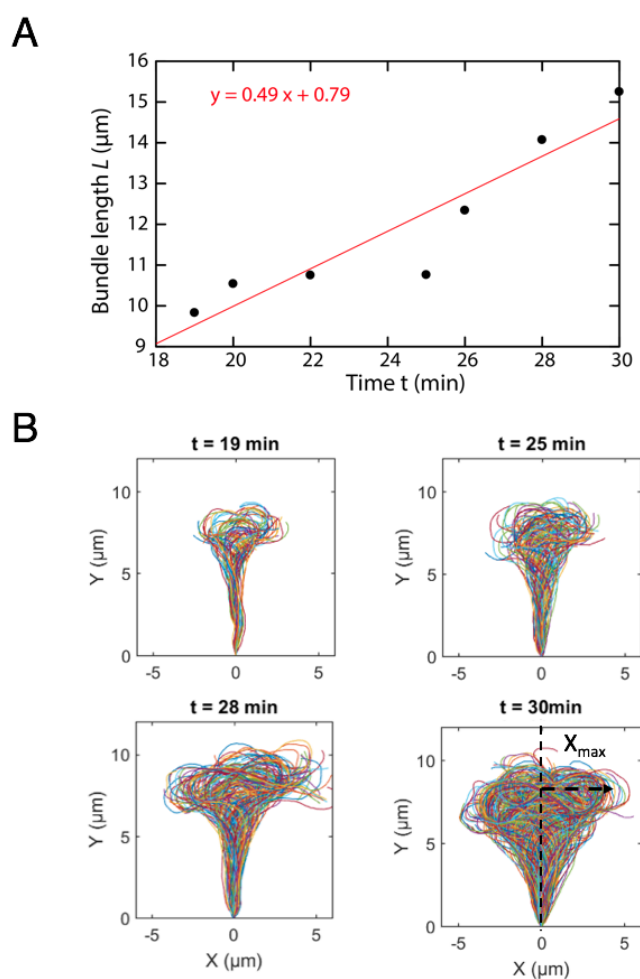


Figure 4.15: Time evolution of the beating pattern as the actin bundle grows. A: The bundle length increases linearly over time; a linear fit (in red) provides an elongation speed of $0.49 \mu\text{m}/\text{min}$. **B:** Beating pattern of a growing bundle at different time points, detected line were recorded every 1 s. Definition of the lateral excursion X_{max} on the last panel. Beating was driven by myosin II (500 nM in the polymerization mix).

We study here only "mature bundles", *i.e.* actin bundles where the heart shape is present in the beating pattern. In the example shown in Figure 4.15.A, the bundle length

increases by 50 % over the record. A linear fit of the relation between the bundle length and time provides an elongation speed of $0.49 \mu\text{m}/\text{min}$. The beating pattern shows a "heart shape" during the whole duration of the experiment (Fig. 4.15.B).

As the bundle grows, we found that the parameter ψ'_1 decreases (Fig. 4.16.A) and the lateral excursion X_{max} of the beating pattern envelope increases (Fig. 4.16.B). Moreover, the maximal angle ψ_{max} shows a compressive growth that indicates signs of saturation at large L ($L \geq 11 \mu\text{m}$; Fig. 4.16.C). Correspondingly, $s^* = \psi_{max} / \psi'_1$ increases as the bundle grows (for $L < 12 \mu\text{m}$) and appears to saturate for $s^* \geq 11 \mu\text{m}$ (Fig. 4.16.D).

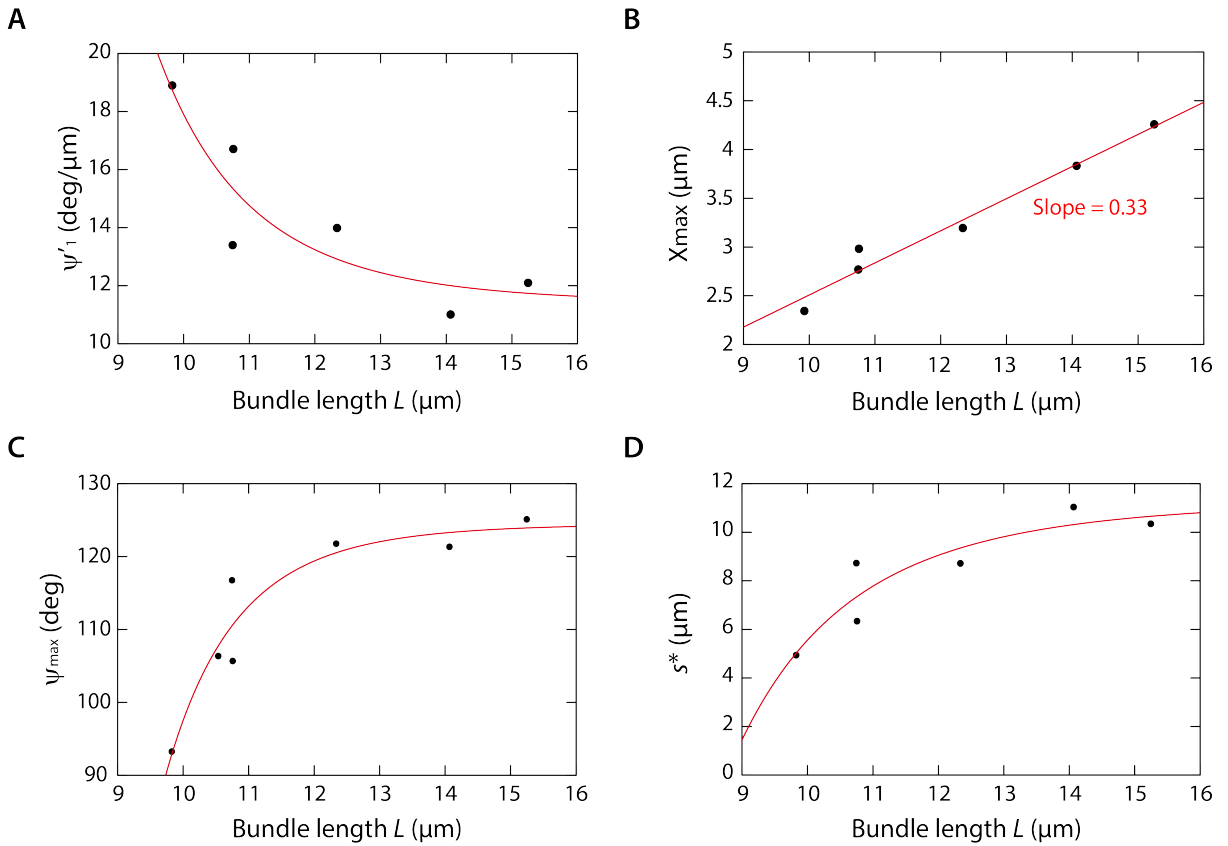


Figure 4.16: Evolution of beating properties of a growing bundle. **A:** ψ'_1 decreases as a function of bundle length L (in red, phenomenological fit of form $y = ax^b + c$, with $a = 5.0 \cdot 10^7$, $b = -6.9$ and $c = 11$). **B:** The lateral excursion X_{max} increases as a function of the bundle length (in red linear fit of equation : $y = 0.33L - 0.78$). **C:** The maximal angle ψ_{max} shows a compressive growth (in red, phenomenological fit of form $y = ax^b + c$, with $a = -3.5 \cdot 10^{10}$, $b = -9.1$ and $c = 125$). **D:** s^* increases as the bundle grows (in red, phenomenological fit of form $y = ax^b + c$, with $a = -7.2 \cdot 10^5$, $b = -5$ and $c = 11$). Beating was driven by myosin II (500 nM in the polymerization mix).

Regarding kinetics, the period T of oscillation increases linearly as a function of bundle length L (Fig. 4.17.A). Thus, the longer the actin bundle, the slower the oscillations. Remarkably, the wave-speed of the bending propagation remains constant over time, and

thus does not depend on bundle length (Fig. 4.17.B). Correspondingly, the wavelength λ varies linearly with the bundle length ($\lambda = v.T$), with a slope of 0.6 (Fig. 4.17.C).

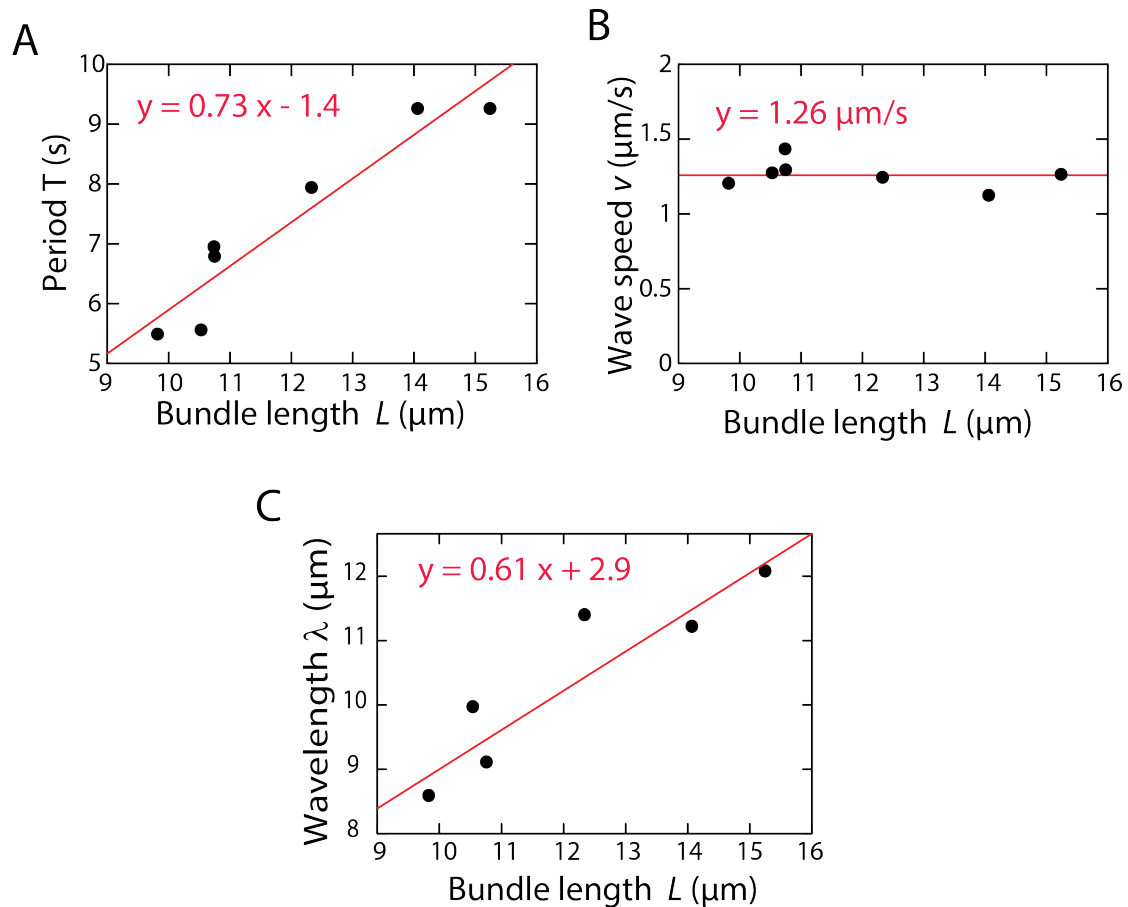


Figure 4.17: Beating properties of a growing bundle. **A:** The beating period T increases with the bundle length (linear fit in red). **B:** The wave speed of the bending wave propagation remains constant with a mean value of $1.3 \mu\text{m/s}$ indicated by the red line. **C:** The wavelength λ of the bending wave increases with bundle length. A linear fit (in red) gives a slope of 0.6. Same bundle as in Fig. 4.15.

- As the actin bundle grows, the oscillation period increases linearly with the bundle length, the oscillations thus slow down.
- The wave speed does not depend on the bundle length.
- The wavelength increases linearly with the bundle length.

Beating properties over an ensemble of actin bundles

In the previous paragraph, we focused on the beating properties of a single bundle as a function of its length, as the bundle grows over time. This experimental configuration allows to control one parameter (the bundle length) and keep all the biochemical parameters constant. Here, we collect the beating properties measured over a large ensemble of actin bundles driven by myosin II or myosin V.

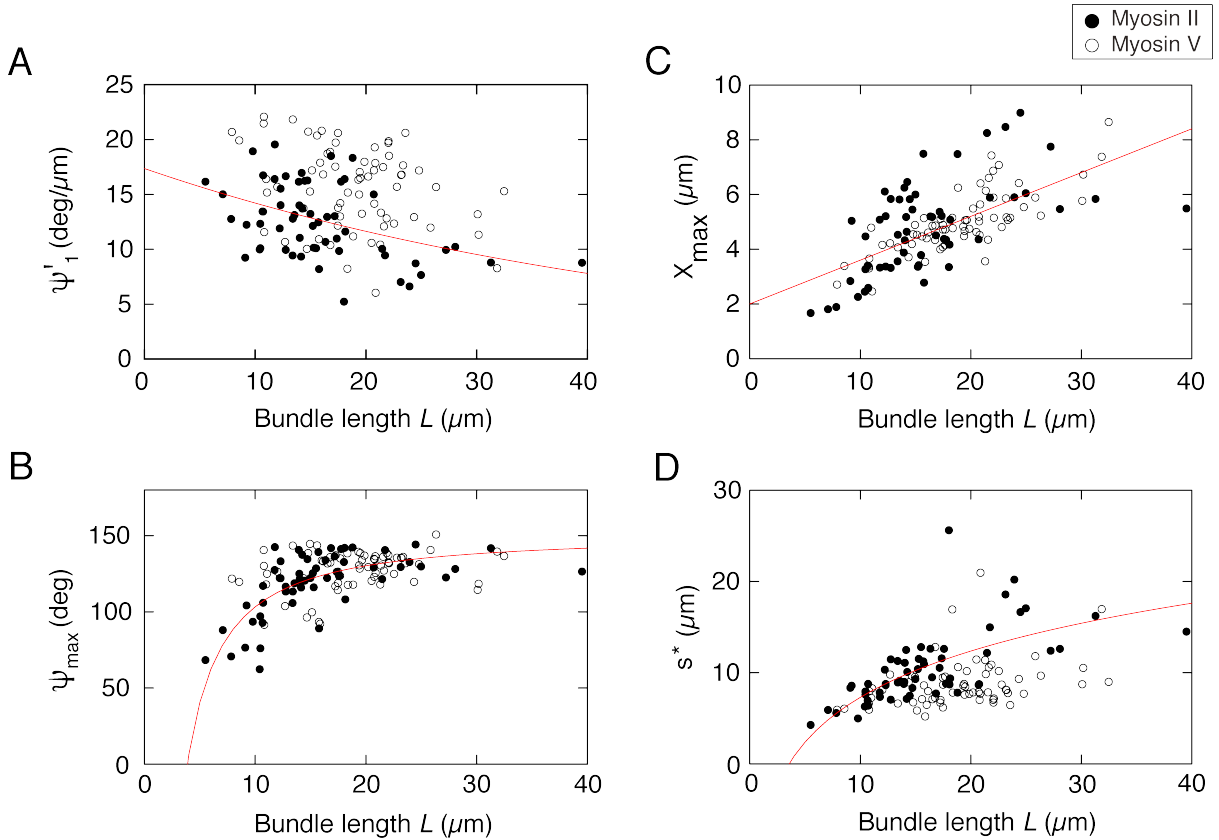


Figure 4.18: Beating pattern properties over an ensemble of actin bundles with myosin II (black disks) and myosin V (white disks). **A:** ψ'_1 as a function of bundle length L . ψ'_1 decreases for both myosin II and myosin V (myosin II: Pearson, $\rho = -0.44$, p-value = $4.3 \cdot 10^{-4}$; myosin V: Pearson, $\rho = -0.29$, p-value = $1.0 \cdot 10^{-2}$), phenomenological fit in red obeys $y = 17.4 \exp(-0.02L)$. **B:** Lateral excursion X_{max} as a function of bundle length L . X_{max} has a strong correlation with bundle length L (myosin II: Pearson, $\rho = 0.58$, p-value = $1.2 \cdot 10^{-6}$; myosin V: Pearson, $\rho = 0.78$, p-value = $3.1 \cdot 10^{-15}$). The linear fit in red obeys $X_{max} = 0.16L + 2$. **C:** Maximal angle ψ_{max} as function of bundle length L . The maximal angle exhibits a compressive growth with myosin II and a saturation for $L > 15 \mu\text{m}$, but is constant for myosin V (myosin II: Pearson, $\rho = 0.55$, p-value = $6.8 \cdot 10^{-6}$; myosin V: Pearson, $\rho = 0.29$, p-value = 0.015) in red, phenomenological fit of form $y = a \cdot x^b + c$, with $a = -784$, $b = -1.2$ and $c = 151$. **D:** s^* as function of bundle length L . s^* is increasing as a function of L with both myosin II and myosin V (myosin II: Pearson, $\rho = 0.66$, p-value = $1.8 \cdot 10^{-8}$; myosin V: Pearson, $\rho = 0.36$, p-value = $2.6 \cdot 10^{-3}$). In red, phenomenological fit of form $y = a \cdot x^b + c$, with $a = 134$, $b = 0.05$ and $c = -143$.

Concerning the shape of the beating-pattern, as shown in Figure 4.18.A, ψ'_1 tends to

decrease as a function of bundle length, (myosin II: Pearson, $\rho = -0.44$, p-value = $4.3 \cdot 10^{-4}$; myosin V: Pearson, $\rho = -0.29$, p-value = $1.0 \cdot 10^{-2}$), as was the case at the level of a single growing bundle (Fig. 4.16.A). The linear correlation between the lateral excursion X_{max} and the bundle length observed for a single actin bundle (Fig. 4.16.A) is maintained at the level of all myosin II bundles collected, as well as for all myosin V actin bundles (Fig. 4.18.B). The maximal angle ψ_{max} also shows the same trend for the ensemble of myosin II data than with the growing bundle (Fig. 4.16.C) and emphasizes the increase of ψ_{max} for short bundles (almost exclusively studied with myosin II). Moreover, we observe a saturation of $\psi_{max} = 127 \pm 12$ deg ($n = 110$), which has the same values for the two types of myosins (Fig. 4.18.C and Fig. 4.12.A). Finally, s^* tends to increase as the bundle becomes longer for both myosin II and myosin V (Fig. 4.18.D), as observed with the single growing bundle (Fig. 4.16.D). This trend is consistent with results obtained for ψ_{max} and ψ'_1 , because $s^* = \psi_{max} / \psi'_1$.

Concerning kinetics of the beating, we have observed in the case of the single bundle that the oscillation period T increases as the bundle grows (Fig. 4.17.A). Taking all myosin II data together, the correlation between oscillation period and bundle length disappears (Fig. 4.19.A, *left*). This absence of correlation also applies to myosin V (Fig. 4.19.A, *right*). Thus, the bundle length cannot be the only control parameter of the oscillation period. In addition, the wave speed v , which was constant for the growing actin bundle (Fig. 4.17.B), still appears to be non correlated with the bundle length for both myosin II and myosin V (Fig. 4.19.B). Finally, we see that the wavelength λ increases linearly with bundle length for both myosins (Fig. 4.19.C, *left*), as was the case for a single bundle (Fig. 4.17.C). Linear fits of the relation between the wavelength and the bundle length are not statistically different between the two myosin types. A global fit to the whole data set (myosin II and myosin V) yields $\lambda = 0.7L + 5$. Furthermore, the shorter actin bundles ($L < 15$ μm) are more likely to have a wavelength higher than their length, whereas longer actin bundles ($L > 15$ μm) are more likely to have a wavelength lower than their length (Fig. 4.19.C, *right*). Thus, the bundle length appears as a robust control parameter of the wavelength of the actin bending waves. We note that the wavelength for myosin II was shorter for myosin V, with $\lambda = 17 \pm 6$ μm ($n = 59$) and $\lambda = 18 \pm 6$ μm ($n = 79$), respectively. This observation makes sense if L indeed controls the wavelength, because we have seen (Fig. 4.5) that the actin bundles analyzed with myosin II were shorter than with myosin V.

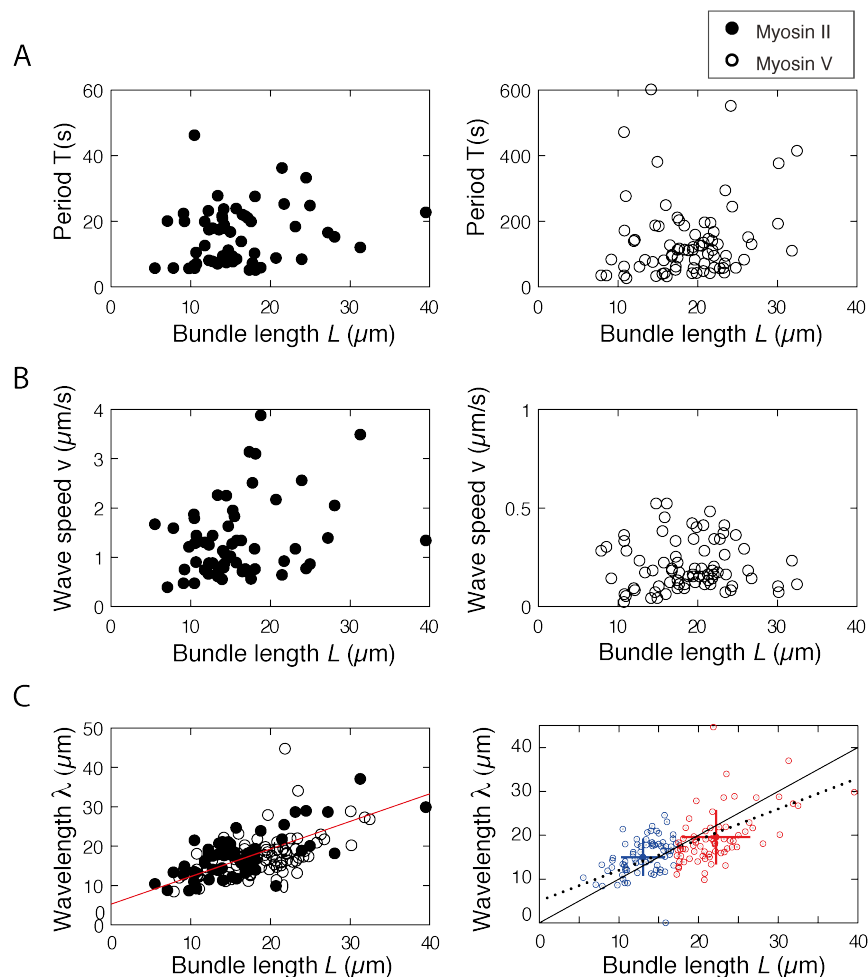


Figure 4.19: Beating properties over an ensemble of actin bundles with myosin II (black disks) and myosin V (white disks). **A:** Oscillation period T as a function of bundle length L with myosin II and with myosin V. For both myosin II (*left*) and myosin V (*right*), there is no significant correlation between the Period T and bundle length L (myosin II: Pearson, $\rho = 0.20$, p-value = 0.13 ; myosin V: Pearson, $\rho = 0.13$, p-value = 0.26). **B:** Speed v of the bending wave as a function of bundle length, with myosin II and myosin V. For myosin II (*left*), there is a slight correlation between wave speed and bundle length but with myosin V (*right*), there is no significant correlation between the wave speed v and bundle length L (myosin II: Pearson, $\rho = 0.28$, p-value = 0.030 ; myosin V: Pearson, $\rho = 0.043$, p-value = 0.71). **C:** Wavelength λ of bending wave as a function of bundle length. *Left:* For both myosin II (black disks) and myosin V (white disks), there is a strong correlation between the wavelength λ and bundle length L (myosin II: Pearson, $\rho = 0.72$, p-value = $1.7 \cdot 10^{-10}$; myosin V: Pearson, $\rho = 0.53$, p-value = $5.7 \cdot 10^{-7}$). The slope of the global linear fit over the two sets of data in red is 0.7. *Right:* The shorter actin bundles ($L < 15 \mu\text{m}$, blue circles) are more likely to have a wavelength higher than their length. The blue (red) disk has coordinates corresponding to the mean values of the wavelength and the bundle length for bundles shorter (longer) than the median bundle length ($L = 15 \mu\text{m}$) measured for the whole ensemble; it is above (below) the black line of slope unity going through origin. The dotted line corresponds to the global linear fit $\lambda = 0.7L + 5$.

- The maximal bending angle ψ_{max} is the same for myosin II and myosin V (127 deg).
- The bundle length is not the only control parameter of the oscillation period.
- The wave speed does not vary with the bundle length
- The wavelength increases with the bundle length, with $\lambda < L$ for short bundles ($L < 15 \mu\text{m}$) and $\lambda > L$ for long bundles ($L > 15 \mu\text{m}$).

4.2.4 Varying the concentration of the molecular motors

In gliding assays, the gliding speed of actin filaments on a myosin-coated surface depends on motor concentration with myosin II but not with myosin V (Chapter 2, Fig. 2.17). Similarly, we wondered whether beating kinetics depends on myosin concentrations. With myosin II, we were unable to observe the reorganization of actin filaments into beating bundles below a motor concentration (double heads) of 250 nM. We compared the period T of oscillation for actin bundles of length $L > 11 \mu\text{m}$ for three myosin II-concentrations : 250, 500 and 750 nM. We found that the oscillation periods are slightly higher at 250 nM than at 500 nM, with respectively $T = 22 \pm 7 \text{ s}$ ($n = 10$) and $T = 16 \pm 8 \text{ s}$ ($n = 23$). Instead, the mean periods are not statistically different between 500 nM and 750 nM, with respectively $T = 16 \pm 8 \text{ s}$ ($n = 23$) and $T = 18 \pm 3 \text{ s}$ ($n = 6$). In addition, the variances were similar at 250 nM and 500 nM, but significantly decreased between 500 nM and 750 nM. The concentration, which is very high in our experiments, does not seem to tune the period but seems to play a role in the noise of our system : the higher the concentration, the smaller the noise (Fig. 4.20.A). With myosin V, we did not observe reorganization and movement for concentrations below 25 nM. Within the range 25 - 40 nM, we observed oscillations of period $T = 306 \pm 172 \text{ s}$ ($n = 9$) that were larger than $T = 112 \pm 98 \text{ s}$ ($n = 34$), the period measured at 50 nM; the latter also showed a significantly higher variability. Above 50 nM, $T = 108 \pm 32 \text{ s}$ ($n = 26$) remained the same, but the variance was significantly lower than at lower myosin concentrations (Fig. 4.20.B).

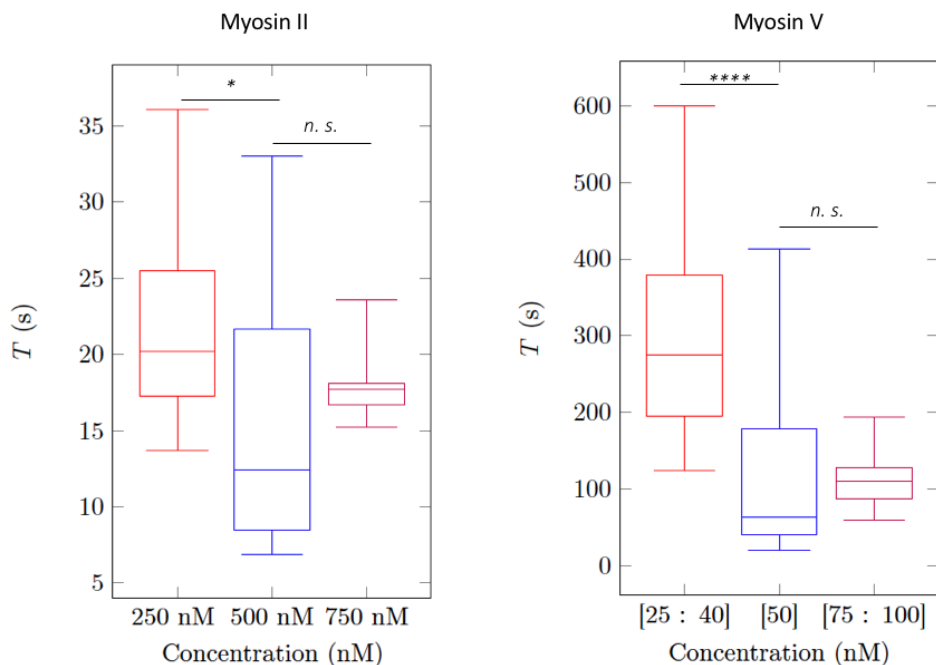


Figure 4.20: Effect of myosin concentration on the oscillation period for bundles of length $L > 11 \mu\text{m}$. Boxplot with myosin II at 3 different concentrations (250, 500, 750 nM ; *Left*) and boxplot with myosin V for three ranges of concentration (*Right*). With myosin II, the oscillation period $T = 22 \pm 7 \text{ s}$ ($n = 10$) is higher at 250 nM than the period observed at 500 nM: $T = 16 \pm 8 \text{ s}$ ($n = 23$) (t-test, p-value = 0.05), but is similar between 500 nM and 750 nM, with $T = 18 \pm 3 \text{ s}$ ($n = 6$) (t-test, p-value = 0.46). In addition, the variances were not statistically different at 250 nM and 500 nM (variance-test, p-value = 0.56), but significantly lower (variance-test, p-value = 0.03) at 500 nM and 750 nM. With myosin V, for low concentrations (between 25 and 40 nM), the period $T = 306 \pm 172 \text{ s}$ ($n = 9$) is significantly higher (t-test = $6.8 \cdot 10^{-5}$) than the periods $T = 112 \pm 98 \text{ s}$ ($n = 34$) observed at 50 nM. At concentration higher than 50 nM, the distribution has the same mean (t-test p-value = 0.96) with $T = 108 \pm 32$ ($n = 26$), but the variance is significantly lower at high myosin concentration (variance test, p-value= $1.5 \cdot 10^{-7}$).

- Enough myosins are required to drive self-organization of beating bundles ($\geq 250 \text{ nM}$ with myosin II; $\geq 25 \text{ nM}$ with myosin V).
- Above these thresholds, oscillations are slower at low concentrations but then the kinetics does not vary with concentrations at higher concentrations.

4.3 Distribution of myosin motors along a beating actin bundle

We used GFP-tagged myosin V to visualize the motors during beating of actin bundles. Unexpectedly, we found that the fluorescence profile along the actin bundle for the motors did not match the profile observed for actin.

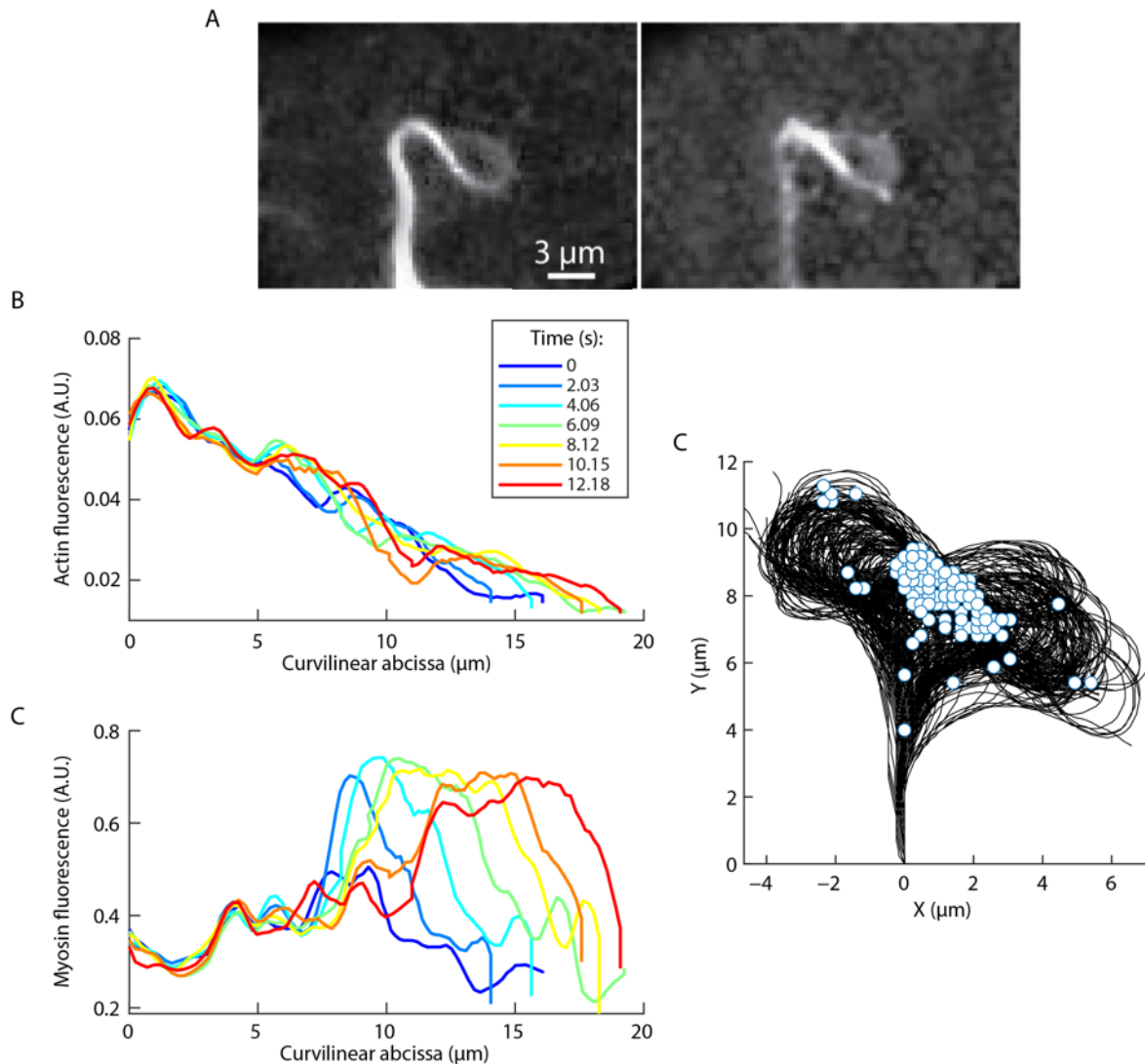


Figure 4.21: Myosin V localization along actin bundle. **A:** Fluorescence images of a beating actin bundle in both the actin channel (*left*) and in the myosin V channel (*right*). Actin was labeled with AlexaFluor™ 568 (10 % labelling, see Chapter 3), whereas myosin V was tagged with GFP. The myosin V concentration was 50 nM. **B:** Fluorescence intensity profiles of actin (*top*) and myosin (*bottom*) signals along the actin bundle at $t = 0 - 12$ s. The actin fluorescence intensity profiles decrease from base to tip of the actin bundle and do not vary over time. The myosin V fluorescence intensity profiles exhibit a peak that emerges at $s = 8.3 \mu\text{m}$, grows and travels towards the bundle's tip. **C:** Superimposition of tracks (sampling time: 2.03 s) over 41 periods of oscillation. White disks indicate positions of the peak of the myosin V signal on the corresponding tracks.

As described before (Section 4.1, Fig. 4.1), the actin fluorescence intensity exhibits more signal near the thick base, from which the signal progressively decreases as one progresses towards the tip and the bundle gets thinner (Fig. 4.21.A, *left*). In addition, the actin fluorescence intensity profile remains the same over time and thus through the beating (Fig. 4.21.B). In contrast, the myosin V fluorescence intensity profile is peaked, revealing that the motor molecules can be concentrated at a specific location along the actin bundle (Fig. 4.21.A, *right*, B and C). As time progresses, the peak travels towards the tip of the actin bundle. Thus, the position of highest myosin V concentration is not fixed at a given position within the actin bundle. By superimposing the beating pattern of the actin bundle and the positions of the peak of myosin V-fluorescence in the XY plane, we observe that myosin V remains concentrated near the center of the lemniscate-like shape (*i.e.* the infinity sign within the beating pattern) that the tip of the bundle draws during the beating (Fig. 4.21.C).

By plotting the curvilinear abscissa of the myosin V signal at the peak as a function of time, we observe a sawtooth oscillation, corresponding to the periodic generation of a concentration wave of myosin V propagating towards the tip of the actin bundle (Fig. 4.21.C and Fig. 4.22.A). Interestingly, the myosin V signal is not traveling throughout the actin bundle but only within the apical section starting at $s = 8.3 \mu\text{m}$ and is periodically generated with a period $T = 16 \text{ s}$ (Fig. 4.22.A). In comparison, the actin bending (tangent angle) at any position along the actin bundle exhibits noisy sinusoidal oscillations with a period $T = 32 \text{ s}$ (Fig. 4.22.B) and the actin bending wave starts at more basal locations (see Figure 4.23 below). Thus, the period of the myosin V oscillation is half the period of the actin bending wave, corresponding to double the frequency. Interestingly, the power spectrum of myosin oscillations (Fig. 4.22.A) also displayed a peak at the frequency of actin-bending oscillations (Fig. 4.22.B). The slope of the relation between the curvilinear abscissa of the myosin peak and time (upward ramps in Figure 4.22.A) gives the speed $v_{MYOSIN} = 0.9 \mu\text{m/s}$ for the myosin V concentration wave, whereas the speed of the corresponding actin bending wave was $v_{ACTIN} = 0.5 \mu\text{m/s}$. We compared the kinetics of the myosin concentration waves and of the actin bending waves over the ensemble of myosin V-GFP actin bundles that we analyzed ($n = 11$). We obtain a speed $v_{MYOSIN} = 0.7 \pm 0.1 \mu\text{m/s}$ for the concentration waves of myosin V, corresponding to a period of myosin oscillation $T_{MYOSIN} = 22 \pm 5 \text{ s}$ ($n = 11$). The corresponding speed and period of the actin bending wave are $v_{ACTIN} = 0.4 \pm 0.1 \mu\text{m/s}$ and $T_{ACTIN} = 44 \pm 10 \text{ s}$ ($n = 11$), respectively. As already noted, the oscillation period of myosin V is half that of the oscillations of the tangent angle (Fig. 4.22.C). In addition, the myosin V waves travel 1.7 times faster than the corresponding actin bending waves (Fig. 4.22.D).

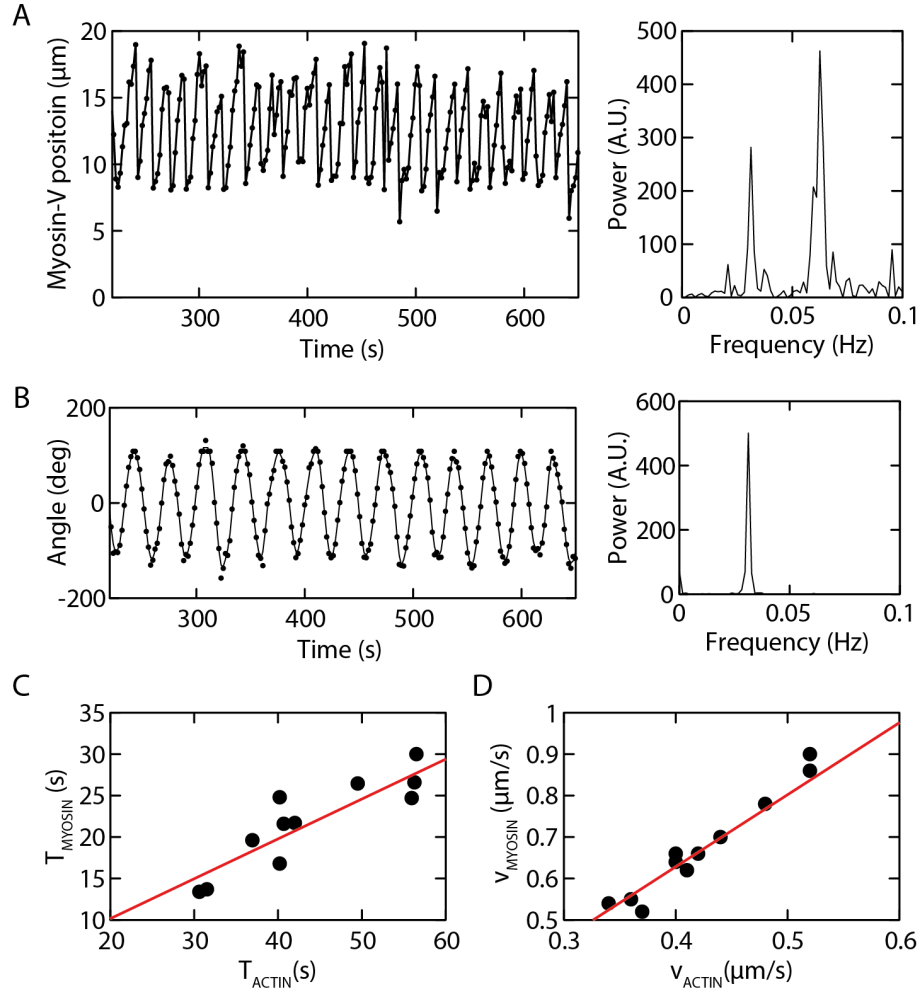


Figure 4.22: Kinetics of myosin concentration waves compared to that of actin beating. **A:** Position of the myosin V concentration peak on a beating actin bundle as a function of time (*left panel*). The myosin V signal shows a sawtooth oscillation, corresponding to the periodic generation of a concentration wave of myosin V propagating towards the tip of the actin bundle from $s = 8.3 \mu\text{m}$ to the bundle's tip, with a speed of $v = 0.7 \mu\text{m/s}$, given by the slope of the upward ramps. The power spectrum of the oscillations (*right panel*) shows a main Fourier mode at the frequency $f_0 = 0.06 \text{ Hz}$ and a second mode at the frequency $f_1 = 0.03 \text{ Hz}$ of the actin bending oscillations (shown in panel B). **B:** Time series of the tangent angle at $s = 10 \mu\text{m}$ (*left panel*). The tangent angle exhibits sinusoidal oscillations as a function of time, with a period $T = 32 \text{ s}$. The corresponding power spectrum (*right panel*) shows only one mode at the frequency $f_0 = 0.03 \text{ Hz}$. **C:** Period T_{MYOSIN} of generation of myosin V concentration wave as a function of the beating period T_{ACTIN} of the actin bundles ; in red, a linear fit $T_{MYOSIN} = 0.5 \cdot T_{ACTIN} + 0.6$. **D:** Speed v_{MYOSIN} of myosin concentration waves as a function of the speed v^{ACTIN} of actin bending waves ; in red, a linear fit $v_{MYOSIN} = 1.7 \cdot v_{ACTIN} - 0.1$.

Notably, the speed of myosin V concentration waves was 1.4 to 3 times higher than the intrinsic myosin V velocity measured in gliding assays ($v_{gliding} = 0.36 \mu\text{m/s}$, see Chapter 2, Table 2.3). This observation suggests that the speed measured does not correspond to myosin V moving processively along the actin filaments. In addition, when we sum the myosin V fluorescence signal along the actin bundle, which reflects the total number of

motors present within the bundle, we get a sawtooth oscillation as a function of time (Fig. 4.23.A). This finding indicates that the number of myosins within the actin bundle increases as the myosin-concentration wave propagates from its position of initiation ($s = 8.3 \mu\text{m}$) to the tip.

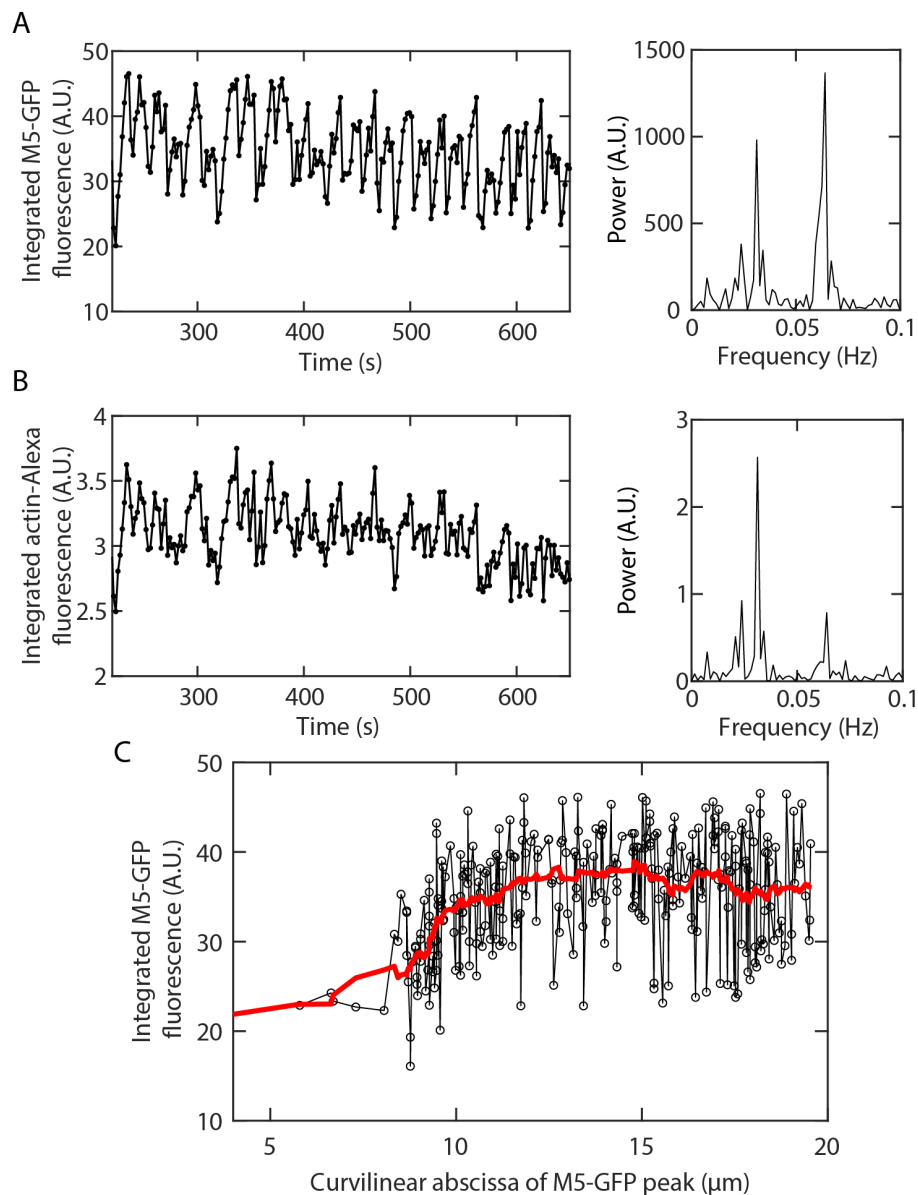


Figure 4.23: Integrated-myosin V and actin fluorescence signals along a beating actin bundle. **A:** The integrated-myosin V fluorescence signal along the actin bundle, which reflects the total number of motors present within the bundle, displays a sawtooth oscillation as a function of time. The power spectrum (*right panel*) shows a main Fourier mode at the frequency $f_0 = 0.06$ Hz and a second mode at the frequency $f_1 = 0.03$ Hz. **B:** The integrated-actin fluorescence signal along the actin bundle, shows a sawtooth oscillation as a function of time, of (much) lower amplitude than in the case of myosin V in (A). The power spectrum (*right panel*) shows a main Fourier mode at the frequency $f_0 = 0.03$ Hz and a second mode at the frequency $f_1 = 0.06$ Hz. **C:** The integrated-myosin V fluorescence signal as a function of the position of myosin V along the actin bundle. A moving average of the data points provides the red line.

Moreover, the power spectrum of the oscillation shows a principal mode at the frequency $f_0 = 0.06$ Hz, indicating that total quantity of myosins in the bundle oscillates at the same frequency than the myosin concentration waves (Fig. 4.22.A), thus at twice the frequency of the actin-bending oscillations (Fig. 4.22.B). The sum of myosin V signal as the same period of $T = 16$ s than the position of the myosin V peak as a function of time. Notably, we also observe a second mode in the spectrum at the frequency $f_1 = 0.03$ Hz, which corresponds also to the period $T = 32$ s of the actin bundle beating. In parallel, when we integrate the actin fluorescence signal along the actin bundle, which is expected to remain stable as a function of time, we also get a (weak) sawtooth signal of period $T = 32$ s (*i.e.* frequency f_1), at the same period as the beating of actin bundle (Fig. 4.23.B). However, the amplitude of these oscillations is more than 10 times lower than that obtained for myosin V. One possible explanation of this observation could be that the beating movement is not totally confined in the plane of observation, but instead moves slightly in and out of this plane, resulting in blinking of the fluorescence signal (both in the actin and the myosin channels) at the frequency of actin bending oscillations. Finally, a plot of the integrated myosin V fluorescence as a function of the position of myosin V peak shows that the number of myosins increases as the peak travels toward the tip of the bundle, in a non linear manner (Fig. 4.23.C). More precisely, the number of myosins remains almost stable for positions below $s = 7$ μm and above $s = 12$ μm , hence integrated myosin V signal almost double between $s = 7$ μm and $s = 12$ μm . This finding indicates that myosin V recruitment by the actin bundle is local, occurring preferentially in a restricted region of the actin bundle. Thus, our observations indicate that the actin beading wave is associated with a myosin-concentration wave traveling in the same direction. There is local myosin recruitment along the bundle and propagation of a concentration wave towards the tip, with myosin release at the back of the concentration peak.

What's the relation between the localization of myosin V and the shape of the actin bundle ? Figure 4.24 correlates the position of the myosin concentration peak to actin curvature. Looking at the fluorescence intensity profile of myosin V GFP along the actin bundle as a function of time (Fig. 4.24.A), we see the propagation of a wave from base to tip. Correspondingly, the curvature profile along actin bundle as function of time (Fig. 4.24.B) also exhibits a traveling wave, but at a slower speed and with a period twice as large as that of the myosin-concentration wave, as already noted. Furthermore, if we compare the localization on the actin bundle of the peak of myosin V fluorescence to that of curvature maxima and minima as a function of time (Fig. 4.24.C), we see that myosin V is positioned in between the positions of the maxima and minima of curvature: The myosin wave is initiated at a position that nearly (but not precisely) coincides with a

position of maximal (minimal) curvature and then travels so fast as to get to the bundle's tip at the same time as the wave of minimal (maximal) curvature that was generated half a period earlier. Again, we see that the myosin V wave does not start at the base but is initiated at some distance towards the apex. As the actin bending wave progresses from base-to-tip of the bundle, the magnitude of tangent angle oscillation increases (Section 4.1, Fig. 4.9), as does the curvature.

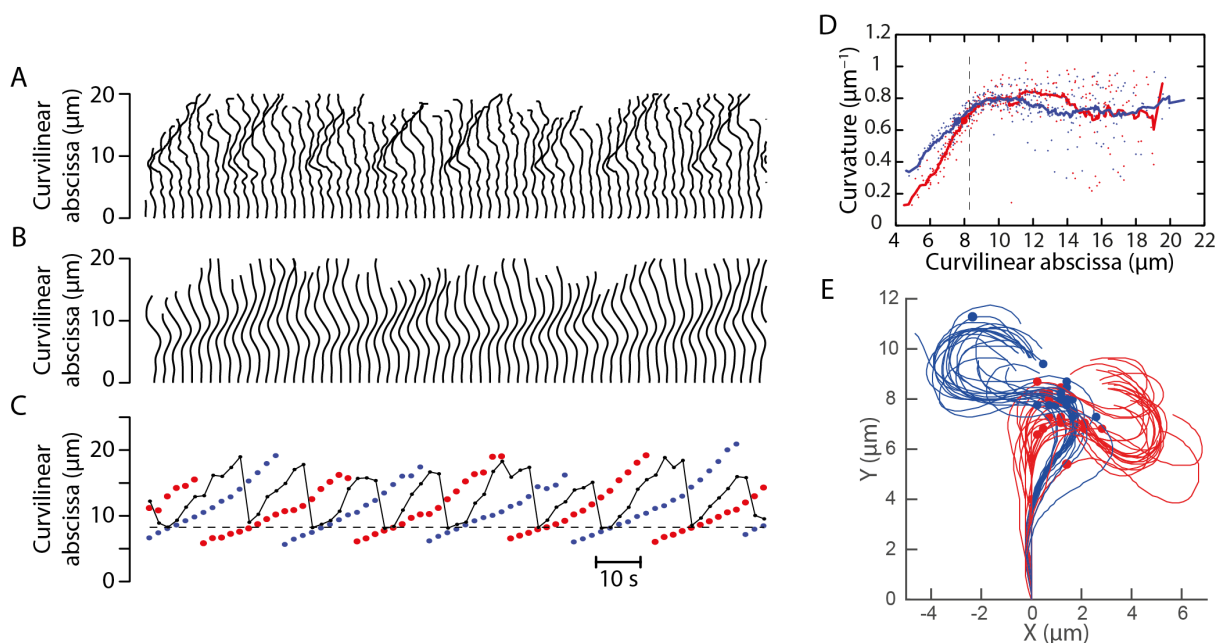


Figure 4.24: Myosin V and actin curvature. **A:** Fluorescence intensity profile of myosin V GFP along a beating actin bundle as a function of time ($dt = 2$ s). It shows the propagation of a traveling wave towards the bundle's tip. The corresponding wave speed is given by following the maximum of the myosin V signal. **B:** The actin curvature (arbitrary units) along the bundle as a function of time also exhibits a traveling wave but with a lower speed and a period twice as large as that of the myosin V-generated waves. **C:** Position on the actin bundle of the peak of myosin V GFP fluorescence (black), of actin curvature maxima (red) and minima (blue) as a function of time. The maxima of myosin V fluorescence are located between the maxima and minima of curvature. Myosin V waves propagate faster than curvature. Moreover we see that curvature signals start in front (*i.e.* at more basal positions) of myosin V signals along the actin bundle ($s = 7.5 \mu\text{m}$ vs $s = 8.3 \mu\text{m}$). **D:** Positive (red line) and negative (blue line) maximal curvatures along the actin bundle as a function of the curvilinear abscissa. The red (blue) disk indicates the position where myosin V is recruited along actin bundle. **E:** Superimposition of actin bending patterns and positions of myosin V fluorescence peaks along the actin bundle at the times (twice every actin-bending oscillation) where myosin V is recruited by the actin bundle. Red (blue) tracks correspond to positive (negative) curvature at the position of myosin V recruitment actin bundles, whereas red (blue) disks indicate the corresponding position of the peak of myosin V signal.

Thus, myosin recruitment happens only when actin bending becomes high enough along the actin bundle (here at $s = 8.3 \mu\text{m}$). Figure 4.24.D displays the magnitude of the maximal positive and negative curvatures as a function of the curvilinear abscissa

along the actin bundle. Myosin V recruitment starts on the actin bundle only when the maximal curvature gets beyond an absolute threshold value of curvature (here $C_{threshold} = 0.65 \text{ m}^{-1}$). Thus, a curvature threshold appears to initiate the myosin concentration wave, which is reached twice at every beating period (once positively, once negatively). This condition can be visualized by superimposing the beating pattern of the actin bundle and the position of the myosin V peak precisely at the times where myosin V is recruited by the actin bundle. We then see that myosin is recruited in the region of highest curvature of the actin bundle (Fig. 4.24.E)

This behavior suggests a mechanical feedback between the myosin affinity for actin and the bundle shape (curvature or the absolute value of tangent-angle oscillation).

- Myosin V motors display a peak of concentration along the actin bundle.
- This peak travels from base to tip of the actin bundle, corresponding to a concentration wave of myosin V.
- Myosin V motors are recruited on the actin bundle as the concentration wave progresses, before they detach at the bundle's tip.
- Myosin V recruitment is initiated when the curvature on the actin bundle reaches an absolute threshold value.
- We conclude from these observations that the affinity of myosin for actin depends on bundle shape (curvature).

Chapter 5

Conclusion and Discussion

In this thesis, we developed a minimal *in vitro* system comprising only 4 purified proteins and the Arp2/3 complex. By controlling the geometry of actin polymerization with surface micropatterns of a nucleation-promoting factor, we were able to demonstrate the emergence of flagellar-like beating of actin bundles in the presence of myosin motors. We worked with both heavy-meromyosin II and myosin V. Both myosins have a movement directed towards the barbed end of the actin filaments, they possess contrasted intrinsic properties and mediate different functions within the cell: myosin II is a non-processive motor, working in large assemblies and acting as a contraction engine, whereas myosin V is a processive motor, acting as a molecular transporter. Yet, both types of motors power very similar bending waveforms, which are nearly two-dimensional, and symmetric and draw a "heart shape" pattern.

When we looked at beating properties, we observed that the tangent angle display quasi sinusoidal oscillations as a function of time, with growing amplitude from base (*i.e.* near the actin nucleation surface) to tip of the actin bundle. Remarkably, the bending wave travels at an uniform speed, despite the varying geometry of the actin bundle, which is thicker at the base and thinner at the tip. We demonstrated that the kinetics of beating was 7 times faster with myosin II than with myosin V, reflecting the difference in kinetics of movements driven by the two motors in *in vitro* gliding assays (Chapter 2, Table 2.3). We identified the bundle length as one of the control parameters of the beating pattern and kinetics. In particular, as the bundle length increases, the beating period increases, *i.e.*, the beating slows down, but the speed of the traveling bending wave remains constant.

Notably, GFP-tagged myosin V revealed the presence of a peak of myosin concentration within the actin bundle. We observed that myosin V motors are locally recruited on the actin bundle, before a concentration wave propagates towards the bundle's tip, where

the motors eventually detach. Moreover, myosin V recruitment is initiated when the curvature on the actin bundle reaches an absolute threshold value. These results revealed a novel form of coupling between the affinity of myosin for actin and the actin bundle shape.

5.1 Comparison to other oscillating systems

We compare here the beating properties of actin bundles (Fig. 5.1.A) to beating of eukaryotic flagella, which has been extensively studied in the bull sperm, the sea urchin sperm and the *Chlamydomonas reinhardtii* flagella (Fig. 5.1.B, here the bull sperm). We also compare our actin bundles to another *in vitro* system, composed of microtubules and kinesins, which has been previously shown to exhibit flagellar-like beating (Dogic group, UCSB, (Sanchez et al., 2011), see Chapter 1, Fig. 1.7). To this end, we analyzed movies of microtubule bundles available as in the supplementary material of the corresponding article (Fig. 5.1.C). Finally, we looked at a simpler *in vitro* system, consisting in a single actin filament gliding on myosin-coated surface. Defects on the surface (either due to defective myosin heads or due to myosin vacancy on the surface) can disrupt the uniform gliding of the filaments (Bourdieu et al., 1995). Defects extending over a segment were shown to clamp the pointed end of the actin filament. As a result of the distributed pushing force applied by the myosin heads, the filament undergoes a buckling instability in the plane of the surface and wave-like beating emerges. In some motility assays with myosin II, Mathieu Richard, during his PhD in the group, observed such flagellar-like undulation of single actin filaments. We analyzed two of his movies (Fig. 5.1.D).

Despite the vast differences between these four systems, they all display very similar "heart shape" beating patterns. Actin and microtubule bundles, as well as single actin filament have in common that one extremity is anchored and that they perform movement in a medium containing depleting agent : methylcellulose for actin bundles and filaments, polyethylene glycol for microtubules. For bull spermatozoan, although the amplitude of tangent angle oscillations is nearly independent on the curvilinear abscissa at low viscosity of the bath (Chapter 1, Fig. 1.11), a "heart shape" beating pattern is observed when either the sperm's head is clamped (Chapter 1, Fig. 1.13. B) or when the bath viscosity is high ($\eta = 3600$ mPa.s, Chapter 1, Fig. 1.16). In the case of our actin bundles, the filaments are both anchored to the nucleation surface and immersed in a very viscous medium ($\eta = 800$ mPa.s.), which naturally impedes motion at the bundle's base. These observations suggest that anchoring of filaments and viscosity play a key role in the formation of the "heart shape" beating patterns, irrespective of the molecular nature of the constituents of the system.

Concerning the beating properties, in these four systems, all the color plots indicate that the tangent angle displays periodic oscillations (horizontal reading), and that a bending wave travels from base to tip, with a growing amplitude.

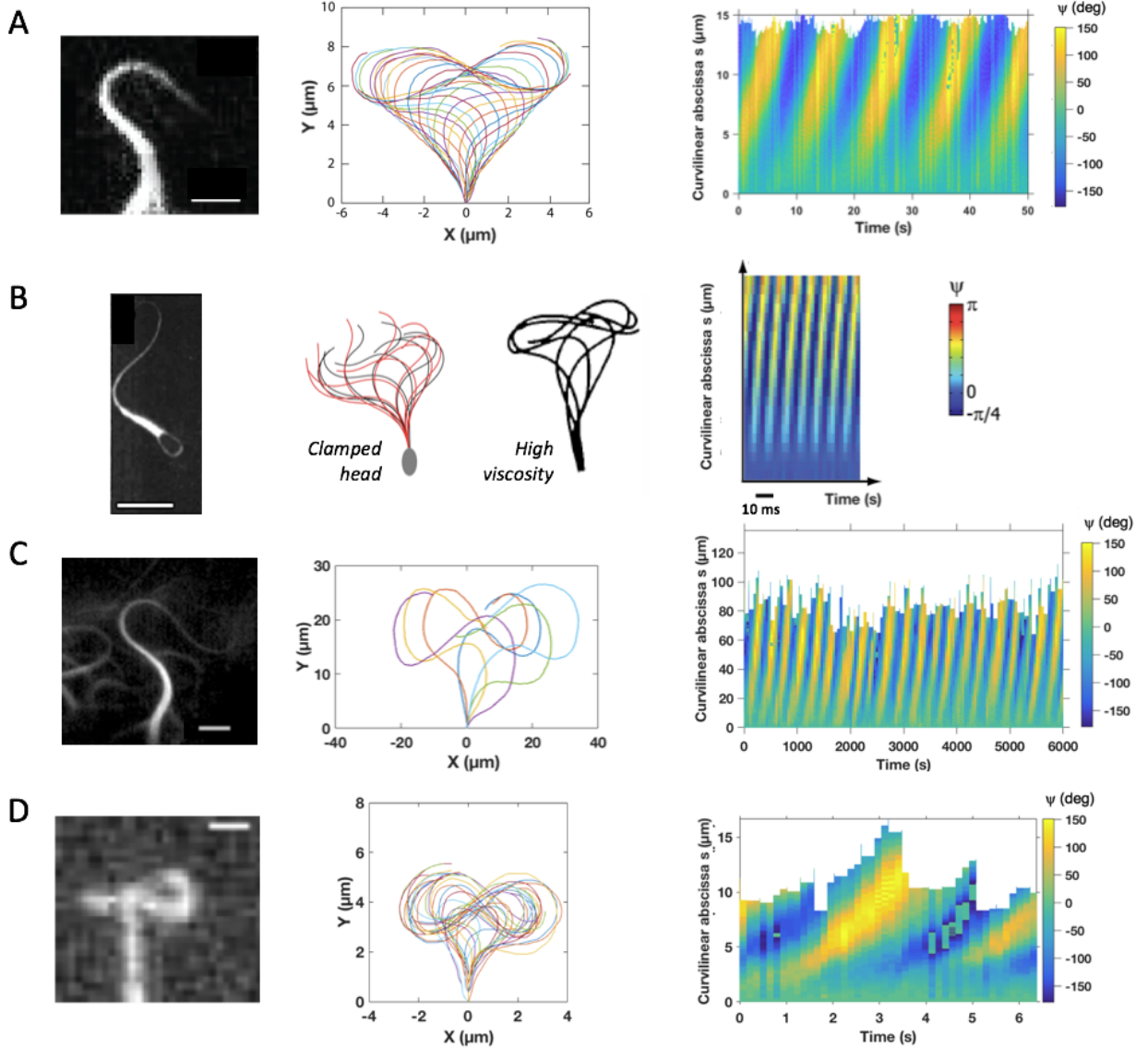


Figure 5.1: Comparison of various oscillating systems. **A:** Beating actin bundle. Fluorescence image. Scale bar : $3 \mu\text{m}$ (*left*) ; Beating pattern (*middle*) ; Color plot of the tangent angle $\psi(s, t)$ as a function of the curvilinear abscissa s and time t (*right*). **B:** Bull spermatozoan. Fluorescence image. Scale bar : $20 \mu\text{m}$ (*left*) ; Beating pattern when the head is clamped and at high viscosity $\eta = 3600 \text{ mPa}\cdot\text{s}$ (*middle*) ; Color plot of the tangent angle $\psi(s, t)$ as a function of the curvilinear abscissa s and time t (*right*). Figures from (Friedrich et al., 2010; Gray, 1957; Ma et al., 2014). **C:** Beating microtubule bundle. Fluorescence image. Scale bar : $10 \mu\text{m}$ (*left*) ; Beating pattern (*middle*) ; Color plot of the tangent angle $\psi(s, t)$ as a function of the curvilinear abscissa s and time t (*right*). Data from Supporting Materials from (Sanchez et al., 2011). **D:** Single actin filament clamped at its pointed end. Fluorescence image. Scale bar : $2 \mu\text{m}$ (*left*) ; Beating pattern (*middle*) ; Color plot of the tangent angle $\psi(s, t)$ as a function of the curvilinear abscissa s and time t (*right*).

Regarding kinetics, the bull sperm, the sea urchin sperm and the *Chlamydomonas reinhardtii* flagella display much faster beating than observed with actin bundles; their oscillation periods are up to 3 orders of magnitude lower: 14 ms for *Chlamydomonas*, 30 ms for sea urchin sperm, 166 ms for bull sperm (Chapter 1, Table 1.1). One reason could be that our actin bundles perform beating in a more viscous medium than biological flagella. It has been shown for the bull sperm that the beating frequency decreases as $1/\sqrt{\eta}$ (Chapter 1, Fig. 1.15), at 800 mPa.s (the macroscopic viscosity in our assay) the beating period of bull sperm is 1 s. This is still one order magnitude larger than the frequencies measured with our myosin-based actin bundles. Another explanation could come from the spatial availability of motors : in an axoneme, which is a highly ordered structure (Chapter 1, Fig. 1.9), all motors are very regularly and densely positioned along microtubule doublets, with a periodicity of 24 nm for outer arm dynein and 96 nm for inner arm dynein (Ishikawa, 2018). In contrast, our system is disordered and myosins have to be recruited from the bulk. If we consider that myosin motors are uniformly distributed, their spacing would be around 150 nm at a concentration of 500 nM (the highest concentration we used) and around 320 nm at 50 nM (the lowest concentration we used), which is significantly larger than motor spacing in flagella. It may then take some time for myosins to be recruited by actin. For microtubule bundles of comparable length as that of our actin bundles (*i.e.* $L < 25 \mu\text{m}$), the beating periods vary in the range of $T = 50 - 200 \text{ s}$, which are comparable to those measured with myosin V actin bundles. Thus, the kinetics of these active microtubule bundles is also considerably slower than the kinetics of eukaryotic flagella. The speed of traveling bending waves $v = 0.3 \mu\text{m/s}$, for microtubule bundles (Fig. 5.1.C, *right*) is 2.7 times lower than the natural speed expected for kinesin, as measured in gliding assays, $v = 0.8 \mu\text{m/s}$ (Howard, 2001). In the case of single actin filaments (Fig. 5.1.D, *right*), the wave speed obtained is similar to those of the fastest speed myosin II-driven actin bundles, which were around $4 \mu\text{m/s}$.

Thus, wave-like beating of cytoskeletal filaments can be observed in a large variety of systems: from the very complex eukaryotic flagella which contain hundreds of proteins and show a highly ordered structure, to bundles of actin or microtubule filaments *in vitro*, to the simplest system of all, a single actin filament attached to a surface. Again, oscillations emerge when the filaments are anchored at one end : the head of the cell for eukaryotic flagella, an air bubble for microtubule bundles in the *in vitro* system developed in Dogic's group, a micropatterned surface for actin bundles in our assay, and a surface defect for actin filament in *in vitro* gliding assays.

5.2 3D beating of actin bundles

When we computed the power spectra of both integrated myosin V and actin fluorescence signals along the length of a beating bundle, we noticed a Fourier mode at the frequency of the actin bending oscillations (Chapter 4, Fig. 4.23.A and B). This observation can be interpreted as a sign of the partial confinement of a three-dimensional beating movement in the observation plane, resulting in a motion periodically slightly in and out of this plane and a blinking of the fluorescence signal (both in the actin and the myosin channels) at the frequency of actin bending oscillations. A "frustrated" three-dimensional movement of actin bundles may be caused by methylcellulose, which pushes the bundles against the substrate, and thus confines the beating movement in two dimensions. This explanation is consistent with what is known for eukaryotic flagella, which perform "unconstrained" three-dimensional motion along a helical path as they swim to find eggs (Corkidi et al., 2008), but display two-dimensional trajectories when they swim near a flat surface at the glass/water interface of shallow observation chambers (Fig. 5.2), as observed in most studies of sperm motility (Chapter 1, Section 1.2, (Friedrich et al., 2010; Gray, 1955, 1957; Riedel-Kruse et al., 2007; Rikmenspoel, 1984)).

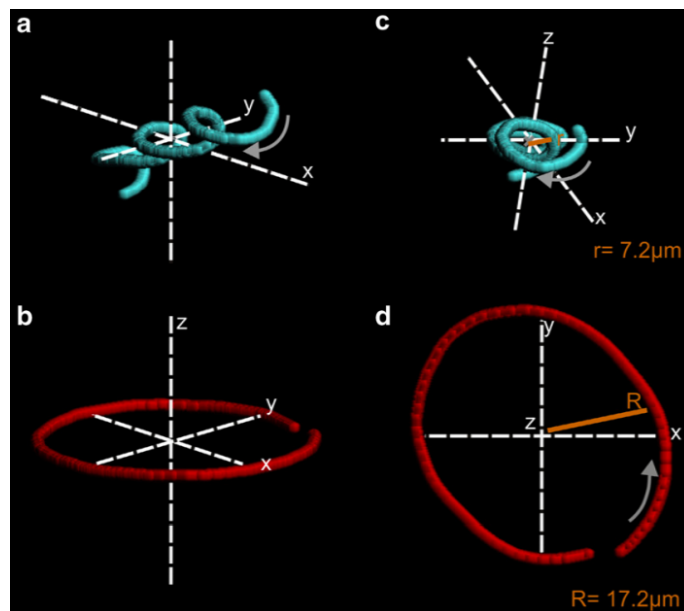


Figure 5.2: 3D and 2D motions of swimming sea urchin spermatozoa. Trajectory of tracked sea urchin spermatozoa swimming during 1 s. (a) Free swimmer, (b) 2D surface-confined, (c) Free swimmer upper view (from helical axis), (d) 2D confined upper view to compare diameters. Figure from (Corkidi et al., 2008)

Moreover, we had experimental evidences confirming that oscillations of our actin bundles could be actually three-dimensional. In the presented example with myosin V,

we indeed observed actin bundles that grow in a direction perpendicular to the micropatterned surface of actin nucleation (Fig. 5.3.A).

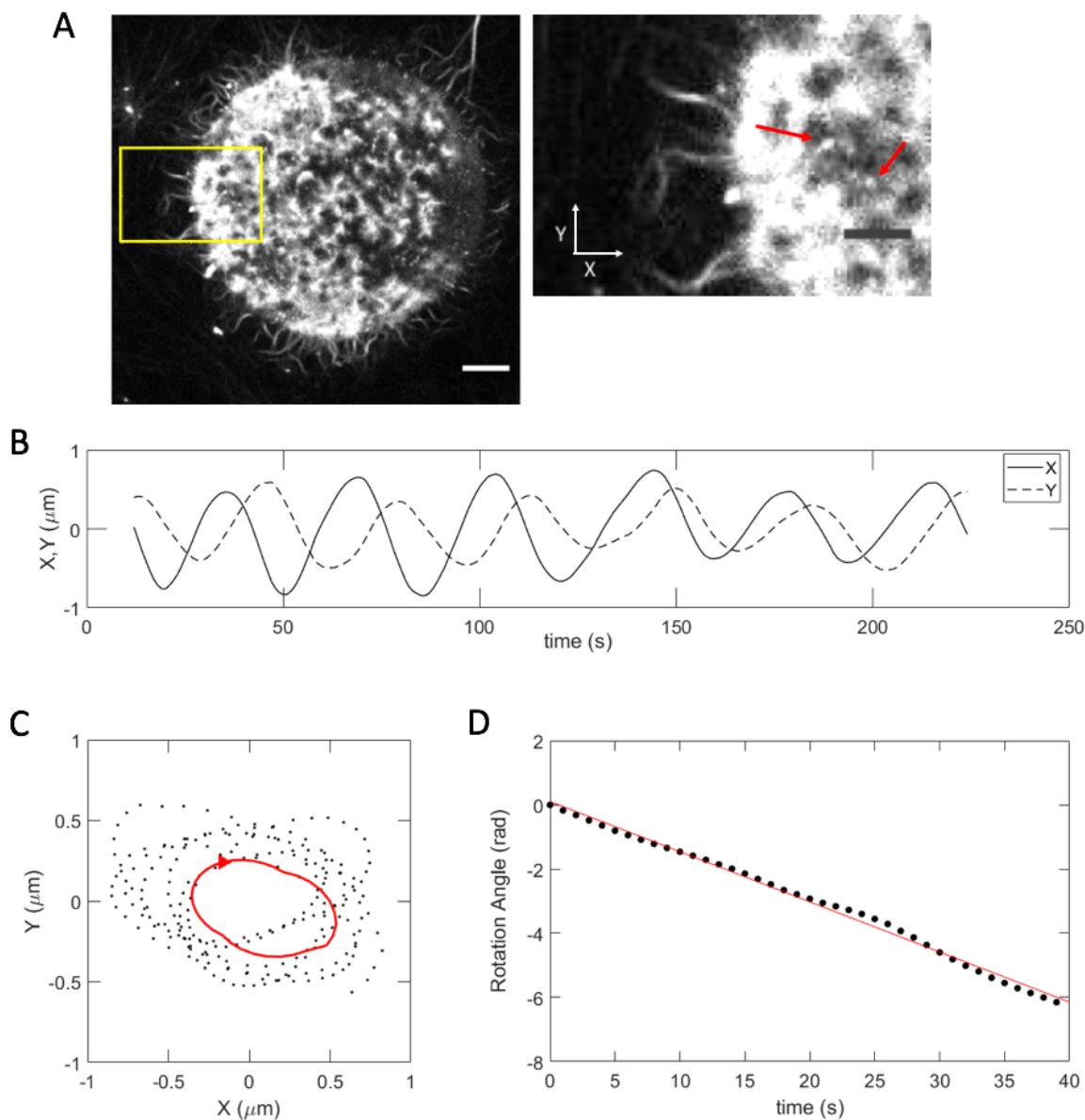


Figure 5.3: 3D-movement of actin bundles. **A:** Fluorescence image of actin bundles obtained with a 60 μm -diameter nucleation disk (*right*), displaying bundles perpendicular to the surface. Scale bar: 10 μm . Zoom of the yellow square on the fluorescence image; red arrows indicate the perpendicular bundles (*right*). Scale bar: 5 μm . **B:** Time series of the X and Y displacements of one of the perpendicular actin bundle. Both X and Y displacements exhibit periodic oscillations of 34 s period. **C:** The corresponding trajectory in the XY plane draws an ellipsoid with clockwise rotation. The red line is obtained from a moving average of the data points. **D:** Rotation angle of the rotary movement over one period of beating. The slope of the linear fit in red gives a pulsation of $0.16 \text{ rad}\cdot\text{s}^{-1}$. The movements are here driven by myosin V motors that were present at a concentration of 250 nM in bulk.

Remarkably, these beating bundles all displayed clockwise rotatory movement along ellipses, thus a three-dimensional movement, with a period $T^{3D} = 31.4 \pm 10.2 \text{ s}$ ($n =$

5). They are within the same range of period than for the actin bundles beating in the fluorescence image plane. Figure 5.3.B, C, D shows the characteristics of this rotary movement for a given bundle in the sample. This observation reinforces the interpretation that the 2D movement that we observed were actually frustrated 3D movement. The selection of one direction of rotation observed here is probably related to the chirality of actin filaments, due to their helical structure.

5.3 How does myosin sense the shape of actin bundles?

Our work has demonstrated the existence of a strong coupling between the generation of myosin V concentration waves and the beating of the actin bundle (Chapter 4, Fig. 4.24). This result suggests that myosin attachment to actin does depend on the shape of the filaments. To our knowledge, coupling between actin-binding affinity and actin shape has never been reported in the case of myosin, but has been already demonstrated with the Arp2/3 complex, which selects the convex face of a curved actin filament (Fig. 5.4), (Risca et al., 2012).

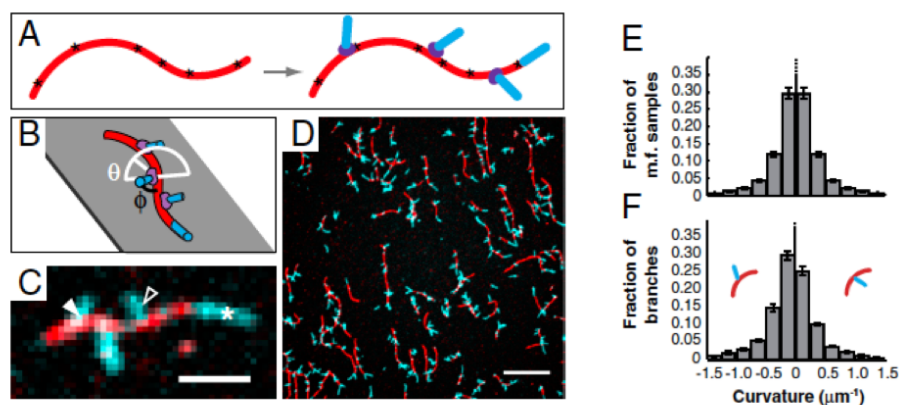


Figure 5.4: The Arp 2/3 complex for actin affinity depends on curvature of actin filament Actin branching is promoted by the Arp2/3 complex on the convex face of the filament. Red refers to mother filaments and blue to actin branches. **A:** Schematic representation of a mother filament immobilized by biotin-streptavidin (stars) before (left) and after (right) nucleation of branches. **B:** Actin branches grow at a branch angle $\phi = 70$ deg from the mother filament (black line) with an azimuthal angle θ from 0 to 180 deg (white line). **C:** Fluorescent image of actin growth with a mother filament and branches. Scale bar : 10 μm . **D:** Sample field of view of actin filaments growing from (curved) mother filaments and forming branches. Scale bar : 10 μm . **E:** Mother filament curvature distribution, centered around zero-curvature. **F:** The distribution of mother filament curvature at branch points shows that the branches are more likely to form on the convex face of the mother filaments. Figure adapted from (Risca et al., 2012)

If actin binding proteins can sense the curvature of an actin filament, it suggests that actin filaments could come in different "flavors", to quote (Jégou and Romet-Lemonne, 2016), here that the actin filament is not the same depending on whether it is curved positive or negative.

On the other hand, it has been proposed that proteins attaching to actin may affect actin conformation according to two scenarios: either they select a conformation and stabilize it or they deform the filament (Galkin et al., 2001; Kozuka et al., 2006).

These working hypotheses rely on the demonstrated plasticity of F-actin, whose conformation and degree of twist can fluctuate between a few discrete states (Galkin et al., 2010; Kozuka et al., 2006). Could there be a selectivity of actin binding proteins to one discrete state of the filament? Notably, in the case of myosin, it has been shown with FRET that binding of myosin V stabilizes preferentially the high-FRET conformational state of F-actin (Kozuka et al., 2006). This observation demonstrates that myosin V binding is coupled to actin conformation.

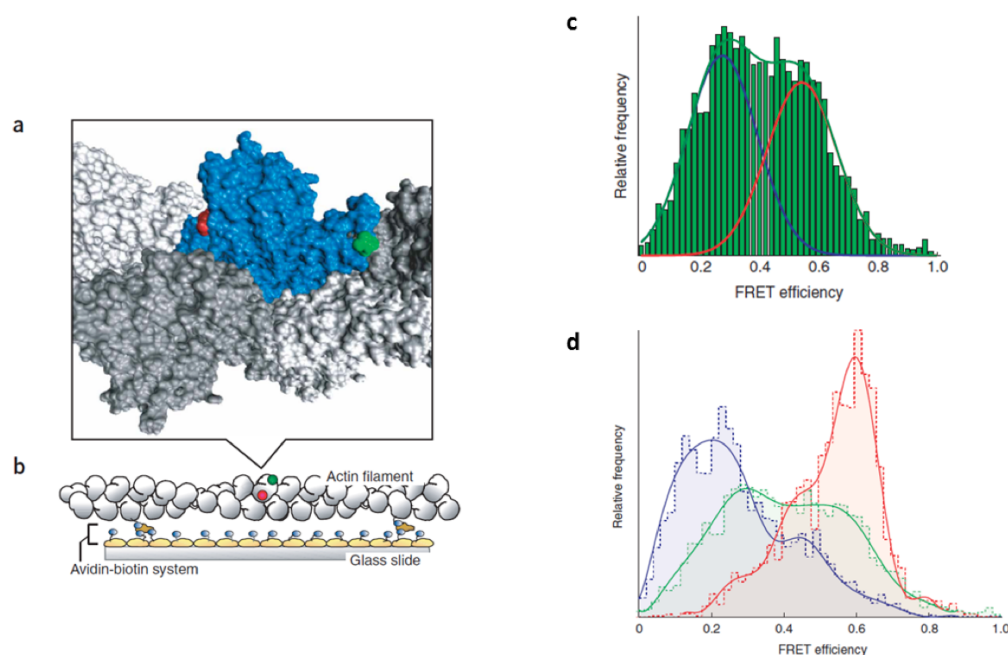


Figure 5.5: Myosin V stabilizes a conformation of F-actin. **a:** FRET labelling of an actin subunit. **b:** Layout of the single-molecule experiment. **c:** Histogram of the FRET signal for bare F-actin and fit with the sum of two gaussian distributions, corresponding to two-conformational states of the actin filament. **d:** Histogram of FRET signals after actin has been fixed by exposure to glutaraldehyde (blue), when actin interacts with myosin V (red) and for bare actin (green; same data as in c). Data from (Kozuka et al., 2006).

In addition, strong binding of myosin II on F-actin has been shown to modify the conformation of F-actin by reducing the helicity of actin by 0.74 deg, as well as elongating the filament (Tsaturyan et al., 2005). Along this line, HMM binding has been proposed

to be cooperative, again suggesting actin distortion over around 25 subunits (Miki et al., 1982; Tokuraku et al., 2009). If a myosin motors can influence the conformation of F-actin, mechanical reciprocity imposes that an external force modulating the helicity of actin also ought to modulate their binding affinity to F-actin. In other words, as strong myosin-II binding (slightly) modulates the twist and length of F-actin (Tsaturyan et al., 2005), changing the actin twist through mechanical force ought also to modulate the affinity of myosin for actin, as observed indirectly by stretching actin filaments (Uyeda et al., 2011).

These results suggest that forces applied to actin filament can change its conformation, which will modulate the affinity of actin-binding proteins for the filament. In this case, actin conformation must be tuned by piconewton forces, which is the order of magnitude of forces applied by proteins such as myosin (Chapter 2, Section 2.2). A single-molecule experiment showed that tension of only a few piconewton is indeed strong enough to distort the actin-filament structure, resulting in quenching in a reporter fluorophore which then acts as a "molecular strain-gauge sensor" (Shimozawa and Ishiwata, 2009).

Altogether, these observations may explain coupling between the attachment of myosin and bending along actin bundle. One can indeed propose that myosin motors that are already interacting with the actin filaments induce its bending, resulting in a change of the binding affinity of detached motors in bulk for the filament, which then promotes the recruitment of myosins at a given position of the actin bundle. Modeling studies are required to determine whether this mechanism can give rise to the generation of periodic concentration waves of myosin and actin beating.

Chapter 6

Perspectives

An interesting perspective for future development would be to use TIRF microscopy to confirm the assertion that the wave-like beating of the actin bundles can be described as three-dimensional movement and also to test whether actin bundles can interact with the surface.

In addition, to correlate the collective behavior of myosins, which drive the beating movement to what happens at the level of a single molecule of myosin V, we could perform single molecule imaging. We already implemented preliminary experiments confirming that we can observe single myosin V with single molecule imaging. This was done by performing our experimental protocol with 1 % of myosin V labeled with GFP (and 99 % unlabeled). Furthermore, to study at lower scales the structure of the actin bundles we could do super resolution imaging.

An interesting question that remains open is the coupling between the formation of tight bundles and myosin activity. In our experiments, we worked with closed experimental chamber. Once the polymerization mix was injected, it was not possible to add another component. To see if the presence of myosin from the beginning is necessary to induce the formation of bundles, an ideal experiment consists in first polymerizing the actin network and then adding homogeneously the myosins. To overcome this difficulty we used blebbistatin in some preliminary experiments. Blebbistatin is a specific and reversible inhibitor of myosin II, which can be photo-inactivated by blue light (Kovacs et al., 2004; Linsmeier et al., 2016; Sakamoto et al., 2005). Without blebbistatin, we see the formation of dense and oscillating bundles (Fig. 6.1.A), whereas in the presence of blebbistatin, myosin motors are inactive and act as passive crosslinkers within the actin network. In this case (with blebbistatin), we see that the actin network is also bundled, but the bundles are less dense, straighter and remain static (Fig. 6.1.B). This observation reveals that the formation of tight actin bundles is linked to myosin activity. It has been shown

that the myosin II-blebbistatin complex adopts a structural state that resembles the starting point of the power stroke (Takács et al., 2010), hence corresponding to a larger spacing between filaments than when myosin can exert the power stroke. Notably, we have also observed that actin bundles are tighter in the presence of active myosin II (without blebbistatin) than in the presence of myosin V (Chapter 4, Figure 4.4). This makes sense because the lever arm is 5 times longer with myosin V than with myosin II (Spudich and Sivaramakrishnan, 2010). In addition, when blebbistatin was photo-inactivated by blue light within the same sample, we observed that the actin bundles became tighter, started curving and exhibiting beating movement (Fig. 6.1.C).

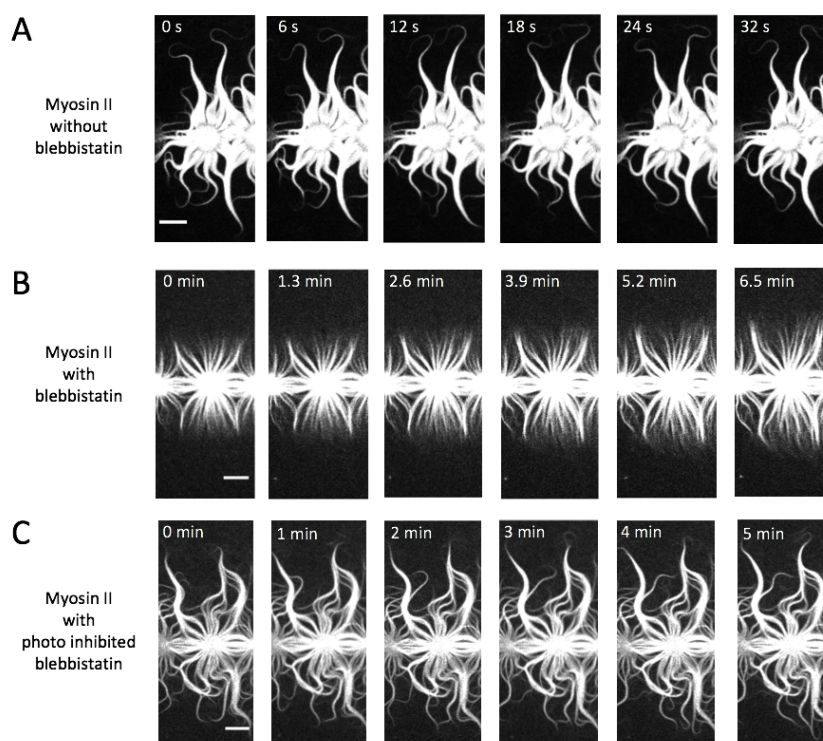


Figure 6.1: Myosin II activity modulated by blebbistatin. Fluorescence images of actin network with myosin II at a concentration of 500 nM. **A:** In the absence of blebbistatin, actin bundles perform beating movement of 20 - 35 s period (sampling time: 6s). **B:** In the presence of blebbistatin at a concentration of 200 μ M, which inactivates myosins. **C:** Photoinactivation by blue light (flash every 10s) of blebbistatin in the region shown in panel B drives bundles formation and oscillation period of 300 s (*i.e.* one order of magnitude slower than in panel A). Scale bars: 10 μ m

It seems that the emergence of movement within the actin network triggers the coalescence of neighboring bundles and hence promotes the formation of tighter bundles. Besides, the beating movement is ten times slower with photo-inactivated blebbistatin than in the absence of blebbistatin (Fig. 6.1.A), $T^{bleb\ inactive} = 300$ s and $T^{ctl} = 30$ s, respectively. It shows that the dynamics of our system is slowed down in the presence

of blebbistatin and might thus potentially be tuned by the frequency of UV-light pulses applied to photo-inhibit blebbistatin and release active myosin II.

Experiments with blebbistatin could help to investigate how myosin activity tunes the beating properties. In our experiments, we varied the myosin concentration to study its effect on beating dynamics (Chapter 4, Section 4.2.4) but either we saw no beating or we saw beating that depended only weakly on the concentration; we observed a sharp transition in the behavior of our system. Using blebbistatin would enable to explore transitional regime of the dynamics and self-organization of actin networks driven by myosins. Moreover, applying blue-light pulses to photo-inactivate blebbistatin and to release active myosin II motors could be used to better control the spatial activity of the system (by photo-inactivating defined region of the sample) or temporal activity (by exploring a range of frequency pulse of blue light to see if self-organization and dynamics of the wave-like beating would be slowed down or accelerated).

In addition, we observed during my PhD a new phenomenon of remodeling-destruction of actin networks that we did not have time to explore. When we worked at very high concentrations of myosin II ($[myosin\ II] > 750\ nM$), we observed a deformation and contraction of the actin network starting from 20 min to 50 min after the injection of the polymerization mix, whereas it was not the case when we worked below 500 nM. This myosin II-induced destruction of the actin network happened abruptly, after a period during which "normal" beating bundles were observed. This phenomenon was only observed with myosin II but never with myosin V. The direct visualization of actin filaments disclosed three orchestrated phases of deformation and contraction of the actin network. The same sequence of events occurred with eight-branch star and a disk patterned substrates (Fig. 6.2.A and B, respectively). During this reorganization, the actin network mainly consists of parallel bundles of actin filaments. First, the actin network is reorganized into beating actin bundles, as described previously (Fig. 6.2; $t = 50\ min$ for A, and $t = 55\ min$ for B). However, this reorganization of the actin network does not remain stable, in contrast to previous experiments at lower myosin II concentrations. At $t = 30 - 50\ min$, the parallel actin bundles start shrinking *i.e.* they get more curved and more snake-like and they come nearer to the nucleation-patterned surface until they completely surround the nucleation pattern (Fig. 6.2; $t = 50\ to\ 60\ min$ for A, and $t = 55\ to\ 63\ min$ for B). Finally, the actin bundles form a constriction ring, contracting the existing nucleation pattern. As the shrinking of the actin bundles triggers the entanglement of bundles, bundles of opposite polarity interact and hence the constriction ring pulls up filaments out of the pattern. After destruction, a new polymerization process takes place on the contracted pattern. For example, in the case of the star with 8 branches, the contraction of

the pattern gives birth to an actin octogone for the new polymerization (Fig. 6.2. A; $t = 60$ to 63 min), whereas a nucleation disk yields a concentrated actin pool at the center (Fig. 6.2.B; $t = 66$ to 67 min).

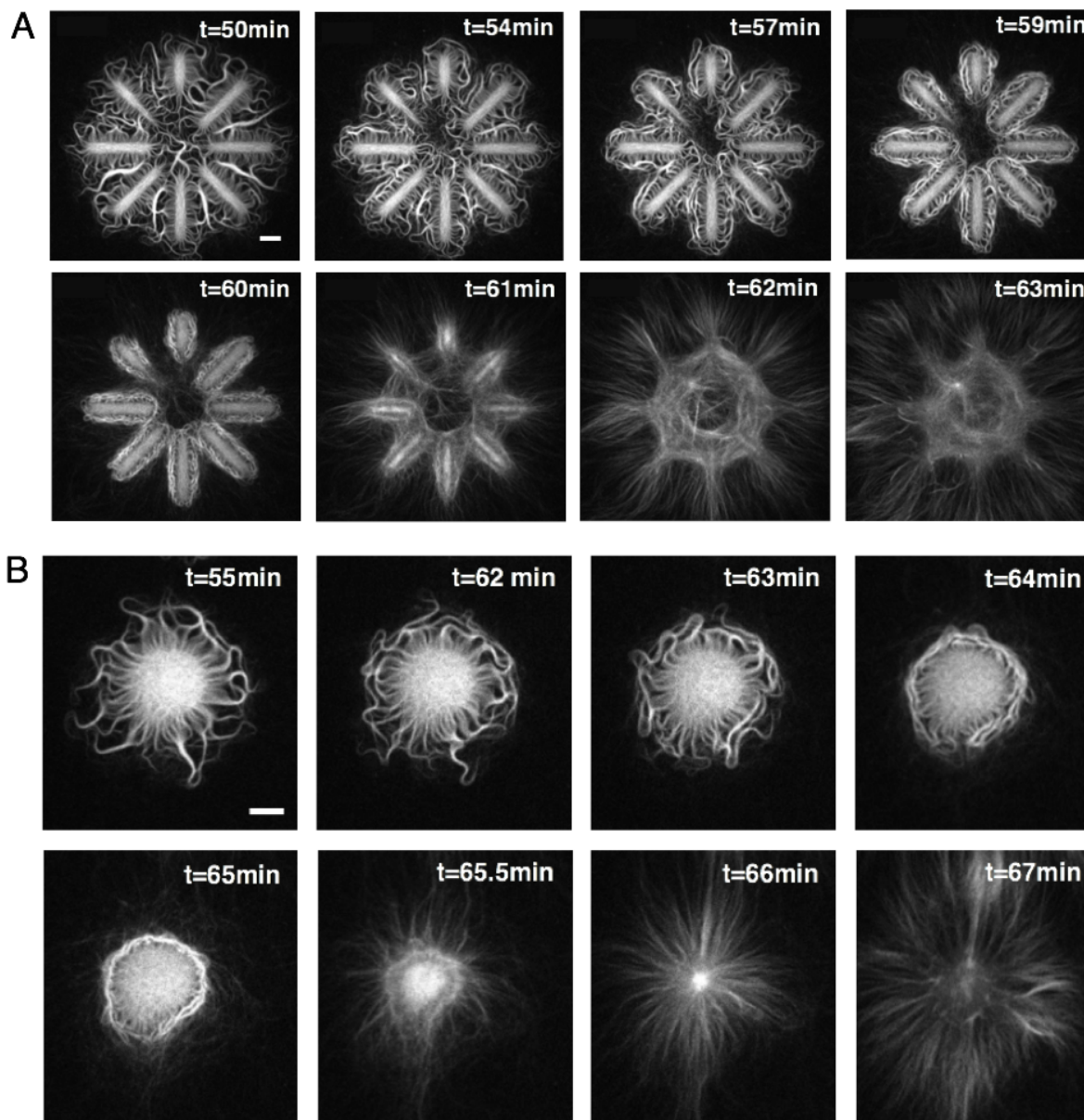


Figure 6.2: Orchestrated collapse of the actin network at high concentrations of myosin II. At 750 nM of myosin II, we observe a collapse of the actin network in three steps, with eight-branch star (A) and disk (B), as actin nucleation pattern. First, the actin network is organized into beating actin bundles, which start shrinking after a certain time ($t = 50 - 60$ min for A, and $t = 55 - 63$ min for B) *i.e.* they get more curved and more snake-like and they come nearer to the nucleation-patterned surface until they surround the nucleation pattern. Then, the actin network is destroyed as the bundles after surrounding the nucleation pattern form a constriction ring, which contracts. Finally, new polymerization takes place on the contracted pattern: in the case of the star with 8 branches, once contracted it gives an octogone for the new polymerization, and thus a radial network ($t = 60$ to 63 min) ; in the case of a disk, the contraction results in a disk of smaller diameter ($t = 66$ to 67 min). Scale bars: 10 μm .

Reorganization of *in vitro* actin networks of controlled geometry induced by myosin motors was previously described with myosin VI and full myosin II (Reymann et al., 2012). In this study, it was shown that myosin VI and myosin II selectively contracted and disassembled anti-parallel actin network structures, while keeping parallel actin bundles unaffected. With parallel networks, myosin VI and myosin II induced disassembly of the network but did not induced contraction of the network. This result differs from our observations, as we do observe deformation and contraction of parallel networks, from the unique arrangement of actin bundles into a contractile ring surrounding the patterns; contraction results from the entanglement of antiparallel bundles. Moreover, in the published study, the disassembly of actin network disconnected actin filaments from the nucleation surface but did not sever them. Thus, repolymerization was not observed in this case.

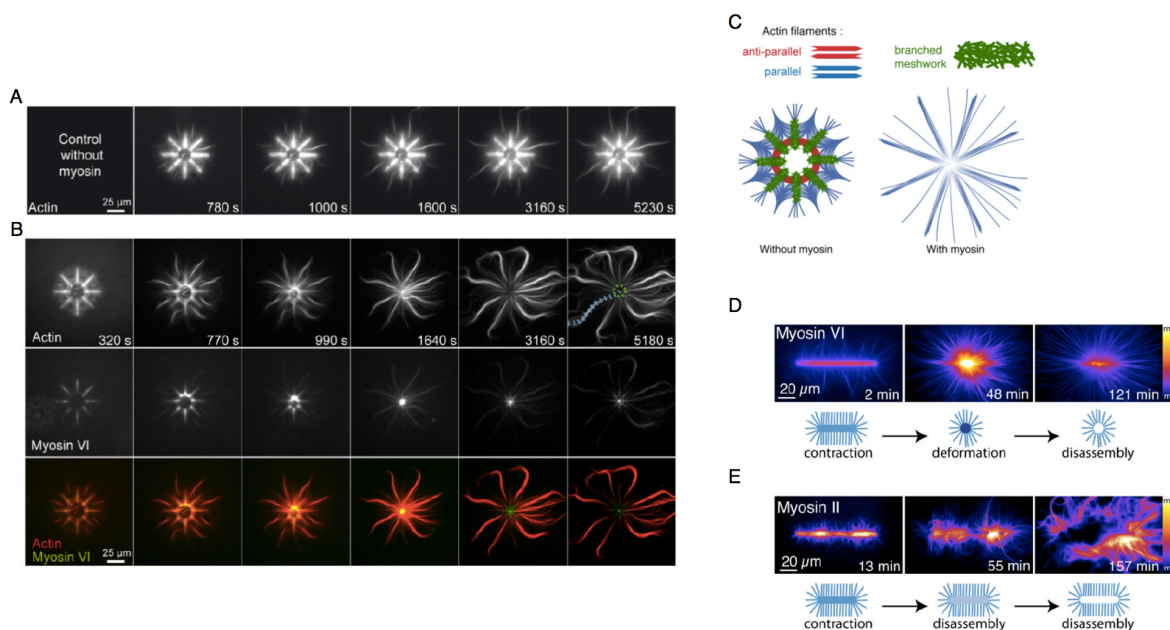


Figure 6.3: Actin network collapse induced by myosin VI and myosin II. **A:** Time-series of network assembly on an eight-branch actin nucleating radial array. **B:** Time-series of myosin VI-induced architecture selective contraction and disassembly (actin, myosin and an overlay are shown). **C:** Schematic representation of the final architecture on an eight-branch actin nucleating radial array in absence and in presence of myosins in solution. **D:** Time-series of myosin VI-induced network contraction on a bar-shaped micropattern. Actin filaments were visualized with fluorescent monomers. "Fire" look-up table color-coding reveals variations in actin network densities, quantified with a linescan along the bar at different time points. Actin density peaks because of network deformation after 48 minutes then falls off because of network disassembly. **E:** Same as (D) with muscle myosin II-induced contraction. Figure from (Reymann et al., 2012)

These preliminary results highlight a new phenomenon emanating from our minimal *in vitro* system: here, we observe a transition from parallel actin bundles to a constriction

ring of antiparallel bundles driven by myosin II. It would be interesting to investigate this new form of actin network disassembly to understand how myosin motors switch from driving beating movement to orchestrating destruction of the actin network.

We restricted the scope of our work to single actin bundles, but studying the collective effect among neighboring actin bundles is an interesting perspective. We observed that oscillations between neighboring actin bundles could synchronize in phase or out of phase during their beating and even switch between in-phase and out-of-phase synchronization after several period of beating. In biological systems, synchronization of cilia covers a large panel of vital functions, for example the synchronization of cilia protects bronchi from infections in the lung. It has been proposed that the highly coordinated behavior of ciliary fields arise from hydrodynamic behavior and steric coupling between neighboring cilia, so that they are capable of fluid transport. We could add beads within our system to see if an ensemble of several bundles are capable of transporting passive materials, similarly to mucus by ciliated epithelia.

A farther perpespective would be to create active materials capable of swimming motion, by nucleating actin polymerization on beads instead of on a flat and fixed surface.

Finally, our study of beating properties of actin bundles and the observation that myosin affinity could be governed by actin curvature could bring ingredients for theory and models of flagellar beating and maybe identify what mechanism explains the oscillation of actin bundles driven by assemblies of motors.

Appendices

Appendix A

Experimental protocol

A.1 Proteins preparation

A.1.1 G actin solution

A stock solution of 60 μM actin containing 10 % fluorescently labeled actin (Actin AlexaFluorTM488 or Actin AlexaFluorTM568) is prepared in G buffer. In order to allow depolymerization of filamentous actin into its globular form, this actin stock solution is stored on ice at least for 2 days at 4 °C and then can be used until two weeks.

A.1.2 Minimal set of proteins which ensures actin polymerization

The day of experiments :

- 10 % labeled actin stock solution and profilin are diluted in fresh G Buffer
- pWA and the Arp2/3 Complex are diluted in fresh 1X KMEI Buffer.
- HMM myosins are diluted in freshly prepared myosin buffer, whose composition is described in the table below.

Table A.1: Myosin Buffer- Shelf life one day on ice

Compound	Concentration	Stock concentration	Volume
10X KEEI	1X	-	50 μL
Na ₂ ATP	5 mM	0.1 M	25 μL
MgCl ₂	5 mM	100 mM	2.5 μL
DTT	2 mM	1 M	1 μL
H ₂ O	-	-	421.5 μL

Table A.2: MgATP Buffer

Compound	Concentration	Stock concentration	Volume
Na ₂ ATP	50 mM	0.1 M	10 μ L
MgCl ₂	10 mM	100 mM	1 μ L
H ₂ O	-	-	9 μ L

Table A.3: Fluorescent Buffer

Compound	Concentration	Stock concentration	Volume
10X KMEI	1X	-	25 μ L
G Buffer	-	-	17 μ L
Glucose	1.8 mM	55 mM	8 μ L
Glucose oxidase	14 units/mL	875 units/mL	4 μ L
Catalase	112 units/mL	3500 units/mL	8 μ L
Na ₂ ATP	2mM	0.1 M	5 μ L
MgCl ₂	5 mM	100 mM	2.5 μ L
DTT	168 mM	1 M	42 μ L
Methyl cellulose	1.1 %	2 %	141 μ L

Preparation remark

The methyl cellulose is added at the end. To easily pipet methyl cellulose, a 200 μ L tip is cut with a chamfered edge and is wetted beforehand with G-Buffer and slowly pipet and inject in the fluorescent buffer.

Table A.4: Polymerization mix

Compound	Final Concentration	Prepared concentration	Volume
10X KMEI	1X	10 X	1.5 μ L
G Buffer	-	-	1 μ L
MgATP Buffer	1X	15 X	1 μ L
BSA 3 %	0.2 %	3 %	1 μ L
Profilin	8 μ M	80 μ M	1.5 μ L
Arp2/3 Complex	80 nM	1.2 μ M	1 μ L
Fluorescent Buffer	1 X	3X	5 μ L
HMM Myosin	1X	10X	1.5 μ L
Actin	2 μ M	2 μ M	1.5 μ L

Appendix B

References of purified proteins

B.1 Actin and actin-related proteins

B.1.1 Preparation of the proteins

Unlabeled Actin

Unlabeled actin is resuspended from powder at a concentration around 200 μM in a buffer containing 5 mM Tris (pH = 7.4), 0.2 mM CaCl_2 and 0.2 mM ATP.

Arp2/3 Complex

A powder of the porcine Arp2/3 complex was resuspended at a concentration of 5 $\mu\text{g}/\mu\text{L}$ in a buffer containing 20 mM Tris (pH 7.5), 25 mM KCl, 1 mM MgCl_2 , 0.5 mM EDTA, 0.1 mM ATP, 1.0 % (v/v) dextran, and 5 % (v/v) sucrose.

Profilin and pWA

Profilin and pWA were purified in the lab by John Manzi, as previously described (Carvalho et al. (2013)).

B.1.2 Characteristics and storage conditions of the proteins

The table below indicates the references and the conditions of storage of the actin and actin related proteins.

Table B.1: Actin and actin related proteins

Compound	Molecular Weight (kDa)	Furnisher - Product reference	Storage Temperature
Actin	43	Cytoskeleton - 2x1mg (AKL99-B)	-80 °C
Actin AlexaFluor™488	43	Life Technology - 200 μg (A12373)	-80 °C
Actin AlexaFluor™568	43	Life Technology - 200 μg (A12374)	-80 °C
Arp2/3 Complex	224	Cytoskeleton - 2x50 μg (RP01P-A)	-80 °C
Profilin	14	John Manzi - BMBC Platform	4 °C
pWA	54.4	John Manzi - BMBC Platform	-80 °C

B.2 HMM Myosins

Myosins were kindly provided by our collaborators.

B.2.1 Methods of purification of the studied HMM myosins

- **HMM myosin II** : Double-headed heavy mero-myosin II (referred to as HMM myosin II) was purified from rabbit pectoral muscle according to (Kron et al. (1991); Okamoto and Sekine (1985); Warrick et al. (1993)).
- **HMM myosin V** : Recombinant double-headed heavy-mero myosin V (HMM myosin V) was purified from insect Sf9 cells as described previously (Olivares et al. (2006)).
- **GFP-HMM myosin V** : Recombinant double-headed heavy-mero myosin V with a GFP tag (GFP-HMM myosin V) was expressed and purified as described before (Jeffrey R. Moore et al., 2001).

B.2.2 Characteristics and storage of the studied HMM myosins

The table B.2 below describes the properties of the HMM myosins used for the experiments

Table B.2: HMM myosin

Compound	Molecular Weight per double head (kDa)	Lab	Storage Temperature
HMM myosin II	350	M. Rief - TUM (Germany)	-80 °C
HMM myosin V	477.4	E. De La Cruz - Yale (USA)	-20 °C
GFP-HMM myosin V	477.4	J. Sellers - NIH (USA)	-196 °C

Appendix C

References of chemical products

C.1 References and storage

The table below indicates the references of the chemicals used for experiments and their conditions of storage.

Table C.1: Chemical products

Compound	Molecular Weight (g/mol)	Furnisher	Reference	Storage Temperature
Blebbistatin (-)	292.33	Calbiochem	203391-1	-20°C
BSA	66,000	Sigma	A3059-10G	4°C
CaCl ₂ ·(H ₂ O) ₆	219.08	Sigma	442909	20°C
Catalase	250,000	Sigma	C1345	-20°C
DTT	154.25	Euromedex	EU0006B	4°C
EDTA	292.24	Euromedex	1310-B	20°C
EGTA	380.35	Sigma	E4378	20°C
Glucose	180.16	Rectapur	24378.294	20°C
Glucose oxidase	160,000	Sigma	G7141	-20°C
Imidazol	68.08	Sigma	I0125	20°C
KCl	74.55	Sigma	P5404	20°C
Methyl cellulose	88,000	Sigma	M0512	20°C
MgCl ₂	203.33	Sigma	M2670	20°C
Na ₂ ATP	551.14	Sigma	A6419	- 20°C
PLL-g-PEG	22,000	JenKem	PLL20K-G35-PEG2K	- 20°C
Tris	121.14	Sigma	T3253	20°C

C.2 Preparation of Methyl cellulose

The protocol used to prepare 2% methyl cellulose is the first mentioned in Sigma datasheet of the product. A solution of 50 mL is prepared every 6 months and stored at 4 °C. 15 mL of water is heated at 80 °C then 1 g of methyl cellulose is added to the hot water with agitation. The mixture is agitated until the

particles are dispersed. Then for complete solubilization, 35 mL of cold water are added upon agitation in the cold room for 1 h.

C.3 Preparation of PLL-g-PEG solution for coverslip passivation

A HEPES solution of concentration of 10 mM is prepared from powder and its pH is equilibrated to 7.4 using NaOH solution. The solution is filtered upon 0.22 μm mesh size filter and aliquoted and stored at -20 °C. pLL-PEG is dissolved at a concentration of 1mg/mL in 10 mM HEPES solution. This solution is filtered upon 0.22 μm filter mesh size and aliquoted and stored at -20 °C. The day before or the day of the experiments, an aliquot of PLL-g-PEG and an aliquot of 10 mM HEPES solution are thawed and PLL-g-PEG is diluted 10 times in HEPES solution, to achieve a concentration of 0.1 mg/mL of PLL-g-PEG. The PLL-g-PEG solution is then stored at 4 °C and used within few days.

C.4 Preparation of aliquots from chemical products

All the solutions are filtered after preparation upon a 0.22 μm mesh and aliquoted.

- **ATP** : Na_2ATP is dissolved in cold water at a concentration of 100 mM, the pH is adjusted at 7.4 with NaOH solution. Aliquots are stored at -20°C.
- **Blebbistatin (-)** : The (-) enantiomer of blebbistatin is resuspended from powder in 90 % DMSO at 75 mg/ml. Aliquots are stored at -20°C.
- **BSA** : BSA is resuspended in water at 3 % in weight, the pH is adjusted at 7 with NaOH solution. Aliquots are stored at -20°C.
- **Catalase** : The catalase is dissolved at a concentration 3500 units/mL in 50 mM potassium phosphate buffer at pH=7.0. Aliquots are stored at -4°C.
- **DTT** : DTT is dissolved in water at a concentration of 1M, the pH is adjusted at 7.8 with NaOH solution. Aliquots are stored at -20°C.
- **Glucose** : The glucose in powder is resuspended in water at a concentration of 55 mM. Aliquots are stored at -20°C.
- **Glucose oxidase**: The powder is dissolved at a concentration of 875 units/ mL in 50 mM sodium acetate buffer (pH=5.1), yielding a clear solution. Aliquots are stored at -20°C.

Appendix D

Role and Composition of Buffers

D.1 Buffer for monomeric actin : G Buffer

G Buffer is used to depolymerize filamentous actin and then to maintain actin on its monomeric state. The table below gives the composition of this buffer.

Table D.1: G Buffer composition

Compound	Molecular Weight (g/mol)	Concentration
Tris	121.14	2 mM
Na ₂ ATP	551.14	0.2 mM
DTT	154.25	0.5 mM
CaCl ₂	110.98	10.1 mM

The role of Tris in the G buffer is to stabilize the pH of the solution at 7.4. The reducing agent DTT prevents aggregation of the proteins so helps to maintain the monomeric state of actin. The Ca-ATP-actin hydrolyzes ATP six times slower than Mg-ATP-Actin (Blanchoin and Pollard (2002)).

Preparation remarks The pH of the Tris solution is adjusted at 7.4 with HCl solution.

Na₂ATP is dissolved in cold water and the pH is adjusted at 7.4 with NaOH solution. The pH of the DTT solution is adjusted at 7.8 with NaOH solution.

After preparation, G buffer is filtered using a 0.22 µm mesh size filter and aliquoted and stored at -20 °C. G buffer has a shelf life of one week at 4 °C.

D.2 Buffer for actin polymerization : 1X KMEI

Initially prepared at 10 times higher concentration, 1X KMEI buffer is obtained by diluting 10 X KMEI in G Buffer and is used to favorize actin polymerization. The table below indicates the composition of 10X KMEI.

Table D.2: 10X KMEI

Compound	Molecular Weight (g/mol)	Concentration
KCl	74.55	500 mM
MgCl ₂	95.21	100 mM
EGTA	380.35	0.5 mM
Imidazol	68.08	0.1 mM

EGTA sequesters the ions Ca²⁺ to switch from Ca-ATP-actin, predominant in G Buffer to Mg-ATP-actin here thanks to MgCl₂ too in 1X KMEI. Mg-ATP hydrolyzes six times faster ATP than Ca-ATP-Actin (Blanchoin and Pollard (2002)). The role of Imidazol in the 1X KMEI buffer is to stabilize the pH of the solution at 7.8. **Preparation remarks** The pH of the Imidazol solution is adjusted at 7.8 with HCl solution. While dissolving the EGTA powder in water, the pH is adjusted at pH=8 with NaOH, because it is very acid and is soluble at pH up to 6. 1X KMEI has a shelf life of one week at room temperature.

D.3 Buffer for myosin activity : 10X KEEI

10X KEEI is diluted 10 times in Myosin Buffer. 1X KEEI is a buffer well-adapted for myosins.

Table D.3: 10X KEEI

Compound	Molecular Weight (g/mol)	Concentration
KCl	74.55	500 mM
EDTA	292.24	0.1 mM
EGTA	380.35	10 mM
Imidazol	68.08	100 mM

Preparation remarks The pH of the Imidazol solution is adjusted at 7.8 with HCl solution. While dissolving the EDTA and EGTA powders in water, the pH is adjusted at pH=8 with NaOH, because these chemicals are very acid and are soluble at pH up to 6. 1X KEEI has a shelf life of one day on ice.

Appendix E

French abstract

Battements oscillants de faisceaux d'actine dans un système minimal actomyosine

Les systèmes vivants consomment de l'énergie pour se déplacer, changer de forme, se diviser et contrôler leur propre morphologie. Pour remplir toutes ces fonctions clés, les systèmes vivants sont hautement dynamiques et font appel à de la mécanique active sur un large panel d'échelles: du transport au sein de la cellule à l'échelle moléculaire, en passant par la mitose et la motilité à l'échelle cellulaire, jusqu'à la morphogénèse des tissus, des organes et des organismes à l'échelle multicellulaire. Cette diversité dynamique est assurée par le cytosquelette. Le cytosquelette est composé de différentes familles de biopolymères capables de s'assembler et de se désassembler en permanence, donnant naissance à des réseaux de différentes architectures. Les microtubules constituent les filaments les plus rigides du cytosquelette, ils ont une structure cylindriques tandis que les filaments d'actine sont semi-flexibles. Au sein des réseaux de microtubule et d'actine, se trouvent des moteurs protéiques, qui exercent des forces pour déformer, contracter les réseaux ou assurer le transport de cargos le long des filaments, qui fournissent des voies pour leurs mouvements dirigés.

Comprendre l'étonnante complexité des processus cellulaires constitue un défi ambitieux pour les physiciens et les biologistes. Pour aborder cette question, deux approches générales ont été développées: L'approche descendante (dite *top-down*) considère la cellule dans toute sa complexité et consiste à perturber le système pour étudier le rôle de ses composants moléculaires. Le développement de la microscopie à super résolution et des nouveaux outils génétiques a permis d'étendre et d'affiner la précision de nos connaissances. La seconde approche cherche à réduire la complexité du système afin d'identifier les principes biophysiques sous-jacents des processus cellulaires. Pour atteindre ce but, de

nombreux systèmes modèles *in vitro* de moteurs et filaments purifiés ont été récemment développés. Cette approche ascendante (dite *bottom-up*) de reconstituer des fonctions biologiques avec le nombre minimal de composants est utile, car elle permet ensuite de distinguer les propriétés génériques des propriétés spécifiques dans les systèmes biologiques plus complexes.

Les filaments du cytosquelette et les moteurs moléculaires ont été extensivement étudiés au niveau de la molécule unique: nous avons une assez bonne représentation de la manière dont les filaments s'assemblent et se désassemblent, de leurs propriétés mécaniques, de leur structure, ainsi que le mécanisme des moteurs moléculaires pour générer des forces et leur mouvement (Howard, 2001). Cependant, leurs comportements collectifs demeurent encore peu compris et ne peuvent pas s'expliquer uniquement à partir des propriétés individuelles des molécules.

Le principal objectif de ma thèse était l'étude d'un système minimal *in vitro* formé d'un réseau d'actine et de moteurs de type myosines. L'usage de micropatrons surfaciques de facteurs de nucléation nous a permis de générer des réseaux d'actine de géométrie contrôlée. En particulier, nous avons fabriqué des réseaux de filaments parallèles, auxquels nous avons ajouté en solution deux types de moteurs, la myosine V et la myosine II, afin d'étudier comment les moteurs réorganisaient ce type de réseau.

Ce dispositif expérimental conduit à l'auto-organisation du réseau d'actine en faisceaux d'actine denses (Fig. E.1) qui se mettent à onduler de manière périodique, comme des flagelles de spermatozoïdes. Mon travail de thèse a fourni une description détaillée de ce spectaculaire phénomène dynamique, afin d'en extraire le mécanisme biophysique sous-jacent et d'en discuter la pertinence pour des systèmes biologiques plus complexes.

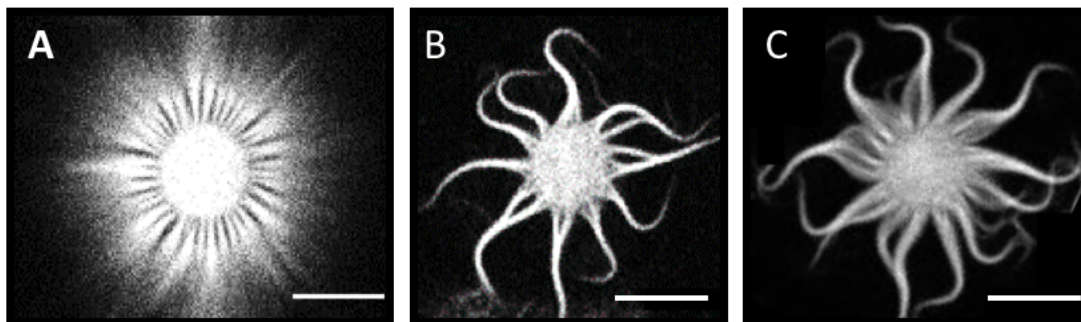


Figure E.1: Réorganisation des filaments d'actine sous l'action de myosines. L'actine est marquée avec le fluorophore AlexaFluor™ 488 (10 % de marquage, cf Chapitre 3). En l'absence de myosine (**A**), un réseau radial d'actine émerge d'un disque de 9 μm de diamètre. En présence de myosine II (**B**), ou de myosine V (**C**) le réseau d'actine s'auto-organise en faisceaux d'actine denses et bien séparés. Ces faisceaux sont courbés, ce qui montre que les myosines exercent des forces sur les faisceaux. La concentration de myosine II était ici de 500 nM, la concentration de myosine V était de 50 nM. Barre d'échelle: 10 μm .

E.1 Analyse dynamique des oscillations spontanées

Nous avons observé des oscillations spontanées aussi bien avec la myosine II qu'avec la myosine V. Ces oscillations pouvaient durer une heure. En pratique, pour caractériser le mouvement des faisceaux, nous avons enregistré des séquences de cinq à vingt périodes. La vitesse d'élongation du faisceau était suffisamment lente (0,1 à 0,5 $\mu\text{m}/\text{min}$) pour que l'on puisse considérer quasi-statistique la longueur du faisceau au cours de nos enregistrements. Nous avons aussi utiliser des enregistrements plus long (supérieurs à 30 min.) pour étudier les effets de l'allongement du faisceau sur les propriétés du battement, en gardant les autres paramètres constants.

E.1.1 Description générale des propriétés du battement dans le cas de la myosine II

En suivant la forme du faisceau au cours du temps, nous pouvons extraire l'angle tangent $\psi(s, t)$ à chaque position s en fonction du temps t . Comme le montre la Figure E.2, la superposition des lignes détectées au cours d'un cycle révèle une forme de battement approximativement symétrique par rapport à l'axe vertical.

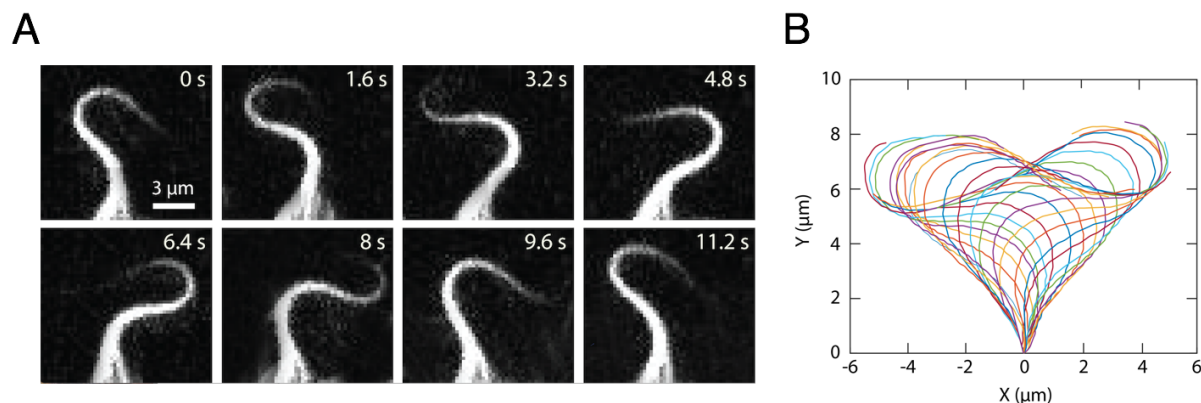


Figure E.2: Image de fluorescence et forme du battement caractéristique d'un faisceau d'actine oscillant. **A:** Image de fluorescence d'un faisceau d'actine oscillant en fonction du temps. L'actine est marquée avec le fluorophore AlexaFluor™ 488 (10 % de marquage, cf Chapitre 3). Le faisceau d'actine présente ici un mouvement oscillatoire avec une période de 11 s. The mouvement est conduit par la myosine II, qui était à une concentration de 500 nM dans le mix de polymérisation. **B:** Superposition des lignes détectées toutes les 0,5 s pendant une période d'oscillation. La forme du battement est approximativement symétrique par rapport à l'axe vertical.

À une abscisse curviligne donnée s , l'angle tangent $\psi(s, t)$ présente des oscillations périodiques au cours du temps, illustrées pour deux positions $s = 5 \mu\text{m}$ et $s = 10 \mu\text{m}$ (Fig. E.3.A (*gauche*)).

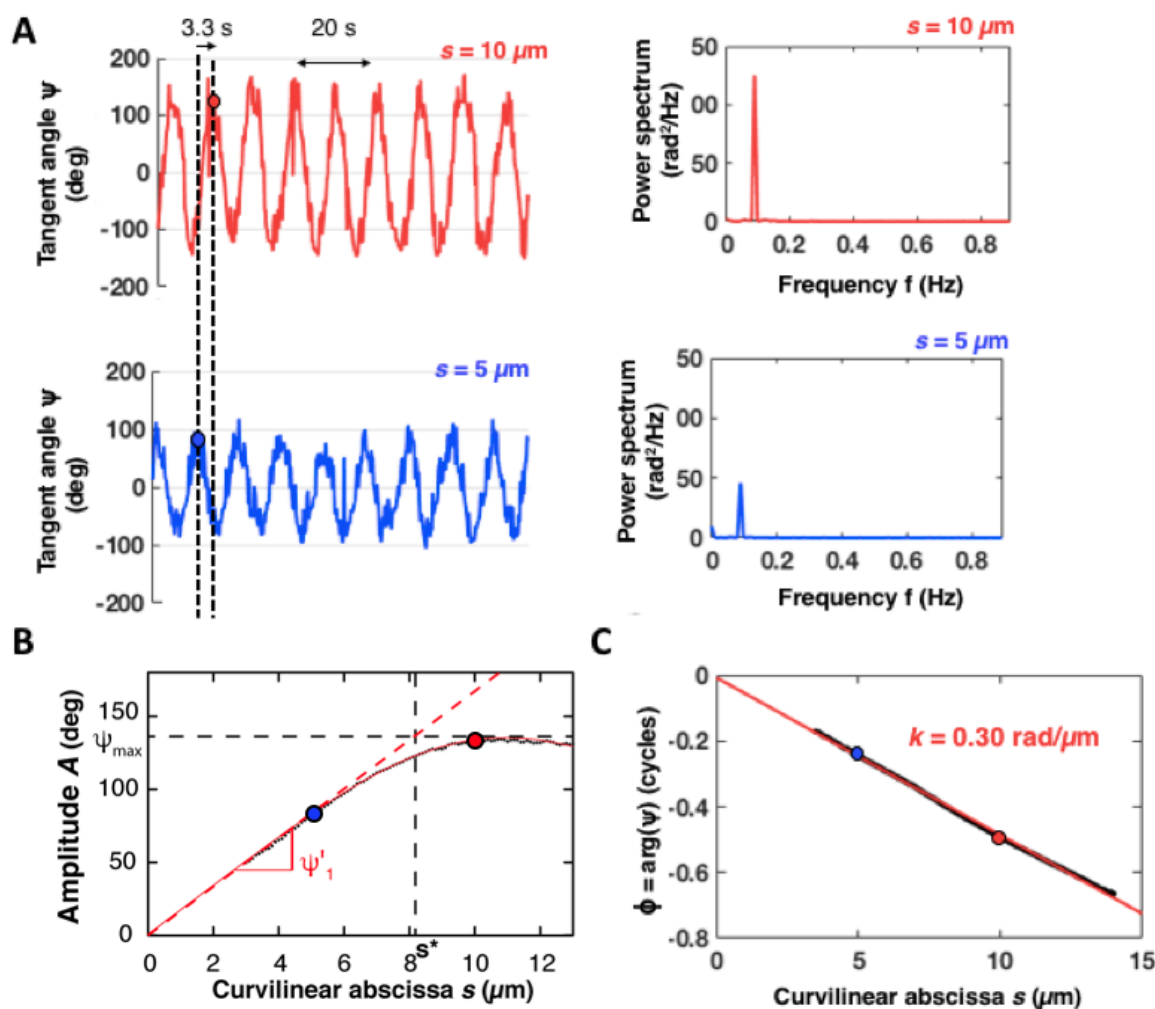


Figure E.3: Oscillations de l'angle tangent en fonction de la position le long du faisceau d'actine. **A:** Angle tangent $\psi(s, t)$ pour $s = 5 \mu\text{m}$ (bleu) et $s = 10 \mu\text{m}$ (rouge) en fonction du temps. L'angle tangent $\psi(s, t)$ présente des oscillations périodiques au cours du temps. Les oscillations ont la même période $T = 11 \text{ s}$ aux deux positions. L'amplitude augmente lorsque la position se rapproche de la pointe. Les spectres en puissance de l'angle tangent $\psi(s, t)$ aux deux positions sont présentés à droite des séries temporelles. Dans les deux cas, le spectre ne montre qu'un seul mode à la fréquence $f_0 = 0.09 \text{ Hz}$. Les lignes pointillées noires indiquent le temps auquel l'angle atteint un maximum sur la même période pour $s = 5 \mu\text{m}$ (point bleu) et $s = 10 \mu\text{m}$ (point rouge) ; il y a $3,3 \text{ s}$ de retard pour l'oscillation à $s = 10 \mu\text{m}$ par rapport à $s = 5 \mu\text{m}$. **B:** Amplitude A de l'oscillation. L'amplitude croît linéairement de la base à la pointe jusqu'à saturation, à 135 deg . **C:** Phase du mode de Fourier présenté en (A) en fonction de l'abscisse curviligne s . Le retard s'accumule linéairement le long du faisceau d'actine.

Les oscillations semblent quasi-sinusoïdales. Les spectres en puissance de l'angle tangent ne contiennent qu'un seul mode donc une seule fréquence caractéristique $f_0 = 0.09 \text{ Hz}$ (Fig. E.3.A (*droite*)), qui est la même quelque soit la position le long du faisceau. L'amplitude A de la sinusoïde augmente lorsque la position se rapproche de la pointe (Fig. E.3.C). L'amplitude croît linéairement de la base à la pointe jusqu'à saturation, ici

à 134 deg. De plus, l'oscillation à $s = 10 \mu\text{m}$ présente un retard de 3.3 s par rapport à l'oscillation à $s = 5 \mu\text{m}$, signature d'une onde de battement se propageant de la base à la pointe (Fig. E.3.A). En traçant la phase du premier mode de Fourier en fonction de l'abscisse curviligne, on obtient une relation linéaire, ce qui correspond à un vecteur d'onde uniforme (donné par la pente) (Fig. E.3.C). Comme la période et le vecteur d'onde sont uniformes, la vitesse de l'onde est aussi uniforme. Cette dernière propriété est surprenante : la vitesse de propagation est uniforme alors que la structure du faisceau ne l'est pas et s'affine en direction de la pointe (Fig. E.2). Les ondes de déformation mécaniques peuvent se visualiser en faisant un arrêt sur image sur l'angle tangent ψ à en fonction de l'abscisse curviligne du faisceau d'actine (Fig. E.4).

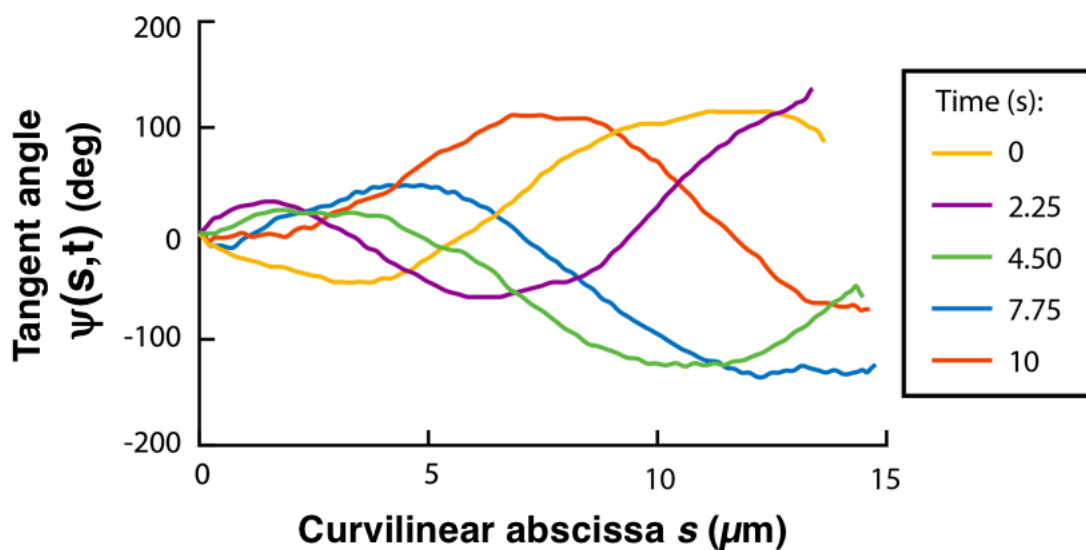


Figure E.4: Relation entre l'angle tangent ψ et l'abscisse curviligne le long du faisceau d'actine. Ces tracés illustrent la propagation d'une onde dont l'amplitude augmente le long du faisceau de la base vers la pointe.

Un tracé de couleurs de l'angle tangent $\psi(s, t)$ en fonction de l'espace (s) et du temps (t) permet de récapituler les propriétés décrites ci-dessus (Fig. E.5).

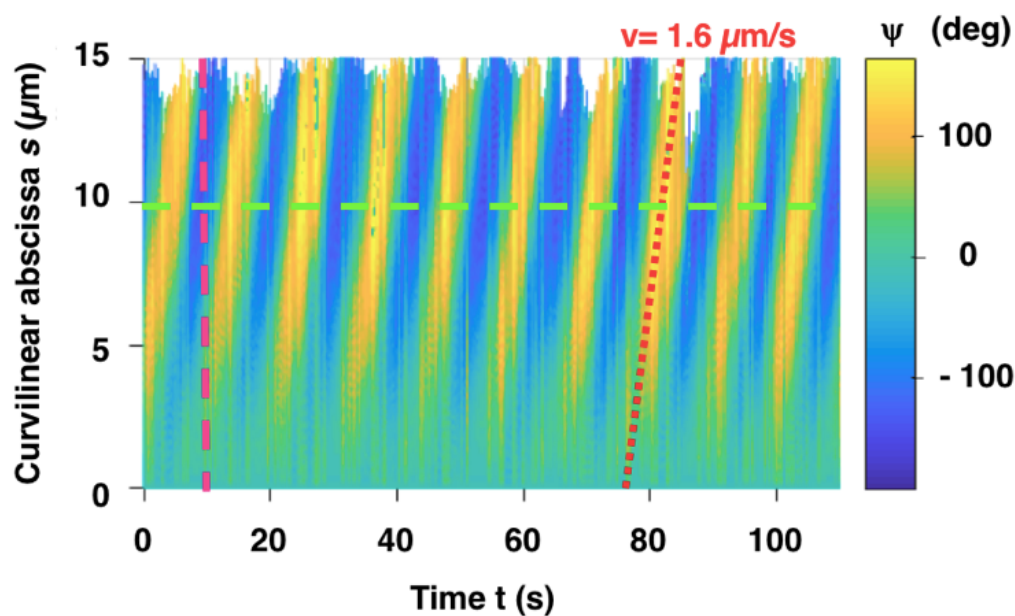


Figure E.5: Tracé de couleurs de l'angle tangent $\psi(s, t)$ en fonction de l'abscisse curviligne s et du temps t . Un tracé de couleurs récapitule toutes les propriétés du battement décrites ci-dessus. Les angles tangent sont représentés selon un code couleur indiqué sur la droite. Une coupe horizontale donne l'oscillation de l'angle tangent en fonction du temps à une abscisse curviligne fixe $s = 10 \mu\text{m}$ (Fig 4.8.A). Quand l'abscisse curviligne s varie, l'augmentation de l'amplitude d'oscillation est décrite par un contraste accru dans les oscillations de couleurs. Une lecture verticale du graphe (à un temps donné) présente la propagation de l'onde de l'angle tangent (Fig. E.4). En suivant une couleur de l'angle tangent, on peut extraire la vitesse uniforme de l'onde de déformation *via* la pente du tracé de couleur (ici $v=1,6 \mu\text{m/s}$).

E.1.2 Comparaison des propriétés de battements avec la myosine II par rapport à celles avec la myosine V

La myosine V réorganise les réseaux d'actine radiaux en faisceaux actifs qui ressemblent étonnamment à ceux obtenus avec la myosine II. En particulier, la forme du battement d'un faisceau unique peut être décrite dans les deux cas par un "cœur". Les angles tangent ont des oscillations périodiques et quasi sinusoïdales à chaque position et l'onde de déformation se propage à vitesse uniforme de la base en direction de la pointe. Cependant, les propriétés cinétiques sont bien plus rapides avec la myosine II qu'avec la myosine V. Dans l'exemple ci-dessous (Fig. E.6), la période est $T = 11 \text{ s}$ pour la myosine II contre $T = 70 \text{ s}$ pour la myosine V. La vitesse est de $1,6 \mu\text{m/s}$ pour la myosine II et de $0,3 \mu\text{m/s}$ pour la myosine V.

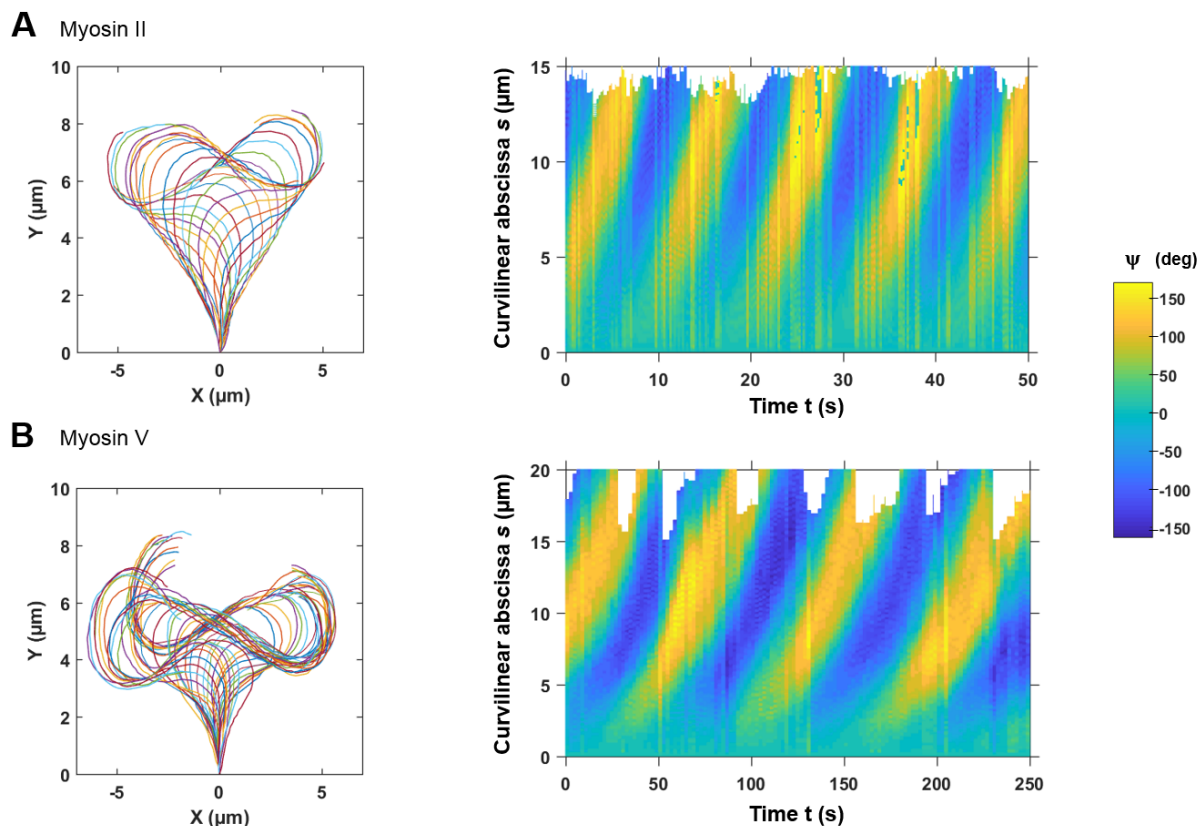


Figure E.6: Comparaison des propriétés de battements avec la myosine II par rapport à celles avec la myosine V. **A:** Forme du battement d'un faisceau d'actine activé par la myosine II (gauche) et le tracé de couleurs correspondant de l'angle tangent $\psi(s, t)$ (droite). Superposition des lignes de détection obtenues toutes les 0,5 s pendant une période d'oscillation. Les oscillations présentent une période de 11 s et une vitesse de 1,6 $\mu\text{m/s}$. **B:** Forme du battement d'un faisceau d'actine activé par la myosine V (gauche) et le tracé de couleurs correspondant de l'angle tangent $\psi(s, t)$ (droite). Superposition des lignes de détection obtenues toutes les 2 s pendant une période d'oscillation. Les oscillations présentent une période de 70 s et une vitesse de 0,3 $\mu\text{m/s}$.

Au sujet de la cinétique, les faisceaux d'actine oscillent en moyenne 7,5 fois plus vite avec la myosine II qu'avec la myosine V (Fig. E.7 (*gauche*)). Dans le cas de la myosine II, la période est de $T^{MII} = 16 \pm 8$ s, pour une valeur médiane de 17 s ($n = 46$), tandis que pour la myosine V la période est $T^{MV} = 120 \pm 84$ s, pour une valeur médiane de 104 s ($n = 71$). De la même façon, les ondes de déformation se propagent 7 fois plus vite dans le cas de la myosine II que dans celui de la myosine V. Avec la myosine II, la vitesse est $v^{MII} = 1,4 \mu\text{m/s} \pm 0,8$, avec une valeur médiane de 1,1 $\mu\text{m/s}$, tandis que dans le cas de la myosine V, la vitesse est $v^{MV} = 0,2 \pm 0,1 \mu\text{m/s}$ ($n = 71$), avec une valeur médiane de 0,2 $\mu\text{m/s}$ (Fig. E.7 (*droite*)).

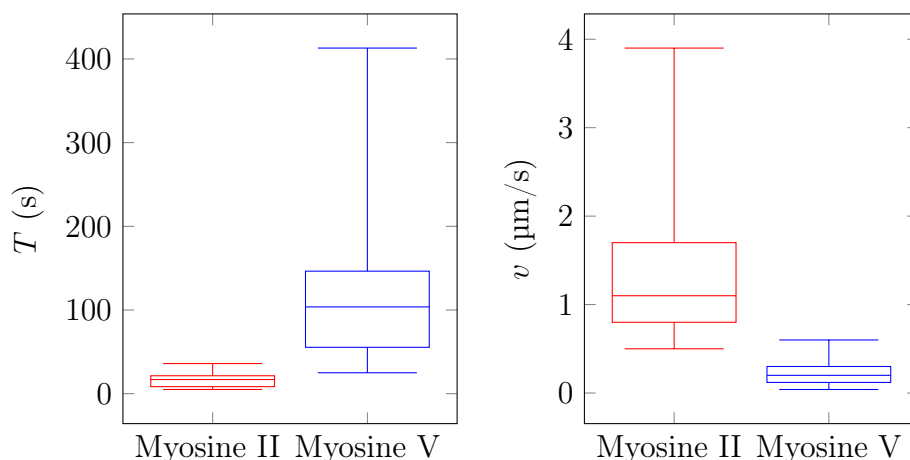


Figure E.7: Le battement est plus rapide avec myosine II qu'avec myosine V. *Gauche:* Boîte à moustache des périodes mesurées avec myosine II et myosine V (Valeurs médianes : $T = 17$ s pour myosine II; $T = 104$ s pour myosine V). La période pour myosine II est $T^{MII} = 16 \pm 8$ s, ($n = 46$) dans le cas de myosine V la période est $T^{MV} = 120 \pm 84$ s ($n=63$). *Droite:* Boîte à moustache des vitesses d'onde mesurées avec myosine II et myosine V (Valeurs médianes : $v = 1.1$ $\mu\text{m/s}$ pour myosine II; $v = 0.2$ $\mu\text{m/s}$ pour myosine V). La vitesse de l'onde pour myosine II est $v^{MII} = 1,4$ $\mu\text{m/s} \pm 0,8$ ($n = 46$), dans le cas de myosine V, la vitesse est $v^{MV} = 0,2 \pm 0,1$ $\mu\text{m/s}$ ($n = 63$). Les rectangles contiennent les valeurs comprises entre le premier et le troisième quartiles.

E.1.3 Effet de la longueur du faisceau sur les propriétés du battement

Au cours de mes expériences, les faisceaux d'actine croissent et battent simultanément. Pour étudier l'effet de la longueur du faisceau sur les propriétés du battement, en gardant les autres paramètres fixes, j'ai suivi le même faisceau à base de myosine II pendant 20 minutes. Pendant cet enregistrement, la longueur du faisceau a augmenté de 50 %, la période d'oscillation augmente linéairement en fonction de la longueur L du faisceau. Ainsi donc, plus le faisceau est long, plus les oscillations sont lentes. De façon remarquable, la vitesse reste constante au cours du temps, et demeure indépendante de la longueur du faisceau. Ainsi, la longueur d'onde augmente linéairement avec la longueur du faisceau avec une pente de 0,6.

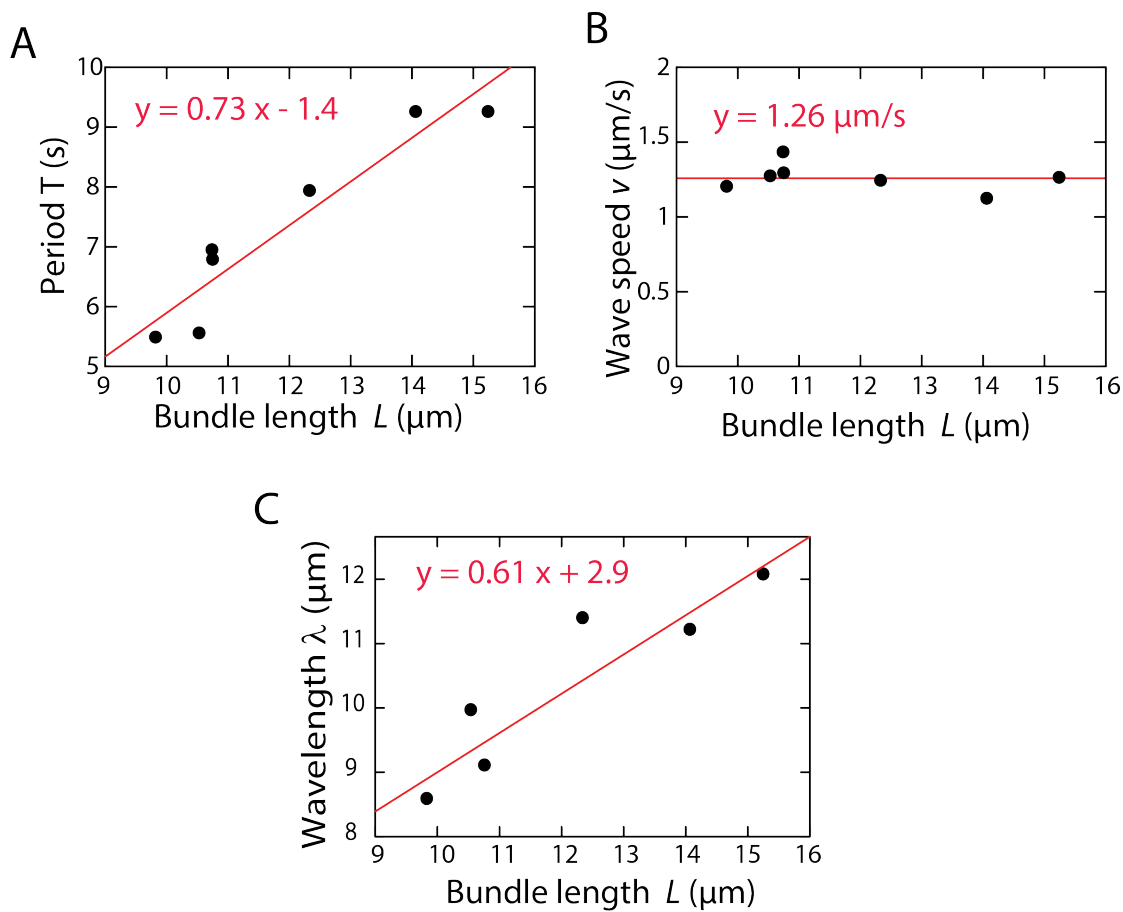


Figure E.8: Propriétés du battement d'un faisceau en croissance. A: La période du battement T augmente avec la longueur du faisceau. **B:** La vitesse de l'onde de déformation reste constante avec une valeur de $1,3 \mu\text{m/s}$. **C:** La longueur d'onde de l'onde de déformation augmente avec la longueur du faisceau.

Dans cette partie, nous avons vu que l'angle tangent effectue des oscillations quasi sinusoïdales en fonction du temps avec une amplitude qui augmente en allant de la base à la pointe. Il est intéressant de noter que la vitesse de l'onde de déformation mécanique se propage à vitesse uniforme, alors que le faisceau n'a pas les mêmes propriétés géométriques le long de son abscisse curviligne, le faisceau est plus large à la base qu'à la pointe. Nous avons aussi montré que la cinétique des battements étaient sept fois plus rapides avec la myosine II qu'avec la myosine V. Enfin nous avons identifié la longueur du faisceau comme un des paramètres de contrôle de la cinétique du battement : lorsque le faisceau s'allonge, la période du battement augmente, mais la vitesse de propagation de l'onde de déformation reste constante.

E.2 Distribution des moteurs le long d'un faisceau d'actine oscillant

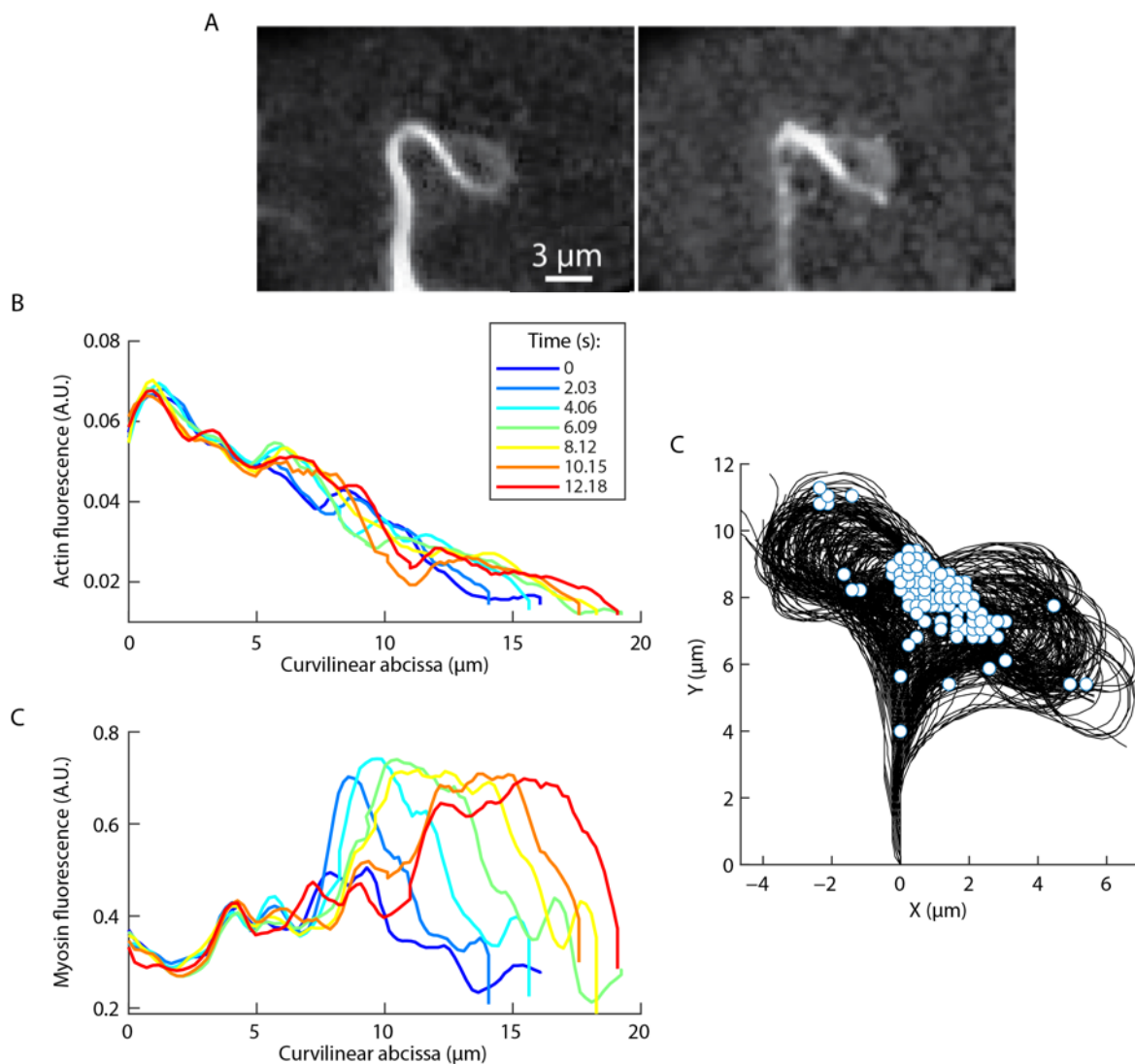


Figure E.9: Localisation de la myosine V le long du faisceau d'actine en battement.

A: Images de fluorescence d'un faisceau d'actine en battement dans les deux canaux : le canal de l'actine (*gauche*) et le canal de la myosine V (*droite*). L'actine est marquée avec le fluorophore AlexaFluor™ 488 (10 % de marquage, cf Chapitre 3), tandis que la myosine V est marquée avec la GFP. La concentration de myosine V était de 50 nM. **B:** Les profils d'intensité de fluorescence de l'actine (*haut*) et de la myosine (*bas*) le long du faisceau d'actine à $t = 0 - 12$ s. Le profil d'intensité de fluorescence d'actine décroît en allant de la base vers la pointe et ne varie pas au cours du temps. Le profil d'intensité de fluorescence de myosine V fait apparaître un pic qui émerge à $s = 8,3 \mu\text{m}$, augmente et se propage vers la pointe du faisceau. **C:** Superposition des lignes de détection (temps d'échantillonnage : 2,03 s) sur 41 périodes d'oscillation. Les disques blancs indiquent les positions des pics de signaux de myosine V sur les lignes détectées correspondantes.

Pour visualiser les moteurs au cours du battement des faisceaux d'actine, nous avons utilisé de la myosine V marquée à la GFP. De manière inattendue, nous avons découvert que le profile d'intensité de fluorescence le long du faisceau d'actine pour les moteurs ne correspondait pas à celui observé pour l'actine (Fig. E.9.A). Le profile d'intensité de fluorescence d'actine décroît en allant de la base vers la pointe et ne varie pas au cours du temps, tandis que celui de myosine V fait apparaître un pic qui émerge à $s = 8,3 \mu\text{m}$, augmente et se propage vers la pointe du faisceau (Fig. E.9.B). D'autre part la superposition des lignes de détection et des positions des pics de signaux de myosine V, nous avons observé que le signal de myosine V reste concentré au centre du signe infini que la pointe du faisceau d'actine dessine au cours du battement (Fig. E.9.C).

En repérant l'abscisse curviligne du pic du signal de myosine V au cours du temps, nous avons obtenu une oscillation en dent de scie, qui correspond à la génération périodique d'une onde de concentration de myosine V qui se propage en direction de la pointe en partant de $s = 8.3 \mu\text{m}$ jusqu'à la pointe du faisceau, avec une période de $T = 16 \text{ s}$ (Fig. E.10.A). La période du battement du faisceau est quant à elle de 32 s (Fig. E.10.B). La période des oscillations en myosine V est donc deux fois plus rapide que celle du battement du faisceau. La vitesse de propagation de l'onde de concentration de myosine est de $v = 0,9 \mu\text{m/s}$, alors que celle de l'onde d'actine est $v = 0,5 \mu\text{m/s}$. En comparant la cinétique des ondes de concentration de myosine et des ondes de déformations du faisceau au cours du battement pour tous les faisceaux myosine-V GFP que nous avons analysés, on obtient $v^{MYOSIN} = 0.7 \pm 0.1 \mu\text{m/s}$ pour les ondes de concentration de myosine, avec une période correspondante de $T^{MYOSIN} = 22 \pm 5 \text{ s}$ ($n = 11$). La vitesse et période de l'onde de déformation sont $v^{ACTIN} = 0.4 \pm 0.1 \mu\text{m/s}$ et $T^{ACTIN} = 44 \pm 10 \text{ s}$ ($n = 11$), respectivement. La période d'oscillation de la myosine V correspond à la moitié de celle de l'angle tangent (Fig. E.10.C). De plus, l'onde de myosine V se propage 1,7 fois plus vite que l'onde de déformation du faisceau (Fig. E.10.D).

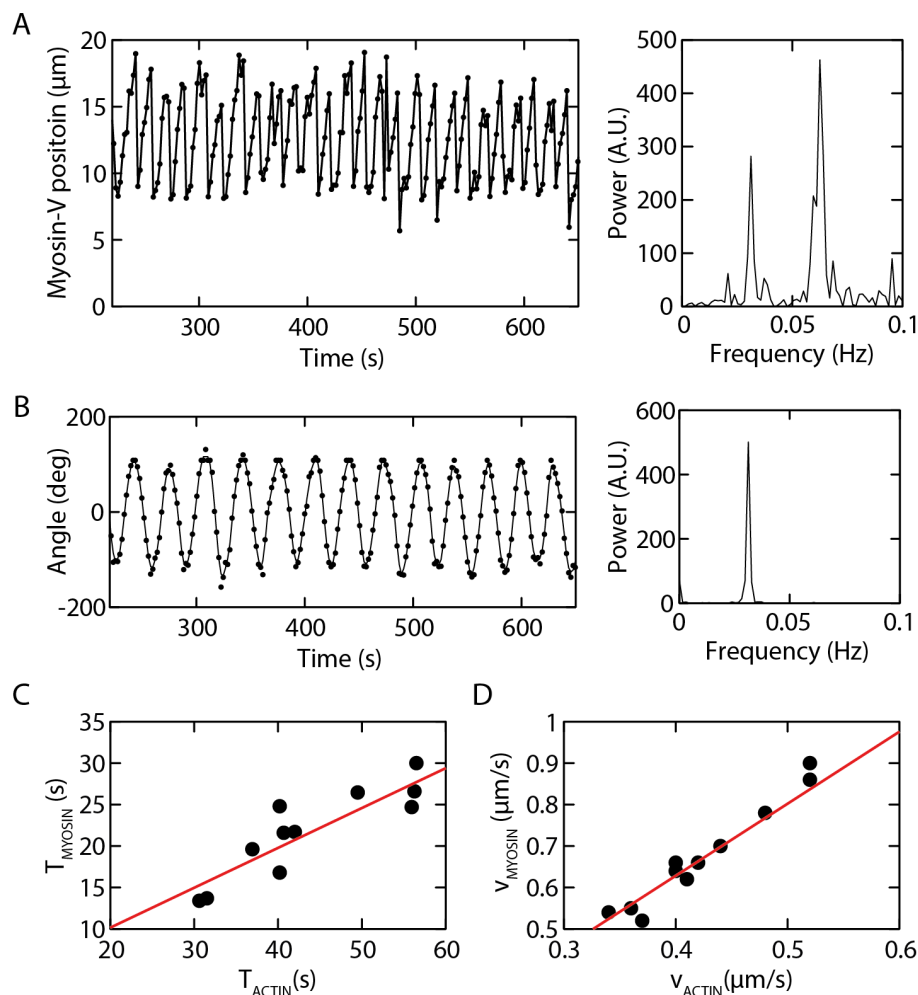


Figure E.10: Cinétique des vagues de concentration de myosine comparée à celle du battement du faisceau. **A:** Position du pic de concentration de myosine V sur le faisceau d'actine en fonction du temps (*panel de gauche*). Le signal de myosine V présente une oscillation en dent de scie, qui correspond à la génération périodique d'une onde de concentration de myosine V qui se propage en direction de la pointe en partant de $s = 8.3 \mu\text{m}$ jusqu'à la pointe du faisceau, avec une vitesse de $v = 0,7 \mu\text{m/s}$, donnée par la pente des rampes ascendante des dents de scie. Le spectre en puissance des oscillations (*panel de droite*) montre un mode de Fourier principal à fréquence $f_0 = 0,06 \text{ Hz}$ et un second mode à la fréquence $f_1 = 0,03 \text{ Hz}$ des oscillation du battement du faisceau (*panel B*). **B:** Évolution temporelle de l'angle tangent à $s = 10 \mu\text{m}$ (*panel de gauche*). L'angle tangent présente des oscillations sinusoïdales en fonction du temps avec une période $T = 32 \text{ s}$. Le spectre en puissance correspondant (*panel de droite*) ne présente qu'un seul mode à la fréquence $f_0 = 0,03 \text{ Hz}$. **C:** Période T^{MYOSIN} de la génération des ondes de concentration de myosine V en fonction de la période de battement T^{ACTIN} ds faisceaux d'actine. **D:** Vitesse v^{MYOSIN} des vagues de concentration de myosine en fonction de la vitesse v^{ACTIN} des ondes de déformation d'actine.

En sommant le signal de fluorescence le long du faisceau d'actine, qui reflète le nombre total de myosines présentes au sein du faisceau au cours du temps, on obtient des oscillations en dent de scie (Fig. E.11.A) à la même période que l'onde de concentration de myosine $T = 16 \text{ s}$. Ce résultat indique que le nombre de moteurs dans le faisceau augmente

lorsque l'onde de concentration de myosine se propage le long du faisceau de sa position d'initiation $s = 8,3 \mu\text{m}$ jusqu'à la pointe du faisceau. De plus, le tracé de l'intégration du signal de fluorescence de myosine V en fonction de la position du pic de myosine V le long du faisceau d'actine au cours du temps montre que le nombre de myosines au sein du faisceau augmente au cours de la propagation de l'onde (Fig. E.11.B). Ce graphe indique donc un recrutement local des myosines le long du faisceau, ici préférentiellement entre $s = 7 \mu\text{m}$ et $s = 12 \mu\text{m}$.

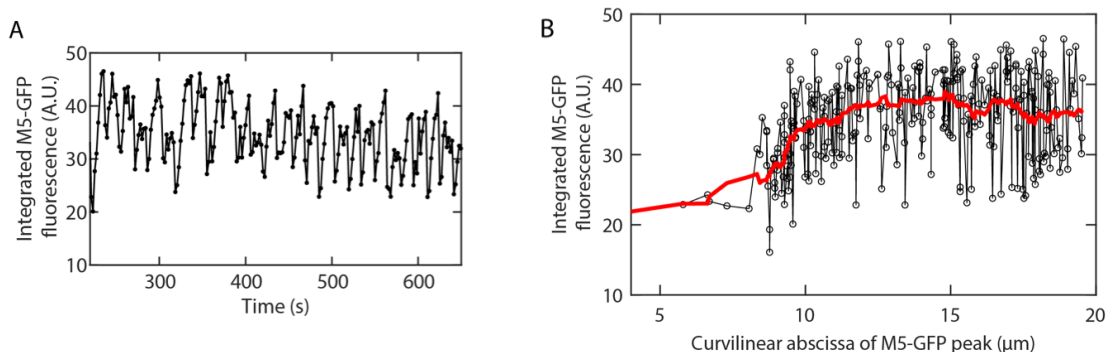


Figure E.11: Intégration du signal de fluorescence de myosin V le long du faisceau d'actine. **A:** L'intégration du signal de fluorescence de myosin V le long du faisceau d'actine, qui reflète le nombre total de myosines présentes au sein du faisceau au cours du temps, donne des oscillations en dent de scie **B:** L'intégration du signal de fluorescence de myosin V en fonction de la position du pic de myosine V le long du faisceau d'actine. La ligne rouge est obtenue par une moyenne mobile des données.

Comment la localisation de la myosin V est-elle reliée à la forme du faisceau d'actine ? En corrélant la position du pic de concentration de la myosine V à la courbure du faisceau (Fig. E.12.A), on observe aussi bien pour le profil d'intensité de fluorescence de la myosine V que pour la courbure (Fig. E.12.B) la propagation d'une onde le long du faisceau.

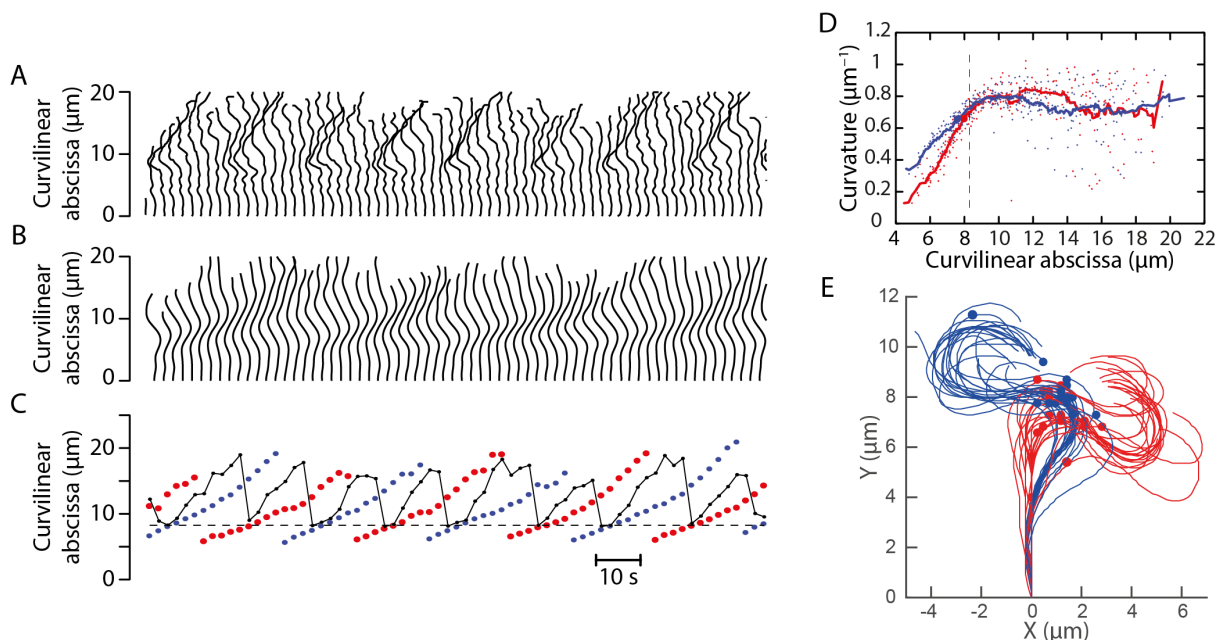


Figure E.12: Myosine V et courbure de l'actine. **A:** Profil d'intensité de fluorescence de la myosine V GFP le long du faisceau d'actine en battement en fonction du temps ($dt = 2$ s). On observe la propagation d'une onde en direction de la pointe du faisceau. **B:** Courbure du faisceau d'actine (unité arbitraire) le long du faisceau en fonction du temps, on observe aussi la propagation d'une onde en direction de la pointe du faisceau, mais avec une vitesse moindre et une période deux fois plus grande que pour les ondes de concentration en myosine. **C:** Position sur le faisceau d'actine du pic de fluorescence de la myosine V GFP (en noir), des maxima de courbure du faisceau (en rouge) et des minima (en bleu) en fonction du temps. **D:** Courbure positive (ligne rouge) et négative (ligne bleue) le long du faisceau d'actine en fonction de l'abscisse curviligne. Les disques rouges (bleus) indiquent la position où la myosine V est recrutée le long du faisceau d'actine. **E:** Superposition de la forme du battement du faisceau et des positions des pics de myosine V aux temps où la myosine V commence à être recrutée sur le faisceau d'(deux fois par oscillation du battement). Les lignes détectées rouges (bleues) correspondent à des positions de recrutement de la myosine V où la courbure est positive (négative). Les disques rouges (bleus) indiquent quant à eux les positions correspondantes du pic de myosine.

En revanche, la vitesse de propagation est moindre dans le cas de la courbure, avec une période deux fois plus importante que pour l'onde de concentration. D'autre part, si l'on compare la localisation du pic de myosine V sur le faisceau aux courbures minimale et maximale du faisceau au cours du temps, on voit que la myosine V reste positionnée entre les positions du maximum et du minimum de courbure. L'onde de myosine est initiée à une position qui coïncide presque avec la position du maximum (minimum) de courbure et se propage suffisamment vite pour atteindre la pointe du faisceau en même temps que l'onde de courbure minimale (maximale) générée une demie période plus tôt (Fig. E.12.C). Tout comme l'angle tangent, l'amplitude de la courbure le long du faisceau en se dirigeant vers la pointe. Le recrutement de myosine V n'est déclenché que lorsque la courbure atteint une certaine valeur seuil (ici pour $s = 8,3$ μm). En traçant l'amplitude maximale positive et négative en fonction de l'abscisse curviligne, on observe

que le recrutement de myosine V ne débute que lorsque le maximum de courbure atteint une valeur seuil (ici $C_{seuil} = 0.65 m^{-1}$) (Fig. E.12.D) . Le seuil de courbure semble donc initier l'onde de concentration de myosine. Ce seuil est atteint deux fois par période de battement (une fois positivement, une fois négativement). Cette condition peut être visualisée en superposant les lignes détectés de la forme du battement du faisceau et la position à laquelle le pic est initié sur le faisceau. On voit alors que la myosine V est recrutée dans la région la plus courbée du faisceau d'actine (Fig. E.12.E) . Ce phénomène suggère un rétrocontrôle mécanique entre l'affinité de la myosine et la forme du faisceau.

Dans cette partie, les myosines V-GFP ont révélé la présence d'un pic de concentration de myosine au sein du faisceau d'actine. Nous avons observé que les moteurs sont localement recrutés sur le faisceau, avant qu'une onde de concentration ne se propage en direction de la pointe, où les moteurs finissent par se détacher. De plus, le recrutement de myosine V est initié quand la courbure atteint une valeur seuil sur le faisceau. Ces résultats mettent en lumière un nouveau mode de couplage entre l'affinité de la myosine pour l'actine et la forme du faisceau d'actine.

List of Figures

1.1	Examples of self-organization at the macroscopic scale	6
1.2	Examples of self-organization in cellular systems	7
1.3	Examples of <i>in vitro</i> cytoskeleton self-organization due to geometrical constraints	8
1.4	Phase diagram in a reconstituted system	10
1.5	Oscillations with cytoskeletal filaments and molecular motors within sarcomere	11
1.6	Cortex oscillations of lymphoblast fragments	12
1.7	A minimal system of microtubules, molecular motors assembles into actively beating bundles.	13
1.8	Diversity of cilia and flagella	14
1.9	Flagellar axoneme	15
1.10	Bending of an axoneme	16
1.11	Beating pattern of three eukaryotic flagella	17
1.12	Beating properties of the <i>Chlamydomonas reinhardtii</i>	19
1.13	Beating properties of the bull sperm	20
1.14	Time series analysis and Fourier modes of beat patterns	21
1.15	Beating frequency of bull sperm as a function of the viscosity of the medium.	22
1.16	Viscosity and Beating Pattern	23
1.17	Variation of beating properties at high viscosity	23
1.18	Effect of flagellum length on beating properties	25
1.19	Asymmetric and symmetric motor filament pairs	25
1.20	The complex structure of the axoneme is reduced to a pair of sliding filaments	26
2.1	Structure of G-actin	32
2.2	Transition from the G-actin conformation to the flat conformation in F-actin	32
2.3	Persistence length of an actin filament	33
2.4	Association/dissociation rates of actin	34
2.5	Schematic of profilin bound to G-actin	37

2.6	Profilin tunes the kinetics of assembly and disassembly of actin filaments . . .	37
2.7	The Arp 2/3 complex mediates branched actin networks	38
2.8	Arp2 and Arp 3 have a structure close to that of actin monomers	39
2.9	A branched actin network results from the autocatalytic branching activity of the Arp2/3 complex	40
2.10	The three parts of a myosin	41
2.11	Dimerized/double-headed myosin II	42
2.12	Myosin II assemblies	42
2.13	Conventional model for the catalytic cycle of myosin	43
2.14	Schematic to explain how a conformational change can generate force . . .	44
2.15	The swinging lever arm hypothesis	45
2.16	<i>In vitro</i> motility assay.	46
2.17	Filament speed in <i>in vitro</i> motility assay	47
2.18	Assays with optical tweezers	48
2.19	Single molecule experiment with a processive motor	49
2.20	Single molecule experiment with a non-processive motor	50
3.1	Schematic representation of the experiment	54
3.2	Surface micropatterning technique	55
3.3	PLL-g-PEG passivation principle	56
3.4	Two examples of patterns drawn on the chrome photomask	57
3.5	Chambers are built on a glass slide using double-sided adhesive tape	57
3.6	Radial actin network obtained with a micropattern of 9- μm diameter disks	60
3.7	Spectra of excitation and emission of fluorophores used in our experiments	61
3.8	The successive steps in ImageJ software for image analysis	63
3.9	Parameterization of the detected line with curvilinear abscissa s and tan- gent angle ψ	65
4.1	From parallel nucleation lines to parallel and antiparallel actin networks . .	68
4.2	Polymerization dynamics of a parallel network	69
4.3	IFluorescence intensity profile of parallel actin networks	70
4.4	Myosin-driven bundling of actin filaments	71
4.5	Distribution of actin-bundle length in the presence of myosin II or of myosin V	72
4.6	Varying the geometry of the patterns	73
4.7	Fluorescence image and typical beating pattern of an oscillating actin bundle	74
4.8	Tangent-angle oscillations as a function of position along the actin bundle .	76

4.9	The relation between the tangent angle ψ and the curvilinear abscissa s along the bundle	77
4.10	Color plot the tangent angle $\psi(s, t)$	77
4.11	Comparing beating properties driven by myosin II with respect to those driven by myosin V	79
4.12	Shape parameters of the beating pattern	80
4.13	Faster beating with myosin II than with myosin V	81
4.14	Birth of a beating myosin V-bundle	82
4.15	Time evolution of the beating pattern as the actin bundle grows	83
4.16	Evolution of beating properties of a growing bundle	84
4.17	Beating properties of a growing bundle	85
4.18	Beating pattern properties over an ensemble of actin bundles with myosin II and myosin V	86
4.19	Beating properties over an ensemble of actin bundles with myosin II and myosin V	88
4.20	Effect of myosin concentration on the oscillation period	90
4.21	Myosin V localization along beating actin bundle	91
4.22	Kinetics of myosin concentration waves compared to that of actin beating	93
4.23	Integrated-myosin V and actin fluorescence signals along a beating actin bundle	94
4.24	Myosin V and actin curvature	96
5.1	Comparison of various oscillating systems	101
5.2	3D and 2D motions of swimming sea urchin spermatozoa	103
5.3	3D-movement of actin bundles	104
5.4	The Arp 2/3 complex for actin affinity depends on curvature of actin filament	105
5.5	Myosin V stabilizes a conformation of F-actin	106
6.1	Myosin II activity modulated by blebbistatin	110
6.2	Orchestrated collapse of the actin network at high concentration of myosin II	112
6.3	Actin network collapse induced by myosin VI and myosin II	113
E.1	Réorganisation des filaments d'actine sous l'action de myosines	126
E.2	Image de fluorescence et forme du battement caractéristique d'un faisceau d'actine oscillant	127
E.3	Oscillations de l'angle tangent en fonction de la position le long du faisceau d'actine	128

E.4	Relation entre l'angle tangent ψ et l'abscisse curviligne le long du faisceau d'actine	129
E.5	Tracé de couleurs de l'angle tangent $\psi(s, t)$	130
E.6	Comparaison des propriétés de battements avec la myosine II par rapport à celles avec la myosine V	131
E.7	Le battement est plus rapide avec myosine II qu'avec myosine V	132
E.8	Propriétés du battement d'un faisceau en croissance	133
E.9	Localisation de la myosine V le long du faisceau d'actine en battement . .	134
E.10	Cinétique des vagues de concentration de myosine comparée à celle du battement du faisceau	136
E.11	Intégration du signal de fluorescence de myosin V le long du faisceau d'actine	137
E.12	Myosine V et courbure de l'actine	138

List of Tables

1.1	Flagellar beating properties in different species	17
1.2	Changes of flagellar beat properties with viscosity	24
2.1	Rate constants for actin polymerization and depolymerization at both ends of the actin filament	35
2.2	Examples of actin-binding proteins and their function	36
2.3	Properties of myosin II and myosin V.	51
3.1	Polymerization mix	59
A.1	Myosin Buffer	117
A.2	MgATP Buffer	118
A.3	Fluorescent Buffer	118
A.4	Polymerization mix	118
B.1	Actin and actin related proteins	119
B.2	HMM myosins	120
C.1	Chemical products	121
D.1	G Buffer composition	123
D.2	10X KMEI	124
D.3	10X KEEI	124

Bibliography

- O. Akin and R. D. Mullins. Capping protein increases the rate of actin-based motility by promoting filament nucleation by the Arp2/3 complex. *Cell*, 133(5):841–851, 2008.
- B. Alberts, A. Johnson, J. Lewis, M. Raff, K. Roberts, and P. Walter. *Molecular Biology of the Cell*. Garland Science, 2002.
- B. Alberts, A. Johnson, J. Lewis, M. Raff, K. Roberts, and P. Walter. *Molecular Biology of the Cell*. Garland Science, 2008.
- J. Allard and A. Mogilner. Traveling waves in actin dynamics and cell motility. *Current Opinion in Cell Biology*, 25(1):107 – 115, 2013.
- J. Alvarado, M. Sheinman, A. Sharma, F. C. MacKintosh, and G. H. Koenderink. Molecular motors robustly drive active gels to a critically connected state. *Nature Physics*, 9(9):591–597, 2013.
- K. J. Amann and T. D. Pollard. Cellular regulation of actin network assembly. *Current Biology*, 10(20):728 – 730, 2000.
- R. S. Anderson. Eolian ripples as examples of self-organization in geomorphological systems. *Earth-Science Reviews*, 29(1):77 – 96, 1990.
- L. Aschenbrenner, S. Naccache, and T. Hasson. Uncoated endocytic vesicles require the unconventional myosin, Myo6, for rapid transport through actin barriers. *Molecular Biology of the Cell*, 15(5):2253–2263, 2004.
- K. Avraham, T. HASSON, K. Steel, D. Kingsley, L. Russel, M. Mooseker, N. Copeland, and N. Jenkins. The mouse snells Waltzer deafness gene encodes an unconventional myosin required for structural integrity of inner-ear hair-cells. *Nature Genetics*, 11(4):369–375, 1995.
- A. Azioune, M. Storch, M. Bornens, M. They, and M. Piel. Simple and rapid process for single cell micro-patterning. *Lab Chip*, 9(11):1640–1642, 2009.

- P. Ball. Pattern formation in nature: Physical constraints and self-organising characteristics. *Architectural design*, 82(2):22–27, 2012.
- J. Bamburg, H. Harris, and A. Weeds. Partial purification and characterization of an actin depolymerizing factor from brain. *FEBS Letters*, 121(1):178 – 182, 1980.
- P. V. Bayly, B. L. Lewis, P. S. Kemp, R. B. Pless, and S. K. Dutcher. Efficient Spatiotemporal Analysis of the Flagellar Waveform of *Chlamydomonas reinhardtii*. *Cytoskeleton*, 67(1):56–69, 2010.
- C. Beta and K. Kruse. Intracellular oscillations and waves. *Annual Review of Condensed Matter Physics*, 8(239-264), 2017.
- L. Blanchoin and T. D. Pollard. Hydrolysis of ATP by polymerized actin depends on the bound divalent cation but not profilin. *Biochemistry*, 41(2):597–602, 2002.
- L. Blanchoin, K. J. Amann, H. N. Higgs, J.-B. Marchand, D. A. Kaiser, and T. D. Pollard. Direct observation of dendritic actin filament networks nucleated by Arp2/3 complex and WASP/Scar proteins. *Nature*, 404(6781):1007–1011, Apr 2000.
- L. Blanchoin, R. Boujemaa-Paterski, C. Sykes, and J. Plastino. Actin dynamics, architecture, and mechanics in cell motility. *Physiol Rev*, 94:235–263, 2014.
- M. J. Bloemink and M. A. Geeves. Shaking the myosin family tree: Biochemical kinetics defines four types of myosin motor. *Seminar in Cell and Developmental Biology*, 22(9): 961 – 967, 2011.
- M. Bornens, M. Paintrand, and C. Celati. The Cortical Microfilament System of Lymphoblasts Displays a Periodic Oscillatory Activity in the Absence of Microtubules - Implications for Cell Polarity. *Journal of Cell Biology*, 109(3):1071–1083, 1989.
- L. Bourdieu, M. O. Magnasco, D. A. Winkelmann, and A. Libchaber. Actin filaments on myosin beds: The velocity distribution. *Phys. Rev. E*, 52(6):6573–6579, 1995.
- C. P. Brangwynne, G. H. Koenderink, E. Barry, Z. Dogic, F. C. MacKintosh, and D. A. Weitz. Bending dynamics of fluctuating biopolymers probed by automated high-resolution filament tracking. *Biophysical Journal*, 93(1):346 – 359, 2007.
- D. Bray. *Cell movements from molecules to motility*. Garland Science, 2001.
- C. Brokaw. Effects of increased viscosity on movements of some invertebrate spermatozoa. *Journal of Experimental Biology*, 45(1):113–139, 1966.

- C. Brokaw. Bend propagation by a sliding filament model for flagella. *Journal of Experimental Biology*, 55(2):289–304, 1971.
- C. Brokaw. Computer simulation of flagellar movement .1. demonstration of stable bend propagation and bend initiation by sliding filament model. *Biophysical Journal*, 12(5):564–586, 1972a.
- C. Brokaw. Flagellar movement - a sliding filament model - an explanation is suggested for spontaneous propagation of bending waves by flagella. *Science*, 178(4060):455–462, 1972b.
- C. Brokaw. Molecular Mechanism for Oscillations in Flagella and Muscle. *Proceedings of the National Academy of Sciences*, 72(8):3102–3106, 1975.
- C. Brokaw and D. Luck. Bending patterns of Chlamydomonas flagella .1. Wild-type bending patterns. *Cell Motility and the Cytoskeleton*, 3(2):131–150, 1983.
- N. Bruot and P. Cicuti. Realizing the Physics of Motile Cilia Synchronization with Driven Colloids. *Annual Review of Condensed Matter Physics*, 7:323–348, 2016.
- S. Camalet and F. Jülicher. Generic aspects of axonemal beating. *New Journal of Physics*, 2(24):24.1–24.23, 2000.
- S. Camalet, F. Jülicher, and J. Prost. Self-organized beating and swimming of internally driven filaments. *Physical Review Letters*, 82(7):1590–1593, 1999.
- S. Camazine, J.-L. Deneubourg, N. R. Franks, J. Sneyd, G. Theraulaz, and B. Eric. *Self-Organization in Biological Systems*. Princeton University Press, 2001.
- M. Carlier and D. Pantaloni. Direct evidence for adp-pi-f-actin as the major intermediate in atp-actin polymerization-rate of dissociation of pi from actin filaments. *Biochemistry*, 25(24):7789–7792, 1986.
- M.-F. Carlier and D. Pantaloni. Control of actin dynamics in cell motility. *Journal of Molecular Biology*, 269(4):459 – 467, 1997.
- K. Carvalho, J. Lemiere, F. Faqir, J. Manzi, L. Blanchoin, J. Plastino, T. Betz, and C. Sykes. Actin polymerization or myosin contraction: two ways to build up cortical tension for symmetry breaking. *Philosophical Transactions of the Royal Society B: Biological Sciences*, 368(1629):20130005, 2013.

- D. Chereau, F. Kerff, P. Graceffa, Z. Grabarek, K. Langsetmo, and R. Dominguez. Actin-bound structures of wiskott-aldrich syndrome protein (wasp)-homology domain 2 and the implications for filament assembly. *Proceedings of the National Academy of Sciences*, 102(46):16644–16649, 2005.
- J. Cooper. Actin dynamics: Tropomyosin provides stability. *Current Biology*, 12(15):523–525, 2002.
- G. Corkidi, B. Taboada, C. Wood, A. Guerrero, and A. Darszon. Tracking sperm in three-dimensions. *Biochemical and Biophysical Research Communications*, 373(1):125–129, 2008.
- D. S. Courson and R. S. Rock. Actin Cross-link Assembly and Disassembly Mechanics for alpha-Actinin and Fascin. *Journal of Biological Chemistry*, 285(34):26350–26357, 2010.
- E. M. De La Cruz and E. M. Ostap. Relating biochemistry and function in the myosin superfamily. *Current Opinion in Cell Biology*, 16(1):61–67, 2004.
- E. M. De La Cruz, A. L. Wells, S. S. Rosenfeld, E. M. Ostap, and H. L. Sweeney. The kinetic mechanism of myosin V. *Proceedings of the National Academy of Sciences*, 96(24):13726–13731, 1999.
- G. Douglas and M. Holwill. Behaviour of flagella isolated from crithidia oncopelti. *J Mechanochem Cell Motil.*, 1(4):213–223, 1972.
- H. Ennomani. *Réponse contractile des systÃšmes actomyosines biomimétiques*. PhD thesis, Université Grenoble Alpes, 2015.
- A. Fabiato and F. Fabiato. Myofilament-generated tension oscillations during partial calcium activation and activation dependence of the sarcomere length-tension relation of skinned cardiac cells. *The Journal of General Physiology*, 72(5):667–699, 1978.
- R. J. Field and H. D. Foersterling. On the oxybromine chemistry rate constants with cerium ions in the Field-Koeroes-Noyes mechanism of the Belousov-Zhabotinskii reaction: the equilibrium $\text{HBrO}_2 + \text{BrO}_3^- + \text{H}^+ \rightleftharpoons 2\text{BrO} + \text{H}_2\text{O}$. *The Journal of Physical Chemistry*, 90(21):5400–5407, 1986.
- J. T. Finer, R. M. Simmons, and J. A. Spudich. Single myosin molecule mechanics: piconewton forces and nanometre steps. *Nature*, 368(6467):113–119, 1994.
- S. B. Forrest and P. K. Haff. Mechanics of wind ripple stratigraphy. *Science*, 255(5049):1240–1243, 1992.

- B. J. Foth, M. C. Goedecke, and D. Soldati. New insights into myosin evolution and classification. *Proceedings of the National Academy of Sciences*, 103(10):3681–3686, 2006.
- B. M. Friedrich, I. H. Riedel-Kruse, J. Howard, and F. Jülicher. High-precision tracking of sperm swimming fine structure provides strong test of resistive force theory. *Journal of Experimental Biology*, 213(8):1226–1234, 2010.
- V. E. Galkin, A. Orlova, N. Lukoyanova, W. Wriggers, and E. H. Egelman. Actin depolymerizing factor stabilizes an existing state of f-actin and can change the tilt of f-actin subunits. *The Journal of Cell Biology*, 153(1):75–86, 2001.
- V. E. Galkin, A. Orlova, G. F. Schröder, and E. H. Egelman. Structural polymorphism in F-actin. *Nature Structural Molecular Biology*, 17:1318–1323, oct 2010.
- B. Gibbons and I. Gibbons. Formation of flagellar rigor waves by abrupt removal of atp from actively swimming spermatozoan. *Journal of Cell Biology*, 63:970–985, 1974.
- I. Gibbons. *The Functional Anatomy of the Spermatozoon*. Pergamon Press, Oxford, 2nd edition edition, 1975.
- M. L. Ginger, N. Portman, and P. G. McKean. Swimming with protists: Perception, motility and flagellum assembly. *Nature Reviews Microbiology*, 6:836–850, 2008.
- M. Glaser, J. Schnauss, T. Tschirner, B. U. S. Schmidt, M. Moebius-Winkler, J. A. Kaes, and D. M. Smith. Self-assembly of hierarchically ordered structures in DNA nanotube systems. *New Journal of Physics*, 18(055001), 2016.
- J. Gray. The movement of sea-urchin spermatozoa. *Journal of Experimental Biology*, 32(4):775–801, 1955.
- J. Gray. The Movement of the Spermatozoa of the Bull. *Journal of Experimental Biology*, 35(1):1–17, 1957.
- J. Gray. The movement of the spermatozoa of the bull. *Journal of Experimental Biology*, 35(1):96–108, 1958.
- S. Grill, K. Kruse, and F. Jülicher. Theory of mitotic spindle oscillations. *Physical Review Letters*, 94(10):108104, 2005.
- S. Guenther and K. Kruse. Spontaneous waves in muscle fibres. *New Journal of Physics*, 9:417, 2007.

- I. Gutsche-Perelroizen, J. Lepault, A. Ott, and M. F. Carrier. Filament assembly from profilin-actin. *The Journal of biological chemistry*, 274(10):6234–6243, 1999.
- J. R. Hammer, John A.; Sellers. Walking to work: roles for class v myosins as cargo transporters. *Nature Reviews Molecular Cell Biology*, 13(1):13–26, 2012.
- Y. Harada, K. Sakurada, T. Aoki, D. D. Thomas, and T. Yanagida. Mechanochemical coupling in actomyosin energy transduction studied by in vitro movement assay. *Journal of Molecular Biology*, 216(1):49–68, 1990.
- T. Hasson. Myosin VI: two distinct roles in endocytosis. *Journal of Cell Science*, 116(17):3453–3461, 2003.
- S. M. Heissler and J. R. Sellers. Kinetic Adaptations of Myosins for Their Diverse Cellular Functions. *Traffic*, 17:839–859, 2016.
- J. Howard. *Mechanics of Motor Proteins and the Cytoskeleton*. Sinauer, 2001.
- J. Howard. Mechanical Signaling in Networks of Motor and Cytoskeletal Proteins. *Annual Review of Biophysics*, 2009.
- H. Isambert, P. Venier, A. C. Maggs, A. Fattoum, R. Kassab, D. Pantaloni, and M. F. Carrier. Flexibility of actin filaments derived from thermal fluctuations. Effect of bound nucleotide, phalloidin, and muscle regulatory proteins. *Journal of Biological Chemistry*, 270(19):11437–11444, 1995.
- A. Ishijima, H. Kojima, H. Higuchi, Y. Harada, T. Funatsu, and T. Yanagida. Multiple- and single-molecule analysis of the actomyosin motor by nanometer-piconewton manipulation with a microneedle: unitary steps and forces. *Biophysical Journal*, 70(1):383–400, 1996.
- T. Ishikawa. *6 - Organization of dyneins in the axoneme*. Academic Press, second edition edition, 2018.
- A. Jégou and G. Romet-Lemonne. Single Filaments to Reveal the Multiple Flavors of Actin. *Biophysical Journal*, 2016.
- F. Jülicher and J. Prost. Spontaneous oscillations of collective molecular motors. *Physical Review Letters*, 78(23):4510–4513, 1997.
- W. Kabsch, H. G. Mannherz, D. Suck, E. F. Pai, and K. C. Holmes. Atomic structure of the actin: DNase I complex. *Nature*, 347(6288):37–44, 1990.

- E. Karsenti. Self-organization in cell biology: a brief history. *Nature Reviews Molecular Cell Biology*, 9(3):255–262, 2008.
- M. K. Kim, Y. Jang, and J. Jeong. Using harmonic analysis and optimization to study macromolecular dynamics. *International Journal of Control, Automation, and Systems*, 4(3):382–393, 2006.
- S. Kohler, O. Lieleg, and A. R. Bausch. Rheological characterization of the bundling transition in f-actin solutions induced by methylcellulose. *PLOS ONE*, 3(7):1–5, 07 2008.
- M. Kovacs, J. Toth, C. Hetenyi, A. Malnasi-Csizmadia, and J. R. Seller. Mechanism of blebbistatin inhibition of myosin II. *Journal of Biological Chemistry*, 279(34):35557–35563, 2004.
- D. Kovar and T. Pollard. Insertional assembly of actin filament barbed ends in association with formins produces piconewton forces. *Proceedings of the National Academy of Sciences*, 101(41):14725–14730, 2004.
- J. Kozuka, H. Yokota, Y. Arai, Y. Ishii, and T. Yanagida. Dynamic polymorphism of single actin molecules in the actin filament. *Nature Chemical Biology*, 2:83–86, 2006.
- S. J. Kron and J. A. Spudich. Fluorescent actin filaments move on myosin fixed to a glass surface. *Proceedings of the National Academy of Sciences*, 83(17):6272–6276, 1986.
- S. J. Kron, Y. Y. Toyoshima, T. Q. Uyeda, and J. A. Spudich. Molecular Motors and the Cytoskeleton. *Methods in Enzymology*, 196(1986):399–416, 1991.
- G. Letort, A. Z. Politi, H. Ennomani, M. Théry, F. Nédélec, and L. Blanchoin. Geometrical and mechanical properties control actin filament organization. *PLOS computational biology*, 11(5):e1004245, 2015.
- C. Lindemann. Geometric Clutch model version 3: The role of the inner and outer arm dyneins in the ciliary beat. *Cell Motility and the Cytoskeleton*, 52(4):242–254, Aug 2002.
- C. B. Lindemann. A geometric clutch hypothesis to explain oscillations of the axoneme of cilia and flagella. *Journal of Theoretical Biology*, 168(2):175–189, 1994a.
- C. B. Lindemann. A model of flagellar and ciliary functioning which uses the forces transverse to the axoneme as the regulator of dynein activation. *Cell Motility and the Cytoskeleton*, 29(2):141–154, 1994b.

- C. B. Lindemann and K. A. Lesich. Flagellar and ciliary beating: the proven and the possible. *Journal of Cell Science*, 123(4):519–528, 2010.
- I. Linsmeier, S. Banerjee, P. W. Oakes, W. Jung, T. Kim, and M. P. Murrell. Disordered actomyosin networks are sufficient to produce cooperative and telescopic contractility. *Nature Communications*, 7:12615, 2016.
- T. Luo and D. N. Robinson. Kinetic monte carlo simulations of the assembly of filamentous biomacromolecules by the dimer addition mechanism. *RSC Adv.*, 5:3922–3929, 2015.
- R. Ma, G. S. Klindt, I. H. Riedel-Kruse, F. Jülicher, and B. M. Friedrich. Active phase and amplitude fluctuations of flagellar beating. *Phys. Rev. Lett.*, 113(4):048101, Jul 2014.
- L. M. Machesky, R. Dyche Mullins, H. N. Higgs, D. A. Kaiser, L. Blanchoin, R. C. May, M. E. Hall, and T. D. Pollard. Scar, a WASp-related protein, activates nucleation of actin filaments by the Arp2/3 complex. *Cell Biology*, 96(7):3739–3744, 1999.
- J.-B. Marchand, D. A. Kaiser, T. D. Pollard, and H. N. Higgs. Interaction of WASP/Scar proteins with actin and vertebrate Arp2/3 complex. *Nature Cell Biology*, 3:76–82, 2001.
- W. F. Marshall. Cellular length control systems. *Annual Review of Cell and Developmental Biology*, 20(1):677–693, 2004.
- P. McClaughlin, J. Gooch, H. Mannherz, and A. Weeds. Structure of gelsolin seglent-1-actin complex and the mechanism of filament severing. *Nature*, 364(6439):685–692, 1993.
- A. D. Mehta, R. S. Rock, M. Rief, J. A. Spudich, M. S. Mooseker, and R. E. Cheney. Myosin-V is a processive actin-based motor. *Nature*, 400(6744):590–593, aug 5 1999.
- M. Miki, P. Wahl, and J. C. Achet. Fluorescence anisotropy of labeled F-actin: influence of divalent cations on the interaction between F-actin and myosin heads. *Biochemistry*, 21(15):3661–3665, 1982.
- J. E. Molloy, J. E. Burns, J. Kendrick-Jones, R. T. Tregear, and D. C. S. White. Movement and force produced by a single myosin head. *Nature*, 378(6553):209–212, nov 9 1995.
- R. D. Mullins, J. A. Heuser, and T. D. Pollard. The interaction of arp2/3 complex with actin: Nucleation, high affinity pointed end capping, and formation of branching networks of filaments. *Proceedings of the National Academy of Sciences*, 95(11):6181–6186, may 26 1998.

- F. J. Nédélec, T. Surrey, A. C. Maggs, and S. Leibler. Self-organization of microtubules and motors. *Nature*, 389(6648):305–308, 1997.
- F. C. Neidhardt, J. L. Ingraham, and M. Schaechter. *Physiology of the Bacterial Cell*. Sinauer, 1996.
- D. Nicastro, C. Schwartz, J. Pierson, R. Gaudette, M. E. Porter, and J. R. McIntosh. The molecular architecture of axonemes revealed by cryoelectron tomography. *Science*, 313(5789):944–948, 2006.
- T. Oda, M. Iwasa, T. Aihara, Y. Maeda, and A. Narita. The nature of the globular-to fibrous-actin transition. *Nature*, 457(7228):441–445, 2009.
- F. Odronitz and M. Kollmar. Drawing the tree of eukaryotic life based on the analysis of 2,269 manually annotated myosins from 328 species. *Genome Biology*, 8(9):196, 2007.
- Y. Okamoto and T. Sekine. A streamlined method of subfragment one preparation from myosin. *Journal of biochemistry*, 98(4):1143–1145, 1985.
- N. Okamura and S. Ishiwata. Spontaneous Oscillatory Contraction of Sarcomeres In Skeletal Myofibrils. *Journal of Muscle Research and Cell Motility*, 9(2):111–119, 1988.
- A. Okubo. Dynamical aspects of animal grouping: swarms, schools, flocks, and herds. *Advanced Biophysics*, 22:1–94, 1986.
- A. O. Olivares, W. Chang, M. S. Mooseker, D. D. Hackney, and E. M. De La Cruz. The tail domain of myosin Va modulates actin binding to one head. *Journal of Biological Chemistry*, 281(42):31326–31336, 2006.
- E. Paluch, M. Piel, J. Prost, M. Bornens, and C. Sykes. Cortical actomyosin breakage triggers shape oscillations in cells and cell fragments. *Biophysical Journal*, 89(1):724–733, 2005.
- G. J. Pazour, N. Agrin, J. Leszyk, and G. B. Witman. Proteomic analysis of a eukaryotic cilium. *Journal of Cell Biology*, 170(1):103–113, 2005.
- R. Philips, J. Kondev, J. Theriot, and H. Garcia. *Physical Biology of the Cell*. Garland Science, 2009.
- P.-Y. Plaças. *Propriétés mécaniques de la myosine II in vitro: de la molécule unique aux effets collectifs*. PhD thesis, Université Pierre et Marie Curie, 2008.

- P.-Y. Plaçais, M. Balland, T. Guérin, J.-F. Joanny, and P. Martin. Spontaneous oscillations of a minimal actomyosin system under elastic loading. *Phys. Rev. Lett.*, 103(15):158102, 2009.
- T. D. Pollard. Purification of a High Molecular Weight Actin Filament Gelation Protein from *Acanthamoeba* That Shares Antigenic Determinants with Vertebrate Spectrins. *Journal of Cell Biology*, 99(6):1970–1980, 1984.
- T. D. Pollard. Rate constants for the reactions of ATP- and ADP-actin with the ends of actin filaments. *Journal of Cell Biology*, 103(7):2747–2754, 1986.
- T. D. Pollard and G. G. Borisy. Cellular motility driven by assembly and disassembly of actin filaments. *Cell*, 112(4):453 – 465, 2003.
- J. Prost, F. Jülicher, and J.-F. Joanny. Active gel physics. *Nature Physics*, 11(2):111–117, 2015.
- C. G. D. Remedios, D. Chhabra, M. Kekic, I. V. Dedova, M. Tsubakihara, D. A. Berry, and N. J. Nosworthy. Actin binding proteins: Regulation of cytoskeletal microfilaments. *Physiological Reviews*, 83(2):433–473, 2003.
- A.-C. Reymann. *Dynamique des réseaux d’actine d’architecture contrôlée*. PhD thesis, Université Grenoble Alpes, 2011.
- A. C. Reymann, J. L. Martiel, T. Cambier, L. Blanchoin, R. Boujemaa-Paterski, and M. Théry. Nucleation geometry governs ordered actin networks structures. *Nature Materials*, 9(10):827–832, 2010.
- A.-C. Reymann, R. Boujemaa-Paterski, J.-L. Martiel, C. Guérin, W. Cao, H. F. Chin, E. M. De La Cruz, M. Théry, and L. Blanchoin. Actin network architecture can determine myosin motor activity. *Science*, 336(6086):1310–1314, 2012.
- A.-C. Reymann, C. Guerin, M. Thery, L. Blanchoin, and R. Boujemaa-Paterski. Geometrical Control of Actin Assembly and Contractility. *Methods in Cell Biology*, 120:19–38, 2014.
- M. Richard. *Activité motrice de myosines dans des réseaux d’actine d’architecture contrôlée in vitro*. PhD thesis, Université Paris Descartes, 2016.
- I. H. Riedel-Kruse, A. Hilfinger, J. Howard, and F. Jülicher. How molecular motors shape the flagellar beat. *HFSP Journal*, 1(3):192–208, 2007.

- M. Rief, R. S. Rock, A. D. Mehta, M. S. Mooseker, R. E. Cheney, and J. A. Spudich. Myosin-V stepping kinetics: A molecular model for processivity. *Proceedings of the National Academy of Sciences*, 97(17):9482–9486, 2000.
- R. Rikmenspoel. Movements and active moments of bull sperm flagella as a function of temperature and viscosity. *Journal of Experimental Biology*, 108:205–230, 1984.
- R. Rikmenspoel and C. A. Isles. Digitized precision measurements of the movements of sea urchin sperm flagella. *Biophysical Journal*, 47(3):395–410, 1985.
- R. Rikmenspoel, A. C. Jacklet, S. E. Orris, and C. Lindemann. Control of bull sperm motility. effects of viscosity, ken and thiourea. *Journal of Mechanochemistry and Cell Motility*, 2:7–24, 1973.
- V. I. Risca, E. B. Wang, O. Chaudhuri, J. J. Chia, P. L. Geissler, and D. A. Fletcher. Actin filament curvature biases branching direction. *Proceedings of the National Academy of Sciences*, 109(8):2913–2918, 2012.
- R. S. Rock, M. Rief, A. D. Mehta, and J. A. Spudich. In vitro assays of processive myosin motors. *Methods*, 22(4):373 – 381, 2000.
- J. D. Rotty, C. Wu, and J. E. Bear. New insights into the regulation and cellular functions of the Arp 2/3 complex. *Nature Reviews Molecular Cell Biology*, 14:7–12, 2013.
- T. Sakamoto, J. Limouze, C. A. Combs, A. F. Straight, and J. R. Sellers. Blebbistatin, a myosin II inhibitor, is photoinactivated by blue light. *Biochemistry*, 44(2):584–588, 2005.
- G. Salbreux, J. F. Joanny, J. Prost, and P. Pullarkat. Shape oscillations of non-adhering fibroblast cells. *Physical Biology*, 4(4):268–284, 2007.
- T. Sanchez, D. Welch, D. Nicastro, and Z. Dogic. Cilia-like beating of active microtubule bundles. *Science*, 333(6041):456–459, 2011.
- P. Sartori, V. F. Geyer, A. Scholich, F. Juelicher, and J. Howard. Dynamic curvature regulation accounts for the symmetric and asymmetric beats of *Chlamydomonas* flagella. *eLife*, 5(13258), 2016.
- P. Satir and S. T. Christensen. Overview of structure and function of mammalian cilia. *Annual Review of Physiology*, 69(1):377–400, 2007.
- C. E. Schutt, J. C. Myslik, M. D. Rozycki, N. C. W. Goonesekere, and U. Lindberg. The structure of crystalline profilin- β -actin. *Nature*, 365(6449):810–816, 1993.

- D. Sept and J. A. McCammon. Thermodynamics and kinetics of actin filament nucleation. *Biophysical Journal*, 81(2):667–674, 2001.
- T. Shimozawa and S. Ishiwata. Mechanical distortion of single actin filaments induced by external force: Detection by fluorescence imaging. *Biophysical Journal*, 96(3):1036–1044, 2009.
- M. Soares e Silva, J. Alvarado, J. Nguyen, N. Georgoulia, B. M. Mulder, and G. H. Koenderink. Self-organized patterns of actin filaments in cell-sized confinement. *Soft Matter*, 7(22):10631–10641, 2011.
- L. Song, E. J. Hennink, I. T. Young, and H. J. Tanke. Photobleaching kinetics of fluorescein in quantitative fluorescence microscopy. *Biophysical Journal*, 68(6):2588–2600, 1995.
- J. A. Spudich and S. Sivaramakrishnan. Myosin VI: An innovative motor that challenged the swinging lever arm hypothesis. *Nature Reviews Molecular Cell Biology*, 11(2):128–137, 2010.
- J. A. Spudich, S. J. Kron, and M. P. Sheetz. Movement of myosin-coated beads on oriented filaments reconstituted from purified actin. *Nature*, 315:584, 1985.
- C. Steger. An Unbiased Detector of Curvilinear Structures. *IEEE Transactions on Pattern Analysis and Machine Intelligence*, 20(2):113–125, 1998.
- K. Summers and I. Gibbons. Adenosine triphosphate-induced sliding of tubules in trypsin-treated flagella of sea-urchin sperm. *Proceedings of the National Academy of Sciences*, 68(12):3092–3096, 1971.
- K. Svoboda, C. F. Schmidt, B. J. Schnapp, and S. M. Block. Direct observation of kinesin stepping by optical trapping interferometry. *Nature*, 365(6448):721–727, 1993.
- H. L. Sweeney and A. Houdusse. Structural and functional insights into the myosin motor mechanism. *Annual Review of Biophysics*, 39(1):539–557, 2010.
- B. Takács, N. Billington, M. Gyimesi, B. Kintses, A. Málnási-Csizmadia, P. J. Knight, and M. Kovács. Myosin complexed with ADP and blebbistatin reversibly adopts a conformation resembling the start point of the working stroke. *Proceedings of the National Academy of Sciences of the United States of America*, 107(15):6799–6804, 2010.
- G. Taylor. Analysis of the swimming of microscopic organisms. *Proceedings of the Royal Society of London Series a Mathematical and Physical Sciences*, 209(1099):447–461, 1951.

- M. Thery, V. Racine, M. Piel, A. Pepin, A. Dimitrov, Y. Chen, J.-B. Sibarita, and M. Bornens. Anisotropy of cell adhesive microenvironment governs cell internal organization and orientation of polarity. *Proceedings of the National Academy of Sciences*, 103(52):19771–19776, 2006.
- K. Tokuraku, R. Kurogi, R. Toya, and T. Q. P. Uyeda. Novel Mode of Cooperative Binding between Myosin and Mg²⁺-actin Filaments in the Presence of Low Concentrations of ATP. *Journal of Molecular Biology*, 386(1):149–162, 2009.
- A. K. Tsaturyan, N. Koubassova, M. A. Ferenczi, T. Narayanan, M. Roessle, and S. Y. Bershitsky. Strong Binding of Myosin Heads Stretches and Twists the Actin Helix. *Biophysical Journal*, 88(3):1902–1910, 2005.
- T. Q. P. Uyeda, Y. Iwadate, N. Umeki, A. Nagasaki, and S. Yumura. Stretching actin filaments within cells enhances their affinity for the myosin ii motor domain. *PLOS ONE*, 6(10):1–12, 2011.
- C. Veigel, M. L. Bartoo, D. C. White, J. C. Sparrow, and J. E. Molloy. The stiffness of rabbit skeletal actomyosin cross-bridges determined with an optical tweezers transducer. *Biophysical Journal*, 75(3):1424 – 1438, 1998.
- C. Veigel, F. Wang, M. L. Bartoo, J. R. Sellers, and J. E. Molloy. The gated gait of the processive molecular motor, myosin V. *Nature Cell Biology*, 4:59–65, 2002.
- C. Veigel, J. E. Molloy, S. Schmitz, and J. Kendrick-Jones. Load-dependent kinetics of force production by smooth muscle myosin measured with optical tweezers. *Nature Cell Biology*, 5(11):980–986, 2003.
- L. Vincensini, T. Blisnick, and P. Bastin. 1001 model organisms to study cilia and flagella. *Biology of the Cell*, 103(3):109–130, 2011.
- V. K. Vinson, E. M. De La Cruz, H. N. Higgs, and T. D. Pollard. Interactions of Acanthamoeba Profilin with Actin and Nucleotides Bound to Actin. *Biochemistry*, 37(31):10871–10880, 1998.
- K. Visscher, M. J. Schnitzer, and S. M. Block. Single kinesin molecules studied with a molecular force clamp. *Nature*, 400(6740):184–189, 1999.
- M. L. Walker, S. A. Burgess, J. R. Sellers, F. Wang, J. A. Hammer, J. Trinick, and P. J. Knight. Two-headed binding of a processive myosin to F-actin. *Nature*, 405(6788):804–807, 2000.

- H. M. Warrick, R. M. Simmons, J. T. Finer, T. Q. Uyeda, S. Chu, and J. a. Spudich. In vitro methods for measuring force and velocity of the actin-myosin interaction using purified proteins. *Methods in cell biology*, 39:1–21, 1993.
- R. Wedlich-Söldner and T. Betz. Self-organization: the fundament of cell biology. *Philosophical Transactions of the Royal Society B: Biological Sciences*, 373(1747):20170103, 2018.
- M. White, S. Bissiere, Y. Alvarez, and N. Plachta. Chapter seven - mouse embryo compaction. In M. L. DePamphilis, editor, *Mammalian Preimplantation Development*, volume 120 of *Current Topics in Developmental Biology*, pages 235 – 258. Academic Press, 2016.
- D. Woolley and G. Vernon. A study of helical and planar waves on sea urchin sperm flagella, with a theory of how they are generated. *Journal of Experimental Biology*, 204(7):1333–1345, apr 2001. ISSN 0022-0949.
- D. M. Woolley, R. F. Crockett, W. D. I. Groom, and S. G. Revell. A study of synchronisation between the flagella of bull spermatozoa, with related observations. *Journal of Experimental Biology*, 212(14):2215–2223, 2009.
- A. Yildiz, J. N. Forkey, S. A. McKinney, T. Ha, Y. E. Goldman, and P. R. Selvin. Myosin v walks hand-over-hand: Single fluorophore imaging with 1.5-nm localization. *Science*, 300(5628):2061–2065, 2003.

Abstract:

The emergent active behaviors of molecular motors assemblies and cytoskeletal filaments systems remain poorly understood, though individual molecules have been extensively characterized. By controlling the geometry of actin polymerization with surface micropatterns of a nucleation promoting factor, we were able to demonstrate *in vitro* the emergence of flagellar-like beating of bundles of parallel actin filaments in the presence of myosin motors. We worked with both myosin V and heavy-meromyosin II. The waveform of oscillation was similar for the two types of motors, but oscillations with myosin II were one order of magnitude faster than with myosin Va. In both cases, a bending wave traveled at a uniform speed from the anchored base of the actin bundle towards the tip. As polymerization occurred, the actin bundle elongated at a constant speed, resulting in an increase of the oscillation period, but the speed of the traveling bending wave remains constant. GFP-tagged myosin V revealed the presence of a myosin concentration peak within the actin bundle. Strikingly, myosin V motors were locally recruited within the actin bundle, before a concentration wave propagated towards the bundle's tip in concert with the actin bending wave. These results revealed a novel form of coupling between the myosin affinity for actin and the actin bundle shape. Our work demonstrates that active flagellar-like beating emerges as an intrinsic property of polar bundles of filaments in interaction with molecular motors. Structural control over the self-assembly process provides key information to clarify the underlying physical principles of flagellar-like beating.

Keywords: actin, myosin, spontaneous oscillations, self-organization, cytoskeleton, *in vitro*

Résumé:

L'interaction d'assemblées de moteurs et de filaments du cytosquelette donne naissance à des comportements actifs qui demeurent peu compris, malgré la large caractérisation de leurs molécules individuellement. En contrôlant la géométrie de polymérisation de l'actine via des micropatrons surfaciques de nucléation, nous avons observé *in vitro* l'émergence de battements de faisceaux de filaments parallèles d'actine en présence de myosines en solution (myosine V ou HMM II (Heavy MeroMyosine II)). La forme du battement est similaire pour les deux types de moteurs, mais avec des oscillations un ordre de grandeur plus rapides avec la myosine II qu'avec la myosine V. Dans les deux cas, une onde de déformation transverse se propage à vitesse uniforme de la base à la pointe du faisceau d'actine. Avec la polymérisation, les faisceaux d'actine s'allongent à vitesse constante : la période croît, mais la vitesse de l'onde mécanique reste inchangée. L'utilisation de myosines-GFP a révélé un pic de concentration et un recrutement localisé des myosines au sein du faisceau d'actine, avant qu'une onde de concentration ne se propage vers la pointe de concert avec l'onde mécanique de l'actine. Ces résultats présentent une nouvelle forme de couplage entre l'affinité des myosines à l'actine et la forme du faisceau d'actine. Ce travail de thèse décrit l'émergence de battements actifs imitant ceux des flagelles comme une propriété intrinsèque de l'interactions de filaments polaires et de moteurs moléculaires. Le contrôle de la structure lors du processus d'auto-organisation fournit des informations clés pour étudier les principes physiques génériques du battement flagellaire.

Mots-clés actine, myosine, oscillations spontanées, auto-organisation, cytosquelette, *in vitro*